Old Dominion University

ODU Digital Commons

Fall 2019

Laser-Spark Multicharged Ion Implantation System – Application in Ion Implantation and Neural Deposition of Carbon in Nickel (111)

Oguzhan Balki
Old Dominion University, obalki@yahoo.com

Recommended Citation

LASER–SPARK MULTICHARGED ION IMPLANTATION SYSTEM –

APPLICATION IN ION IMPLANTATION AND NEURAL DEPOSITION OF CARBON

IN NICKEL (111)

by

Oguzhan Balki
B.S. August 2006, Istanbul University
M.S. May 2010, Old Dominion University

A Dissertation Submitted to the Faculty of
Old Dominion University in Partial Fulfillment of the
Requirements for the Degree of

DOCTOR OF PHILOSOPHY

ELECTRICAL AND COMPUTER ENGINEERING

OLD DOMINION UNIVERSITY
October 2019

Approved by:

Hani E. Elsayed-Ali (Director)

Helmut Baumgart (Member)

Shu Xiao (Member)

Geoffrey Kraft (Member)

ABSTRACT

LASER−SPARK MULTICHARGED ION IMPLANTATION SYSTEM – APPLICATION IN ION IMPLANTATION AND NEUTRAL DEPOSITION OF CARBON IN NICKEL (111)

Oguzhan Balki
Old Dominion University, 2019
Director: Dr. Hani E. Elsayed-Ali

Carbon ions generated by ablation of a carbon target using an Nd:YAG laser pulse (wavelength λ = 1064 nm, pulse width τ = 7 ns, and laser fluence of 10-110 J/cm^2) are characterized. Time-of-flight analyzer, a three-mesh retarding field analyzer, and an electrostatic ion energy analyzer are used to study the charge and energy of carbon ions generated by laser ablation. The dependencies of the ion signal on the laser fluence, laser focal point position relative to target surface, and the acceleration voltage are described. Up to C^{4+} are observed. When no acceleration voltage is applied between the carbon target and a grounded mesh in front of the target, ion energies up to ∼400 eV/charge are observed. The time-of-flight signal is analyzed for different retarding field voltages in order to obtain the ion kinetic energy distribution. The ablation and Coulomb energies developed in the laser plasma are obtained from deconvolution of the ion time-of-flight signal. Deconvolution of the time-of-flight ion signal to resolve the contribution of each ion charge is accomplished using data from a retarding field analysis combined with the time-of-flight signal. The ion energy and charge state increase with the laser fluence. The position of the laser focal spot affects the ion generation, with focusing ∼1.9 mm in front of the target surface yielding maximum ions. When an external electric field is applied in an ion drift region between the target and a grounded mesh parallel to the target, fast ions are extracted and separated, in time, due to increased acceleration with charge state. However, the ion energy accelerated by the

externally applied electric field is less than the potential drop between the target and mesh due to plasma shielding.

By coupling a spark discharge into a laser-generated carbon plasma, fully-stripped carbon ions with a relatively low laser pulse energy are observed. When spark-discharge energy of ~750 mJ is coupled to the carbon plasma generated by ~50 mJ laser pulse (wavelength 1064 nm, pulse width 8 ns, intensity 5×10^9 W/cm^2), enhancement in the total ion charge by a factor of ~6 is observed, along with the increase of maximum charge state from C^{4+} to C^{6+}. Spark coupling to the laser plasma significantly reduces the laser pulse energy required to generate highly-charged ions. Compared to the laser carbon plasma alone, the spark discharge increases the intensity of the spectral emission of carbon lines, the electron density n_e, and the electron temperature T_e. The effective ion plasma temperature associated with translational motion along the plume axis T_{ieff} is calculated from the ion time-of-flight signal.

Carbon laser plasma generated by an Nd:YAG laser (wavelength 1064 nm, pulse width 7 ns, fluence 4-52 J/cm^2) is studied by optical emission spectroscopy and ion time-of-flight. Up to C^{4+} ions are detected with the ion flux strongly dependent on the laser fluence. The increase in ion charge with the laser fluence is accompanied by observation of multicharged ion lines in the optical spectra. The time-integrated electron temperature T_e is calculated from the Boltzmann plot using the C II lines at 392.0, 426.7, and 588.9 nm. T_e is found to increase from ~0.83 eV for a laser fluence of 22 J/cm^2 to ~0.90 eV for 40 J/cm^2. The electron density n_e is obtained from the Stark broadened profiles of the C II line at 392 nm and is found to increase from ~2.1×10^{17} cm^{-3} for 4 J/cm^2 to ~3.5×10^{17} cm^{-3} for 40 J/cm^2. Applying an external electric field parallel to the expanding plume shows no effect on the line emission intensities. Deconvolution of ion time-of-flight signal

with a shifted Maxwell-Boltzmann distribution for each charge state results in an ion temperature $T_i \sim 4.7$ and ~ 6.0 eV for 20 and 36 J/cm^2, respectively.

Carbon ion emission from femtosecond laser ablation of a glassy carbon target is studied. A Ti:sapphire laser (pulse duration $\tau \sim 150$ fs, wavelength $\lambda = 800$ nm, laser fluence $F \leq 6.4$ J/cm^2) is used to ablate the carbon target while ion emission is detected by a time-of-flight detector equipped with a three-grid retarding field analyzer. A strong effect of the laser pulse fluence on the yield of carbon ions is observed. Up to C^{6+} ions are detected. The carbon time-of-flight ion signal is fit to a shifted Maxwell-Boltzmann distribution and used to extrapolate the effective plasma ion temperature $T_{ieff} = 6.9$ eV. Applying an external electric field along the plasma expansion direction increased ion extraction, possibly due to the retrograde motion of the plasma-vacuum edge.

The laser ion source is utilized for carbon ion implantation of Ni(111), aiming for graphene synthesis. Ni(111) thin films are prepared with magnetron sputter coater on mica substrates at 500 °C with 400 nm thickness. Ni(111) thin films are analyzed with XRD and showed that the surface mostly contains single crystal Ni(111). Carbon at +5, -5, -10, and -15 keV of Ni (111) biasing with a series of dosages were implanted into Ni(111) films at room temperature. Carbon nanostructures such as amorphous carbon and diamond-like carbon were synthesized on Ni(111) substrates by the laser generated carbon ion implantation.

This thesis is dedicated to my loved ones.

ACKNOWLEDGMENTS

There are many people who have contributed to the successful completion of this dissertation. I acknowledge and thank the members of my dissertation committee. I would like to express my grateful appreciation to Dr. Helmut Baumgart, Dr. Shu Xiao, and Dr. Geoffrey Kraft not only for their time and extreme patience, but for their intellectual contributions and comments.

Most of all, Dr. Hani E. Elsayed-Ali, my advisor, has been an excellent mentor and guide throughout the graduate experience. He has provided insightful thoughts and wise understanding into my scientific research. I am proud that despite the hard work of graduate studies in the laser lab; his strong support, confidence, and research directions along his ability to provide the best tools available, has encouraged and energized me to continue in academic research which made me the kind of scientist I am today.

To my lab-mates, thanks for all the support and fun. My experience with Md. Haider Ali Shaim and Md. Nizam Sayeed has extended my insights for the research I have conducted. Despite the hard sides and devoting endless efforts of setting up a new lab and its equipment, Md. Mahmudur Rahman has offered his personal time to help me which eventually made him an excellent lab-mate, friend, and a source of great support. Most of all, their great suggestions, feedback, and help throughout my graduate studies shaped the outcome, professionally and personally, of my life. The assistance of Dr. Wei Cao for the instruments and his friendship is also valuable.

I am truly grateful to my mother and father for all their help and support throughout this challenging work. The completion of this work would not be possible without the inspiration, encouragement, and understanding that my wife, Meltem has provided. You and my daughter, Meryem, are the ones who actually sustained me to successfully complete this chapter of my life.

TABLE OF CONTENTS

LIST OF TABLES

LIST OF FIGURES

CHAPTER 1

INTRODUCTION

Multicharged ion (MCI) sources have uses in nanoprocessing, secondary ion mass-spectroscopy, and ion implantation [1, 2]. When used for surface modification, MCIs with low kinetic energies have high surface selectivity causing strong local excitation not accessible with singly-charged ions. An MCI interaction with a surface can trigger local surface modification by potential sputtering resulting in the formation of a nano-scale crater, a feature that may be useful for nanopatterning [3]. MCIs can be used in semiconductor surface processing due to their high potential energy combined with low kinetic energy which allows for localizing the ion potential energy at the surface. In some applications, the use of MCIs is attractive since their high potential energy is localized to the surface and they can be accelerated with reduced electrostatic field and bent and focused with reduced magnetic field.

Laser-generated plasmas have been widely used as a source of intense MCIs that are capable of generating MCIs from any solid target [4]. Nanosecond lasers are used in most laser ion sources, however, femtosecond lasers have also been demonstrated to yield MCIs with high charge states [5]. Laser ion sources have the capability of providing pulsed MCI beams with high currents which is attractive as an ion injector for ion accelerators [6]. Many techniques are used to probe laser generated ion characteristics namely time-of-flight spectrometer, ion energy and mass spectrometers, and retarding field analyzers [7]. Calculations of ionic energy distributions are critical for the ion implantation of materials aiming to change surface properties. Plasma characteristics such as electron density n_e and temperature T_e, can be diagnosed with optical emission spectroscopy (OES) [4], Thomson scattering [8], and laser interferometry [9].

Multicharged ions are generated by ablating a solid target with a focused laser pulse where the power densities are between $10^9 - 10^{16}$ W/cm^2 [10]. In a laser produced plasma, the Knudsen layer is formed within a few particle free paths near the target surface in which as few as 3 collisions per particle occurs [11]. Particles vaporized, sputtered, or desorbed reach equilibrium with each other within the Knudsen layer formed in a near-surface region during the laser ablation due to strong gas-phase interactions. This leads to a directional expansion perpendicular to the target surface. The ions are freely drifting into the vacuum, and ion charge-states are frozen at large distances. Furthermore, introducing an electric field increases the kinetic energy of ions, thus separation of ions occurs with faster arrival time at the Faraday cup. More electrons are repelled and more ions are exposed to the accelerating field. Space-charge limited flow in the ion sheath governs the ion extraction if the ion density is neglected during ion extraction by the external electric field [12].

The process of ion acceleration is initiated by electron acceleration by inverse Bremsstrahlung within the laser pulse duration. Due to the slower mobility of ions compared to the electrons, large Coulomb forces are formed between fast electron and ion layers in the early stages of plasma plume formation. The electric field due to the Coulomb forces accelerates ions with higher degree of ionization to higher kinetic energies. The ions with higher kinetic energies are located in the outer position of the plasma plume due to their higher flow velocity [13].

1.1 Laser Ion Source (LIS) For Ion Implantation

Laser-induced ion implantation is a competitive method to use for semiconductor nanocrystals, metallic layer deposition, and surface modification [14]. As a robust and efficient source of ion generation with energies reaching to MeV, studies on developing new implantation

techniques also consider that LIS has a potential as a compact source of ions of many elements and with different charges [15]. High repetition rate laser can deliver high ion doses for commercial applications whereas single pulse operation is widely adopted for research. LIS has a unique feature, compared to traditional deposition and sputter technologies, that is the newly formed layer is not on the substrate surface, it is inside the substrate surface. Adhesion issues are thus eliminated. LIS can implant ions deeper due to higher charge states with high energies. A laser pulse at a low intensity operating with high energy can deliver a sufficiently high ions dose to meet the demanding needs for ion implanters. LISs provide several advantages over the traditional ion implanting systems. LIS can generate ions from any element especially from high-melting materials such as tungsten (W) and tantalum (Ta). Implantation depth is related to the charge state of the ions. Target to substrate distance, electrostatic ion selection, annealing conditions, and biasing of either a moving target or substrate can be adjusted accordingly. A major requirement is that delivering a beam of ions at same specific energy, free of any impurities, and at high doses. An electrostatic deflection system and a focusing Einzel lens can be incorporated to meet these requirements. High ion doses with minimal energy distribution are needed for ion implantation, which is the main difficulty for LISs.

There have been numerous investigations of laser-induced ion implantation. Rosinski *et al.* reported on the direct ultra-low-energy Ge ions implantation in thin layers of semiconductor for modification of optical and electrical properties with a laser-produced (Nd:glass, $\lambda = 1064$ nm, 2 Hz, $\tau = 3.5$ ns, $I = 10^{10}$ W/cm^2) ion beam [16]. They introduced an electrostatic field for ion acceleration and formation of laser-generated ions to control the parameters of current density and ion energy ranges. Electrostatic field also filtered out the ions of not interest. The depth profiles of post-accelerated Ge ions implanted into SiO_2 were characterized using Auger electron

spectroscopy (AES) [16]. They showed most of Ge ions were implanted at a depth of 10 nm with concentrations reaching to 5% at a depth of 7 nm. Ge ions were also detected at 20 nm depth with a concentration greater than 1% [16]. Fominski *et al.* reported on fabricating a hydrogen sensor on a 6H-SiC single crystal with a combination of platinum (Pt) thin film deposition and Pt ions implantation [17]. This approach provided efficient and controlled Pt doping of the SiC surface layers. Pt target was positively biased when plasma was expanding to the SiC substrate. Pt^{2+} ions were accelerated to an energy of ∼100 keV. Nanocomposite layer was formed near the surface of SiC crystal which acted as a Schottky diode [17].

1.2 Previous Studies of Graphene Fabrication by Carbon Ion Implantation

One group used 200 nm Ni films deposited on SiO_2 and 80 keV carbon ions implantation with a dose of 1.6×10^{16} cm^{-2} (equivalent to 4 layers of graphene) followed by thermal annealing [18]. Graphene layers were mostly formed by nucleation on the Ni surface. Garaj *et al.*, also reported on graphene films grown on thermally-annealed polycrystalline Ni substrates [19]. They evaporated 500 nm of Ni on Si/SiO_2 wafers at 1000 °C in Ar and H_2 flow for two hours at ambient pressure (no other information). 30 keV singly-charged carbon ions were implanted with doses of ∼10^{15} cm^{-2}. Post annealing at 1000 °C for 2 hours with controllable cooling at a rate of 5-20 °C/min until room temperature was reached and resulted in graphene formation.

Kim *et al.*, reported on graphene fabrication with carbon ions that are accelerated to 20 keV with a dosage of 1×10^{15} cm^{-2} on substrates of $Ni/SiO_2/Si$ that is heated to 500 °C [20]. The annealing temperature and time were of critical importance and temperatures of 600-900 °C showed that this technique can be used for growth of graphene on Si substrates [20].

Graphene can be synthesized using magnetron sputtering at low temperatures on different substrates. One study synthesized single and multilayer graphene [21]. They reported that the crystalline structure depends on the process parameters such as target temperature, hydrogen pressure, temperatures, and the foil position in the chamber. Higher deposition temperatures resulted in smaller crystalline size and higher electrical conductivities compared to CVD prepared graphene layers [22]. CVD growth of graphene introduces contaminations into the material [23]. Bangert *et al.* studied doping of graphene with low energy boron ion implantation, and suggested that the contamination issues can be solved with ion implantation [24].

1.3 Scope of the Dissertation

This dissertation is structured as following: Chapter 2 gives an overview of thin film growth mechanisms, and discusses the vacuum deposition methods; chemical vapor deposition (CVD), and sputter deposition, focusing especially on carbon based thin films. This chapter also provides an overview of diamond-like carbon films, and graphene. Chapter 3 presents the widely used ion sources, namely radio frequency (RF) ion source, electron cyclotron resonance (ECR) ion source, magnetron sputtering ion source, and laser ion source (LIS). Chapter 4 discusses the carbon ions generation by a nanosecond pulsed laser ion source. The characterization is carried out by a time-of-flight analyzer equipped with retarding field energy analyzer, and an electrostatic ion energy analyzer. The dependencies of the ion signal on the laser fluence, laser focal point position relative to target surface, and the acceleration voltage are described. Chapter 5 explains the studies on carbon laser plasma by optical emission spectroscopy and ion time-of-flight analyzer. The laser fluence increases the ions generation yield which is accompanied by the observation of multicharged carbon ion lines in the optical spectra. Chapter 6 describes the coupling of a spark discharge into a laser-generated carbon plasma. Significant enhancement in the ion's generation

yield and charge state up to fully stripped C^{6+} is observed, where relatively low laser pulse energy is used. The characterization is mainly conducted by varied spark discharge energy that is shaped by a pulse forming network. Diagnostics are carried by an optical emission spectrometer, time-of-flight analyzer, and electrostatic energy analyzer. Chapter 7 deals with the generation of carbon ions by a femtosecond laser ablation. Carbon ion emission is detected by a time-of-flight analyzer equipped with a three-grid retarding field analyzer. A strong effect of the laser pulse fluence on the yield of carbon ions is observed. Up to fully stripped C^{6+} ions are detected. Chapter 8 provides insights into carbon films synthesis by carbon ions direct implantation to Ni(111) thin films. The main characterization is conducted by a Raman spectrometer, field emission scanning electron microscopy (FESEM), X-ray diffraction (XRD), and energy dispersive spectroscopy (EDS). Finally, Chapter 9 summarizes the results of this work. Technical details about the maintenance, operation and instruments used throughout the studies are given in the appendices.

CHAPTER 2

DEPOSITION METHODS OF CARBON THIN FILMS

2.1 Introduction

Carbon atoms can form four identical covalent bonds to a variety of other atoms which results in a tetrahedral structure. Carbon has four electrons in its valence shell, and thus, it can reach a noble gas configuration by gaining, sharing, or losing four electrons. However, losing four electrons would need large amounts of energy, not possible to overcome by a chemical reaction. In turn, carbon atoms cannot form an ionic bond, and only participate for covalent bonding. Carbon has a number of allotropes due to the way that carbon atoms arrange in space, like graphite, graphene, diamond, and fullerenes with different properties ranging from being extremely hard to very soft [25-27].

Carbon exists in three hybridizations; sp^3, sp^2, and sp^1 so it can form variety of structures. When carbon is bonded to four atoms, that is with no electron pairs available, the sp^3 hybridization occurs with a tetrahedral arrangement, as in diamond. When bounded to three atoms, that is two single bonds and one double bond, sp^2 hybridization occurs. An arrangement of triangular with 120° angles between bonds form, as in graphite. When carbon bounds to two other atoms with either two double or one triple and one single bond, a linear arrangement with 180° angle between bonds is achieved [28-30].

Graphite has an atomic arrangement of carbon atoms as planar layers with hexagonal structure in a honeycomb lattice that allows electrons to freely move between the planes. This arrangement results in conducting heat, electricity, and absorption of light [31]. The diamond is known for its high hardness, durability, and thermal conductivity due to its rigid three-dimensional

structure, and tetrahedral atomic arrangement. Diamonds are good conductors of heat and sound, but are good insulators for electricity with a bandgap of 5.5 eV, the largest of any solid. In addition to the known crystalline forms of graphite and diamond, there are amorphous forms such as glassy carbon. Carbon nanomaterials can be in several shapes and among those are: carbon nanofibers, graphene, buckminsterfullerene (C_{60}), and diamond-like carbon (DLC) [32]. Fig. 2.1 shows the phase diagram of pure carbon, identifying the conditions required for each phase [33]. Solid lines indicate the boundaries for which some experimental evidence is present. Dashed lines represent the theoretically proposed phase boundaries. The binding energy between atoms of carbon is very large; for instance the cohesive energy of diamond is 717 kJ/mol [34]. Once carbon atoms are locked into a given phase configuration, typically a large amount of activation energy is required to produce a different stable phase; in other words, very high temperatures are required to initiate spontaneous transformations from one phase to another. For the pressure and temperatures of up to 3.7×10^8 Torr and 6,000 K, carbon is in a form of a graphite and diamond solid phase at low temperatures, and liquid phase at higher temperatures. This transformation can be carried out by irradiating a graphite sample with a pulsed laser radiation above 0.9×10^8 Torr pressures [34]. The complete transformation of graphite to diamond can be achieved by pressurizing diamond and rapid heating by a pulse of an electric current to the threshold temperatures. The diamond, graphite, and vapor phases are well-known, however liquid and boundary conditions are little known due to lack of supporting experimental evidence.
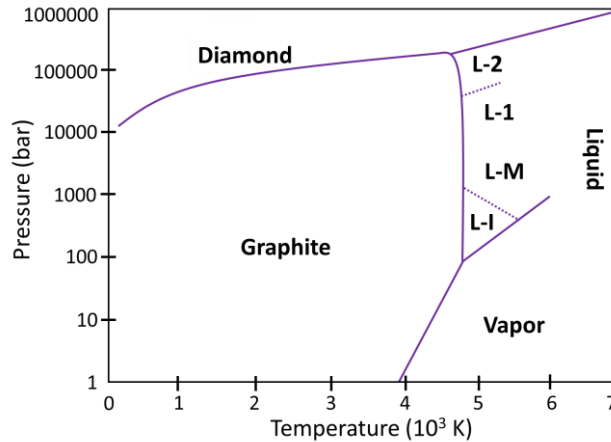
Fig. 2. 1 Pressure-temperature phase diagram of carbon. Solid lines are experimentally observed, dashed lines are theoretically proposed boundaries. (L-I: liquid insulator, L-M: liquid metal, L-1: graphite liquid, and L-2: diamond-like liquid). Redrawn from Ref. [33].

Some of the common applications of carbon are for heat resistant devices, tools, and cooling systems. The electrical conductivity of carbon depends on the degree of orientation of the carbon layers so that carbon materials can operate at a wide range of conductivity allowing a variety of applications [35]. On the other hand, carbon thin films possess unusual structural properties and have significant research interests [36, 37]. Diamond-like carbons are more resistive to chemical reactions, possess high hardness and wear resistance, and have dense morphology compared to other carbon-based materials [37]. Carbon nanotube electronic properties are variable, and depending on the structure, they can be used either as semiconductor or conductor [37].

2.2 Thin Film Growth Mechanisms

Thin films are applied to materials to modify, protect their surfaces, or assemble devices. The microstructure of the thin film affects the electrical, mechanical or optical properties, thus,

has great influence on how they operate. Synthesis of thin films is generally referred as deposition. Metal thin films deposition technique is classified either chemical or physical, depending on the primary thin film formation process [38]. In chemical deposition, a chemical change by a precursor occurs at a solid surface resulting in a solid layer [38]. The deposition occurs on every surface so the chemical deposition is regarded as conformal. The precursor can be in liquid, sol-gel, plasma, or gaseous forms. In physical deposition, a physical mechanism transfers the particles of a material to the substrate that are extracted from the material surface by energetic means such as ions, plasma, or laser pulse [39]. The extracted particles generally follow a straight path so the physical deposition is considered as a directional process. The suitable deposition technique is chosen based on the desired application and utilization expenses. Aside from the applied technique, the formation of thin film growth process depends on fundamental steps: separation of the particles from the source material, their transport, and interaction with the substrate [39]. The whole process consists of several steps in order: absorption of the atom, surface diffusion, chemisorption; molecule-molecule or substrate-molecule bond formation, nucleation, structure formation, and changes in bulk properties (grain growth, diffusion, etc.) [39].

Impinging atoms need to be absorbed by the substrate. This is possible if the impinging atoms lose enough energy to stay on the substrate surface. After they collide with the substrate, most of their kinetic energy is lost, and their potential energy is minimized as the adsorption takes place. The diffusion of the adatoms (adsorbed atoms) is governed by surface diffusion coefficient, D [40]:

$$D = \frac{1}{4}a^2\Gamma = D_0 e^{-\frac{E_d}{k_B T}} \tag{2.1}$$

where Γ is the jump rate of the adatoms, a is the separation of adsorption sites, E_d is the diffusion barrier, T is the substrate temperature, and k_B is the Boltzmann's constant. D_0 and E_d are

experimentally determined surface diffusion parameters [40]. Here, the diffusion barrier is affected from the adatoms and impurities but mostly depends on the surface atomic structure so its value depends on the type of the materials. The diffusion rate increases with temperature. This step is followed by the chemical bond formation (chemisorption). Adatoms bound to substrate or other adatoms which they can bind to. All these events result in a formation of several cluster adatoms, referred as nuclei, the first stage of the film growth. Adatoms diffuse randomly in the early stages of the growth but they grow into clusters when encountered to other atoms.

The nucleation process can be manipulated by the addition of impurities or having defects on the substrate to introduce more nucleation sites. Substrate temperature and deposition rate affect the nucleation. The nucleus and their subsequent merge will form the final thin film structure. A schematic in Fig. 2.2(a) shows the growth steps of a thin film. The thin film formation on a substrate has three major growth modes: Frank-van der Merve (2D morphology, layer-by-layer growth), Volmer-Weber (3D morphology, island growth), and Stranski-Krastanov (initial 2D growth; layer, then 3D morphology; island) as seen in Fig. 2.2(b), (c), and (d) [41].
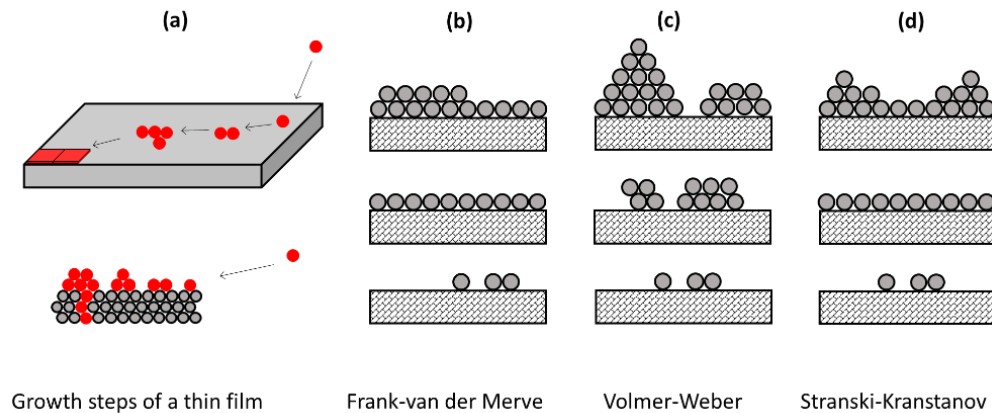
Fig. 2. 2 The schematic of different growth mechanisms on a crystalline substrate. Redrawn from Ref. [41].

Thin film growth is layer-by-layer, on top of another for Frank-van der Merve mode. This mode achieves strong atomic bond interactions to the substrate with smooth film formation at high crystalline quality. However, the interactions between atoms are weak in this mode. Stranski-Krastanov (mixed) grows one or two monolayers initially grow and the island formations follow. Interactions between atoms are strong in Volmer-Weber mode. The growth is not uniform and the diffusion is slow. The total surface energy of the film interface is larger than that of the substrate-vapor interface.

2.3 Deposition Methods for Carbon Thin Film

Different methods can be employed to generate carbon thin film coated materials. The deposition method and process properties directly affect the physical characteristics of the synthesized thin films. Among those methods, chemical vapor and sputter deposition techniques are widely employed in industry and research facilities [42, 43]. Here, we will briefly discuss the carbon deposition methods; chemical vapor and sputter deposition, and carbon-based materials of diamond-like carbon and graphene. Carbon implantation technique for graphene synthesis will also be discussed.

2.3.1 Chemical Vapor Deposition

Chemical vapor deposition (CVD) is a synthesis process for the coating of high-purity solid materials on a substrate surface that is heated. The deposition of atoms or molecules rises when chemical constituents react with the substrate is in the vapor phase. Precursor gases undergo a reaction at the substrate if the right conditions (temperature, gas pressure, and energy) are satisfied. One of the products from this chemical reaction is deposited on the substrate while by-products are diffused away from the surface and evacuated. The temperatures typically vary

between 200-1600 °C. Some CVD processes involve use of ions, plasma, photons, lasers, or hot filaments to increase the deposition rates or lower the operation temperatures. This technology is widely used in semiconductor industry for thin film applications (insulation dielectrics, SiO_2; thin films depositions, doped Si; interconnections, tungsten) and coating processes (corrosion and wear resistance). Fiber optic cables and solid-state diode laser components are manufactured by CVD methods which helped great advancements in communications [44].

A theoretical work for fundamental processes to predict all of the by-products, mechanism of the reaction chain, deposition compositions, and structural analysis is essential for clear understanding of CVD mechanisms [42]. It is required to know the thermodynamic properties of the reactant gases, especially the Gibbs free energy (free energies of formation), ΔG_f. To ensure whether the CVD reaction will occur, a thermodynamics condition has to be met; that is if the energy transfer; reaction free energy change, ΔG_r is negative [42].

$$\Delta G_r^o = \sum \Delta G_f^o \, products - \sum \Delta G_f^o \, reactants \qquad (2.2)$$

This value is not fixed and can be controlled by the type and molar ratio of reactants, process temperature and pressure. The entire process to meet satisfactory conditions for CVD reaction is dependent on many factors; the process temperature, chamber pressure, molar ratios and types of the reactant gases. Moreover, thermodynamic investigations ensure to predict the outcomes when the reactant gases reach the substrate surface for a given deposition temperature. This process is governed by a mass transport mechanism, so important that the reaction rate and the design considerations are based on this mechanism [42].
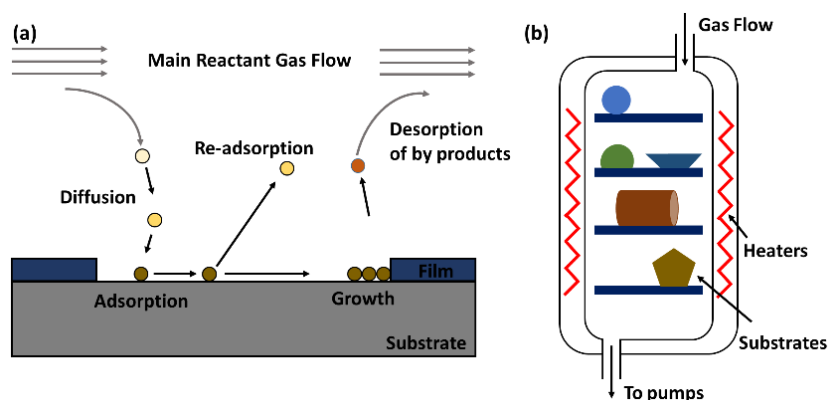
Fig. 2. 3 Fundamental CVD sequential processes (a). CVD chamber with hot walls (b). Multiple substrates with different geometries can be coated. Redrawn from Ref. [45].

Fig. 2.3(a) shows the sequential process for the CVD. The reactant gases diffuse and contact the substrate surface. The reactions occur resulting in a deposition on the substrate surface followed by the diffusion of by-products out of the chamber. The deposition rate is limited; mostly by the surface interactions or the mass-transport, and the reactions are governed by the slowest step. Surface reactions are dependent on the reactant gas density. The rate for film growth increases exponentially with substrate temperature ($\propto e^{E_A/kT}$). When low temperatures and pressures are present, surface reactions govern the process; whereas for high temperature and high pressures, the mass transport controls the deposition rate. E_A is the activation energy, k is the Boltzmann constant, and T is the temperature [42, 45]. Since the CVD process is mainly governed by the chemical reaction, the direction and the rate of the reaction is of critical importance. In CVD, materials with diverse properties can be grown if the conditions such as the substrate, temperature, composition of the gas mixture, and gas flow rate are adjusted properly. Experimental results that correlate the theoretical calculations are very important to ensure a reliable investigation for CVD reactions.

Fig. 2.3(b) shows a schematic that is mainly used in microelectronics fabrication. Heating with hot walls allows to process large quantities of substrates (such as silicon wafers) with uniform coating properties [45]. However, the walls get coated over time, that increases the energy use, thus needs maintenance frequently. Cold wall chambers, on the other hand, heats the substrates with either a lamp or resistive materials and cools the chamber walls. In contrast to hot wall reactors, their design minimizes the coatings to the chamber walls, the energy use, and the use of vacuum equipment. However, the substrates may suffer from non-uniform coatings, and possible thermal stresses, due to fast cooling of the substrates.

CVD offers several advantages and among those is having conformal film thickness (thickness of sidewalls and top of the substrate is comparable). Therefore, shaped substrates and holes can be evenly coated. This is a unique feature of CVD and related deposition techniques such as atomic layer deposition (ALD) over physical vapor deposition and sputtering techniques that require a specific positioning of the substrate relative to the source target. In CVD, the deposition rate is high so coatings with high thickness can be achieved. CVD does not require a high vacuum so their adaptation to processing systems are relatively easy. However, the substrates are heated to increase the deposition quality to temperatures exceeding 600 °C where many substrates are not thermally stable at these temperatures. Moreover, chemical precursors to start the chemical processes increase the operation cost and possess hazardous situations.

CVD is an important production method for DLC and graphene synthesis [46, 47]. CVD method can produce such carbon thin films with high purity and quality crystalline structures at limited film adhesion to the substrate. In CVD, a hydrocarbon gas, methane is used as a carbon source for producing DLC films. CVD method includes radio frequency, arc, or sputter methods in which the produced DLC film characteristics are different [46]. Radio frequency method can

deliver smooth DLC films that can also be grown on insulating films with low adhesive properties. Arc method generates DLC films with hardness that is very close to that of diamond. However, the film thickness is limited and growth is dependent on the surface conditions. Monolayer or a few layer thick graphene can be grown using CVD on polycrystalline Ni films due to grain boundaries of the Ni films [47]. The monolayer formation can be increased when single-crystalline Ni(111) surface, smooth and free of grain boundaries, is used. Graphene that are synthesized by CVD method have applications for organic photovoltaic cells and field effect transistors as flexible transparent conductors [47]. However, the CVD method requires high deposition temperatures (~1000 °C), and rather has multi-step procedures that are quite complex.

2.3.2 Sputter Deposition

Sputtering is widely accomplished by plasma that generate charged particles accelerating towards the substrate surfaces. Sputtering takes place if a particle with enough energy strikes a surface to displace an atom, so called the "sputtered atoms" from it. In this process, the sputtering depends on the transfer of kinetic energy and physical momentum of the incident particle to the surface atoms. Sputter deposition is widely used for deposition of thin films and erosion of the surfaces. Among these applications include coatings of tools, thin film deposition on semiconductor wafers, and reflective coatings of glass. Sputtering method has several advantages; it is easy to scale, many materials can be used with it, possesses high degree of film adhesion, and low temperature deposition. The deposition environment can easily be controlled by the target power and gas pressure independent of the substrate conditions.

Thin films of DLC and graphene can be obtained with sputtering [21, 43]. Sputtering methods for DLC can provide good thin film adhesions to the substrate. Yet, these methods cannot achieve thin films with high purity due to the contaminations from the plasma. The growing film

transforms to DLC with the impact of energetic ions that induces sp^3 bond. A dc or rf sputtering of graphite electrode is conducted with an Ar plasma. Using magnets behind the graphite target increases the deposition rate due to an increase of the electrons path length which subsequently increases the ionization rate of the plasma. A dc bias is applied to the target increasing the ion energy. However, the hardest DLC films cannot be produced due to the relatively low levels of energetic ions compared to neutrals. Using magnetron sputtering technique, direct graphene films can be prepared from a graphite sputtering target. This technique is low-cost, fast, and scalable for large manufacturing quantities [21].

2.4 Diamond-Like Carbon Films (DLC)

Diamond-like carbon is a metastable amorphous form of carbon that carries several similar properties to those of crystalline diamond and graphite [48]. Although diamond has unique properties, its fabrication is still expensive and hard. Diamond-like carbon carries similar characteristics to diamond and can be deposited with high rate at lower temperatures. DLC films carry properties such as low friction coefficient, high hardness, and chemical inertness. They are considered as low-mobility semiconductors with a bandgap of 1–4 eV and possess photoluminescence [49]. Mechanical, optical, and electrical properties of DLCs depend on the mean C-C coordination, so on the amount of the fraction of C–C sp^3 bonding [36]. While carbon with sp^2 bonding is soft, the diamond-bonded carbon (sp^3) exhibits extreme hardness. The higher sp^3/sp^2 ratio becomes, the mechanical properties of the DLC gets closer to that of diamond. The deposition method, plasma enhanced chemical vapor deposition (PECVD) can generate a-C:H, a diamond-like material with a large hydrogen content. More sp^3 bonded materials (ta-C:H) can be produced inside PECVD chambers with high plasma densities [36]. Both sp^3 and sp^2 bonds are always present in DLC, so its electronic structure is always different from that of diamond. Since

sp³ bonding is not stable compared to sp² bonding, hydrogen is introduced to generate C-H bonds to stabilize the sp³ bonding which improve the mechanical properties of DLC films [25]. Several modifications can be made on the properties of DLCs specifically with addition of elements such as silicon and fluorine.
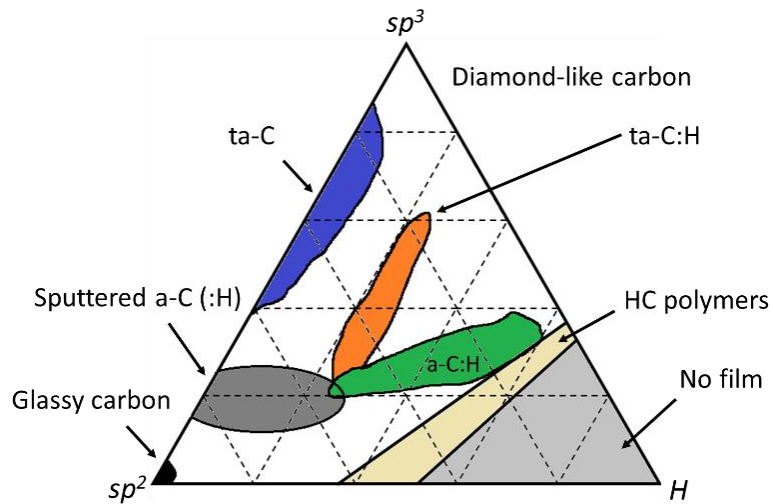
Fig. 2. 4 Phase diagram of bonds in amorphous carbon-hydrogen alloys. ta-C: Tetrahedral amorphous carbon (pure sp3 bonding, the hardest and strongest, such ta-C is considered as pure DLC), ta-C:H: Tetrahedral amorphous carbon with hydrogen content. Redrawn from Ref [25].

DLC is composed of hydrogenated alloys (a-C:H) and amorphous carbon (a-C). The variations of the C-H alloy compositions is presented as in Fig. 2.4 [25]. Glassy carbon and sputtered a-C are found in the bottom at left in the diagram. Sputtering can transform the structure from sp² bonding towards sp³ bonding. These materials are classified as ta-C (tetrahedral amorphous carbon) that separates them from sp² a-C type. Advancements in the deposition techniques allowed formations of a-Cs with enhanced sp³ bonding [25]. A comparison of DLC films with diamond and the graphite along some properties are summarized in Table 2.1[50].

Table 2. 1 Comparison of typical properties of diamond, ta-C, a-C:H, and graphite [50].

	Diamond	**ta-C**	**a-C:H**	**Graphite**
Crystal system	Diamond cubic	Amorphous	Amorphous	Hexagonal
Mass density, g/cm^3	3.51	2.5-3.3	1.5-2.4	2.26
sp^3 content, %	100	50-90	20-60	0
Hydrogen content, %	0	~1	10-50	0
Hardness, GPa	100	50-80	10-45	<5
Friction coefficient *In humid air*	0.1	0.05-0.25	0.02-0.3	0.1-0.2
In dry air	0.1	0.6	0.02-0.2	>0.6
Bandgap, eV	5.5	1-2.5	1-4	-0.04
Electrical resistivity, Ω cm	10^{18}	10^6–10^{10}	10^4–10^{12}	10^{-6}–10^{-2}
Thermal stability in air, °C	800	400-600	300-350	>500

DLC films have wide application areas due to their properties such as wear resistance, chemical inertness, low electrical conductivity, and optical transparency in the IR spectral range [25]. A very thin layer (<10 nm) of DLC provides an efficient protection of the sample surface. This feature makes ultrathin DLC layers an attractive material. Phosphorus-doped DLC thin films can be used as a coating material for implants in the human nervous system to produce patterned neuron networks [51]. They are also used as protective DLC films for head/disc interface (a few nm thick) in magnetic storage applications [52].

2.5 Graphene

Graphene, a two-dimensional crystalline material, is a single-atom thick (3 Å) layer of graphite in a hexagonal lattice structure. It was believed that isolating a stable graphene layer and testing its electronic properties was not possible [26]. Although graphene sheets exist in the form of nanotubes and fullerenes, it was recently extracted as one layer and transferred to another substrate which allowed an electrical characterization [53]. Ever since the interest for graphene research has been popular owing to its unusual properties.

2.5.1 Electronic Properties of Graphene

Carbon nanotubes, graphite, and C_{60} can be realized as graphene sheets arranged in a honeycomb lattice structure as shown in Fig. 2.5(a) [54, 55]. The electronic structure of a C atom is $(1s)^2(2s)^2(2p)^4$ and 1s electrons remain inert whereas 2s and 2p electrons can hybridize. In the case of diamond, four sp^3 orbitals establish a tetrahedral bond, occupying all the valence electrons. DLC films always carry sp^3 and sp^2 orbitals, and the electronic configuration is different from that of diamond due to the available sp^2 configuration. In the case of graphene, however, three sp^2 orbitals are established. Since a p orbital is available, the arrangement of sp^2 orbitals occur in a place with 120° angles forming a lattice with honeycomb shape.

In a graphene structure, each carbon atom is 0.142 nm (distance of AB in Fig. 2.5(a)) apart from its three neighbor atom and it shares one covalent σ bond with each of them. The other bond is a π bond that is oriented in the z-direction that is out of the plane. The primitive lattice vectors a_1 and a_2 with (x, y) notation are given by [55]:

$$a_1 = \frac{a}{2}(3, \sqrt{3}) \quad \text{and} \quad a_2 = \frac{a}{2}(3, -\sqrt{3}) \tag{2.3}$$

Here a is the nearest C-C distance (0.142 nm). The lattice spacing can be calculated from the magnitude of the primitive vectors as $\tilde{a} = \sqrt{3}a = 0.24\ nm$, and the unit cell area is $A_{uc} = \sqrt{3}\tilde{a}^2/2 = 0.051\ nm^2$. Each carbon atom has one π bond which are hybridized to generate π and π^* bands. These bands give the unique properties to the electronic structure of graphene [54].
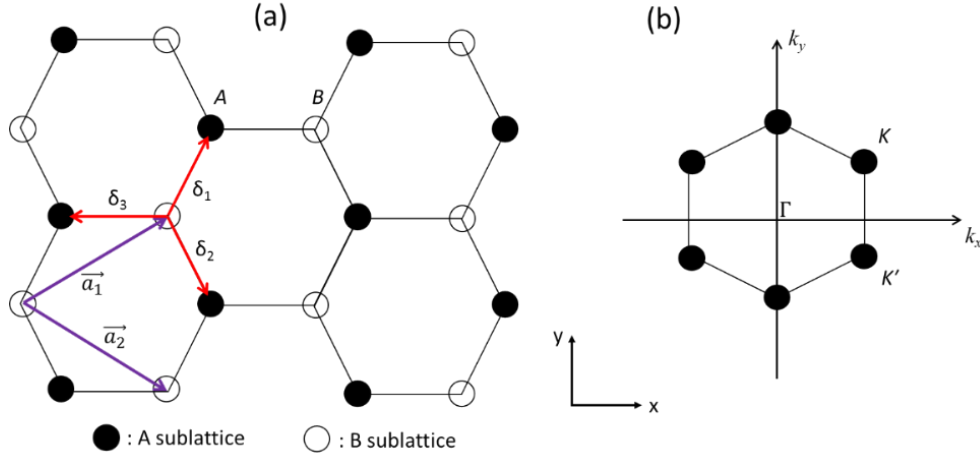
Fig. 2. 5 (a) Honeycomb lattice structure (due to sp^2 hybridization) of graphene unit cell. Sublattices are labeled as A and B. Each atom in a triangular sublattice (A or B) has three nearest neighbors in other sublattice. $\overrightarrow{a_1}$ and $\overrightarrow{a_2}$ are the basis unit vectors for Bravais lattice. δ_1, δ_2, and δ_3 vectors connect carbon atoms with a distance 0.142 nm. (b) Brillouin zone (Γ is the center) of the honeycomb lattice and the Dirac points K and K' at the corners. Redrawn from Ref. [54].

The three vectors that connect carbon atoms in B sublattice ($\delta_1, \delta_2, and\ \delta_3$) in real space are defined by:

$$\delta_1 = \frac{a}{2}\left(1,\ \sqrt{3}\right),\ \ \delta_2 = \frac{a}{2}\left(1, -\sqrt{3}\right),\ \ \delta_3 = -a(1,0) \tag{2.4}$$

When we consider the primitive cell, the first Brillouin zone in the reciprocal lattice, is defined as the planes that bisect the vectors to the closest reciprocal lattice points. The lattice is still

honeycomb, but rotated by 90° as seen in Fig. 2.5(b). When two equivalent corners in the Brillouin zone is considered, their positions are defined by

$$K = \frac{2\pi}{3a}\left(1, \frac{1}{\sqrt{3}}\right), \quad K' = \frac{2\pi}{3a}\left(1, -\frac{1}{\sqrt{3}}\right) \tag{2.5}$$

Raman spectroscopy is a powerful tool to characterize the vibrational and electronic properties of crystalline structures through inelastic scattering of photons by phonons. Graphene has prominent Raman phonon modes known as G, D, and 2D bands. The presence, integrated intensity (I), position, and line-shape of Raman spectra gives valuable insights about the properties of graphene [56]. For instance, the equation below provides the nanocrystalline size of graphene [57];

$$L_a(nm) = (2.4 \times 10^{-10})\lambda_l^4 \left(\frac{I_D}{I_G}\right)^{-1} \tag{2.6}$$

where L_a is the crystalline size diameter, λ_l is the Raman laser wavelength and I_D/I_G is the ratio for integrated D and G peaks intensities.

Graphene shows high intrinsic electron mobilities (200000 cm^{2}V^{-1}s^{-1}) with zero bandgap and high optical transparency [58]. It is a transparent conductor and is stronger than steel with a stretchable nature. Graphene absorbs only 2.3% of the light in the visible region [59]. The electrical and thermal conductivity is very high, a promising useful feature as a flexible transparent conductor. However, it was reported that the graphene has a finite minimum conductivity limit, so that it affects the functionality of field-effect transistors where the on/off ratio for graphene based transistors is relatively low [60].

Graphene has a zero bandgap semiconductor property, as opposed to traditional semiconductors with finite bandgap, because the valence and conduction bands meet at the six

Dirac points, that is a location in a momentum space on the edge of the Brillouin zone [61]. The charge carrier behavior changes at the Dirac point from a hole to an electron or from an electron to a hole, whereas the electron and hole transport in a semiconductor is achieved by different doping of materials. The Fermi level in a traditional semiconductor is within the bandgap, however it is always inside the valence or conduction band in graphene. Electronic properties of the semiconductors (Si, Ge, and GaAs) are compared to those of the graphene are listed in Table 2.2 [62].

Table 2. 2 Electronic properties of Si, Ge, GaAs, and graphene. E_g, energy bandgap, electron effective mass (m^*/m_e), electron mobility (μ_e), and electron saturation velocity (v_{sat}) [62].

Property	Si	Ge	GaAs	Graphene
E_g at 300 K (eV)	1.1	0.67	1.43	0
m^*/m_e	1.08	0.55	0.067	0
μ_e at 300 K ($cm^2V^{-1}s^{-1}$)	1350	3900	4600	~2 x 10^5
v_{sat} (10^7 cm/s)	1	0.6	2	~4

2.5.2 Fabrication of Graphene

The major concern has been obtaining the graphene with high carrier mobility and low defects. Mechanical removal, which is time consuming, and not cost effective for large scale production, that produces high-quality graphene flakes. Production of large-scale graphene layers is a very important issue for applications such as transistors and transparent electronics.

Another technique is thermally heating silicon carbide (SiC) in high vacuum up to ~1500 °C. The reaction results in Si sublimation by thermal decomposition and a surface that is carbon

rich is left behind. In fact this method promises wafer scale graphene synthesis and mobilities of 1100 $cm^2V^{-1}s^{-1}$ for fabricated electronic devices [63].

Sputtering does not contain chemical interactions between the species present in the deposition. The operation temperatures can be as low as room temperature. Owing to these features, sputtering is a widely adopted technique. Using RF magnetron sputtering, graphene layers can be grown on metallic foils and silicon [64]. Graphene can be synthesized using magnetron sputtering at low temperatures on different substrates. One study synthesized single and multilayer graphene [21]. Graphite target was sputtered with hydrogen background gas and as a result, hydrocarbons were generated using a dc magnetron source. Graphene layers formed on a hot Ni-Fe foil surface with hydrocarbons in the background. They reported that the crystalline structure depends on the process parameters such as target temperature, hydrogen pressure, temperatures, and the foil position in the chamber. The crystalline structure was better on top of the foils where the distance to the magnetron source was maximum [29]. Higher deposition temperatures resulted in smaller crystalline size and higher electrical conductivities were achieved compared to CVD prepared graphene layers [22].

High quality graphene can be also be grown by carbon ions implantation in nickel with controllable thickness [19]. The quality of the films is comparable to other methods. The advantage is that this technique can be applied to a variety of metallic substrates with various growth temperatures and directly be integrated with silicon-based electronics offering wafer scale fabrication. Garaj *et al.*, also reported a study on graphene films growth on thermally annealed polycrystalline Ni substrates [19]. They evaporated 500 nm of Ni on Si/SiO$_2$ wafers at 1000 °C in Ar and H$_2$ flow for two hours. 30 keV carbon ions were implanted with doses of $\sim 10^{15}$ cm^{-2}. Post annealing was applied to the substrates at 1000 °C with controllable cooling. The quality of

graphene film revealed by Raman analysis is comparable to other common synthesis methods. Synthesis through ion implantation can be modified for a variety of growth temperatures and metallic substrates. Kim *et al.*, reported graphene fabrication with carbon ions that are accelerated to 20 keV energy with a dosage of 1×10^{15} cm^{-2} on substrates of Ni/SiO$_2$/Si heated to 500 °C. Annealing at 600-900 °C resulted in sp^2 bonded honeycomb formation. Annealing temperature and time were of critical importance and temperatures of 600 °C showed that this technique can be used for direct growth of graphene on Si substrates [20]. Another study used 200 nm Ni films deposited on SiO$_2$ and 80 keV carbon ions implantation with a dose of 16×10^{15} cm^{-2} (equivalent to 4 layers of graphene) followed by annealing [18]. They concluded that the graphene layers were mostly controlled by the nucleation process on the Ni surface. Zhang *et al.*, reported graphene layer synthesis directly on to nickel film (300 nm, evaporated on SiO$_2$/Si substrate) by negative carbon ions implantation with the energy of 20 keV for various dosages [65].

The key factor for industrial graphene production is the cost-effective technologies that permit large size synthesis of graphene at moderate temperatures. For semiconductor devices, low temperatures are desired. To achieve this requirement, substrates such as glass, aluminum, and plastics with low melting point can be processed with graphene. To achieve this requirement, substrates such as glass, aluminum, and plastics with low melting point can be processed with graphene. Ion implantation has an advantage over chemical vapor deposition (CVD) and sputtering of controlling the graphene thickness by ion dosage adjustments and operating at low temperatures. Ion implantation is a candidate for large scale hybrid devices fabrication with an interpretation of graphene synthesized on insulating substrates. New types of materials that are flexible and wearable layered with graphene structures will be of immense importance for next generation devices.

CHAPTER 3

ION SOURCES

3.1 Introduction

There is a great interest in ion sources for applications in biomedicine, nanoprocessing, cancer therapy, and secondary ion mass-spectroscopy [2, 14, 66, 67]. There is no ideal ion source for all applications because as high currents are desired with high charge states, the intensity of the beam decreases as the charge state increase [68]. The ion sources discussed in this study are the radio frequency (RF) [69], electron cyclotron resonance (ECR) [70], and laser ion sources (LIS) [71]. The magnetron type sputter ion source is also discussed. A feature over all ion sources is having multiple components that serve to generate, extract, and transport these ion beams to the final application.

The most developed sources of ions are radio frequency (RF) and electron cyclotron resonance (ECR) ion sources [69, 70]. RF sources use radio-frequency voltage to create a plasma with either inductive or capacitive coupling. They can be operated with different background gases, so they have wide applications in ion beam etching and doping. ECR ion sources generate plasma with microwave power coupled to the plasma at microwave frequency matched to the electron cyclotron frequency in the presence of a magnetic field. If high plasma confinement rates are achieved with relatively low background gas pressures, resonating microwave field can transfer enough energy to the electrons in the plasma, thus the ions can be stripped by the electron-ion collisions to high states. Laser ions sources use intense laser beams focused on a solid target to form a plasma. They possess simple operation, low cost maintenance, and offer applications in particle accelerators. Laser ion sources can be used for ion implantation [72]. They can generate high currents of ions

at several keV energies from any solid material. The laser beam can be used for micromachining and annealing of the substrate, under the same vacuum chamber in multiple stages in numerous cycles. Magnetron sputtering is a deposition method that generates ions from a solid target with confined plasma [43]. The target surface is eroded by high energy ions within the plasma and released target atoms travel towards the substrate to deposit a thin film. Magnetron sputters can be operated at low pressures with low voltages. They use very strong magnetic fields to confine the secondary electrons in the plasma near the target surface. It is the high confinement that protects the deposited film on the substrate from any electron damages which leads to a very dense plasma to increase the efficiency, ionization rate, and deposition rates.

Ion sources usually consist of an ionizer, an extraction system, accelerator, and focusing components. Ion sources are widely used as an essential part in mass spectrometers, particle accelerators, ion implanter systems, and in medical applications [67, 72, 73]. Their design and specifications differ mostly based on the desired application which directly affects the charge states and the ion current yields. Operating parameters of different types of ion sources show that high j_e (electron current density) and n_0 (neutral particle density) result in high ion beam current. However, such configurations result to low charge states. This is due to the short τ_c, the lifetime of ion without ionization. On the other hand; high electron energy, low background pressure, and long lifetime of ions are needed for high charge states. Based on these results, the diagram in Fig. 3.1 shows the different ion yields for ion sources, given as $n_e \tau_c = j_e \tau_c / v_e$. In this equation, v_e is defined as electron velocity and E_e is given as electron energy in eV [70].
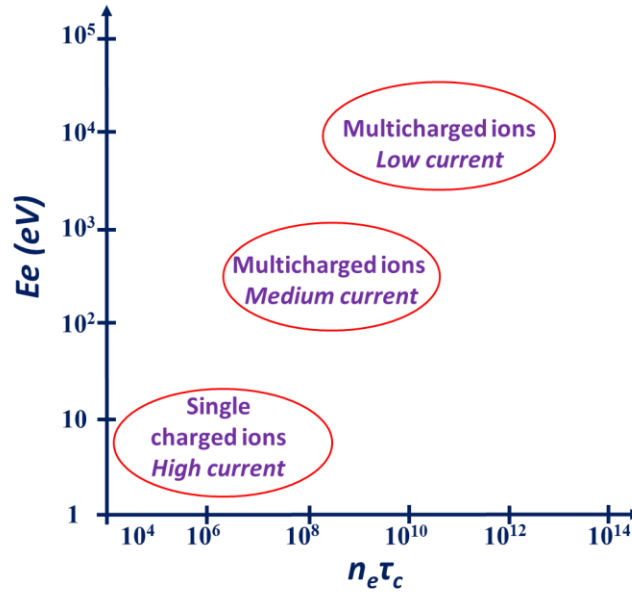
Fig. 3. 1 Parameters of operation for different types of ion sources. Redrawn from Ref. [70].

3.2. Radio Frequency (RF) Ion Source

The radio frequency (RF) ion sources are simple and possess long operation life with a stable and clean plasma production. Since they contain no filament, contaminations are minimized that lead to easier maintenance. An RF discharge is established in a chamber that is filled with a gas at a pressure range of 10^{-2} to 10^{-3} Torr. The RF frequency has an operation range of a few megahertz to tens of megahertz. Required RF power to maintain a stable discharge is a few hundred watts. A schematic for a typical RF ion source is shown in Fig. 3.2 [74]. This type of ion source is mainly used in semiconductor industry and in particle accelerators. Most of the RF sources operate with an induction type coil which generates an alternating magnetic field in the discharge zone. RF ion sources can function with most types of background gases such as oxygen, nitrogen, argon, hydrogen, krypton with ion densities in the order of 10^{11} cm^{-3}. The materials can be in liquid or solid form which are evaporated in an oven and introduced to the discharge chamber as a gas to

generate the plasma. The electrons in the gas are excited to oscillate by the electric field in the discharge region. However, electrons in the gas may be lost to the source chamber walls. Ignition of a high-density plasma requires that electrons must undergo enough ionizing collisions before being lost to the chamber walls or by recombination. This process can be adjusted by either increasing the gas pressure or the volume of the chamber. The mean free path for the electrons is defined as:

$$\lambda = 1/n\sigma \tag{3.1}$$

Where σ is the collision cross section, and n is the number of gas molecules per unit volume. When their kinetic energy gain is enough to ionize the background gas particles, the plasma is generated. The ions contained in the plasma are then extracted. When an electrostatic extraction is used, the ions are focused electrostatically or magnetically, they can produce ion beams for semiconductor and micro-machining applications. The external factors that changed the discharge and produced ion characteristics are background gas pressure, the magnetic field strength, the extraction voltage, and the RF field magnitude. Because all of these parameters are correlated to each other, it is very difficult to diagnose the dependence of the process with only one variable.
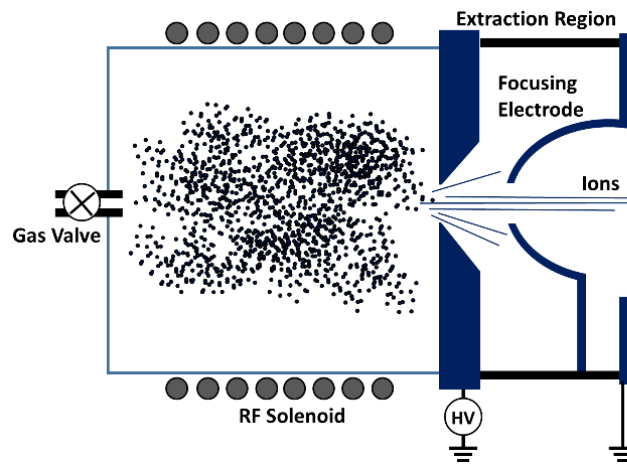
Fig. 3. 2 Schematic of an inductive RF ion source with extraction region. Redrawn from Ref. [74].

Large currents flow through the inductive wiring which in turn generates RF magnetic flux, penetrating to the discharge region. In turn, an inductive electric field is generated and the energy is coupled from the RF source to the ionized gas. Electric field accelerates the free electrons in the discharge region and maintains the plasma. In an RF ion source, an electric field with high frequencies accelerates the free electrons to high energies leading to ionization of molecules and atoms which they collide. RF power is typically adjusted by an automated mechanism so that the RF power is always calibrated to the dynamic conditions of the plasma. An inductive RF solenoid biased with high frequency RF (13 MHz) power surrounds discharge chamber in which background gas pressure is typically kept at $\sim 10^{-3}$ Torr or lower. The gas introduction can be controlled by a mass flow controller. Water cooling of the induction coils are necessary to prevent overheating of the components. The typical has ion densities at about 10^{11} ions cm^{-3}. A stable low temperature and low-pressure plasma is generated from RF voltage at these pressures. Ions in the extracted beam are mainly atomic ions. Some of the major drawbacks of this type of ion source are the thermal limitations for high power RF discharge and conducting films deposited on the chamber walls [70].

3.3. Electron Cyclotron Resonance (ECR) Ion Source

ECR ion sources can produce highly-charged ions and are commonly applied to the heavy ion accelerators, atomic physics research, cancer treatment, and semiconductor processing facilities [70]. A schematic for a typical ECR source can be seen in Fig. 3.3 [69]. They are equipped with microwave power which provides sufficient energy to heat the electrons to high energies in the plasma chamber. The ionizing electrons do not gain energy by the electrostatic acceleration from a cathode or in a plasma sheath, but the electrons of the plasma itself are accelerated by an

oscillating electromagnetic wave [75]. If this energy gain of the plasma electrons is more than the ionization potential, then the low-pressure background gas is ionized by electron collusions, igniting the plasma.
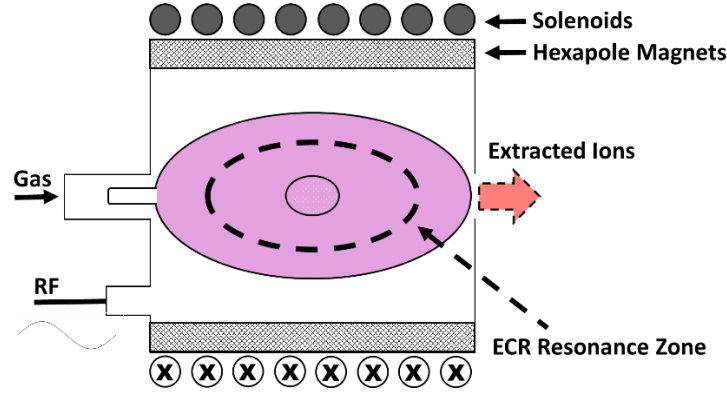
Fig. 3. 3 ECR ion source structure. Redrawn from Ref. [69].

They operate with a gas or vapor injected into a vacuum chamber while microwaves feeding the cavity in the presence of an appositely shaped magnetic field. Electrons spiraling around the magnetic field lines are accelerated and subsequently heated by the microwave. The ignition occurs below 10^{-1} Torr of gas pressure and the plasma can be sustained without any electrodes down to 10^{-9} Torr if good magnetic confinement is provided by solenoids and hexapolar magnetic fields [69]. Multicharged ions are generated by the sequences of ionization steps caused from electron impacts. An electron will move in a spiral orbit in the presence of a magnetic field B and will have a gyration frequency w_g at resonance [76]:

$$w_g = (e.B)/m_e \tag{3.2}$$

where B is the magnetic field, e is the electron charge and m_e is the electron mass. When an external ultra-high frequency field with w is applied, the electrons that are in phase with the electric field

will experience acceleration while out of phase electrons decelerate. The energy gain is maximum when magnetic field [76]:

$$B = B_{ecr} = \frac{wm_e}{e} = \frac{f}{28} \tag{3.3}$$

is satisfied. Given the radian frequency $w = 2\pi f$, f is the microwave frequency in GHz and resonant magnetic field $\boldsymbol{B_{ecr}}$ is given in Gauss. For a widely used microwave frequency of 2.45 GHz, the resonance magnetic field $\boldsymbol{B_{ecr}}$ is about 875 G. Some of the ECR sources operate at 14-28 GHz frequency range. Higher frequency operations usually need superconducting magnets to achieve the required fields. The complexity and expense of the microwave power increase proportionally with frequency. Electrons will gain energy every time they pass this resonance region, eventually will be heated, having energies of hundreds of keV. The typical electron temperature can be varied from 1 to 20 keV. An optimum adjustment of the frequency of electromagnetic waves that is introduced to the plasma electron cyclotron frequency ensures that an efficient energy transfer happens between the electromagnetic waves and the electrons [76]. Another important design consideration is that magnetic field is not uniform and is minimum at its center. In order to couple the maximum energy to the electrons, a closed surface that has the maximum magnetic field should be positioned inside the source chamber wall. The propagation of the electromagnetic wave inside a plasma depends on the plasma frequency [74]:

$$f_p = \frac{1}{2\pi} \sqrt{\frac{n_e e^2}{\varepsilon_0 m_e}} \tag{3.4}$$

where e is the electron charge, n_e is the electron density, m_e is the electron mass, and ε_0 is the permittivity of free space. The plasma behaves as a filter so the lower frequency microwaves (f_{rf}) reflect back while higher frequencies can propagate for a given critical frequency (plasma frequency) [74]. The ECR sources have a critical density value $n_{crit} = 1.26 \times 10^{-8} f_{rf}^2$ in units

of cm^{-3} that is the upper limit of the plasma density which is defined as a boundary of optimum operation and charge state generation. Consecutive ionization steps will generate multicharged ions but their existence strongly depends on the confinement times and the plasma electron energies [76]. The electron–atom collisions allow the generation of multicharged ions, and very high charge states can be generated if long confinement times are achieved. The ion and electron confinement times vary by the temperature of ions and electrons. If the confinement time is too short, then the ions cannot reach high charge states however if the ion confinement time is too long, the high charge state ions start decaying by charge exchange before they are extracted. The temperature of ions should be minimized because they are responsible for the energy distribution of the extracted ions [76]. High T_e can be achieved through the use of microwave frequencies with sufficient confinement of the plasma which is an attractive feature for ions production [77].

ECR ion sources provide high ion currents with high stability and long-life time since sputtering contaminations are neglected with no use of hot cathode. They can be operated in pulsed or continuous modes. The major drawback of these sources is that very high values of the magnetic fields are needed for the source operation. High power consumption, expensive and complex components, and difficulties for metallic ion beam production are major challenges with these ion sources.

3.4. Magnetron Sputtering Ion Source

To produce thin film coatings by vacuum deposition, there are mainly two groups of methods: thermal evaporation and ionic sputtering. Thermal evaporation heats the materials in vacuum where the vapor pressure becomes higher than the ambient pressure, then the deposition starts. Ionic sputtering involves high energetic ions to strike the solid target where the atoms are

knocked off the surface. Among the ionic sputtering techniques, magnetron sputtering method is a standard process for the deposition of many important microelectronics fabrication. This technique can deposit metals, alloys to a variety of materials with a thickness of up to a few micrometers. Coatings for hardness, corrosion resistance, low friction, and specific electrical properties are a few examples. Although conventional magnetron was the first technique introduced, the major transformation of this technique was established after the introduction of unbalanced magnetron. Among those, especially the closed-field unbalanced magnetron sputtering is capable of commercially depositing high quality films of a wide range of materials [43].

The main advantages of magnetron sputtering are; high rate of deposition, use of any metal, compounds or alloys, thin films with high purities and uniformity even for large area substrates, and very high adhesion of deposited thin films. Even though there are several sputtering techniques such as RF, DC, diode or reactive sputtering, they fundamentally work on the same principle that molecules or atoms of a material are ejected by high energy particle bombardment. The ejected material is then coated onto the substrates. The first criteria is to generate ions with sufficient energy and direct them to the target to eject atoms from the material. The second criteria is that the ejected atoms must be freely moving towards the substrate to be coated. The plasma can be generated by DC or RF power. DC powered discharges can deposit metallic films such as gold, copper, or tungsten. RF powered sputters can be used for deposition of insulating films such as ceramics and oxides.

The low pressures are necessary to maintain high ion energies and prevent dominating atom-gas collisions. The mean free path, the distance that atoms can travel with no collision with another gas atom, is of critical importance. In order to maintain a reliable atom transfer to the substrate, the pressure of 7.5 Torr or lower are required when the background gas is supplied to

the vacuum chamber. Otherwise, the collisions are high and depositions rates become very low. The best practice is pumping the chamber to ultrahigh vacuum pressures in order to eliminate contaminations. However, there is a certain pressure range to initiate the plasma generation, required for sputtering. When the pressure is further decreased, the mean free path for electrons increases. As a consequence, the ions are generated far from the target and the ionization efficiency is reduced, thus the plasma generation rate gets diminished, and sputtering is terminated. In magnetron sputtering however, the ionization efficiency is increased at lower pressures with the introduction of specifically designed magnets that trap the primary and secondary electrons in a race track so that the collisional processes with gas atoms are greatly increased near the target. The impedance of the plasma is then reduced due to the ionization rate increase, which affects the material removal rate from the target. The schematic for a DC diode magnetron sputter is shown in Fig. 3.4. The cathode is equipped with magnets that produce dc magnetic fields to confine the secondary electrons. These permanent magnets are placed behind the target and magnetic lines enter and leave through the cathode plate. Magnetic field bends the electron trajectories into helices, so that their travel path is increased resulting to higher collision rates. The magnetic field strength for proper magnetron operation is relatively small; 300 G which can easily be achieved by permanent magnets. When a voltage of 200 V or more is applied, the discharge gets formed. The current-voltage characteristic for the magnetron discharge is given as [78]:

$$I = \beta (V - V_0)^2 \tag{3.5}$$

where V_0 is the threshold voltage to maintain the discharge and β is the pressure dependent parameter. For an estimated maximum current density of 0.25 A cm^{-2} at the target which is mostly limited to this value due to the cooling and operation limits, the power supply should have a rating that can provide this maximum current with voltage values reaching to several hundreds of volts.

Typical magnetron sputtering chamber operates at 10^{-3} Torr pressure, 500 V discharge voltage, 20 mA cm^{-2} current density, and 300 G magnetic field strength.
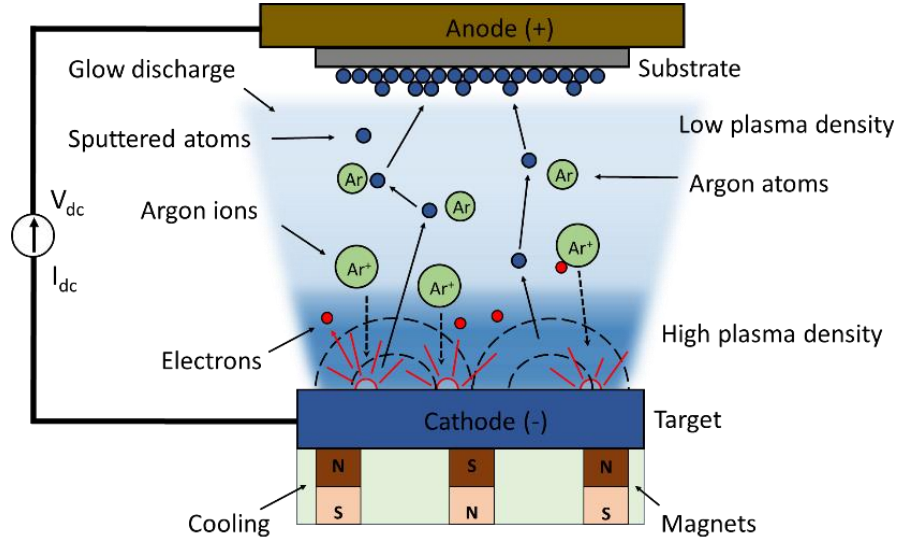
Fig. 3. 4 DC diode magnetron sputtering schematic. Redrawn from Ref. [79].

The magnetron discharge occurs in the form of a bright glowing circular plasma. However, the electric field is not uniform between the cathode and the anode. The electric field is shielded by the plasma and a cathode sheath is developed with a thickness of $\approx$ 1 mm. Most of the applied voltage is sustained by the cathode sheath. Sheath thickness is given by Child-Langmuir law [76]:

$$s^2 = \frac{4\varepsilon_0}{9j} \sqrt{\frac{2e}{m}} \frac{V^{3/2}}{s^2} \tag{3.6}$$

where j is the current density of ions for cathode voltage V, e is the electron charge, ε_0 is the permittivity of free space, m is the ion mass, and s is the length of the cathode sheath which is called "cathode dark space" in glow discharges. The sheath thickness increases with the cathode voltage and decreases with pressure through the j, the current density of ions.

Argon is commonly used as a background gas in magnetron sputters. The sputtering occurs when impacting ions have a threshold energy of ≥50 V. For many applications, argon ions with energies of several hundreds of volts (200-1000 V) are ideal for sputter deposition. Ar ions are accelerated towards the cathode and strike it with high energies which sputters the cathode target and produces secondary electrons emission. Further ionization collisions are sustained by these accelerated secondary electrons emission which maintains the discharge. The sputtered film morphology is mainly determined by the substrate temperature and deposition pressure. The deposition rate is given by [76]:

$$D_{sput} = ɣ_{sput}\Gamma_i A_t / n_f A_s \quad \text{(cm/s)} \tag{3.7}$$

where Γ_i is the incident ion flux (cm^{-2}s^{-1}), n_f is the deposited film density in cm^{-3}, A_t is the sputtered target area in cm^2, A_s is the substrate area and $ɣ_{sput}$ is the sputtering yield (atoms sputtered per incident ion). The discharge causes erosion track to the cathode substrate material. In this case, the sputtering target should be replaced when the erosion track is comparable to its thickness.

When we consider the glow discharge current-voltage curve for the conduction of electricity in a gas environment at low pressures, the sputtering occurs in a region where the current densities are high. In order to maintain a stable operation, the power supplies driving the sputtering system should be specifically designed to maintain voltage and current values because rapid changes can cause to arching and eventually disrupt the proper operation.

3.5. Laser Ion Source (LIS)

Ion sources based on laser generated plasma from solid materials are efficient sources delivering high ion current beams with single step ionization. Laser pulse focused by a lens is used to form a plasma from a target. A rapid vaporization of the target material occurs if the power

density of the laser pulse is high enough. This process allows the production of a plasma plume that contains neutral particles, ions, and electrons. Electrons in the plasma are heated by the laser pulse up to several hundreds of eVs. It is important to know how the laser energy is deposited in the plasma when studying the interactions between laser light and the plasma. Inverse bremsstrahlung, one of the absorption mechanisms in effect, is defined as the absorption of the energy of the electric field induced by the laser via electron-ion collisions [80, 81]. The attenuation of the laser pulse with intensity I when the laser light propagates through the plasma is given by

$$\frac{dI}{dx} = -\kappa_{ib} \times I,$$
(3.8)

where the inverse Bremsstrahlung absorption coefficient κ_{ib} is defined as [80, 81]

$$\kappa_{ib} \propto \left(\frac{\rho}{\rho_c}\right) Z \lambda^{-2} T_e^{-\frac{3}{2}} \left(1 - \frac{\rho}{\rho_c}\right)^{-\frac{1}{2}}.$$
(3.9)

Here ρ is defined as the mass density, Z is the atomic number of the material, λ is the laser wavelength and T_e is the electron temperature. The density ρ_c is defined as the mass density that corresponds to the critical density n_c for the laser wavelength λ. It is obvious that the fractional absorption due to inverse Bremsstrahlung increases significantly where the density ρ approaches to ρ_c. The maximum absorption coefficient κ_{ib} is given as $Z \lambda^{-2} T_e^{-\frac{3}{2}}$. The wavelength of the laser pulse significantly affects the absorption process and leads to higher efficiency of collisional absorption at shorter wavelengths. However, low Z materials and high temperatures lead to lowered absorption processes.

The plasma expansion is longitudinal and ion pulse duration is substantially longer than the laser pulse duration due to the ionic energy spread. The drift zone where the plasma expansion happens plays a critical role for the ion pulse duration. As the plasma expands away from the

ablated target through vacuum after the laser pulse is terminated, generated maximum charge state decreases spatially due to the rapid temperature drop in the expanding plasma. This reduction is due to the three-body recombination that is between highly exited states, and this rate is expressed as [71]:

$$R_t \approx 10^{-26} z^3 (n_e / T_e^{9/2}) \qquad (3.10)$$

In this equation, n_e is the electron density, and T_e is the electron temperature, respectively. For shorter laser operating wavelengths ($\lambda = 1064$ nm for Nd:YAG and carbon dioxide lasers, $\lambda = 248$ nm for excimer lasers), higher laser intensities can be achieved and in turn, higher electron temperatures and higher electron densities are possible that leads to ions with higher charge states. For a typical laser ion source, laser power intensities in the order of 10^{10} W/cm^2 or above are required. The plasma plume exhibits an adiabatic expansion along the direction normal to the target surface, regardless of the angle of incoming laser pulse. The ions emitted follow a shifted Maxwell-Boltzmann (slow ions) and Gaussian velocity distribution (fast ions) and get more energetic as the charge state increases. Ionic charge state, current density, energy and angular distributions can be modified by the laser pulse parameters (intensity, focal point, pulse duration) and target material [82]. The ion current density is proportional to the spot diameter of the laser pulse on target and this spot diameter is given by [83]:

$$d_f = 1.22 \lambda F / D \qquad (3.11)$$

where λ is the wavelength of the laser, D is the laser beam diameter at the lens, and the F is the focal length of the lens. The pulse-to-pulse stability and the incoming angle of the laser pulse directly affect the ion pulse stability of the laser ion source. This stability is ±20% for about 10^5 laser pulse shots [83].
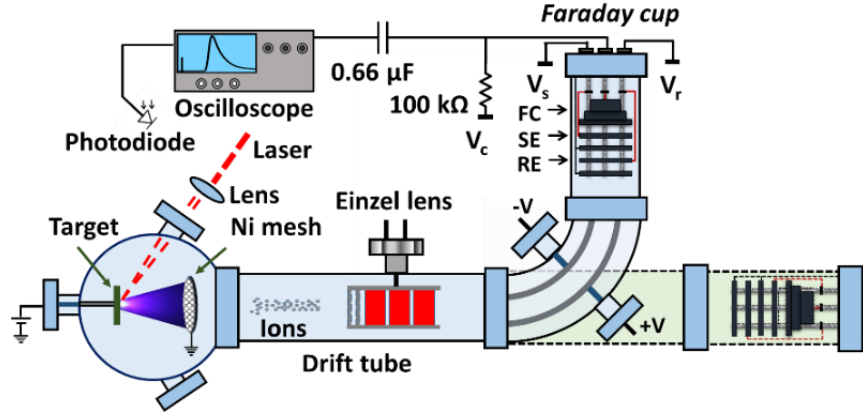
Fig. 3. 5 LIS system equipped with ToF, retarding field, and electrostatic ion energy analyzers.

Laser ion source schematic built in our laser lab is presented in Fig. 3.5. This ion source consists of several components as target, transport line, extraction system, electrostatic deflector, and Faraday cup. The target is mounted on an insulated holder to allow applying high voltages up to +30 kV for external acceleration of ions. Any type of solid material can be used as target. The laser ablates the target with pulse energies up to 450 mJ at a variable repetition rate up to 50 Hz for Nd:YAG laser and 1 kHz for the Ti:sapphire femtosecond laser. Electrostatic deflection plates allow to select a specific energy-to-charge (*E/z*) ratio. The analyzer has a range of *E/z* obtained by the relation [84]:

$$E/z = eR_0E_r(R_0) = eU/2 \ln\left(\frac{R_2}{R_1}\right) \approx keU \tag{3.12}$$

where *E* is the kinetic energy of the ion, *e* is the unit charge E_r is the radial electric field inside the deflection plates, R_0 is the mean radius, R_1 is the inner radius, R_2 is the outer radius, *U* is the potential across the deflection plates, and $k = R_0/2\Delta R$ is the geometric factor. This design has a 90° deflection angle but alternatively 127° deflectors are also available. A Faraday cup can be used as a detection system. This cup can be equipped with retarding field electrodes to measure the total

energy of the generated ions. The suppressor electrodes are used to block the secondary electron emission from the Faraday cup due to positive ion collisions. LIS can produce high charge state ion beams of almost every element with high currents at relatively simple operation and source system. Depending on the parameters of the laser radiation and the target material, ions with charge states up to 50^+ can be achieved with ion kinetic energies reaching hundreds of MeV due to internal electric field at high current densities without need of external acceleration [85].

The ions with higher charge states are densely present at smaller angular distributions [86]. If ion implantation is desired, conditions can be modified by laser parameters such as ion energy to change the implantation depth) and ion flux to change the concentration of implantation [14]. The plasma source chamber needs to be evacuated below 10^{-6} Torr to neglect the collisional processes [87]. Ions produced from laser plasma can provide a cost-effective add-on to existing pulsed laser deposition systems, generate ion pulses, and reduce equipment size and cost [6]. LISs are capable of generating highly intense ion beams with various charge states from any solid material at low cost and power consumption. Laser rod cooling for high-intensity lasers is one of the limitations to the use of LIS in accelerator facilities. Although LIS has significant advantages, there are numerous issues to overcome; angular and spectral control of the beam, broad ion energy distribution, contaminations with the dopant, and the stability of the acceleration parameters [6].

CHAPTER 4

MULTICHARGED CARBON ION GENERATION

4.1 Introduction

Multicharged ion (MCI) sources have uses in nanoprocessing, ion implantation, ion lithography, biomedicine, cancer therapy, and secondary ion mass-spectrometry. In an MCI interaction, both its potential and kinetic energies are involved. The potential energy of highly charged ions can exceed their kinetic energy, particularly for ultraslow ions. When used for surface modification, MCIs with low kinetic energies have high surface selectivity causing strong local excitation not accessible with singly-charged ions. An MCI interaction with a surface can trigger local surface modification by potential sputtering resulting in the formation of a nano-scale crater, a feature that may be useful for nanopatterning and nanoidentification [3]. The ability to independently control MCI potential and kinetic energies is useful for surface analysis and surface modification. MCI implantation in metals can modify the surface tension, hardness, and corrosion resistance [2, 88, 89]. Slow highly-charged ions can be used in semiconductor surface processing due to their high potential energy combined with low kinetic energy which allows for localizing the ion potential energy at the surface. Using ultraslow Ar^{q+}, (q > 1) MCIs with high potential energy, native silicon oxide was removed from the Si surface with less surface damage than possible when singly-charged Ar^{1+} ion is used [90]. After slow Ar MCI etching, the surface roughness was increased by only 0.05 nm root-mean-square (rms) [90].

The most developed sources of MCIs are electron beam ion sources (EBIS) and the electron cyclotron resonance ion sources (ECRIS) [91]. Both EBIS and ECRIS generate MCIs from gases. Generating MCI from a solid target involves its vaporization and introduction of the vapor in the

EBIS or ECRIS. Laser multicharged ion sources (LMCI) uses laser ablation of a solid target to generate dense plasma containing MCIs. Thus, LMCI can operate in ultrahigh vacuum requiring only small pumping capacity. MCIs produced from laser plasma can provide a cost-effective add-on to existing pulsed laser deposition systems, generate MCI pulses, and reduce MCI equipment size and cost [92]. Several groups have studied laser generated MCIs. Mróz *et al.* reported on the generation of Ta, Al, and Cu MCIs with iodine laser (λ = 1315 nm, τ = 350 ps) with an intensity up to 10^{15} W/cm^2. The maximum charge states obtained were Cu^{22+}, Ta^{9+}, and Al^{13+} [93]. Al MCIs up to Al^{4+} were obtained at maximum laser intensity of 8.7×10^{10} W/cm^2 with Nd:YAG laser (λ = 1064 nm) [94]. Henkelmann *et al.,* used CO_2 and Nd:YAG lasers (λ = 10.6 μm and 1064 nm, respectively) together to show the influence of the combined laser interaction with a solid Ta target [95]. The charge state generation increased from Ta^{11+} to Ta^{13+} depending on the delay between the laser pulses. The CO_2 laser increased the electron temperature in the expanding plasma reducing the recombination rate resulting in increased extraction of higher charge states. Nassisi *et al.,* reported using low energy XeCl excimer laser (λ = 308 nm) pulses to produce MCIs from a Cu solid target [96]. The MCI generation was strongly dependent on the focal lens used for the same laser fluence on target. Using a lens with 15 cm focal length, the maximum total charge observed was ~0.035 μC for a laser fluence of 17 J/cm^2. Up to Cu^{5+} was observed when the different charges were separated by a 30 kV acceleration voltage. Lorusso *et al.,* used a XeCl excimer laser (λ = 308 nm, τ = 20 ns, pulse energy = 70 mJ, intensity = 3.5×10^8 W/cm^2) to study the charge extraction characteristics of the generated Cu^{q+} ion pulses [97].

Laser ablation was previously used to generate carbon MCIs [98-103]. Kashiwagi *et al.,* reported the observation of fully stripped C^{6+} ions using Nd:YAG (λ = 1064 nm, τ = 15 ns, pulse energy = 400 mJ, intensity = 1.6×10^{11} W/cm^2). The ions were injected into a radio frequency

quadruple linac. The total number of C^{6+} ions injected into the linac was 6.0×10^9 with a current of 17 mA [98]. Emission of C MCIs were reported for CO_2 laser ($\lambda = 10.6$ µm, $\tau = 85$ ns, fluence of 1.2 J/cm^2) [99]. An electrostatic deflector ion filter was used to analyze the carbon ions with ion charge up to C^{5+} reported. Constantinescu *et al.,* reported on the interaction of C_{60} molecules with ultrashort high-intensity femtosecond laser pulses ($\lambda = 790$ nm) with an intensity of 10 - 1000 TW/cm^2. Carbon ions up to C^{4+} were produced [100]. Witanachchi *et al.* produced carbon plasma with C^{1+} and C^{2+} using a combination of an excimer KrF laser ($\lambda = 248$ nm) and a CO_2 laser ($\lambda = 10.6$ µm) suggesting the ionization, kinetic energy of ions, and the plasma temperature increase when two lasers are used [101]. Torrisi *et al.* studied MCI generation from ablation of graphite by frequency-doubled Nd:YAG laser ($\lambda = 532$ nm, $\tau = 3$ ns). At a fluence of 5.7 J/cm^2, up to C^{4+} ions were detected. Ion acceleration by $\sim$85 eV/charge state was measured [102]. Okihara *et al.* reported C^{4+} ions above 5 MeV/charge state using Ti:sapphire laser system ($\lambda = 815$ nm, 2.4×10^{12} W, maximum intensity $= 3 \times 10^{18}$ W/cm^2, $\tau = 50$ fs) [103].

Carbon ions have applications in thin film deposition, semiconductor processing, ion implantation, and radiotherapy. Carbon ions implantation into the floating gate surface is used in flash memory devices that minimizes the polysilicon grain growth and smooths the surface [104]. This helps to reduce the interfacial trap density and improves the integrity and uniformity of the thin dielectrics deposited between the floating and polysilicon gates of nonvolatile memory devices. Carbon implantation into Ti-6Al-4V alloy enhances surface wear resistance, increases hardness due to TiC formation, and reduces the surface friction coefficient [105]. Simultaneous implantation with different charge carbon ions results in a plateau like depth profile that is dependent on the ion energy distribution [105]. Graphite-like carbon (GLC) has uses as a coating material, offering high hardness and high flexibility required in implants such as in artificial joints

[106]. Carbon ions have more favorable dose-depth distribution than photons and are the new frontiers of cancer therapy [107, 108]. The use of carbon ions in radiotherapy results in localized energy targeting hard-to-reach tumors with minimum effects to other tissues. Fully stripped C^{6+} are used in radiotherapy because of the relative ease in their acceleration, bending, and focusing and their high potential energy which can be deposited in a localized volume [108].

We report on carbon LMCI source using a Nd:YAG laser ($\lambda = 1064$ nm, $\tau = 7$ ns). The charge state and energy of carbon MCIs are studied by time-of-flight (TOF) analyzer, a three-mesh retarding field analyzer, and an electrostatic ion energy analyzer (EIA). Charge states up to C^{4+} were observed with laser pulse energy of 34 mJ. Ion energy distributions are measured using an EIA that selects ions with different energy-to-charge (E/z). The dependencies of the carbon ions extracted from the laser plasma on the laser pulse energy, laser focal spot position, and external accelerating electric field are studied. Carbon MCI generation was previously reported [98, 100, 102, 103]. The present work extends previous studies by measuring the energy distribution of each carbon ion charge using an energy-to-charge (E/z) electrostatic ion energy analyzer (EIA). The ion energy follows a shifted Maxwell-Boltzmann distribution that is dependent on the ablation velocity and Coulomb potential developed in the double layer of the expanding laser plasma [109]. Calculations of carbon ions energy distribution are critical for the carbon ion implantation of materials aiming to change surface properties. The deconvolution of time-of-flight (TOF) ion signal using data obtained from the retarding field analysis allows us to resolve the ion signal from each charge more accurately than solely from the TOF signal. Also, we show that the position of the lens focusing the laser on target affects carbon ion yield and ion energy distribution.

4.2 Experimental

The carbon MCIs are generated in a vacuum chamber schematically shown in Fig. 4.1. A Q-switched Nd:YAG laser (Continuum Surelite SL I-10, $\lambda = 1064$ nm, $\tau = 7$ ns) was used to ablate a glassy carbon disc target of 99.99% purity, 0.58 mm thickness, <50 nm surface roughness, as characterized by the manufacturer (HTW, Germany). The laser is focused inside the chamber using a plano-convex lens to a diameter of ∼200 µm at focus, as measured by the knife edge method at the target equivalent plane. The lens was mounted on a translational stage to allow for changing the position of focus relative to target surface. The laser pulse enters the chamber through a BK7 viewport and is incident on the target at an angle of 60° from the target normal. The laser pulse energy was varied by a combination of a half-waveplate and a thin film polarizer. The laser pulse energy was 4-38 mJ measured before the chamber window and the reported values were adjusted for the 8% loss in the glass window. The target was mounted on insulated support to allow for applying an acceleration voltage while maintaining the chamber grounded. The chamber pressure was about 6×10^{-8} Torr, therefore, the loss of MCIs by charge transfer with the background gas is negligible [110]. The Faraday cup is placed 1.54 m away from the carbon target. The ion drift tube had a 10-cm inside diameter. Grounded nickel mesh 8 cm in diameter with an open area of 70% is placed 10 cm in front of the surface of the carbon disk.

The TOF detection consists of a 5-cm diameter Al Faraday cup with a suppressor ring electrode placed 1 cm away from the Faraday cup entrance. The MCI signal is detected with the Faraday cup biased at -80 V. We observed the shape of the MCI signal as we changed the suppressor voltage from -80 V to more negative values. Applying -120 V resulted in an all positive single-peaked pulse. Applying more negative voltage did not change the shape of the pulse.
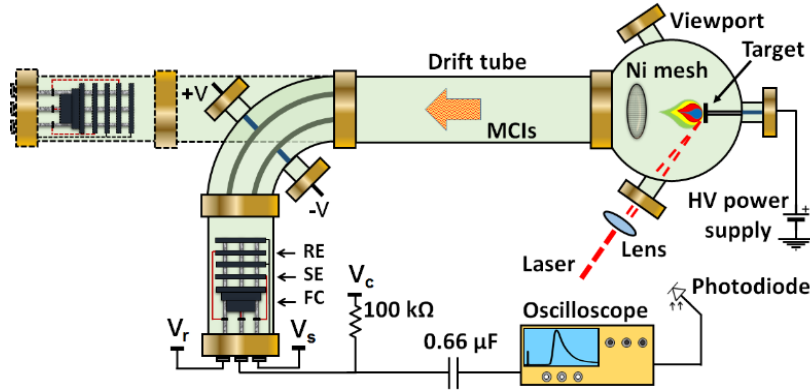
Fig. 4. 1 A schematic diagram of the laser multicharged ion (LMCI) chamber equipped with drift tube, electrostatic ion energy analyzer (EIA), three-mesh retarding field analyzer (RFA), and time-of-flight (TOF) analyzer. V_r, V_s, V_c: Biasing for retarder electrode (RE), suppressor electrode (SE), and Faraday cup (FC). The system can be configured with and without the electrostatic ion energy analyzer (EIA) while maintaining the same distance between the target and the Faraday cup.

Therefore, applying -120 V to the suppressor ring was adequate to suppress the secondary electron emission from the Faraday cup due to positive ion collisions. This suppressor voltage was maintained throughout the experiment. The retarding field ion energy analyzer (RFA) consists of three 5-cm in diameter nickel grids with 70% open area separated by 1 cm. The two outer grids were grounded while the central grid was held at a variable voltage, V_r. The central retarding electrode was positively biased to analyze the extracted ion energy distribution. An oscilloscope (Tektronix DPO 3034, 50 Ω termination) was used to record ion signals through a 0.66 µF coupling capacitor. In order to compensate for pulse-to-pulse fluctuations, 20 consecutive laser pulses hitting the same target spot were averaged. For our experimental conditions, the shot-to-shot fluctuations of total ion yield was up to ∼20%. However, no noticeable decline in the averaged ion signal was observed when hitting the same spot with up to 60 shots.

In experiments observing the MCIs with selected energy-to-charge ratio, *E/z*, part of the straight connection was replaced with the EIA maintaining the ion drift length the same as without the EIA. The EIA has a radial cylindrical design with a deflection angle of 90°. The EIA analyzer has a range of *E/z* obtained by the relation $E/z = eR_0E_r(R_0) = eV/2\ln(R_2/R_1) \approx \kappa eV$ [111] where E is the kinetic energy of the ion, E_r is the radial electric field inside the deflection plates, R_0 is the mean radius, and $\kappa = R_0/2\Delta R$ is the geometric factor. EIA has an inner radius, R_1 of 5.69 in and outer radius, R_2 of 7.19 in. The energy resolution *ΔE/E* was determined to be 7%−10% because no slit was used on both ends of the EIA.

4.3 Results and Discussion

The laser-generated carbon ions are detected by the Faraday cup. The experimental results are divided into two sections. In section 4.3.1, the carbon ions are generated without any acceleration voltage applied to the target; while in section 4.3.2, the target is positively biased, which introduces an external electric field between the target and the grounded mesh that is located parallel to the target. The effects of laser pulse energy, laser focal point location relative to target surface, and the applied voltage on target are studied.

4.3.1 Plasma Ions Emitted without External Acceleration

4.3.1.1 Analysis of Multicharged Ions with Retarding Field Analyzer

When no voltage is applied to the target, the ions generated in the laser plasma are accelerated only by the plasma expansion and the internal electric field developed in the expanding plasma. A retarding field energy analyzer combined with time-of-flight ion spectra are used to probe the energy-to-charge *E/z* of the carbon ions and resolve the ion charge state *z*. The retarding

potential modifies the ion signal displaying cut-offs in the signal that are dependent on z. With the increase in the retarding potential, different ions are stopped at a threshold value of V_{th}^2 described as $V_{th}^2 = 2zeV_r/m$ [96] where V_r is defined as the retarding potential, m is the mass of carbon in kg, and e is the unit charge in Coulomb. The retarder potential stops all ions having kinetic energy below zeV_r. Higher charge state ions gain more kinetic energy when they are accelerated in the internal electric field of the expanding plume, thus are detected earlier by the Faraday cup. Regardless of the target material, a temporal distribution of charge states is observed in the extracted ions.

The TOF carbon ion signal observed for different retarding potentials is shown in Fig. 4.2. Similar analysis using a 3-grid retarding field analyzer was previously reported for Cu MCIs generated using excimer laser ablation [96]. The positive fast signal observed near time zero is due to the photoelectric effect where photons generated from the laser plasma with energy above the work function of the Faraday cup material cause electron emission. The inset in Fig. 4.2(a) is a closer look at the effect of retarder potential on carbon ion signal for the range of 180-300 V. Ions with lower kinetic energy than the applied retarding potential are blocked, whereas ions with higher kinetic energy lose some of their energy then, between the central and final grid, are accelerated back to their energy before entering the RFA. For instance, the cut-off at ~20 µs corresponds to C^{2+} ions with lower energy than $2eV_r$ (150 V retarding potential), whereas the cut-off at ~17 µs corresponds to C^{3+} ions with energy lower than $3eV_r$ (180 V retarding potential). The cut-off at ~11 µs corresponds to the C^{4+} ions with lower energy than $4eV_r$ (210 V retarding potential). The time at which the cut-offs are observed gets shorter with increasing the retarding potential. The knee in the ion signal at ~18 µs or more for various retarding potentials is ascribed to C^{1+} ions with energies lower than eV_r. Fig. 4.2(b) shows the square threshold velocity V_{th}^2 as a

function of the retarding voltage. The corresponding threshold velocity for each cut-off in the plasma signal is calculated by dividing the ion propagation length by the cut-off time. Depending on the z, modified ion signals display cut-offs, which are used to calculate V_{th}^2 for each data point in Fig. 4.2(b). Using a linear fit to the experimental data, the values for each slope was calculated giving charge state information. This analysis revealed that carbon ions up to C^{4+} were detected by the Faraday cup. The total ion charge reaching the Faraday cup is obtained from $Q_i = (\int V_F(t)dt)/R$, where $V_F(t)$ is the voltage signal in the Faraday cup, and R is the 50 Ω oscilloscope internal resistance. The inset in Fig. 4.2(b) shows the total charge reduction with the increase of retarding potential. Total charge decreases from ~ 18 to ~ 0 nC when the retarding potential is set to ~ 460 V. The value of Q_i does not account for the ion loss in the extraction grid and the three grids of the RFA. Fig. 4.2(c) shows the energy spectrum of the carbon ions when no retarding field is applied. In order to determine the best fitting parameters to the ion signal, we used the information obtained from retarding field analysis in selecting the parameters used in the fit. The deconvolution was obtained for charge states up to C^{4+} since this was the highest charge state observed at this laser energy. Knowing the retardation potential which retards a subgroup of ions, we can construct the ion energy distribution width and introduce this into the fitting parameters. For example, the C^{3+} ions start to be modified between +90 and +300 V, indicating a kinetic energy from ~ 270 to ~ 900 eV. This information was used for all charges when fitting parameters in Fig. 3.2(c) are defined. In the plasma core, fast electrons develop a double layer (DL) that splits different charge states, generating a self-consistent ambipolar electric field (double layer), which is primarily responsible for ions acceleration. The role played by prompt electrons in ion acceleration was previously studied [112]. Prompt electron emission from the plasma leaves a positive ion layer in the plasma-vacuum interface and during their escape repel part of the electron

in the plasma. With the increase in the initial electron density at the front of the expanding plasma, a condition can be reached where the ion oscillation frequency is not sufficient to compensate for electron compression in the plasma by the forces of the prompt electrons. This effect was concluded to lead to ion cloud fragmentation and a complex ion acceleration mechanism [112]. Thermal interactions, coulomb interactions, isothermal and adiabatic expansion in vacuum are also responsible for accelerating the ions in plasma [113]. The drift and expansion of carbon plasma in our experiment can be attributed to the adiabatic expansion due to the Knudsen layer.

In a laser produced plasma, the Knudsen layer is formed within a few particle free paths near the target surface in which as few as 3 collisions per particle occurs [11]. Particles vaporized, sputtered, or desorbed reach equilibrium with each other within the Knudsen layer formed in a near-surface region during the laser ablation due to strong gas-phase interactions. This leads to a directional expansion perpendicular to the target surface. The ions are freely drifting into the vacuum, and ion charge-states are frozen at large distances. A shifted Maxwell–Boltzmann distribution due the collisions between ions during the initial phase of the plasma expansion can characterize the motion of ions far from the target. The ion current can be expressed with shifted Maxwell–Boltzmann distribution for the ion current analysis [11, 114]. For laser plasma, the adiabatic expansion velocity (ablation) can be defined as $u_f = 2C_0/(\gamma - 1)$, where $C_0 = (\gamma kT/m)^{1/2}$ is the sound speed at the surface, where T refers to the Knudsen layer temperature, γ is given as 1.3 for monoatomic species [109]. Using this equation, and taking $T = 20,000$ K, ablation velocity is found to be $u_f = 4 \times 10^4$ m/s, or 99 eV as ablation energy. If we consider that the ions with different charges have energies corresponding to the sum of that due to the adiabatic expansion $E_{ablation}$ plus energy gain due to acceleration in the double layer by the Coulomb
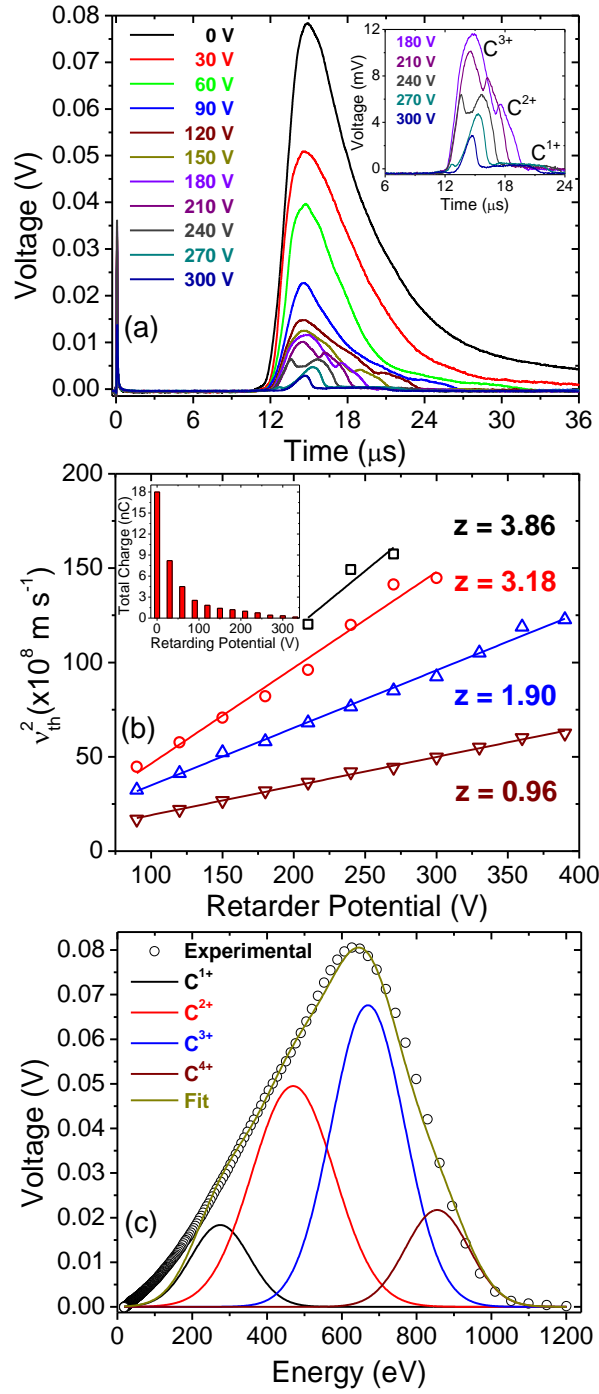
Fig. 4. 2 (a) Carbon ion signal for various retarding voltages. *Inset:* The effect of the retarder potential on the stopping of different charges. (b) Charge state *z* is determined from the slope of v_{th}^2 versus retarding potential. *Inset:* Total ion charge with the increase of retarding potential. (c) Deconvolution of energy spectrum for carbon ion species showing energy distributions up to C^{4+}.

potential $E_{coulomb}$, then the ion energy E is $E = E_{ablation} + zE_{coulomb}$, where z is the ion charge. By fitting this equation to the experimental results, we calculate the ablation and coulomb energies as 80 and 195 eV, respectively. Bulgakova *et al.,* reported similar calculations using a graphite target ablated with Nd:YAG laser operating at 1064 nm wavelength with 13 ns pulse width and laser fluence below 25 J/cm^2 using T up to 4 eV. In their study, T was found to vary in the range $\sim$2-8 eV for laser-generated carbon plasmas with laser intensities of 10^9-10^{10} W/cm^2 for 70 ns pulses [109]. Harilal *et al.,* reported an electron temperature of 1.45 eV at a distance of 3 mm from the target for carbon plasma with a laser intensity of 2.8×10^{10} W/cm^2 [115].

4.3.1.2 Laser energy dependence

The carbon ions were detected by their time-of-flight signal for different laser pulse energies applied to the target. All measurements were conducted with all other conditions kept constant. Results are shown in Fig. 4.3(a). The ion signal has a well-defined single peak at the high laser energies used. There is an apparent reduction of the arrival time of the fast ion peak with the increase in the laser pulse energy. The behavior of TOF signal with increasing laser pulse energy shows that an increase in ion signal with laser pulse energy and a shortened arrival time due to increased ion energy. Below a pulse energy of $\sim$15 mJ, the signal has a double peak form with a shoulder appearing at $\sim$40 µs. This shoulder in the TOF signal disappears within the background at high laser energies. The process of ion acceleration is initiated by electron acceleration by inverse Bremsstrahlung within the laser pulse duration. Due to the slower mobility of ions compared to the electrons, large Coulomb forces are formed between fast electron and ion layers in the early stages of plasma plume formation. The electric field due to the Coulomb forces accelerates ions with higher degree of ionization to higher kinetic energies. The ions with higher

kinetic energies are located in the outer position of the plasma plume due to their higher flow velocity [13]. For laser pulse energies higher than 24 mJ (1×10^{10} W/cm^2), the increase in ion velocity slows down. Fig. 4.3(b) shows that the maximum and most probable ion velocities with the laser energy. For 29 mJ pulse energy, the most probable carbon ion velocity is 9.6×10^4 m/s, corresponding to a kinetic energy of ∼570 eV. Ions kinetic energy increase with increasing laser pulse energy. The carbon ion signal was fitted to a shifted Maxwell-Boltzmann function $I(t) = At^{-5}exp[-m(L/t - u_f)^2/2kT_{eff}$ where A is a normalizing constant, u_f is the flow velocity, and T_{eff} is the effective temperature associated with translational motion along the plume axis [109]. Fig. 4.3(c) show the TOF data and corresponding fits. The observed data fit with the shifted Maxwellian-Boltzmann distribution is an indication of the thermalization of the plume particles. The cloud dimension along the target normal can be estimated from $L_0 = u_t\tau$, where τ is the laser pulse duration and u_t is the thermal velocity of the particles given by $u_t = \sqrt{8kT_s/\pi m}$. The surface temperature T_s is given by $T_s = 0.9T_c$, where T_c is the thermodynamic critical temperature [109]. T_c value was given in the literature for graphite to be in the range of 1-1.3 eV [13]. When we take the T_s as 14,000 K, the thermal velocity is calculated as $u_t = 5 \times 10^3$ m/s, and cloud dimension $L_0 = 0.035$ mm, which implies that the plasma is undergoing planar expansion during the laser pulse. Using these parameters, the plume dimension from $L_z = u_f t + L_0$ is ∼4 cm at time $t = 1$ μs. These calculations can be used for estimating angular distribution of accelerated ions from plasma [113].
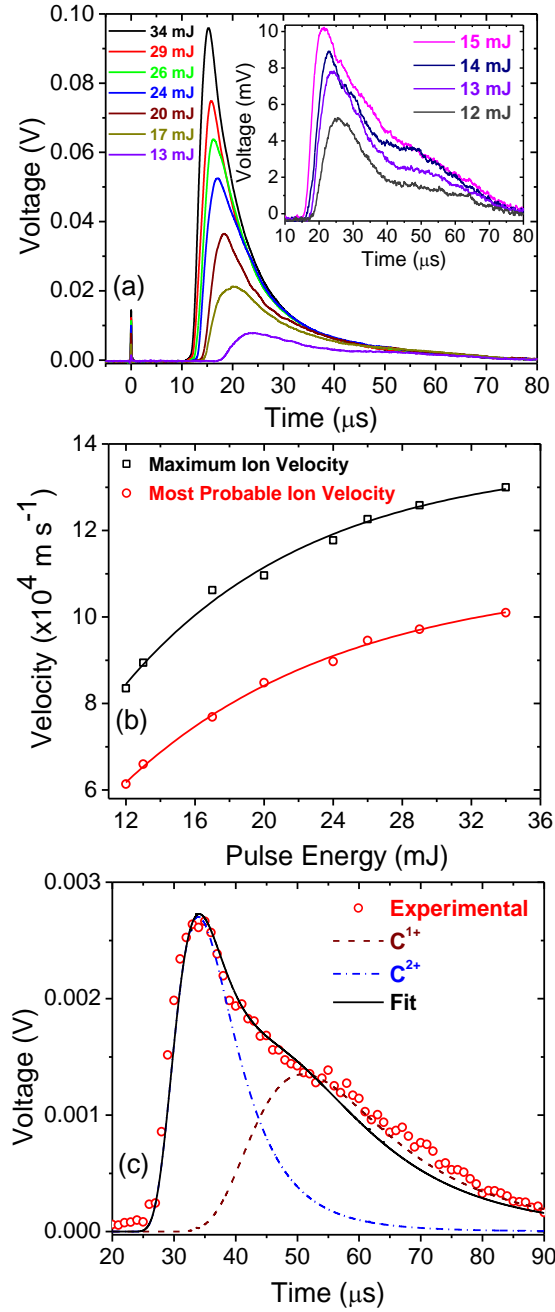
Fig. 4. 3 (a) Time-of-flight ion detection from carbon laser plasma for different laser pulse energies. *Inset:* Carbon ion signal components; slow ions start after ~40 μs for the lower laser energies. For laser energies > 15 mJ, the shoulder in the TOF signal disappears. (b) Ion velocities for different laser pulse energies. (c) Deconvolution of the carbon ion current recovered by the shifted- Maxwellian fit at pulse energy of ~8 mJ (25 J/cm^2).

4.3.1.3 Focal point dependence

The laser focusing position on the target was found to affect the production of the higher charge state ions. The distance between the focusing lens and the target is 202 mm. The lens was mounted on a linear translational stage to vary the focal point relative to target. Fig. 4.4 shows the Faraday cup signal at different laser focus positions with a laser pulse energy of ∼32 mJ. As the lens is moved so that the focal point position is varied from inside the target (- values) to in front of the target surface (+ values), the recorded ion signal is modified. Positioning the lens so that the focal spot is in front of the target by up to ∼5.0 mm, the ion signal has earlier arrival times with one significant peak. Beyond ∼5 mm, a slow peak appears at ∼40 µs which is small compared to the fast one. Likewise, with focusing the laser ∼7.0 mm inside the target surface, a similar double-peaked signal is observed. The inset in Fig. 4.4 shows the total charge detected versus the lens position. The ion yield decreases when the laser focal spot is shifted inside the target surface, reaching to its minimum at ∼9.5 mm. The maximum ion signal is observed at a lens focal position of ∼1.9 mm in front of the target surface which also yields the fastest peak arriving at ∼11.9 µs with a maximum velocity of ∼1.3×10^5 m s^{-1} and total charge of ∼26 nC. The ion TOF signal is modified as the lens focusing spot is moved from positions that gives the higher yields since, for the low yield positions, the predominant ions are singly and doubly charged. Placing the focus a few mm inside or in front from the target surface leads to a larger irradiated area on surface, leading to higher ionization of carbon ions due to slower heat dissipation on a larger surface area during the plasma formation [96]. The dependence of ion yield on the position of the focal spot was discussed for MCI generation from Au, Pb, Ta, and C [116, 117]. The larger laser spot area on target results in lower laser power density, in general, results in lower ion charge state and energy. However, over a certain focal spot distance away from the target surface, the ion yield is increased

due to the larger surface area ablated and the resulting larger volume of the laser plasma [118].

Having the highest power density in the waist of the laser beam does not necessarily result in the

highest total number of ions due to the effect of reduced plasma volume [119]. When the focal

position is in front of the target surface, the interaction of part of the laser pulse with the generated

plasma further heats the expanding plasma and contributes to ion yield. This explains the higher

total charge obtained at a lens position of 1.9 mm in front of the target. On the other hand, the

plasma propagation angle becomes smaller with increasing spot dimension. Since the Faraday cup

is positioned at a fixed angle and location, higher yields of carbon ions are detected. Focusing the

laser inside the target has a contribution from the increased spot size only. The lens position was

kept at ~1.9 mm in front of the target throughout the study. This focal point location results in the

highest ion yield and fastest ion peak arrival time.
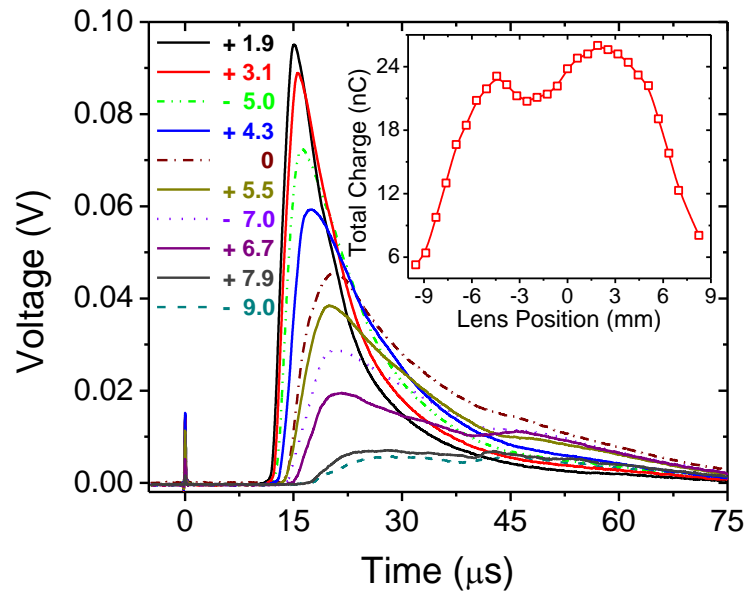
Fig. 4. 4 Carbon plasma ion current signal when the position of lens is varied (mm). Inset: Total

charge change by varying the longitudinal position of the lens.

4.3.2 Ion Extraction with External Electric Field

4.3.2.1 Extraction Voltage Dependence

For this part of the study, the laser pulse fluence was maintained at 95 J/cm² throughout the measurements. With the target grounded, the carbon ion pulse containing all the charges travels as a bunch with most probable kinetic energy of ~597 eV corresponding to ion velocity of 9.8×10^4 m/s. When an acceleration voltage is applied to the target, ions with different charges spread in time with the higher charge state arriving at the Faraday cup earlier. Neglecting the initial ion velocity from the plasma plume, the TOF for the carbon ions is $t_a + t_d = d\sqrt{2m/zqV} + S\sqrt{m/2zqV}$, where t_a is the acceleration time for an ion from target to the extraction mesh, t_d is the time that ions drift at a constant velocity from extraction mesh to the Faraday cup, d is the distance between target and the extraction mesh, S is the total distance from the extraction mesh to the Faraday cup, both in meters, m is the atomic mass of C in kg, z is the charge state, q is the electron charge, and V is the acceleration voltage applied on the carbon target. The above equation for TOF does not consider the effect of plasma shielding limiting the ion acceleration by the external electric field and the ion acceleration in the expanding plume. The electric field between the grounded mesh and the target does not fully penetrate the plasma plume, thus the ions experience the applied electric field at a location between the target and the grounded mesh and, therefore, are accelerated less than the potential applied to the target. Fig. 4.5(a) shows the extraction and separation in time of carbon MCIs. Besides the initial velocity from the internal electric field, the carbon ions gain velocity due to the external electric field. Introducing an electric field increases the kinetic energy of ions, thus separation of ions occurs with faster arrival time at the Faraday cup. More electrons are repelled and more ions are exposed to the accelerating field. Space-charge limited flow in the ion sheath governs the ion extraction if the ion density is

neglected during ion extraction by the external electric field [12, 120]. The inset in Fig. 4.5(a) shows the accelerated carbon ions at 4 kV voltage applied to target. The ions accelerate according to their *z/m* ratio. Up to C^{3+} ions are observed. By combining the EIA with TOF energy analyzer, we measured the kinetic energy that the carbon ions gained. Knowing the energy *E/z* selection band of the EIA and from the TOF signal detected on the Faraday cup for that selected *E/z* band, the ion charge state and energies are determined. The Faraday cup signal is shown in Fig. 4.5(b) for a laser pulse energy of ~30 mJ. The acceleration voltage on target was set to 5, 7, and 9 kV while varying the *E/z* selection of the EIA to achieve maximum current delivered to the Faraday cup. The ion energy is dependent on the acceleration voltage but is reduced by plasma shielding effects. When 5 kV is applied to target, the ion energy gain per charge z is about 3.2 keV, and up to C^{4+} is detected.

In our geometry, the ion acceleration occurs during plasma expansion. The large ion peak in Fig. 4.5(a) are the ions separated from the expanding plasma without acceleration. Due to the retrograde forces, the stronger the applied electric field in the target-to-mesh region, the more ions are extracted from the plasma and accelerated [12]. These ions give the signal shown in Fig. 4.5(b). As the electric field in the target-to-mesh region is increased the extracted ions diverge more and do not reach the Faraday cup. The reduction in the plasma ion signal in Fig. 4.5(a) is due to the ions extracted from which only a portion reaches the Faraday cup. What appears like a shift in the plasma ion peak is due to the extraction of the faster ions in the double-layer region developed in the plasma plume while traversing the target-to-mesh region. Ion energies of about 5.1, 10.6, 13.2, and 18.2 keV were obtained for C^{1+}, C^{2+}, C^{3+}, and C^{4+}, respectively at 9 kV acceleration voltage. During the early stage of laser plasma expansion, recombination of highly charged ions may occur, which can depress ion yield for higher charge states. The ablated material attenuates the incoming

laser radiation as the plasma becomes optically dense at high laser fluences and the plasma absorbs or reflects the later part of the laser pulse [121]. Electron-atom inverse bremsstrahlung, and Mie absorption are among the main absorption mechanisms [122].
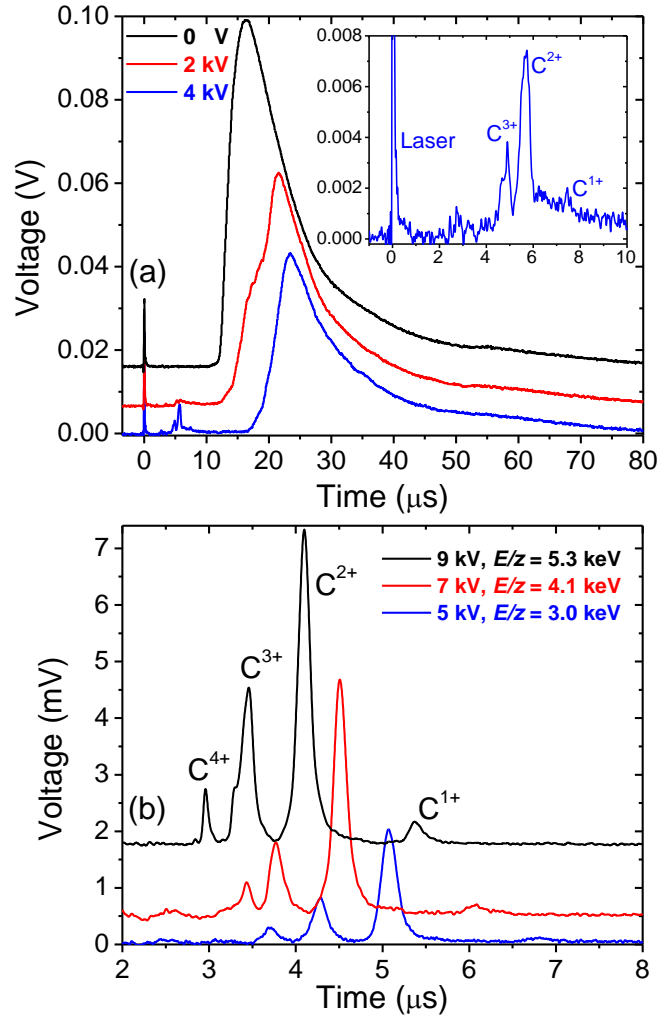
Fig. 4. 5 (a) MCI pulse from the carbon laser plasma. Inset: Extraction up to C^{3+} at 4 kV acceleration voltage. (b) Total charge and C MCI extraction with acceleration voltage.

4.3.2.2 Laser Energy Dependence

The MCI detected is strongly dependent on the laser pulse energy which increases the plasma density and temperature, allowing for generation of higher state carbon ions. To study the

dependence of MCI generation on the laser pulse energy, the acceleration voltage and the EIA selection were kept at 5 kV and $E/z = 3.0$ keV, respectively. The MCI spectrum obtained at laser pulse energies from 4 mJ (12 J/cm^2) to 36 mJ (108 J/cm^2) are shown in Fig. 4.6(a). The threshold energy for the carbon ion generation was found to be ~6 mJ (19 J/cm^2). At low laser pulse energies, only C^{1+} and C^{2+} were observed. The average charge state, peak ion energies and corresponding intensities are increased accordingly with the laser pulse energy. For laser energies of 18 and 24 mJ up to C^{3+} and C^{4+} are observed, respectively. We did not observe C^{5+} or C^{6+} at these laser energies. The reduced TOF time with the laser energy observed in Fig. 4.6(a) is due to the increase in kinetic energy of the ions drifting out of the expanded plasma. Fig. 4.6(b) is showing the total charge dependence on laser pulse energy. The total charge detected by the Faraday cup increases with the laser energy with the biggest contribution coming from C^{2+} ions.
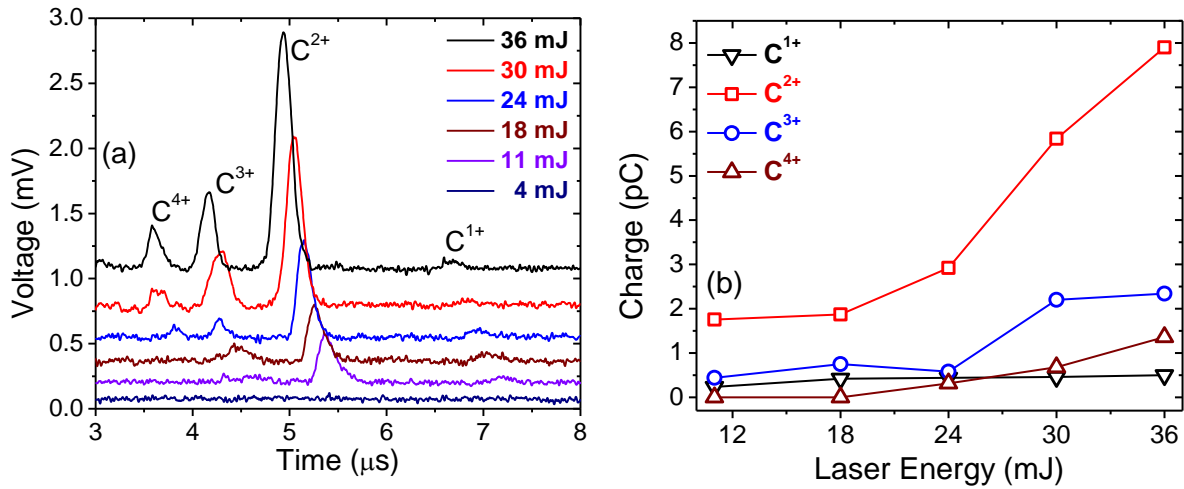
Fig. 4. 6 (a) Carbon MCIs detected at different laser pulse energies. Results indicate that up to C^{4+} can be extracted with a laser fluence of 76 J/cm^2 (24 mJ). (b) Charge detected for each carbon ion.

4.3.2.3 Focal Point Dependence

The maximum charge state and the total charge delivered to the Faraday cup increase with the laser pulse energy. The threshold value for the carbon ion generation was found to be dependent on the laser spot size on target. The core temperature decreases more slowly for a larger laser spot size due to the lower thermal diffusivity which decreases the threshold value. The effect of the laser focus position on carbon ion generation is shown in Fig. 4.7. The voltage applied to the carbon target was 9 kV while the laser pulse energy was ∼30 mJ. Higher charge states are detected when the laser is focused in front of the target surface because a larger irradiated area causes slower heat dissipation and changes the angular distribution of ejected carbon ions. At a lens position for a focus ∼5.5 mm in front of the target's surface, C^{1+}, and C^{2+} ions are detected. Observation of C^{3+} and C^{4+} ions depends more strongly on the laser spot size as both are detected only when the lens is positioned for a focus ∼1.9 mm in front of the target' surface. The EIA plates were biased at ± 1.25 kV to achieve MCI kinetic energy selection centered at $E/z = $ ∼5.3 keV. The maximum ion charge state of C^{4+} was obtained when the laser radiation was focused at 1.9 mm in front of the target. This optimum position was determined from the measurements shown in Fig. 4.4. The optimum focus position for ion yield was at 1.9 mm in front of target surface is consistent with results in the inset of Fig. 4.4. This is in agreement with previous results [117]. In Fig. 4.7, the EIA analyzer is set to allow ions with central energy-to-charge ratio of $E/z = 5.3$ keV which corresponds to the maximum of the ion energy distribution for the target biased at 9 kV. For the focus positions of 5.5, 4.3, and 1.9 mm in front of the target, the maximum carbon ions generated are C^{2+}, C^{3+}, and C^{4+}, respectively. We observed a similar trend of ion generation when the laser is focused inside the target. Only C^{1+} and C^{2+} ions are detected when the laser pulse is focused at ∼7.0 mm inside the target.
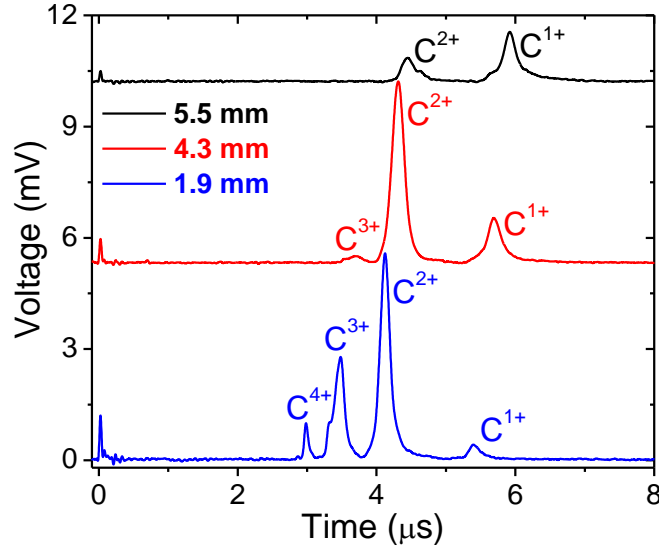
Fig. 4. 7 Carbon ions detected by the Faraday cup when focus is positioned in front of the target's surface.

4.3.2.4 Ion Energy Distribution

The EIA was used to obtain the energy distribution of the C MCIs. The laser pulse energy was 30 mJ with 5 kV applied to target. The focal position was kept at ~1.9 mm in front of the target. Faraday cup signals were recorded for different E/z ratios in order to construct the MCI energy distribution. The voltage was varied from ±350 to ±900 V on the deflection plates of the EIA to transmit ions with different E/z ratios. Fig. 4.8(a) and Fig. 4.8(b) show a typical EIA spectrum of the C^{2+} and C^{3+} ions emitted. The signal for C^{2+} and C^{3+} ions were stronger than the signal C^{1+} and C^{4+} and, therefore, gives more accurate measurement of the resolution of the EIA. Ten distinctive peaks correspond to C^{2+} ions, and eleven distinctive peaks correspond to C^{3+} ions. As the voltage applied to the EIA plates is increased, high energy components of the C^{2+} and C^{3+} ions appear in the energy spectrum. The C^{2+} and C^{3+} intensities are maximum with a kinetic energy of about 2.6 kV/per charge state z. Further increasing, the EIA plate voltage shows the more energetic components of the C^{2+} and C^{3+} ions. The peak widths of C^{2+} and C^{3+} before the EIA

analyzer is ∼2.5 µs. The ions seem to be overlapped in time before deflection. The FWHM slightly increases with increasing the E/z as shown on top of each curve in Fig. 4.8(a) and (b). The FWHM for C^{2+} was 340 eV and 530 eV with $E/z = 1.7$ keV and $E/z = 3.5$ keV, respectively. However, the resolution of the EIA ($\Delta E/E$) remains within 7%-10% for the entire range. Using the data collected for a certain E/z, we can reconstruct the carbon ion energy distribution before the EIA.
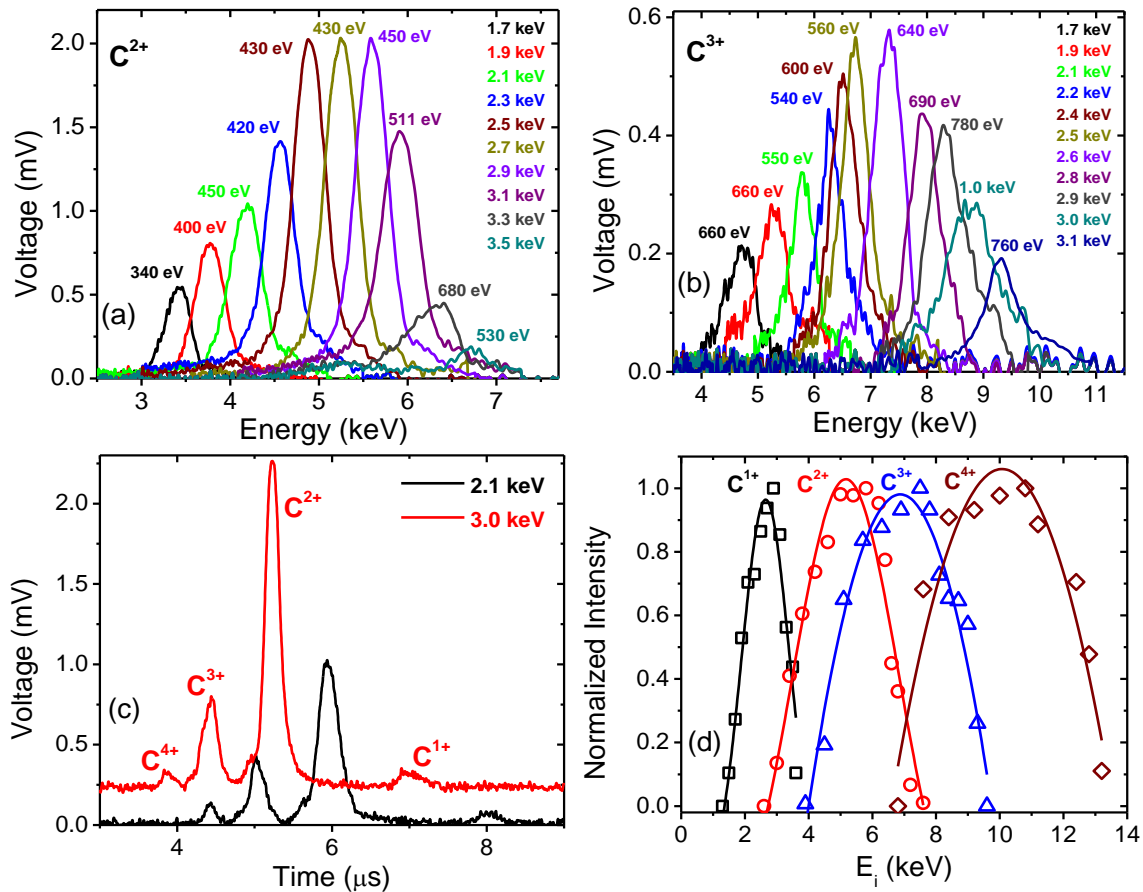
Fig. 4. 8 (a), (b) Signal for C^{2+} and C^{3+} ions for IEA operated in a range of E/z selection. FWHM values of each curve are presented in eV. FWHM values are stated on top of each curve corresponding to different E/z selection. (c) Carbon ions spectra at two different E/z selection. (d) Ion energy distribution as a function of the charge state.

We report this in Fig. 4.8(c) for all charges detected when the E/z is varied from 2.1 to 3.0 keV. We also report on ion energy distributions from C^{1+} to C^{4+} in Fig. 4.8(d) constructed from E/z selection between ~1.7 to ~3.5 keV. The distributions are peaked at about 2.6, 5.1, 7.2, and 10.0 keV in the case of C^{1+}, C^{2+}, C^{3+}, and C^{4+}, respectively. The energy shift is ~2.6 keV per charge z, and proportional to z. The ions are accelerated with respect to their charge state and shifted towards the higher energy according to the Coulomb-Boltzmann shifted model [123].

4.4 Conclusion

Using a Q-switched Nd:YAG laser, carbon ions generation is studied. Ion charge state and ions kinetic energy are strongly dependent on the laser pulse energy. Lens focusing point revealed a direct relation with the maximum charge generated. Using retarding field analysis data, we have calculated the ablation and coulomb energies of the plasma. Moreover, the retarding field data also helped calculate more accurate deconvolution parameters that could be gathered solely from the TOF signal.

CHAPTER 5

OPTICAL EMISSION SPECTROSCOPY OF PLASMA ION SOURCE

5.1 Introduction

Laser multicharged ion (MCI) sources are attracting significant interest as they offer a pulsed, high flux source of ions from practically any solid [124]. Carbon ions are used in wide applications that include cancer therapy [125], deposition of diamond-like and carbide thin film [126, 127], and ion implantation [20, 128-130]. Carbon ion doping was shown to modify TiO_2 thin films, lowering the band-gap energy from 3.3 eV to 1.8 eV [127], thus, making it photoacatalytically active to visible light. Carbon ion implantation on thin Ni film grown on a SiO_2/Si substrate was used for the synthesis of grapheme layers on top and under the Ni film [20]. Carbon ion implantation on high temperature growth of heteroepitaxial GeSn/Si and SiSn/Si structures was shown to suppress Sn segregation and precipitation, improve the thermal stability of SiSn supersaturated layers, and prevent dislocation in the formation of loops [129]. In these applications of carbon ions only the singly-charged C^{1+} ions were used. In some applications, the use of MCIs is attractive since their high potential energy is localized to the surface and they can be accelerated with reduced electrostatic field and bent and focused with reduced magnetic field.

Many techniques are used to probe plasma characteristics such as density n_e, electron temperature T_e, ion temperature T_i, and sheath potential. For pulsed plasma, *e.g.*, laser plasma, diagnostic techniques include optical emission spectroscopy (OES) [8], Thomson scattering [8], laser interferometry [9], and probing of ion emission from the laser plasma [131]. Laser-target interaction generates transient species such as excited atoms, molecules or ions, which emits radiation that includes the ultraviolet to near-infrared parts [8] of the spectra. Line emission from

laser plasma have been extensively used to diagnose n_e and T_e [115]. OES is widely used to probe n_e using Stark broadening of spectral lines, for n_e values ranging between 10^{14}-10^{18} cm^{-3}, and to probe T_e using the ratio of integrated line intensities based on the Boltzmann's method for plasma in local thermal equilibrium (LTE) [132, 133].

Several studies were conducted on carbon laser plasma. OES of carbon laser plasma in air generated by an Nd:YAG laser (pulse width τ = 5 ns, frequency F = 10 Hz, wavelength λ = 1064 nm, maximum pulse energy E = 130 mJ/pulse, and for λ = 532 nm, maximum E = 72 mJ/pulse) [115]. The electron density n_e was calculated from the Stark broadening profile of the C I line at 247.85 nm. The electron temperature T_e was calculated from the neutral C I lines at 247.85, 394.22, 396.14, 588.95, and 591.25 nm. At a distance of 0.05 mm from the target surface, n_e was reported as 4.6×10^{17} cm^{-3} for 130 mJ at λ = 1064 nm, and 5.98×10^{17} cm^{-3} for 72 mJ at λ = 532 nm. The corresponding T_e values were 0.85 and 0.81 eV for the λ = 1064 and 532 nm laser radiance, respectively [134]. For ablation of graphite by an Nd:YAG laser (λ = 1064 nm, F = 10 Hz, intensity I = 59 GW/cm^2), n_e and T_e were reported as 2.1×10^{17} cm^{-3} and 2.43 eV, respectively, at a distance 1 mm from the surface of the target decaying to 1×10^{17} cm^{-3} and 1.6 eV at 11 mm from the target surface for a laser radiance of 59 GW/cm^2 [115]. Dual-laser ablation of carbon plasma (τ = 7 ns, 10 Hz, λ_1 = 1064 nm, λ_2 = 532 nm at fluence of 25 and 17 J/cm^2, respectively) showed up 5-fold intensification of C II emission lines for a delay of 500-1000 ns between the two laser pulses [135]. Changing the delay between the two laser pulses was shown to affect the ion kinetic energy. Ion time-of-flight (TOF) measurement and UV spectroscopy were conducted for the Al, Ti, Mo, and Au plasmas generated by irradiation with a Nd:YAG laser (τ = 3 ns, single-shot or up to 10 Hz, λ = 1064 nm, at a fluence up 18 J/cm^2) [136]. They probed the plasma plume by optical spectroscopy and deconvolution from TOF. For ablating with 18 J/cm^2, the reported ion temperatures for Al, Ti,

Mo, Au, were 40, 41, 42, 44 eV, respectively. These values were obtained from deconvolution of the ion TOF signal based on a shifted-Coulomb-Boltzmann distribution. The electron temperatures reported with optical spectroscopy were in the order of 1.0 eV. The difference in T_i and T_e was attributed to the different zones of the laser plasma where the ions and optical radiation were generated at [136].

We report on a combined OES and ion TOF study of carbon plasma generated by laser ablation using an Nd:YAG laser operating at $\lambda = 1064$ nm with $\tau = 7$ ns. Time-integrated T_e and n_e are measured by OES, while ion TOF is used to obtain T_i. Carbon spectral lines up to C IV (C^{3+}) and carbon ions with charge states up to C^{4+} are observed for ablation by a laser fluence of ≥ 27 J/cm^2. The Stark-broadened profile of the singly-ionized C II line at 392.0 nm is used for the measurements of n_e, while the relative line intensities of the C II lines at 392.0, 426.7, and 588.9 nm are used to calculate T_e. Applying an external electric field parallel to the direction of plume propagation increases the carbon MCI extraction, however, no change in the carbon emission lines was observed.

5.2 Experimental

A schematic of the experimental setup is shown in Fig. 5.1. The vacuum chamber has a background pressure of $\sim 2 \times 10^{-8}$ Torr. At such pressure, the loss of MCIs by charge transfer to the background gas over the transport line length is negligible [137]. A Q-switched Nd:YAG laser (Continuum Surelite SL I-10, $\tau = 7$ ns, $\lambda = 1064$ nm, $F = 4$-52 J/cm^2) is used for plasma generation from a glassy carbon disc target of 5.8 mm thick, 99.99% purity, <50 nm surface roughness. The carbon target is electrically insulated from the chamber to allow applying a positive bias while the

chamber is grounded. The laser pulse energy is controlled by a half-wave plate and a polarizing beam splitter. The laser pulse is incident on the target at an angle of 60° from the target normal and focused using a lens with a focal length of 200 mm to an elliptical spot on the surface of the target with an area of 0.12 mm^2. The laser spot size was measured by scanning the laser spot with a knife edge parallel and perpendicular to the spot's major axis at target-equivalent plane in a direction 60° from the beam propagation direction. The reported laser fluences are adjusted for the losses in the BK7 glass window and the lens. A grounded nickel mesh 8 cm in diameter with an open area of 70% is placed 10 cm in front and parallel to the surface of the carbon disk. A voltage of 0-9 kV is applied to the carbon target using a high-voltage power supply (CPS Inc.,100-R, 30 kV, 1 mA) while keeping the chamber grounded. Ions with a range of kinetic energy-to-charge E/z ratios are selected by an electrostatic ion energy analyzer (EIA) with a radial cylindrical design at a deflection angle of 90°. The EIA has a range of E/z obtained by the relation $E/z = eU/[2\ln(R_2/R_1)]$, where E is the kinetic energy of the ion, e is the electron charge, U is the total potential across the plates, R_1 is the inner radius, and R_2 is the outer radius [84, 138]. Ion entrance and exit slits can be placed in the EIA to reduce the spread in E/z selected. All results reported are without slits in order to increase ion transmission. The ions are detected by a Faraday cup (FC) made out of Al and placed 154 cm away from the carbon target. The ion transport line is a stainless-steel tube with 10 cm ID. The signal from secondary electron emission is suppressed by a suppressor ring electrode that is 5 cm in diameter placed 1 cm away from the FC entrance. The MCI TOF signal is detected with the FC biased at -80 V. The secondary electron emission signal from the FC due to positive ion collisions is found to be completely suppressed when biasing the suppressor electrode at -120 V. More details on the experimental setup were previously reported [139]. An oscilloscope (Tektronix DPO 3034, 50 Ω termination) records the carbon ion signals

through a 0.66 µF coupling capacitor. For MCI TOF data collection, twenty consecutive laser pulses hitting the same target area are averaged in order to increase the signal-to-noise ratio. An optical spectrometer (Avantes, ULS3648) is used to record the spectral lines emitted from the carbon plasma. The carbon spectral emission is recorded through an optical fiber (Avantes, FC-UV-1000-1-ME) placed ~15 cm away from the target at an angle of $60°$ from the target normal. The laser is operated at 10 Hz. The optical spectra are obtained by integrating for 20 s in a dark room. Background noise was recorded before any spectrum was acquired and subtracted from the optical spectra. The effect of applying an external electric field on the optical spectra is probed with another optical spectrometer (Avaspec-3648). This spectrometer covers the spectral range of 180-750 nm. In that case, the laser is operated at 1 Hz, while each spectrum is obtained by integrating the optical signal for 10 s. In this case, the optical feedthrough is replaced with a quartz viewport and a lens with focal length of 200 mm is used to image the plume onto the fiberoptic cable entrance.
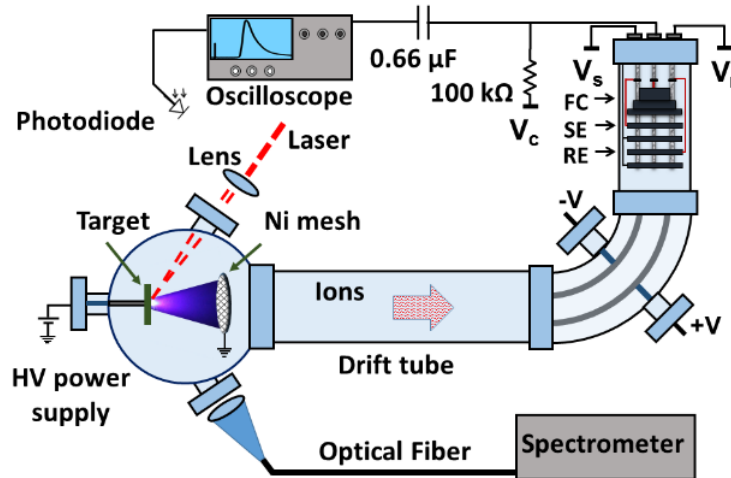
Fig. 5. 1 A schematic of the experimental setup. The laser multicharged ion (MCI) chamber is connected to with a transport line with electrostatic ion analyzer (EIA), three-mesh retarding field analyzer (RFA), and time-of-flight (TOF) analyzer.

5.3 Results and Discussion

5.3.1 Optical Emission Spectra

In this section, time-integrated optical emission spectra of the laser plasma are discussed. The effects of the laser fluence on the electron density n_e and electron temperature T_e are reported. We also report on the optical emission spectra when an external electric field is present across the laser plasma.

5.3.1.1 Lines Intensities

The optical emission spectra obtained for different laser fluences are shown in Fig. 5.2. The carbon laser-plasma consists of ionization emission lines of C II, C III, and C IV transitions. A particular feature for the higher laser fluences is the increase in the intensities of all carbon lines and generation of higher ionization states. The line profile of the C^{1+} ion (C II at 392.0 nm) is used for the electron density n_e calculations.
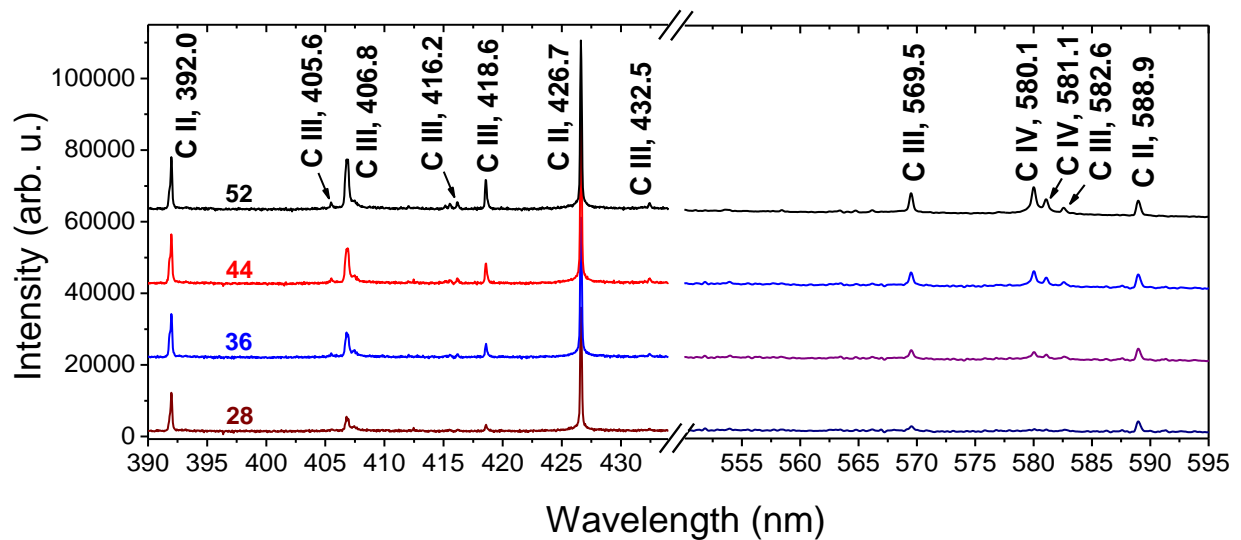
Fig. 5. 2 Carbon laser plasma spectra acquired over the wavelength range 390-595 nm.

For a laser fluence at 28 J/cm^2, C II transitions at 392.0, 426.7, and 588.9 nm, and weak C III lines at 406.8, and 569.5 nm are observed. As the fluence is increased, the C III transitions at 405.6, 406.8, 416.2, 418.6, 432.5, 569.5, 582.6 nm, *and C IV transitions at 580.1, and 581.1 nm are* detected. While all line intensities depend on the laser fluence dependence, the C IV lines are most affected by the laser fluence.

5.3.1.2 Electron Density

For high density plasmas, such as for laser plasma, OES is often used to probe the electron density n_e based on Stark broadening of emission lines [140]. For our calculations, we use the profile of the C II 392.0 nm line to determine the electron density n_e [141]. Harilal *et al*. studied carbon laser plasma for similar laser conditions (λ = 1064 nm and E = 275 mJ) and reported that the effects of pressure and Doppler broadening on the linewidth of the C II line at 392 nm are negligible compared to that of Stark broadening [115]. Stark broadening in plasmas occurs due to collisions of the emitting neutral or ion with charged particles, which results in a shift in the peak wavelength, and a broadening of the line. The full-width at half-maximum (FWHM) of the Stark-broadened lines $\Delta\lambda_{1/2}$ is related to n_e by [133]:

$$\Delta\lambda_{1/2} = 2w \left[\frac{n_e}{10^{16}}\right] \tag{5.1}$$

where w is the electron impact broadening parameter in $\mathring{A}$ and n_e is the electron number density in cm^{-3}. The value of w is retrieved from Griem as 0.0245 $\mathring{A}$ depending on the plasma temperature T_e of 0.86 eV (10,000 K) for C II line (λ = 392.0 nm, $4s^2S_{1/2} \rightarrow 3p^2P_{3/2}$ transition) assuming local thermodynamic equilibrium (LTE) [133]. For n_e to satisfy LTE, the condition $n_e \geq 1.4 \times 10^{14}T_e^{1/2}\left(\Delta E_{ji}\right)^3 cm^{-3}$ must be valid, where ΔE_{ji} is the energy difference between the upper and the lower levels of the transition [23]. This is a necessary, but insufficient condition for LTE. For

the transition of C II at 392.0 nm ΔE_{ji} = 3.16 eV, and the lowest limit for n_e is 5.4×10^{15} cm^{-3} for

T_e = 1.5 eV [141, 142]. In our calculation, correction was made for the instrumental broadening of

0.09 nm, as measured by the FWHM of the Hg 435.8 nm line from a low pressure Ar-Hg lamp.

The line width is determined by a numerical fit of a Lorentzian profile to the measured C II line

profiles at 392.0 nm. Fig. 5.3 gives the variation of electron density n_e of the carbon plasma with

the laser fluence. With an increase in the laser fluence from 4 to 40 J/cm^2, the calculated n_e

increases from ~2.1 × 10^{17} to ~3.5 × 10^{17} cm^{-3}.The saturation in n_e at the higher laser fluences is

due to plasma shielding by the reflection or absorption of the laser photons by the expanding

carbon plasma [115, 143].
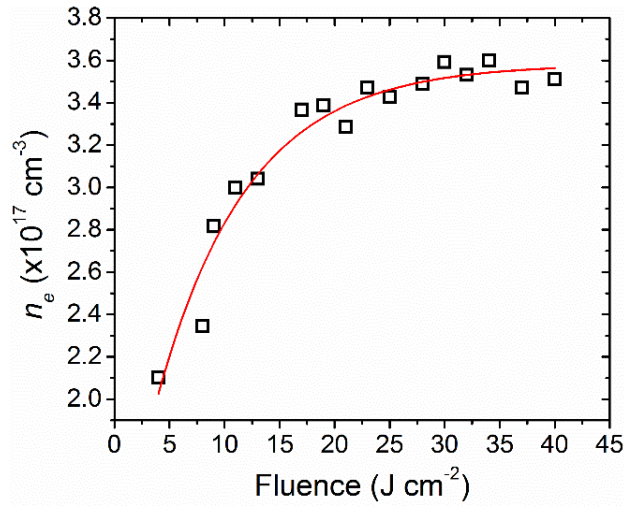
Fig. 5. 3 The variation of n_e with the laser fluence. The line profiles of C II at 392.0 nm is used to

determine the electron density n_e.

5.3.1.3 Electron Temperature

The C II 392.0, 426.7, and 588.9 nm lines are used for electron temperature T_e calculation.

Considering the detected carbon species, these lines have the biggest difference between their

corresponding upper energy levels, and provide the best straight line fit in the Boltzmann plot,

which led to better accuracy in T_e determination from the Boltzmann plot [144]. The corresponding

upper energy level transitions E_j for these lines are 157,234.07, 168,978.34, 162,524.57 cm^{-1},

respectively [145]. Since the lowest electron density observed in Fig. 5.4 is 2.1×10^{17} cm^{-3}, the n_e

satisfies the local thermodynamic equilibrium (LTE), and for laser plasma, T_e can be determined

from the Boltzmann plot method [133, 134]. The fitting parameters of the Lorentzian function to

the line profile affects the deduced electron density n_e. The following relation is used for T_e

calculations [134]:

$$ln\left[\frac{\lambda_{ji}I_{ji}}{g_jA_{ji}}\right] = ln\left[\frac{N(T)}{U(T)}\right] - \frac{E_j}{kT_e} \tag{3.2}$$

where, λ_{ji} is the transition wavelength, I_{ji} is the temporally and spatially-integrated line intensity

of the transition involving the upper level j and the lower level i, g_j is the statistical weight of the

level j, A_{ji} is the transition probability, $N(T)$ is the total number density, $U(T)$ is the partition

function, E_j is the energy of the upper level, k is the Boltzmann constant, and T_e is the excitation

temperature. A plot of $ln(\lambda_{ji}I_{ji}/g_jA_{ji})$ versus the energy E_j for the observed spectral lines follows

a straight line and its slope $-1/kT_e$ gives the T_e. Spectroscopic parameters (λ_{ji}, A_{ji}, g_j, E_j), listed in

Table 5.1 are obtained from the NIST database [145].

Table 5. 1 Spectroscopic parameters of C II transition lines.

Wavelength λ (nm)	Transitions	Statistical weight g_j	Transition probability A_{ji} (s^{-1})	Upper level energy E_j (cm^{-1})
392.06	$4s^2S_{1/2} \rightarrow 3p^2P_{3/2}$	2	1.27×10^8	157,234.07
426.72	$4f^2F_{7/2} \rightarrow 3d^2D_{5/2}$	8	2.38×10^8	168,978.34
588.97	$4p^2P_{3/2} \rightarrow 3d^2D_{5/2}$	4	3.15×10^7	162,524.57

The calculated T_e are reported in Fig. 5.4. The value of T_e for the plasma produced at 24 J/cm^2 fluence is presented in the inset of Fig. 5.4 as ∼0.85 eV calculated using C II (392.06, 426.72, and 588.97 nm) lines. When the laser pulse fluence is increased from 22 to 40 J/cm^2, the T_e increases from ∼0.83 eV to ∼0.90 eV, where a saturation is observed for ≥32 J/cm^2 laser fluence. Hanif *et al.* reported T_e values with the Boltzmann plot method for carbon plasma generated by an Nd:YAG laser (λ = 1064 nm, E = 400 mJ, τ = 5 ns, and λ = 532, E = 200 mJ,) as ∼0.85 eV and ∼0.81 using the C I neutral lines [134]. The laser-generated plasma is affected by the laser parameters (wavelength, pulse duration, and intensity) and the physical properties of the material [146]. Both n_e and T_e measurements are reported for time-integrated signals measured at an angle of 60° from the target normal. The spatial variations of the rapidly varying electron temperature T_e was not considered due to the collection of data from a fixed angle.
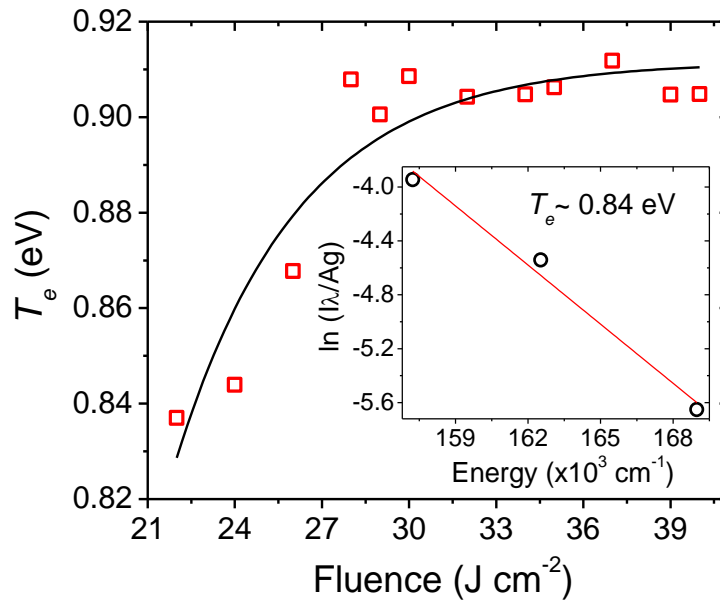
Fig. 5. 4 Electron temperature T_e variation with laser pulse fluence range of 22-40 J/cm^2. Inset is electron temperature T_e for laser fluence of 24 J/cm^2 calculated using C II lines at 392.0, 426.7, and 588.9 nm with the Boltzmann plot method.

5.3.1.4 Effect of External Electric Field on Optical Spectra

We studied the effect of applying an external electric field to the expanding plasma plume. A voltage of 6 kV is applied to the carbon target, which introduces an electric field between the grounded mesh and the target. The optical spectra were measured with the target at 0, 2, 4, and 6 kV. The applied electric field had no observable effect on the intensity of the C II, III, and IV spectral lines, as shown in Fig. 5.5, in which the optical spectra are given with the target grounded and when 6 kV is applied to the target. Variations in the line intensities are believed to be within the experimental errors. There is also no noticeable change in the number of carbon lines or line profiles with the applied voltage up to 6 kV. The lines at 495.5 and 610.3 nm may be due to impurities from oxygen. Additional measurements of current and voltage on the positively-biased target are conducted using a current pick-up coil (Pearson 6595) and a fast high-voltage probe (Tektronix, P6015A). The IV measurements show that the plasma is shorted through the grounded mesh with current flowing through the mesh. For the present experimental conditions, the optical emission line intensities and profiles were not affected by the electric field set between the target and the grounded mesh. A stainless steel target, mounted in the middle of a two parallel plate charged capacitor, was irradiated by an Nd:YAG laser (λ = 1064 nm, τ = 7 ns, E = 350 mJ) in air. No change in the shape and intensity of the emission spectra was observed in applied electric fields up to 10 kV/cm [147]. An enhancement in the electron temperature with the application of a 140 MHz radio-frequency electric field to laser plasma with the electron temperature increasing from 0.3 to 1.0 eV when 1.0 W radiofrequency power was applied [148]. For laser plasma generated by ablation of $YBa_2Cu_3O_7$ by an ArF excimer laser (λ =193 nm) in an oxygen environment, applying an electric field in the plume propagation direction enhanced emission lines [149].
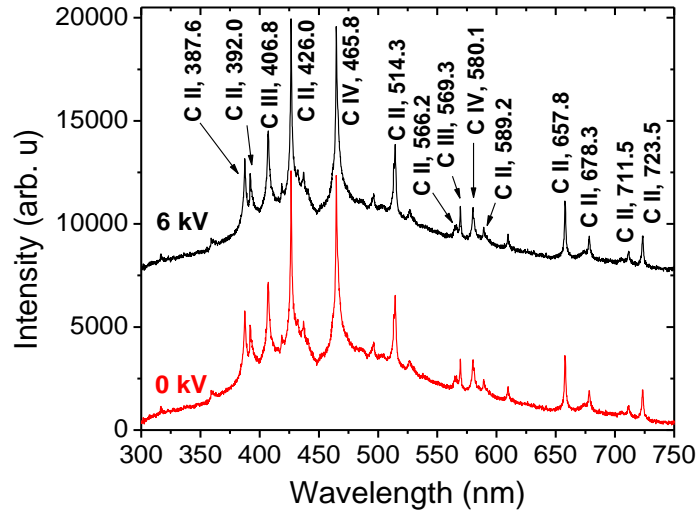
Fig. 5. 5 Optical emission spectra of carbon laser plasma expanding in an external electric field. The carbon target is grounded for the lower spectrum and biased to 6 kV for the upper spectrum.

5.3.2 Ion Time-of-Flight

The carbon ions emitted from the plasma plume when the target is grounded or positively biased were observed. The effects of the laser pulse energy on the ion charge, charge state, and ion temperature T_i is studied for a grounded target. When the target is positively biased, we used the electrostatic ion analyzer EIA to select ions with a specific energy-to-charge ratio E/z. The effects of the laser pulse energy and applying voltage to the target on the ion's generation are studied.

5.3.2.1 Ion Signal for Grounded Carbon Target

The kinetic energy distribution of ions emitted from the laser plasma is often used to obtain the ion plasma temperature in the core of the plume, where these ions are mostly generated [136]. The electrons are accelerated by inverse bremsstrahlung within the laser pulse duration and gain higher speeds with forward and lateral directions establishing an electric field at the plasma-

vacuum interface due to charge separation [122]. In the early stages of the plasma plume formation, large Coulomb forces are formed between these fast electrons and ion layers due to the slower mobility of ions compared to the electrons. The electric field due to the Coulomb forces accelerates ions with a higher degree of ionization to higher kinetic energies [150]. Some ions recombine with electrons as they travel forward and form either neutrals or low charge-state ions [151].

The carbon ions are detected by the Faraday cup FC. All other conditions except the pulse fluence are kept constant for the measurements conducted. The ions with higher kinetic energies are located in the front of the plasma plume due to their higher drift velocities. Ion TOF signals are shown in Fig. 5.6. In this configuration, the EIA is replaced with a straight tube, while maintaining the ion drift length the same. The ion signals have a well-defined single peak. There is an apparent reduction in the arrival time of the fast ion peak with the increase in the laser pulse fluence. This behavior of TOF signal with increasing laser pulse fluence indicates an increase in ion signal and a shortened arrival time due to the increased ion energy.
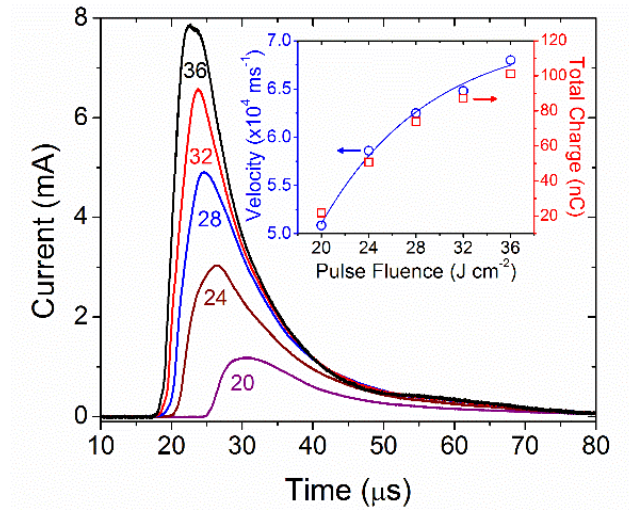
Fig. 5. 6 Time-of-flight ion detection from carbon laser plasma for different laser pulse fluence (J/cm^2). Inset shows the total ion charge and most probable ion velocities with the increase of laser pulse fluence.

The total charge detected by the FC is increased from ~22 to ~101 nC when the laser fluence is increased from 20 to 36 J/cm^2. For a laser pulse fluence higher than 28 J/cm^2, the increase in ion velocity slows down. For 32 J/cm^2 fluence, the most probable carbon ion velocity is ~6.5 × 10^4 m/s, corresponding to a kinetic energy of ~262 eV, shown in the inset of Fig. 4.6.

5.3.2.2 Ion Temperature for Grounded Carbon Target

For our laser ablation conditions, the laser plasma can be described as having an achieved LTE [132]. Under these conditions and considering the double-layer potential developed between the expanding plume and vacuum interface, the ion velocity distribution emitted from the plasma plume follows a shifted-Maxwell-Boltzmann (SMB) distribution [11, 150]. TOF ion signals are fitted to a SMB distribution function $I(t) = At^{-5}exp\left[-m((L/t) - u_f)^2/2kT_i\right]$, where A is a normalizing constant, m is the atomic mass of carbon, L is the distance from the target to the Faraday cup, u_f is the flow velocity, k is the Boltzmann constant, and T_i is the ion temperature associated with translational motion along the plume axis [150]. Achieving ions with SMB distribution assumes the thermalization of the plume particles and that the flow velocity u_f is fixed after a short distance from the target [146, 150]. The background pressure in the laser ablation chamber and in the ion transport line must be sufficiently low to allow ion drift with negligible recombination. The total scattering cross section for ions with different charge states was reported previously [152]. From these cross sections, the mean-free-path of the carbon ions for background pressure of 3 × 10^{-8} Torr is ≳1.8 × 10^3 m. Ion recombination in the drift tube is negligible since the drift distance of the carbon ions from the target to the Faraday cup is 1.54 m. The ion charges are frozen and the SMB distribution is applicable for ions drifting in vacuum for these conditions [97, 153]. We previously reported on the deconvolution of TOF signal for carbon and aluminum ions [84, 154, 155]. For laser pulse fluence of 28 J/cm^2, carbon ions up to C^{2+} are used for the SMB fitting, while for a laser pulse fluence of 120 J/cm^2

ions up to C^{4+} are used for the fit [84]. Aluminum ablation with a fs laser ($\lambda = 800$ nm, $\tau = 100$ fs, $I = 10^{13}$-10^{14} W/cm^2) showed that equivalent ion temperature was 25 eV for a grounded Al target at 7.6 J/cm^2 pulse fluence [155]. In one study [156], ions generated from tin laser plasma using a Q-switched Nd:YAG laser ($\lambda = 1064$ nm, $\tau = 5$ ns, $I \sim 10^{11}$ W/cm^2) were fitted to SMB distribution and the reported T_i was 34.4 eV for 77 mJ pulse energy. The ion pulse that contains contributions of ions with different charges is deconvolved into separate signals each corresponding to a charge state with its own SMB distribution. The sum of these signals is fitted to the TOF signal from all ions [156]. Another study reported on the expansion dynamics of Al plasma generated by ns Nd:YAG ($\lambda = 1064$ nm, $\tau = 7$ ns) and a Ti:sapphire laser ($\lambda = 796$ nm, $\tau = 100$ fs) pulses using SMB fitting to ion TOF signal [146]. A reasonable fitting was achieved, which indicates mostly thermal contributions to the velocity. Flow velocity $u_f = 14.4 \times 10^3$ m/s and an ion temperature $T_i = 21.96$ eV were retrieved from the fit. For ablation with a 7 ns laser pulse, two ion velocity components (slow and fast) were present in the TOF signal. While the slow component showed a good fit with $u_f = 5 \times 10^3$ m/s and $T_i = 1.74$ eV, the fast component was fitted better with a Gaussian distribution, an indication that the fast peak had a non-thermal nature [146, 157]. Bulgakova *et al.* reported $T_i = 6.46$ eV for a graphite target ablated with an Nd:YAG laser ($\lambda = 1064$ nm, $\tau = 13$ ns, $F = 16$ J/cm^2) [150]. They suggested that the TOF is poorly described for a low laser fluence due to the non-Maxwellian tail in the signal [150].

Fig. 5.7 shows the ion TOF signal and corresponding SMB deconvolution fits. The sum of individual fitting curves from the carbon ions compose the total ion current. The tails in Fig. 5.7(a) and (b) at the longer time indicate the presence of slow C^{1+} (C_s^{1+}) ion components that contribute to the TOF signal. When the slow C^{1+} ions are considered, a better fit to the data was achieved. For a laser pulse fluence of 36 J/cm^2 as in Fig. 5.7(a), we determined u_f from the SMB fit as 3.6×10^4 m/s for C^{1+} and 2.0×10^4 m/s for C_s^{1+}, whereas for a lower pulse fluence of 20 J/cm^2 as in Fig. 5.7(b), the value of u_f decreased to 3.4×10^4

m/s for C^{1+} and 1.6×10^4 m/s for C_s^{1+}, respectively. The equivalent T_i of the ejected ions obtained by the ion TOF deconvolution in Fig. 5.7(a) and (b) are 6.0 and 4.7 eV, respectively, when no accelerating voltage is applied.
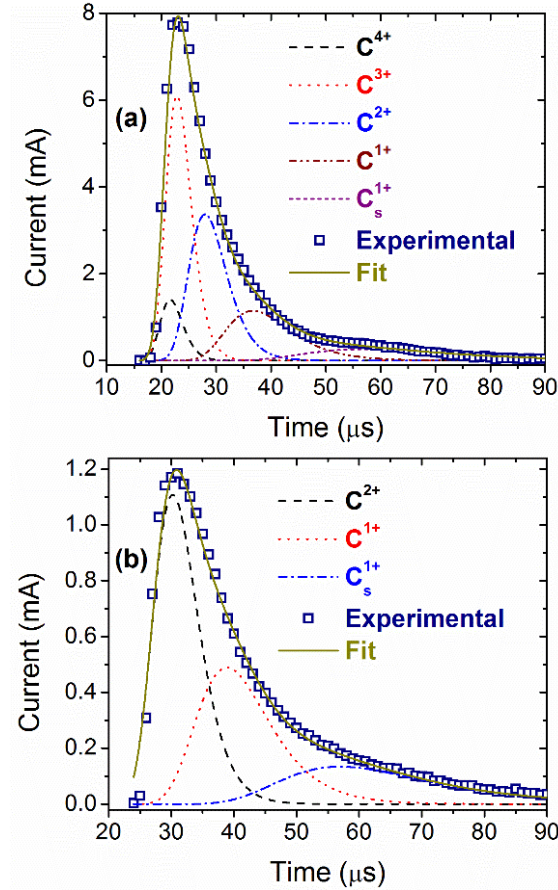
Fig. 5. 7 Deconvolution of the TOF signal from C ions into different ion charges each following the SMB distribution. C_s^{1+} refers to the slow ion component of the singly-ionized carbon ion. The laser pulse fluence is 36 J/cm^2 (a) and 20 J/cm^2 (b).

5.3.2.3 Ion Emission for Plume Expanding in External Electric Field

We next report on the carbon ion TOF signal when different voltages are applied to a carbon target. Due to the double-layer potential and the externally applied electric field, ions with different charges spread in time with the higher charge states arriving at the FC earlier. The TOF

for the carbon ions is $t_a + t_d = d\sqrt{2m/zeV} + S\sqrt{m/2zeV}$, where t_a is the acceleration time for an ion from target to the extraction mesh, t_d is the time that ions drift at a constant velocity from the extraction mesh to the FC, d is the distance between target and the extraction mesh, S is the total distance from the extraction mesh to the FC, both in meters, m is the atomic mass of C in kg, z is the charge state, e is the electron charge, and V is the biasing voltage applied on the carbon target. The initial ion velocity from the plasma plume, mainly due to the double-layer potential, is neglected in this equation as it is much smaller than the velocity component due to the applied potential considered here. This equation also does not account for the effect of plasma shielding limiting the ion acceleration by the external electric field and the adiabatic ion acceleration in the expanding plasma plume. Introducing an external electric field increases the kinetic energy of ions, thus temporal separation of ions, according to their charge state, occurs. Fig. 5.8(a) shows carbon signal detected by the FC after the ions pass the EIA. C^{1+} is easily generated because the amount of energy to remove the loosely bound electron is already contained within the laser carbon plasma. Considering the similar C^{1+} intensity profiles recorded, it is also possible that most of the C^{1+} ions are converted to C^{2+} ions since the ionization energy levels are comparable by a factor of 2. We observed C^{1+}, C^{2+}, and C^{3+} for target voltages below 5 kV. C^{4+} is observed along with lower charge states when the target voltages are 5 kV or more. The electric field between the grounded mesh and the target does not penetrate the plasma plume and affects only the lower density outer part of the plume. Thus; the ions experience the applied electric field at a location between the target and the mesh, and therefore, are accelerated less than the potential applied to the target. Nassisi *et al.* reported on the diagnostics of laser-induced ion beams of Y, Cu and Ag targets with acceleration [158]. They showed that introducing two gaps for acceleration can reduce the breakdowns through the grounded chamber walls, and increase the efficiency of delivered currents [158]. Energy-to-

charge selection E/z is adjusted according to the applied voltage on target to maximize the detected ion current. We previously reported that the energy resolution $\Delta E/E$ was determined to be 7%-10% because no slit was used on both ends of the EIA [84].
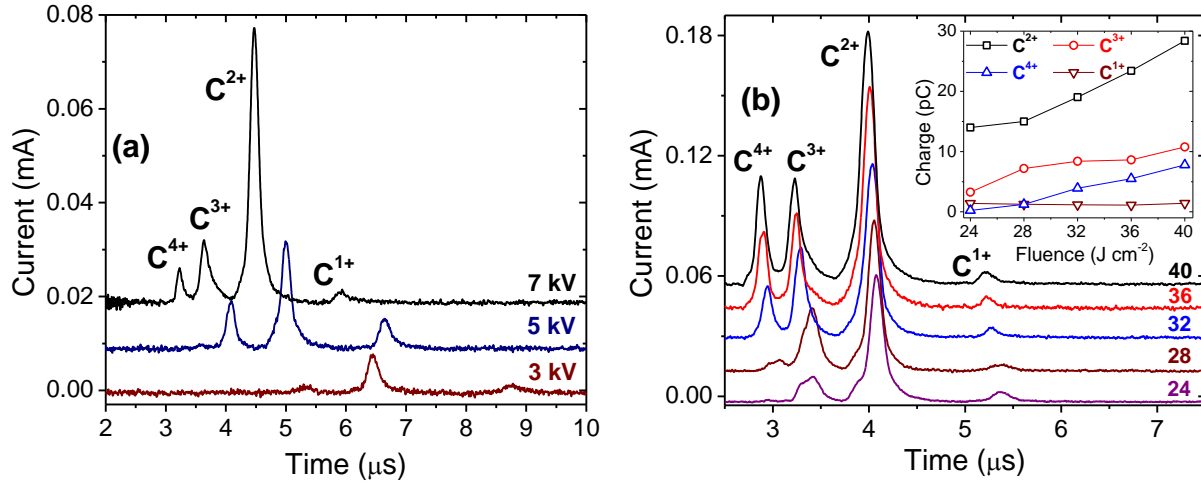
Fig. 5. 8 Carbon ions charge state generation at different biasing voltage applied on carbon target at 32 J/cm^2 laser pulse fluence (a). Energy-to-charge selection E/z is adjusted accordingly to maximize the detected ion current: E/z = 1.8, 3.2, and 4.3 keV for 3, 5, and 7 kV, respectively. Carbon ion generation with increasing laser fluence at E/z = 5.3$\pm$0.3 keV, and 9 kV applied to target (b). Results indicate up to C^{4+} can be extracted with 40 J/cm^2 fluence. *Inset* is charge detected for each carbon ion.

The carbon ions detected by the Faraday cup are strongly dependent on the laser pulse fluence which increases the electron density n_e and temperature T_e allowing for the generation of higher state carbon ions. The dependence of ion generation on the laser pulse fluence is studied for a target voltage of 9 kV and the EIA voltage selected for E/z = 5.3 keV, which provides maximum signal as detected by the FC. The ion signal obtained at laser pulse fluence from 24 to

40 J/cm^2 are shown in Fig. 5.8(b). We observe that the threshold pulse fluence for the carbon ion detection is 5 J/cm^2 per pulse. C^{1+} and C^{2+} ions are always observed for pulse fluence above 5 J/cm^2. The average charge state, peak ion energies, and corresponding intensities are increased accordingly with the laser pulse fluence. For laser pulse fluence above 24 J/cm^2, C^{4+} ions are also generated. We did not observe C^{5+} or C^{6+} at these laser pulse fluence. The reduced TOF with the laser pulse fluence observed in Fig. 5.8(b) is due to the increase in kinetic energy of the ions drifting out of the expanding plasma. The inset of Fig. 5.8(b) shows the total ion charge dependence on the laser pulse fluence for each carbon ion charge generated. The total charge detected by the FC increases with the laser pulse fluence having the most contribution from C^{2+} ions. The total charge recorded for 40 J/cm^2 pulse fluence are 1.4 pC for C^{1+}, 28.4 pC for C^{2+}, 10.7 pC for C^{3+}, and 7.8 pC for C^{4+}.

5.4 Conclusion

Carbon ions and corresponding spectral lines are generated and analyzed by TOF and optical spectroscope. C IV spectral lines and C^{4+} ions are observed when 3 kV target voltage and laser pulse fluence above 28 J/cm^2 are used. Kinetic energy is calculated as 5.3 keV per charge with 9 kV target voltage. Boltzmann plot method revealed electron temperatures $T_e = 0.90$ eV for C II lines at 40 J/cm^2. Furthermore, plasma temperature $T_i = 6.0$ eV for 36 J/cm^2. A maximum electron density of 2.1×10^{17} cm^{-3} which saturates after 25 J/cm^2 is calculated.

CHAPTER 6

GENERATION OF C^{6+} IN A SPARK-COUPLED LASER PLASMA

6.1 Introduction

Carbon ions sources are used in various applications that include surface hardening, growth of diamond-like thin films, synthesis of graphene, and carbon ion radiotherapy [20]. Implantation of C^{1+} has been used for the synthesis of high-quality multi-layer graphene on Ni/SiO$_2$/Si substrates [20]. This approach facilitates graphene integration in advanced Si-based circuits. C^{1+} doping can locally modify TiO$_2$ films lowering their band-gap from 3.3 to 1.8 eV, thus, making it photocatalytically active in the degradation of organic compounds under both visible and UV light irradiation [128]. Fully stripped C^{6+} ions are used in radiotherapy due to their high potential energy, convenient dose-depth distribution, and ease of their acceleration and focusing [130, 159]. The use of carbon ions have certain advantages over conventional radiation therapies, as carbon ions deposit high energy in the tumor tissue, so they are considerably more destructive to the tumor with minimal exit dose to healthy tissues [160].

Laser-generated plasma has been widely used as a source of intense multicharged ions (MCIs) that is capable of generating MCIs from any solid target [161]. Nanosecond lasers are used in most laser ion sources, however, femtosecond lasers have also been demonstrated to yield MCIs with high charge states [5]. The charge yield and state of laser-generated MCIs are dependent on the laser pulse parameters such as pulse energy, pulse width, wavelength, and laser focusing on target. To increase the charge state, higher laser pulse energies are used [98]. Aside from the added complexity, increasing the laser pulse energy, generally, limits the pulse repetition rate. The resulting dense plasma becomes opaque to the laser pulse limiting interaction with the core of the expanding plasma [162]. Here, we discuss the use of spark-coupled laser carbon ion source. Coupling of the spark-discharge (SD) to the laser plasma increases the plasma density n_e and temperature T_e, and results in the generation of higher charge state ions and larger total charge

yield. Fully stripped C^{6+} ions are readily achieved by spark coupling to the laser plasma. We calculate n_e and T_e based on the optical emission spectroscopy (OES) data. The effective plasma ion temperature T_{ieff} is calculated from deconvolution of the MCIs time-of-flight (TOF) signal. The ion temperature obtained from the MCI TOF signal is much higher than T_e measured by OES since T_{ieff} represents the core plasma temperature, while OES probes the outer region of the expanding laser plasma.

6.2 Experimental

The carbon plasma is generated by ablating a glassy carbon target with laser pulses from a Q-switched Nd:YAG laser (wavelength 1064 nm, pulse duration of 8 ns measured at full width at half maximum). The carbon target (99.99% pure, 0.58 mm thickness, <50 nm surface roughness, as characterized by the manufacturer HTW, Germany) is mounted in a vacuum chamber that is evacuated to a pressure in the low 10^{-8} Torr. At these low pressures, the loss of ions by charge transfer to the background gas is negligible [10]. A nickel mesh 8 cm in diameter with an open area of 70% is grounded and placed 10 cm in front of the target. Ion analysis is accomplished by a 90° radial cylindrical electrostatic ion energy analyzer (EIA) placed between the ion source and a Faraday cup that is connected to an oscilloscope (Tektronix, MDO 3034) with 50 Ω termination and used to detect the ion signal. The EIA has a range of E/z obtained by $E/z = eU/2\ln(R_2/R_1)$, where E is the kinetic energy of the ion, U is the potential across the deflection plates, e is the electron charge, $R_1 = 14.5$ cm is the inner radius, and $R_2 = 18.3$ cm is the outer radius [138]. A fixed voltage of 5 kV (CPS, 100-R) was applied to the target while keeping the chamber grounded. Using $E/z = 2.3$ keV maximized the detected total charge. The Faraday cup is placed 154 cm away from the target and consists of a 5-cm diameter aluminum cup (biased at -80 V) with a suppressor ring electrode placed 1 cm away from the cup entrance. The suppressor electrode is biased at -120 V,

enough to suppress the secondary electron emission from the Faraday cup due to positive ion collisions. The design of the Faraday cup and its use for ion detection in TOF mode was previously discussed [84].

The angle of incidence of the laser beam on the surface of the target was 60° and the laser intensity was $\sim 5 \times 10^9$ W/cm^2 for a pulse energy of 50 mJ. Two laser intensities of 3.5×10^9 and 1.5×10^{10} W/cm^2 were used to collect TOF data from a straight drift tube. In this geometry, the carbon target was grounded and the MCIs were obtained with the laser pulse alone. A schematic of the pulsed-power circuit for the SD is shown in Fig. 6.1. The spark electrodes are made of 3.0 mm diameter cylindrical graphite rods with rounded tips. These electrodes are placed in front of the target, 12 mm from the center of the rods to the target surface. The gap between the two electrodes is 5 mm. To protect the capacitor charging power supply (Glassman, PSLG30R5), a 350 kΩ charging resistor (R_1) is used.
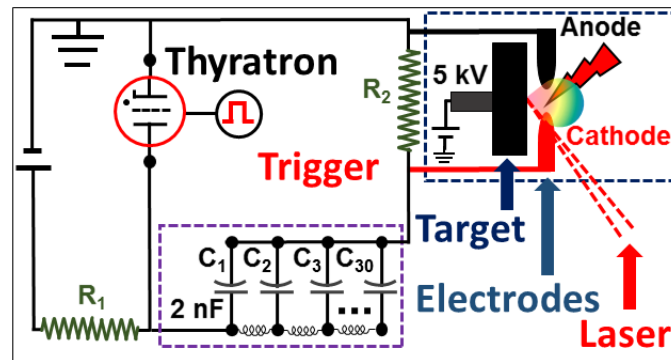
Fig. 6. 1 Schematic of the pulse forming network used for the SD. The thyratron is triggered after a set delay from the laser pulse to maximize SD coupling to the laser plasma. The anode and cathode are graphite rods.

The pulse forming network is terminated with a 300 Ω resistor (R_2) connected in parallel with the spark. The value of R_2 is chosen to provide best coupling between the SD and the laser plasma. A pulse forming network consisting of 30 high voltage capacitors (UHV 9 A, 2 nF, 40 kV TKD) is used. A thyratron is used as a switch for the SD. The thyratron (L3 Technologies, L4945A) is triggered at a set delay from the laser pulse. The capacitor bank was charged up to 5.5 kV. High voltage (Tektronix, P6015A) and

current pick-up (Pearson Electronics, 6595) probes are used to record the voltage across the SD electrodes, voltage on target, SD current, and current through target. The plasma emission is recorded by an optical spectrometer (Avantes, ULS3648-2) connected to fiber optics placed external to the vacuum chamber. The optical spectra observed are spatially and time averaged.

6.3 Results and Discussion

Once the laser interacts with the target, the laser plasma plume expands perpendicular to the surface of the target. Triggering the spark voltage with a delay from the laser pulse provides control over the SD timing and allows to maximize the spark energy coupling to the laser plasma. Placing a 50 ns delay (using Stanford Research Systems digital delay generator, DG645) between the laser pulse and the trigger pulse of the thyratron gives the highest ion yield. The voltage on the cathode and anode of the spark electrodes and the current passing through the cathode and anode of the spark were measured using the fast high-voltage probe and the current pick up coil. Similar measurements were also conducted for the voltage on the carbon target and current though it. The voltage and current measurements are taken with only one high-voltage probe and one current probe switched to measure voltage on and current through the cathode, anode, and target using different laser pulses. All experimental conditions were kept the same for the different pulses. Pulse-to-pulse fluctuations occur and are evident in the shape of the spark voltage, but less observed in the spark current. Pulse-to-pulse fluctuations are also observed in the shape of the target voltage and current. The magnitudes of the voltage on and current through the spark electrodes are relatively stable from pulse-to-pulse. The target voltage and current depend on fluctuations in the laser pulse energy and strongly depends on the ablation location on the target. Therefore, care was taken to keep the ablation location fixed relative to the spark electrodes. Fig. 6.2 shows the voltage signals on the spark electrodes (a), the current signals measured with the current pick-up coil placed around the cathode and anode of the spark electrodes (b),

and voltage on and current through the target (c). The spark capacitor bank was charged to 3.0 kV, the target bias was 5.0 kV, and the laser pulse energy was ∼50 mJ on target. The ∼7 ns laser pulse interacts with the target at time $t = 0$. The cathode voltage shows a fast drop in ∼0.1 µs, followed by oscillations, and rise back to near ground potential. The voltage oscillations measured on the anode is due to the stray inductance of the wires in the circuitry. The cathode voltage pulse width in Fig. 6.2(a) is ∼0.8 µs. The current through the spark electrodes is shown in Fig. 6.2(b). The current flow is mainly between the two spark electrodes with small coupling between the cathode and target as the current through the cathode was consistently higher than that through the anode. Fig. 6.2(c) shows the voltage on the carbon target and current through it. When the spark is initiated, the 5 kV bias voltage decays from 5 kV to ~1 kV in ~0.2 µs. The recovery of the voltage on the target to its 5 kV value is determined dominantly by the power supply topology. The initial drop in the voltage on target can be due to the edge of the carbon plasma shorting the gap between the target and the spark electrodes, and as the plasma further expands, shorting the target to the grounded mesh. Since the ions escaping the plasma drifts with velocities significantly more than the plasma expansion velocity, they escape the grounded mesh before it is shorted. The target current is significantly lower than the spark electrodes current (∼15 A peak current through target compared to ∼222 A through cathode, and ∼200 A through anode). The observed voltage and current signals depend on several factors in addition to the circuit parameters and delay between the laser pulse and the electrical pulse triggering the thyratron. These parameters include the spark geometry, laser spot position and size on target, laser pulse energy, stray inductance of the cables, power supply topology, pulse-to-pulse variations in the laser energy, in addition to fluctuations arising from the nature of the SD. The SD energy deposition into the laser plasma is calculated from the voltage across the spark electrodes and current through the cathode shown in Fig. 5.2. For 3.0 kV charging voltage, the SD deposits ∼256 mJ in the carbon laser plasma. Similar measurements conducted for SD voltage of 5.5 kV gives a deposited energy of ∼750 mJ.
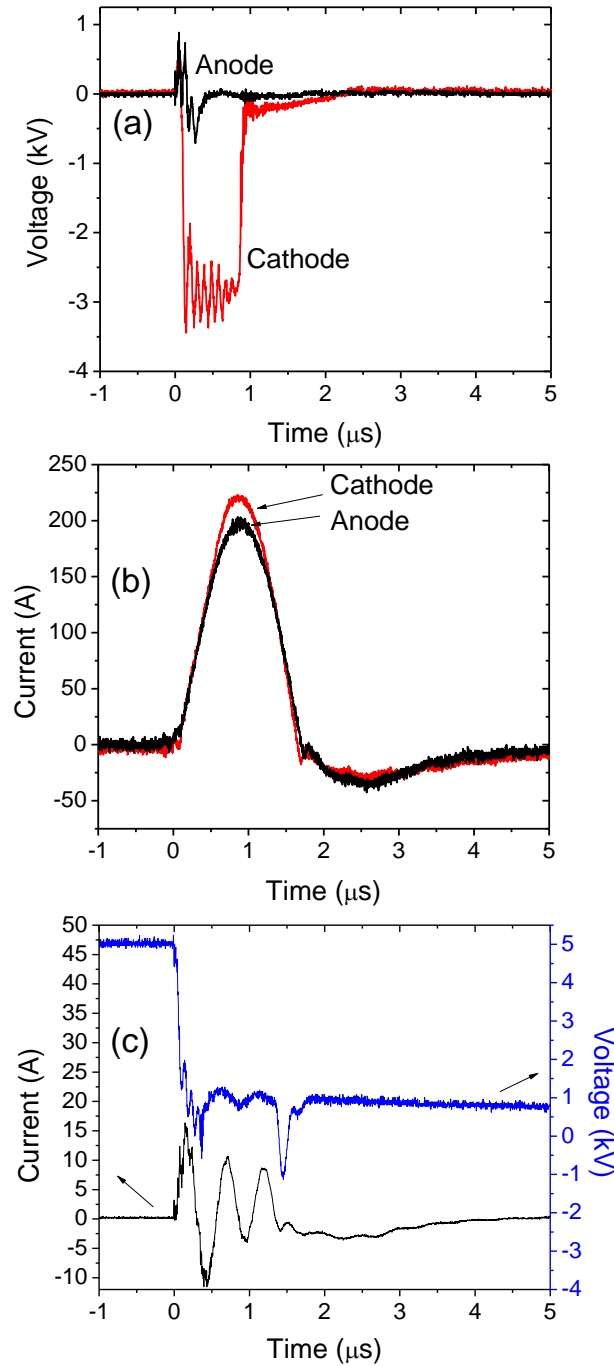
Fig. 6. 2 Voltage signals detected with the high-voltage probe placed on the anode and cathode of the spark (a). Current across the spark electrodes is measured by a current pick-up coil (b). Voltage on carbon target and current through it (c). The pulse forming network is charged to 3 kV with the carbon target biased at 5 kV. The laser pulse energy is ∼50 mJ.

Fig. 6.3(a) shows the Faraday cup signal of carbon ions with the EIA set to select an E/z centered at 2.3 keV. The MCI spectra reported in Fig. 6.3(a) are an average of 20 laser pulses with each laser pulse ablating a fresh surface area of the moving target. With the spark coupled to the laser plasma, C^{5+} and C^{6+} ions are detected at a charging voltage ≥ 3.5 kV, whereas ion charge up to C^{4+} are detected with the laser pulse only. The inset in Fig. 6.3(a) shows a schematic of MCI detection setup. The use of the EIA for detection allows clear identification of the ion charge state. Fig. 6.3(b) shows the TOF signal from the carbon ions detected without the EIA analyzer. The total charge Q_i is obtained from the Faraday cup signal, $Q_i = (\int V_F(t)dt/R)$, where $V_F(t)$ is the voltage signal of the Faraday cup, and R is the 50 Ω oscilloscope internal resistance. The total ion charge is amplified by a factor of ~ 4.5 for 3.5 kV and ~ 6.0 for 5.5 kV spark voltage. These measurements are based on the TOF signals in Fig. 6.3(b) taken with a single laser pulse. Multiple peak formations are observed in Fig. 6.3(b), possibly due to slow components of C^{1+} and C^{2+} ions. Observation of a fast and slow components of ions in laser ion sources, with each component described by a shifted Maxwell-Boltzmann (SMB) distribution was previously observed [117, 163, 164]. The fast component is due to direct multiphoton laser ionization, while the slow component arises from collisional processes in the expanding plume [163, 164]. When using the electrostatic ion energy analyzer (EIA) to select $E/z = 2.3 \pm 0.3$ keV, the charges with that E/z values are amplified by a factor of ~ 9 with the SD. The charge amplification depends on the ion charge state as C^{5+} and C^{6+} are not observed without the SD. We did not observe an intensity amplification for laser energies below ~ 35 mJ as the SD did not initiate. The SD ionizes more carbon atoms, leading to a significant increase of detected charges and an increase of the charge state. When the SD is used, C^{5+} and C^{6+} are detected for > 3.5 kV SD in the carbon plasma.
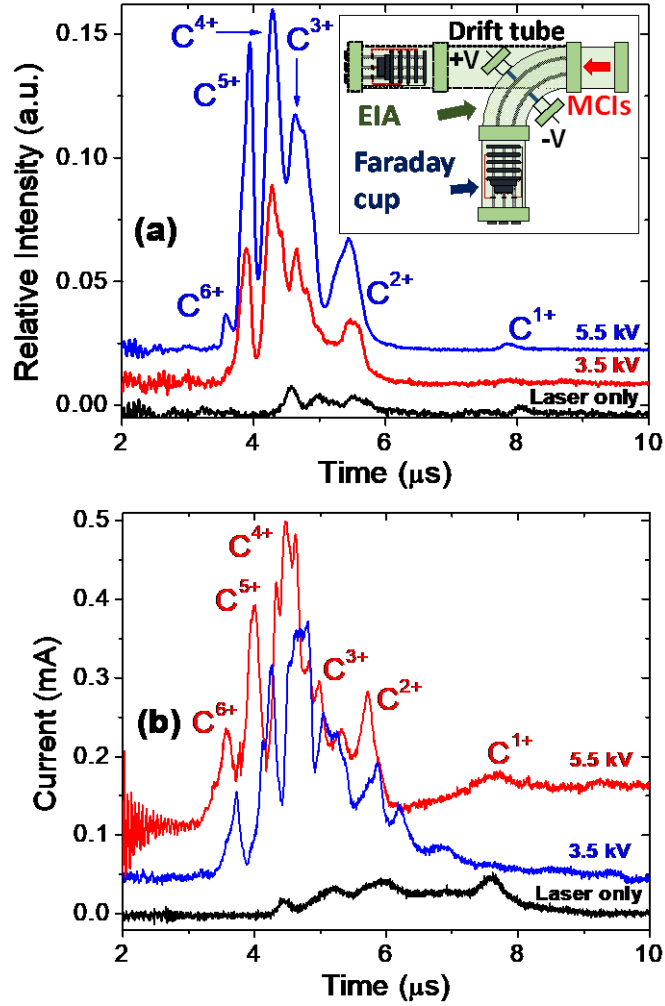
Fig. 6. 3 Multicharged ion (MCI) time-of-flight (TOF) signal from SD-coupled to laser carbon plasma (a). The SD charging voltages were 0 (laser only), 3.5, and 5.5 kV. The inset in (a) shows the MCI detection chamber components. The electrostatic ion energy analyzer (EIA) is operated at $E/z = 2.3\pm0.3$ keV. TOF signals of carbon ions without EIA analyzer for different SD charging voltages (b).

OES is often used to probe the electron density n_e and plasma temperature T_e. The n_e can be estimated from the Stark broadening of the C II line (transition in C^{1+} ion) at 392.0 nm. This method is well-established for measuring the electron densities in high density plasmas, and is applicable to SD plasmas [141]. Stark broadening in plasmas occurs from collisions with charged particles, which results in a shift in

the peak wavelength, and a broadening of the line. The full-width at half-maximum (FWHM) of the Stark broadened $\Delta\lambda_{1/2}$, line due to electron collisions is related to the n_e by [133]:

$$\Delta\lambda_{1/2} = 2w \left[\frac{n_e}{10^{16}} \right] \tag{6.1}$$

where w is an electron impact broadening parameter in Å and n_e is the electron density in cm^{-3}. In Eq. (1), only broadening due to electron collisions are considered since this is the most dominant term contributing to Stark broadening [133]. The value of w depends on the plasma temperature and, assuming local thermodynamic equilibrium (LTE), was calculated to be 0.0245 Å for C II line ($\lambda = 392.0$ nm, $4s\,^2S_{1/2} \rightarrow 3p\,^2P_{3/2}$) at T_e of 0.86 eV (10,000 K) [133]. The electron density n_e for LTE to be satisfied is $n_e \geq 1.4 \times 10^{14}T_e^{1/2}(\Delta E_{ji})^3 \ cm^{-3}$ [133], where ΔE_{ji} is the energy difference between the upper and lower levels of the transition. This is a necessary, but insufficient, condition for LTE. For the transition of C II at 392.0 nm, $\Delta E_{ji} = 3.16$ eV, and the lowest limit for n_e is 5.4×10^{15} cm^{-3} for $T_e = 1.5$ eV [141, 165]. Correction was made for the instrumental broadening of 0.09 nm, as measured by the FWHM of the Hg 435.8 nm line. From Eq. (1), $n_e \sim 3.7 \times 10^{17}$ cm^{-3} for laser intensity of 5×10^9 W/cm^2 without the application of any SD. The n_e we observe is increased to $\sim 4.2 \times 10^{17}$ cm^{-3} when the SD is applied with 5.5 kV charging voltage while the same laser parameters are used. Under these conditions, the LTE approximation is justified and T_e can be determined from the Boltzmann plot [133, 166]. We use spectral emission lines from C II (392.0, 426.7, and 588.9 nm) for T_e calculations. The corresponding upper energy level transitions E_j for these lines are 157,234.07, 168,978.34, and 162,524.57 cm^{-1}, respectively [145]. The following relation is used to calculate T_e [134]:

$$ln\left[\frac{\lambda_{ji}I_{ji}}{g_jA_{ji}}\right] = ln\left[\frac{N(T)}{U(T)}\right] - \frac{E_j}{kT_e} \tag{6.2}$$

where $\lambda_{ji,}$ is the transition wavelength, I_{ji} is the temporally and spatially integrated line intensity of the transition from the upper level j to the lower level i, g_j is the statistical weight of the level j, A_{ji} is the transition probability, $N(T)$ is the total number density, $U(T)$ is the partition function, E_j is the energy of the upper level, k is the Boltzmann's constant, and T_e is the electron temperature. A plot of $\ln(\lambda_{ji}I_{ji}/g_jA_{ji})$ versus energy E_j for the observed spectral lines follows a straight line with a slope $-1/kT_e$. Enhanced line emission from a laser plasma by coupling it to a SD was previously reported [167]. In that case, the signal enhancement was mainly attributed to the increased emission time since the SD time was significantly longer than the laser plasma [167]. Fig. 6.4(a) shows the enhanced line intensities relative to that observed without the SD. Emission of the C_2 Swan band in the green (460 nm - 600 nm) is observed. These molecular bands are commonly observed in laser carbon plasma [165, 168]. Fig. 6.4(b) shows the calculated n_e and T_e of the laser-spark carbon plasma for different spark charging voltages. The T_e is calculated to be 1.06 eV for the laser-generated carbon plasma. When SD at 5.5 kV charging voltage is coupled to the laser plasma, T_e is increased to 1.46 eV. The results show that T_e increases with the charging voltage. The line emission intensities were previously observed to depend on both the deposited energy and the discharge electrode geometry [169]. Enhanced optical line emission intensity for laser plasma generated in an external electric field was previously reported [170]. Electron heating by the external field in the plume region where the external electric field is not shielded could be responsible for the enhanced line emission intensity.
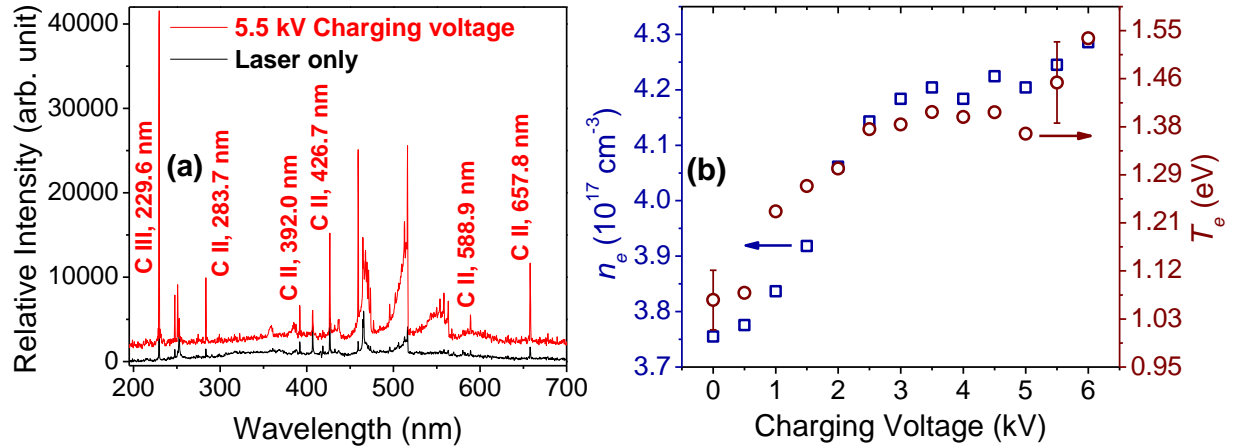
Fig. 6. 4 Optical emission spectra with no SD (black) and 5.5 kV charging voltage (red) (a). C II line (392.0 nm) is used for calculations of ne. C II lines (392.0, 426.7, and 588.9 nm) are used for T_e calculations. The variation of n_e and T_e with charging voltage (b).

For dense plasma with significant self-absorption, OES measures the spectral emission from the outer part of the expanding plasma, providing no information on the plasma core where most ions are generated. Alternatively, the carbon TOF ion signal can be used to extrapolate the ion temperature under LTE condition. To accomplish this, the TOF ion signal is fitted to a SMB distribution function $I(t) = At^{-5}exp[-m((L/t) - u_f)^2/2kT_{ieff}]$, where A is a normalizing constant, m is the atomic mass of carbon, L is the distance from the target to the Faraday cup, u_f is the flow velocity, k is the Boltzmann constant, and T_{ieff} is the effective ion plasma temperature associated with translational motion along the plume axis [150]. The background pressure in the laser ablation chamber and in the ion transport line must be sufficiently low to allow ion drift with negligible recombination. The total scattering cross section for ions with different charge states was reported previously [152]. From these cross sections, the mean free path of the C ions for background pressure of 3×10^{-8} Torr is $\gtrsim 1.8 \times 10^3$ m. Since the drift distance of the carbon ions from the target to the Faraday cup is 1.5 m, ion recombination in the drift tube is negligible. At

these conditions, the ion charges are frozen and the SMB distribution is applicable for ions drifting in vacuum [97, 153]. Fig. 6.5 shows the TOF signal and corresponding SMB fits. We previously reported on the deconvolution of TOF spectra for carbon ions [84]. We determined the maximum number of charge states from the retarding field analysis for laser intensity conditions similar to the laser intensities presently used. For laser pulse intensities of 3.5×10^9 W/cm^2, carbon ions up to C^{2+} are used for the SMB fitting, while for a laser intensity of 1.5×10^{10} W/cm^2, ions up to C^{4+} are used for the fit. We did not fit the ion TOF signal when the SD is coupled to the laser plasma because the distortion of the recorded ion signals by the spark results in a signal that cannot be deconvolved into ion signals with SMB distributions. The SD distorts the electric field in the target-mesh region and introduces additional energy to the ions due to plasma heating as previously observed [171]. The tails in Fig. 6.5(a) and (b) at the longer time indicate the presence of slow C^{1+} (C_s^{1+}) ions that contribute to the TOF signal. When the slow C^{1+} ions are considered, better SMB fit was achieved. For a laser intensity of 3.5×10^9 W/cm^2, we determined u_f from the SMB fit as 2.5×10^4 m/s for C^{1+} and 7.5×10^3 m/s for C_s^{1+}, whereas for a higher laser intensity of 1.5×10^{10} W/cm^2, the value of u_f increased to 4.9×10^4 m/s for C^{1+} and 2.7×10^4 m/s for C_s^{1+}, respectively. The equivalent T_{ieff} of the ejected ions obtained by the ion TOF deconvolution in Fig. 6.5(a) and (b) are 8.2 and 16.8 eV, respectively, when no accelerating voltage is applied. Bulgakova et $al.$ reported values from 1.5 to 4 eV using a graphite target ablated with an Nd:YAG laser ($\lambda = 1064$ nm, $\tau = 13$ ns) at laser intensities of 0.5-2×10^9 W/cm^2 [150].
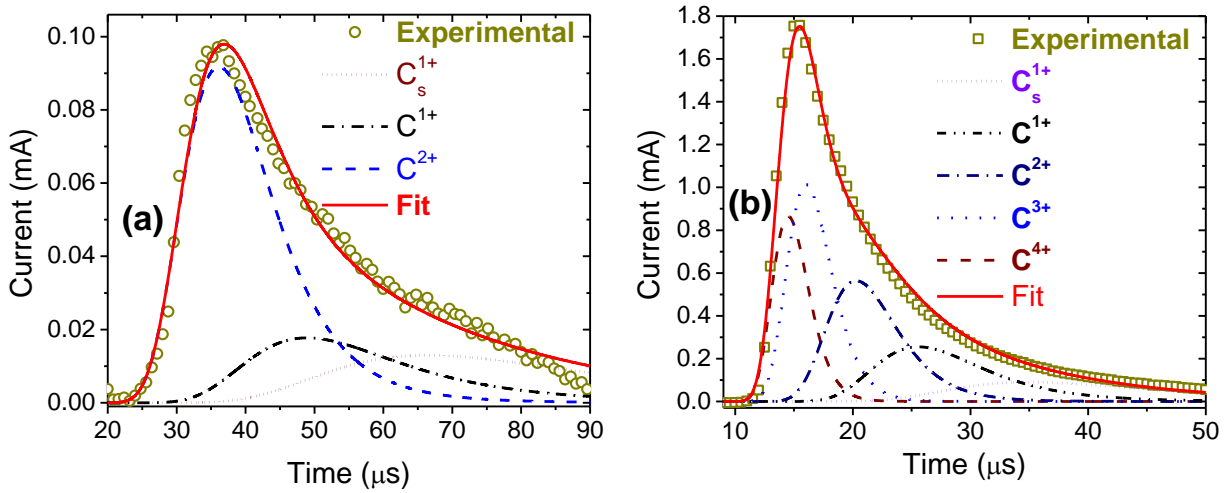
Fig. 6. 5 Deconvolution of the TOF signal from C ions into different ion charges each following the SMB distribution. C_s^{1+} refers to the slow ion component of the singly-ionized carbon ion. The laser pulse intensity is 3.5×10^9 W/cm^2 (a) and 1.5×10^{10} W/cm^2 (b).

6.4 Conclusion

Spark-discharge is coupled to a laser generated carbon plasma. Using $\sim$750 mJ SD energy with a 5.5 kV capacitor bank voltage with respect to relatively low 50 mJ laser pulse energy significantly amplified the charge generation, the spectral lines, and fully stripped C^{6+} ions are observed. The electron temperature T_e is 1.06 eV for laser generated plasma, however using SD increased it to 1.46 eV when 5.5 kV charging voltage is coupled to the plasma.

CHAPTER 7

MULTICHARGED IONS BY FS LASER ABLATION

7.1 Introduction

Laser ablation of a solid target in vacuum generates dense plasma in which the electrons are heated by the intense laser photons to energies up to several hundred electron-volts leading to multiple collisional ionizations. The dense laser plasma contains multicharged ions that are accelerated and extracted by the double-layer potential formed at the expanding plasma-vacuum edge [150]. Laser multicharged ion sources (LMCI) can provide multicharged ion (MCI) beams with high currents from any solid target, which is attractive as an ion injector for ion accelerators [6].

Interest in MCI sources stems from their applications in ion implantation, ion deposition, atomic-scale surface etching, surface pattering at the nanoscale, and in secondary ion mass-spectrometry [66, 172, 173]. MCI implantation in metals has been shown to modify the surface tension and corrosion resistance [88, 172]. An MCI interaction with a surface involves release of significant potential energy in addition to kinetic energy and, therefore, can remove electrons from the impacted region, resulting the formation of nano-meter craters, a useful feature that has applications in nanopatterning and nanoidentification [3]. Slow MCIs have high surface selectivity with strong local excitation that results in potential sputtering [174] with applications in semiconductor surface processing. Using slow MCIs with high potential energy, it was reported that native SiO_2 was removed from the Si surface with less surface damage than possible when using singly-charged Ar^{1+} ions for sputtering. The surface roughness was increased by only 0.05 nm root-mean-square (rms) after slow Ar MCI interaction [175].

Carbon MCIs have applications in ion implantation [105], diamond-like thin film growth [126], and radiotherapy [176]. It was reported that polysilicon grain growth, on floating gate surface used in flash memory devices, can be minimized with carbon ions implantation [177]. This feature can improve the uniformity and integrity of the thin dielectrics deposited between the floating and polysilicon gates of nonvolatile memory devices. Microstructural modifications on Ti-6Al-4V alloy after carbon MCI implantation was studied [105]. The surface wear resistance was enhanced, the surface friction coefficient was reduced, and hardness was increased in the first 300 nm due to TiC formation [105]. The use of carbon ions in radiotherapy allows localized ion energy deposition targeting hard-to-reach tumors with minimal damage to the surrounding tissues and no exit dose. Fully-stripped C^{6+} are used in radiotherapy because of the relative ease in their acceleration, bending, and focusing [176, 178].

Generation of MCIs by femtosecond laser ablation was previously reported [5, 179-181]. Copper, aluminum, and carbon ions were generated by femtosecond laser ($\tau = 70$ fs, $\lambda = 800$ nm, $F < 1.0$ J/cm^2) ablation [179]. The results showed higher ion yield for C than for Cu and Al due to the larger skin depth of C that allowed deeper laser pulse penetration into the target and released more electrons resulting in more ionization collisions and ion acceleration. Ion time-of-flight (TOF) measurements showed that the Cu and Al ions had fast and slow components (double peaked), whereas the fast component for C was significantly slower. This was attributed to the fact that the fast electrons that escaped from the target in C ablation have less kinetic energy than for ablation of Cu and Al because extra energy is required to carry electrons to the conduction band [179]. Si and Ti plasma produced by femtosecond laser ($\tau = 200$ fs, $\lambda = 616$ nm, $F < 4$ kJ/cm^2) ablation was studied by ion TOF measurement [180]. Highly energetic ions with maximum charge states of Si^{6+}, C^{6+}, and O^{4+} were recorded [180]. In that case, the C and O ions were reported to

originate from impurities on the Si surface. In a study of femtosecond laser ($\tau = 100$ fs, $\lambda = 780$ nm, $F \sim 100$ J/cm^2) of graphite, charge states up to C^{4+} were detected [181]. Shaim and Elsayed-Ali observed Al ions up to Al^{6+} using femtosecond laser ($\tau = 100$ fs, $\lambda = 800$ nm, $F < 7.6$ J/cm^2) ablation of an Al target [155]. In comparison to the nanosecond laser ablation, femtosecond laser ablation required significantly lower ablation threshold and generated ions with higher charge state [155].

We report on development of a carbon LMCI source using a femtosecond laser source (Ti:sapphire, $\tau = 150$ fs, $\lambda = 800$ nm, $F \leq 6.4$ J/cm^2). The ions are detected using a Faraday cup in a time-of-flight configuration. A three-mesh retarding field energy analyzer is also used to analyze the ion energy-to-charge. Charge states up to the fully-stripped C^{6+} are observed with a laser fluence of 6.4 J/cm^2. From the deconvolution of the MCI TOF signal with a shifted Maxwell-Boltzmann (SMB) distribution, we calculate the effective plasma ion temperature T_{ieff} to be ~ 6.9 eV. T_{ieff} is characteristic of the core plasma temperature where the ions are generated.

7.2 Experimental

A chirped pulse amplified Ti:sapphire laser source (Quantronix Integra-E, 1 kHz) emitting at a center wavelength of $\lambda = 800$ nm pulse with a pulse duration $\tau \sim 150$ fs is used to ablate the glassy carbon target (0.58 mm thickness, 99.99% purity, <50 nm surface roughness, as characterized by the manufacturer HTW, Germany). The maximum laser energy is ~ 2.2 J at 1 kHz repetition rate measured before the chamber window. The reported values are adjusted for the 8% loss in the glass window. A mechanical fast shutter (Vincent Associates, Uniblitz VMM T1) is triggered by the laser controller and used to select a single laser pulse for carbon ablation. The laser pulse enters the source chamber through a viewport and is incident on the carbon target at an

angle of $60°$ from the target normal. The laser is focused inside the chamber using a lens to an area of $\sim 2 \times 10^{-6}$ cm^2 at focus as obtained using the knife-edge method at the target-equivalent plane. The target is mounted on an insulated support to allow for applying a 3 kV acceleration voltage while maintaining the chamber grounded. A grounded Ni mesh 8 cm in diameter with an open area of 70% is placed 10 cm in front and parallel to the surface of the carbon disk. The chamber pressure is in the low 10^{-6} Torr. Therefore, the loss of ions by charge transfer with the background gas is negligible [10]. The Faraday cup is placed 1.54 m away from the carbon target. The ion transport line is a stainless-steel tube with a 10-cm inner diameter. A 5-cm diameter Al Faraday cup (FC), biased to -80 V, is used to collect the TOF signal of the carbon ions. A suppressor ring electrode is placed 1 cm in front of the FC entrance. The secondary electron emission signal from the FC, due to positive ion collisions, is completely suppressed when biasing the suppressor electrode at -120 V, and its voltage is maintained throughout the experiment. The retarding field ion energy analyzer (RFA) consists of three 5-cm in diameter Ni grids with 70% open area separated by 1 cm. The two outer grids were grounded while the central grid is held at a variable voltage, V_r. The central retarding electrode is positively biased to analyze the extracted carbon ions energy distribution. An oscilloscope (Tektronix DPO 3034, 50 Ω termination) is used to record ion signals through a 0.66 µF coupling capacitor. More details on the experimental setup were previously reported [84, 182]. Ion signals from 10 consecutive laser pulses hitting the same target spot are averaged to increase the signal-to-noise ratio. No noticeable decline in the averaged ion signal was observed when hitting the same spot with up to 50 laser pulses. High voltage (Tektronix, P6015A) and current pick-up (Pearson Electronics, 6595) probes are used to record the voltage on target and current through target and mesh. An illustration of the ion generation and detection geometry is shown in Fig. 7.1.
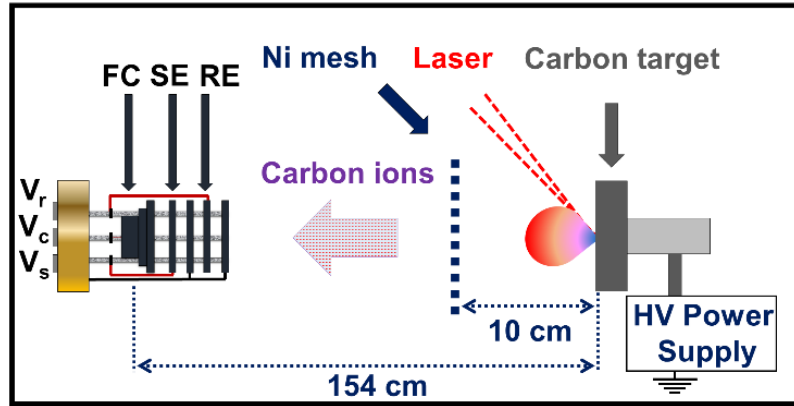
Fig. 7. 1 Experimental arrangement including TOF energy analyzer equipped with a Faraday cup (FC), suppressor electrode (SE), and retarding electrode (RE).

7.3 Results and Discussion

The experimental results are divided into two sections. In Section 7.3.1, the carbon ions are generated without any acceleration voltage applied to the carbon target. In Section 7.3.2, a fixed 3 kV positive bias voltage is applied to the target introducing an external electric field between the target and the grounded Ni mesh. The effects of the laser pulse fluence and acceleration voltage applied to target on the measured carbon ion signal are studied.

7.3.1 Carbon Ions Generation with No External Electric Field

The carbon ions are detected by their TOF signal for different laser fluences. Fig. 7.2 shows the TOF signal of carbon ions detected by the FC for a laser pulse fluence of 3.2-6.4 J/cm^2. There is a reduction in the arrival time of the fast ion peak with the increase in the laser pulse fluence. When no voltage is applied to the target, the ions generated are accelerated only by the plasma expansion and the internal electric field developed at the expanding plasma-vacuum interface, referred to as the double-layer potential [150]. Carbon ions have slower mobility compared to the

electrons, thus large Coulomb forces are formed between the fast electrons and ion layers in the early stages of plasma plume formation. The electric field due to the Coulomb forces accelerates the carbon ions to higher kinetic energies with higher degree of ionization. The ions with higher kinetic energies are located in the outer position of the plasma plume due to their higher flow velocity [13]. Higher charge state z carbon ions arrive at the FC earlier than those with a lower charge state due to the dependence of ion kinetic energy gain from the double-layer potential on their charge. The total ion charge reaching the FC is obtained from $Q_i = (\int V_F(t)dt)/R$, where $V_F(t)$ is the voltage signal measured by the FC and R is the 50 Ω oscilloscope internal resistance. The inset in Fig. 7.2 shows the detected total charge which increases from 0.32 to 2.26 nC when the laser pulse fluence is increased from 3.2 to 6.4 J/cm^2. The calculations do not account for the ion loss in the mesh positioned in front of the target, and the three mesh grids of the RFA in addition to all other transport losses due to ion diversion out of the FC area.
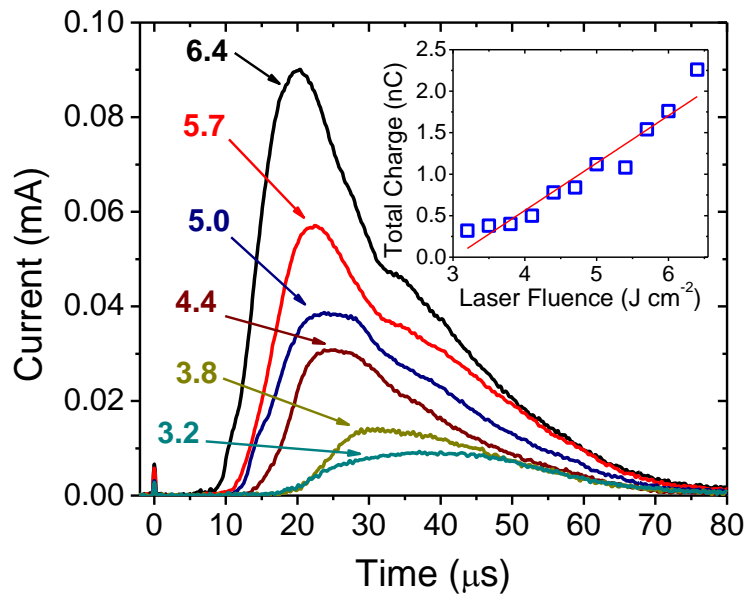
Fig. 7. 2 (a) Time-of-flight ion detection from carbon plasma for laser pulse fluence between 3.2 and 6.4 J/cm^2. *Inset* is total ion charge with the increase of laser pulse fluence.

Fig. 7.3 shows the RFA analysis of carbon plasma generated at 5.7 J/cm^2 laser pulse fluence. The TOF signal for 0-350 V reflects the decrease in the measured current with the retarding field voltage. We previously reported that the ion signal measured with different voltages applied to the RFA can be used to gather charge state information from the cut-off points in the TOF signal [84]. Current due to each carbon ion charge is reduced by the retarding field according to the charge state and the current reduction is observed throughout the measured signal due to the temporal separation of the different ion charges. When there is no external electric field, the measurements taken at ~350 V applied on RFA electrode reduces the charge collected by the FC to ~20% of that with no retardation. The total charge measured for 5.7 J/cm^2 fs laser fluence is calculated to be 1.42 and 0.28 nC for 0 and 350 V retardation voltages, respectively, as shown in inset of Fig. 6.3.
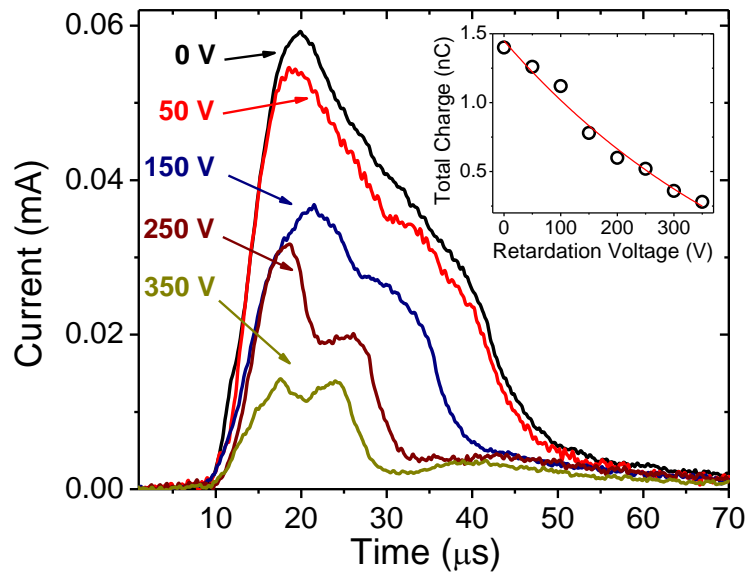
Fig. 7. 3 (a) Carbon ion signal for various retarding voltages for laser pulse fluence of 5.7 J/cm^2. *Inset* is the effect on the total ion charge with the increase of retardation voltage.

Far from the irradiated target, the ion energy distribution is described by the shifted Maxwell Boltzmann (SMB) distribution [150]. An important condition for transport of multicharged ions is a low background gas pressure ($<10^{-5}$ Torr), where the collisional excitation and the recombination processes are negligible for laser generated ions [183]. The cross section of total scattering for different charge state ions was reported [152]. The mean free path of the carbon ions at background pressure of 3×10^{-5} Torr is $\gtrsim 4.7$ km. Since the drift distance of the carbon ions from the target to the Faraday cup is 1.54 m, ion recombination in the drift tube is negligible. Therefore, the charge-states are frozen and the SMB distribution is applicable for ions in the drift tube [97, 153]. The carbon TOF ion signal is used to extrapolate the effective plasma ion temperature T_{ieff}, representing the core plasma ion temperature, from the deconvolution of the MCIs TOF signal. To accomplish this, the TOF carbon ions signal for the laser pulse fluence of 6.0 J/cm^2 is fitted to the SMB distribution function $I(t) = At^{-5}\exp[(-m/2kT_{ieff}) \times [(L/t) - (\sqrt{YkT_{ieff}/m} + \sqrt{2zeV_0/m})]^2]$, where A is a normalizing constant, m is the atomic mass of carbon, k is the Boltzmann constant, T_{ieff} is the effective ion plasma temperature associated with translational motion along the plume axis, L is the distance from the target to the Faraday cup, Y is the adiabatic coefficient ($Y = 1.66$ for carbon), z is the charge state, $\sqrt{YkT_{ieff}/m}$ is the adiabatic expansion velocity, $\sqrt{2zeV_0/m}$ is the velocity due to Coulomb acceleration, and V_0 is the equivalent acceleration voltage developed inside the plasma due to the double-layer potential formed at the plasma vacuum interface [150, 155, 184]. The sum of the adiabatic expansion velocity and the velocity that is due to Coulomb acceleration is expressed as the flow velocity, uf. These parameters are used for estimation of adiabatic and Coulomb potentials on different ion species. We define the term $\sqrt{YkT_{ieff}/m} + \sqrt{2zeV_0/m}$ as u_f, which is the flow velocity. The parameters used to fit the TOF ion signal with this equation are sensitive to the T_{ieff} and the equivalent acceleration voltage V_0 developed inside the plasma. The deconvolution can be executed for different charge states of carbon ions with the assumption of local thermal equilibrium (LTE) in the

expanding laser plasma plume [153]. The LTE condition is assumed when in a transient event, such as in the laser generated plasma, the collisions between atom-electron and ion-electron are occurring much faster than radiative processes [185]. The validity of LTE for femtosecond laser generated plasma was previously reported [186]. Aluminum was ablated with a fs laser ($\tau = 100$ fs, $\lambda = 800$ nm, $F < 7.6$ J/cm^2) and an equivalent ion temperature of 25 eV for a grounded Al target at 7.6 J/cm^2 pulse fluence was reported [155]. In one study [156], ions were generated from tin plasma using a Q-switched Nd:YAG laser ($\tau = 5$ ns, $\lambda = 1064$ nm, $F \sim 100$ J/cm^2). TOF signals were fitted to SMB distribution and the reported T_i was 34.4 eV for 77 mJ pulse energy. The ion pulse that contains contributions of ions with different charges was deconvolved into separate signals each corresponding to a charge state with its own SMB distribution. The sum of these signals was fitted to the TOF signal from all ions [156]. Another study reported on the Al plasma for the expansion dynamics generated by ns Nd:YAG ($\tau = 7$ ns, $\lambda = 1064$ nm, $F = 70$ J/cm^2) and a Ti:sapphire laser ($\tau = 100$ fs, $\lambda = 796$ nm, $F = 70$ J/cm^2) pulses using SMB fitting to ion TOF signals [146]. For ablation with a 7 ns laser pulse, two ion velocity components (slow and fast) were present in the TOF signal. While the slow components were fitted with $u_f = 5 \times 10^3$ m/s and $T_i = 1.74$ eV, the fast component was fitted better with a Gaussian distribution which indicates that the fast peak has a non-thermal nature [146]. A graphite target was ablated with an Nd:YAG laser ($\tau = 13$ ns, $\lambda = 1064$ nm, $F = 16$ J/cm^2) with a reported value of $T_i = 6.46$ eV [150].

The kinetic energy gain of ions accelerated by the electric field over the same distance d is the same for ions with a particular charge and that kinetic energy scales with the ion charge. The ions are accelerated by the combined effects of the electric field developed in the plasma-vacuum interface, due to the double-layer potential [109], and the externally applied electric field. We use fast and slow ion components in the deconvolution of the TOF signal because the observed

multiple peak structure in the TOF signal cannot be fitted well using only the fast component. In our previous work on femtosecond laser ion generation, we have observed the slow ion components which was explained based on the enhanced recombination of the slower ions [155]. Therefore, the slow component of the ions is observed mainly for the singly-charged ions [155]. After the ions separate from the plasma, the ions freely drift in the vacuum. Under these conditions, the SMB fit applies [155].

Fig. 7.4 shows the corresponding SMB fit of each individual carbon ion in the TOF spectra. There are two ion groups present in the TOF spectra. Plasma ions are accelerated by the ambipolar quasi-electrostatic field at the plasma-vacuum interface. The energy spectrum of the accelerated ions consists of two components, namely 'slow' and 'fast' ions [163]. The fast group of ions are due to multiphoton laser ionization, whereas slow ions are attributed to the collisional processes [163].

When a laser pulse with intensity of $\geq 10^{13}$ W/cm^2 interacts with a solid, multiphoton ionization dominates the laser interaction and the laser-plasma properties strongly depend on the laser wavelength, laser intensity, and the ionization potential of the material [187]. An intense fs laser pulse ionizes the target instantaneously. The escape of the hot electrons from the dense laser plasma results in the establishment of a space-charge region at the expanding plasma-vacuum interface. The ions are accelerated in the developed double-layer potential. The hydrodynamic expansion of the plasma that follows results in thermalized ions and electrons expanding in vacuum [188-190].

This distribution is obtained due to the ablated particles in the Knudsen layer and a good SMB fit is an indication of thermalization of the particles in the plasma plume [150]. The overall fitting curve is the sum of these individual carbon ions SMB distributions where the parameters of

the fitting function are strongly dependent on the effective ion temperature T_{ieff}, and the flow velocity u_f. The best fit is achieved when the T_{ieff} and u_f are used as free variables.
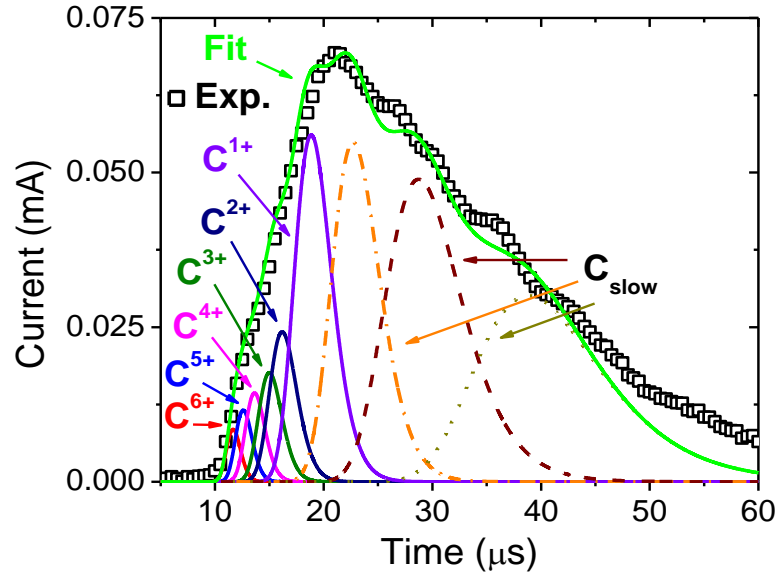
Fig. 7. 4 Deconvolution of the C ions by the SMB distribution at laser pulse fluence F $\sim$6.0 J/cm^2. Parameters of fitting are: T_{ieff} ~ 6.9 eV and u_f = 7.9 x 10^4 m/s for C^{1+}. T_{ieff} ~ 5.5 eV and u_f = 6.4 x 10^4 m/s for the slow ions (dashed-dotted line and dashed line), respectively. Slow ions (dotted line) has T_{ieff} ~ 4.6 eV and u_f = 3.5 x 10^4 m/s.

The effects of the Coulomb, thermal, and adiabatic potentials on different carbon charges can be estimated using T_{ieff} and u_f. We followed these steps to conduct the deconvolution approach to the TOF signals: (1) The ions energy distribution is assumed to follow the SMB equation as described in Section 7.3.1. (2) The extracted charge state z is based on the TOF signal with the external electric field discussed in Section 7.3.2. (3) The effective plasma ion temperature T_{ieff} and the equivalent acceleration voltage V_0 developed inside the plasma are set as free variables in agreement with the ion energy measured by the retarding field energy analyzer. (4) The most

probable energy of ions is separated by V_0, proportionally to their charge state. (5) The sum of the individual fits is plotted with the actual TOF signal of all ions that is observed using Faraday cup.

Flow velocity u_f value is proportional to the square root of the charge state z, so this parameter is increased in the fitting equation by introducing the corresponding charge state z, accordingly. The sensitivity of the deconvolution is checked by performing the fit to the TOF signal with different z, T_{ieff}, and V_0 values. Since the ions are temporally separated when an external electric field is applied, the maximum number of charge state z is experimentally known, in this case up to the fully-stripped C^{6+} is detected. The sum of the fit for individual ions is used to fit the TOF signal detected due to all ions. Performing the deconvolution using various values for T_{ieff} and V_0 showed that the pulse width is mostly affected by T_{ieff}, whereas ion energy shift is affected by V_0, which is associated to the Coulomb energy. Higher T_{ieff} values widen the pulse width for each charge state. The fitting function is more sensitive to the T_{ieff} but higher charge state ions are affected more with the V_0 variations. More details on the deconvolution parameters were previously reported for various materials that include Al and C [136, 155].

Previous studies introduced the use of slow and fast ion components in their deconvolution analysis. Gordienko *et al.* studied femtosecond laser ($\tau = 200$ fs, $\lambda = 616$ nm, $F \sim 6$ kJ cm^{-2}) ablation of Si and up to Si^{11+} (fast) and Si_s^{6+} (slow) were reported [5]. They concluded that the detected ion signals contain slow ions, which experience longer times in the high electron density region during ion acceleration, thus they experience more recombination rates [5]. Farid *et al.* reported an ion TOF study with a laser produced plasma for several elements (Al, Mo, Si, C, Cu, W, Ta) using a ns Nd:YAG laser ($\tau = 6$ ns, $\lambda = 1064$ nm, pulse energy $E = 450$ mJ) [191]. Their TOF signal showed the existence of fast and slow ion components regardless of the ablated material. For carbon, they reported better SMB fit to the ion TOF signal when slow carbon ions were introduced [191]. The

presence of these slow ions was explained by multiphoton laser ionization and collisional processes [5, 163, 191]. Amoruso et al. reported multiple peak distribution of ions during fs laser ($\tau = 120$ fs, $\lambda = 780$ nm, pulse energy E = 1 mJ) ablation. They attributed the high energy fast ion components to expansion of a space-charge electron layer during Coulomb explosion that creates a time-dependent ambipolar electric field. The slow ion component that follows the fast ions consists of ions ejected by thermal vaporization process [189, 190]. In our fit to the ion TOF signal, we introduce a slow ion component C_{slow} that consists of multiple peak structures. Different ion peak components are present due to the different kinetic energy gains and different ion temperatures of these slow ions. A good fit to our TOF signal requires including slow ions of C^{1+} and C^{2+}.

In our fit, $T_{ieff} = 6.9$ eV and the equivalent acceleration voltage $V_0 = 300$ V are used for the fast ions C^{z+}, while $T_{ieff} = 5.5$ eV and $V_0 = 105$ V are used for the slow ions (dashed-dotted line and dashed line), and $T_{ieff} = 4.6$ eV and $V_0 = 46$ V for slow ions (dotted line). Here, z is the charge state ($1 \leq z \leq 6$). The flow velocity u_f was 7.9 x 10^4 m/s for C^{1+}. The T_{ieff} value remained the same (5.5 eV) for the slow ions (dashed-dotted line and dashed line) with corresponding u_f values of 4.6 and 6.4 x 10^4 m/s, respectively. The plasma density of the inner core near the target surface is high resulting in high T_{ieff}, which is related to the u_f [136, 154]. We recovered up to C^{6+} by deconvolution of the ion signal. Ion TOF signal with 3 kV acceleration voltage also confirmed that up to C^{6+} ions are generated. When the deconvolution parameters of T_{ieff} and u_f were applied to the equation, the intensities of individual charges also similarly corresponded to intensity profiles that are extracted with acceleration voltage.

7.3.2 Carbon Ions Generation with External Electric Field

When an acceleration voltage is applied to the carbon target, ions with different charges spread in time with the higher charge state ions arriving at the FC earlier. The electric field between the grounded mesh and the target does not fully penetrate the plasma plume, due to the plasma shielding prior to ions separation from the plume, thus the ions experience the applied electric field at a location between the target and the grounded mesh. Therefore, ions are accelerated less than the potential applied to the target. The plasma shielding in the femtosecond laser ablation is significantly reduced and, therefore, the ions gain energy from the external electric field [192]. Since higher charge state ions are located in front of the lower charge state ions, during plasma expansion, the electric field is reduced for the lower charge state ions. Neglecting the initial ion velocity from the plasma plume, the TOF for generated ions is expressed as $t_a + t_d = d\sqrt{2m/zeV} + S\sqrt{m/2zeV}$ where t_a is the acceleration time for an ion accelerated from the target location to the extraction mesh, t_d is the time that ions drift at a constant velocity from extraction mesh to the FC, d is the distance between target and the extraction mesh, S is the distance from the extraction mesh to the FC, both in meters, m is the atomic mass of C in kg, z is the ion charge state, e is the electron charge, and V is the acceleration voltage applied on the carbon target. The ion accelerating time t_a is small compared to the ion drift time t_d.

Fig. 7.5(a) shows the carbon ions TOF signal at a fixed 3 kV acceleration voltage. The inset shows the TOF signals for 3.2 and 3.8 J/cm^2. When the laser fluence is 3.2 J/cm^2, only C^{1+} ions are detected with a maximum current of ~5 µA. As the laser fluence is increased, the charge state and total ion yield also increase. Carbon ions up to the fully-stripped C^{6+} are detected with a maximum current of ~0.05 mA at the FC for 6.4 J/cm^2 laser fluence. Ion kinetic energies are calculated from the TOF signal as ~13.0 keV and 1.4 keV for C^{6+} and C^{1+}, respectively. The main

mechanism for the enhanced ion extraction is thought to be the retrograde motion of the expanding plasma and vacuum, which exposes more ions to the accelerating field [193]. Fig. 7.5(b) shows the deconvolution of the C ions when the target is positively biased at 3 kV. The pulse width is mostly affected by T_{ieff}, whereas ion energy shift is affected by V_0, which is associated to the ion energy gain by the Coulomb potential of the double-layer potential. Higher T_{ieff} values widen the pulse width for each charge state. The best fitting parameters for 3 kV biased target are $T_{ieff} = 60$ eV and $V_0 = 1.6$ kV.
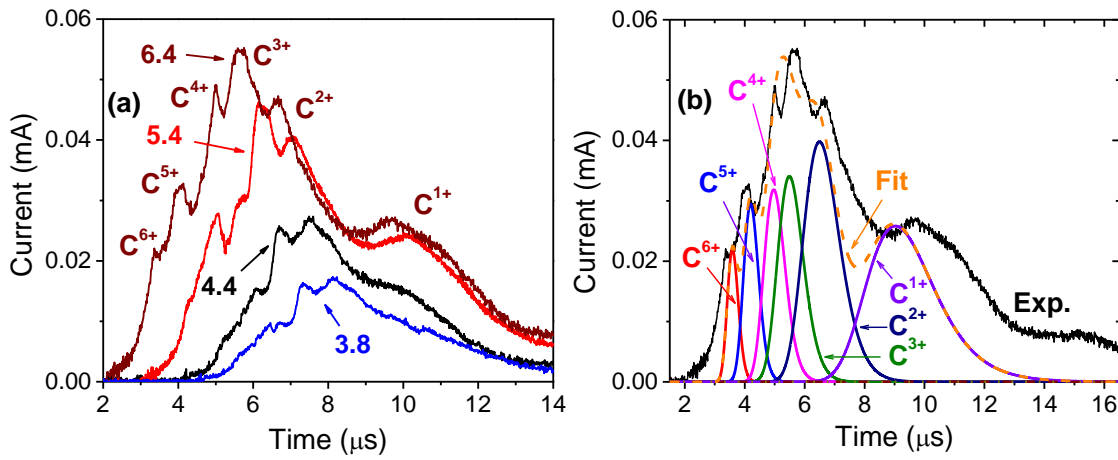
Fig. 7. 5 (a) TOF signal of accelerated carbon ions at 3 kV target biasing. Deconvolution of the extracted C ions with shifted Maxwell-Boltzmann distribution at 6.4 J/cm^2 and 3 kV target biasing (b). $T_{ieff} = 60$ eV and $V_0 = 1.6$ kV.

We reported on ion emission from fs laser ablation of carbon at a fluence of 7.6 J/cm^2, while the target had a voltage applied to it. Ion energies less than the applied voltage to the target was reported. The ion energy peaks were ~2.3/z keV for 5 kV applied to the target. The ion effective temperature T_{ieff} was 40 eV [155]. For a ns laser fluence of 36 J/cm^2, the flow velocity u_f was 3.6×10^4 m/s for C^{1+}. With the increase in the laser fluence from 20 to 36 J/cm^2, the generated carbon ion charge increased from C^{2+} to C^{4+}, while the T_{ieff} increased from 4.6 to 6.0 eV [4]. Fig.

7.5(b) shows that the accelerated carbon ions gained ~1.6 keV/z energy from 3 kV voltage applied to target. From Fig. 7.5(a), the maximum number of charge state is C^{6+}. The presence of charge states up to C^{6+} is used in our TOF signal fit. The ion temperature T_{ieff} was estimated to increase from 6.9 to 60 eV when the 3 kV bias is applied to the target.

Fig. 7.6(a) shows the target voltage when 3, 5, and 7 kV are applied at 3.2 and 4.8 J/cm^2 pulse fluence. When 7 kV is applied, the voltage drop occurs within 2 µs and it is ~1.3 kV for 4.8 J/cm^2. For our experimental conditions, the applied voltage on target is maintained for the first 1 µs which is sufficient for the carbon ions to reach and pass the grid. The drop of voltage in Fig. 7.6(a) takes effect after the initial 1-1.5 µs and, therefore, occurs after the ions passed the grounded grid. During this stage, ions are accelerated and pass the grid. Fig. 7.6(b) shows the current measured through the target at a bias voltage of 3, 5, and 7 kV.
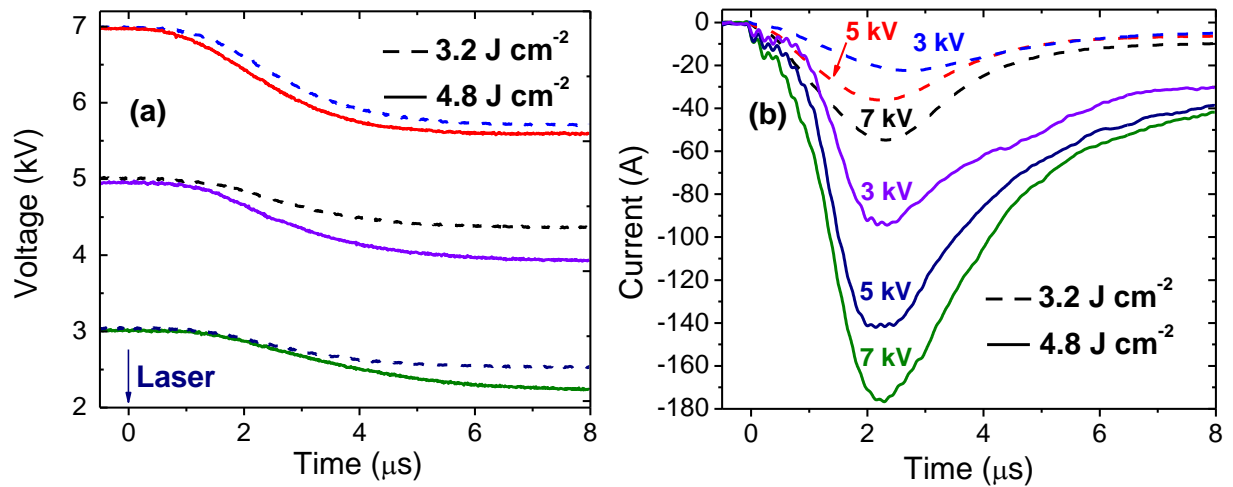
Fig. 7. 6 Measurement of voltage (a) across and current (b) through the spark gap of target and mesh when DC biasing voltage of 3, 5 and 7 kV are applied. Laser pulse fluence are 3.2 J/cm^2 (dash line) and 4.8 J/cm^2 (solid line), respectively.

The voltage and current values measured for 3 kV are 22 and 93 A for a laser fluence of 3.2 and 4.8 J/cm^2, respectively. The current through the target and the mesh increases when higher bias

voltage is applied to the target, which indicates the shorting of plasma with mesh. Plasma currents up to 55 and 175 A are observed for 7 kV voltage on target at laser fluences of 3.2 and 4.8 J/cm^2, respectively. Introducing an electric field-free expansion cup for ions separation was shown to avoid target-grid shorting problems and allows separation of the ion extraction region from the acceleration region [96].

7.4 Conclusion

Ti: Sapphire fs laser ($\tau = 150$ fs and $\lambda = 800$ nm) pulse ablated a carbon target with a fluence range of 3.2-6.4 J/cm^2. Fully stripped carbon ions with a maximum total ion current of 2.26 nC is detected by the Faraday cup. Using SMB distribution for C^{1+}, an effective ion temperature of T_{ieff} of 6.9 eV and a flow velocity of 7.9×10^4 m/s, are calculated. The ions energy gain from a 3 kV fixed target biasing is calculated as 13 and 1.4 keV for C^{6+} and C^{1+}, respectively.

CHAPTER 8

ION IMPLANTATION AND NEUTRAL DEPOSITION OF CARBON IN NICKEL (111)

8.1 Introduction

Graphene is intensively studied for the last decade due to its unique properties and promising potential in a variety of applications [58, 194-196]. Low crystalline quality graphene has several applications, but high-quality defect free graphene films are required for electronics applications. However, the synthesis of wafer-scale high-quality graphene is still one of the challenges.

Chemical vapor deposition (CVD) on Ni or Cu thin films promises wafer-scale synthesis of graphene [197, 198]. One group used polycrystalline e-beam evaporated Ni films and exposed it to diluted hydrocarbon flow (H_2 and CH_4 gas mixture) under ambient pressure [198]. They generated 1-10 layers of continuous graphene. Graphene growth was governed by the precipitation of graphite from carbon species within the Ni film [198]. Addou *et al.*, reported on CVD method at low temperature (550 °C) graphene growth on Ni(111) using C_2H_4 as precursor [199]. They reported that the graphene nucleation requires different ethylene exposure parameters if the growth temperature is changed. Generally, control of the thickness, uniformity and reproducibility of the CVD process are very challenging. The graphene growth using CVD is sensitive to such factors as the chamber size, gas flow rate, and decomposition rate of the hydrocarbon. Such problems originate from the use of hydrocarbon gas as a carbon source, which makes it difficult to control the amount of carbon atoms exposed to the catalytic metal surface.

Ion implantation is widely adapted for semiconductor industry, especially for doping the drain and source regions of CMOS transistors. In recent years, there is a growing trend for wafer scale

graphene synthesis that employs the carbon ions implantation [18, 200]. Direct graphene growth with controlled thickness after thermal annealing is achieved using transition metal films as supporting mediums that are implanted by carbon ions.

Different transition metals that have high carbon solubility and different interactions with graphene were previously reviewed [201]. Noble metals such as Ru, Ir, Pt have high carbon solubility and their usage leads to a segregation growth process for graphene which is also shared by most of the transition metals [202, 203]. The high melting temperature and catalytic activity of Pt promotes the growth of graphene at high temperatures [204]. However, the noble metals are economically unfavorable.

Graphene synthesis by carbon ions implantation has been previously reported [19, 65, 205]. Carbon ions are implanted onto SiO_2 substrates and several layers of graphene were grown [65]. Another group reported graphene growth on SiO_2 samples and achieved mobilities of 2900 $cm^2V^{-1}s^{-1}$ [205]. Carbon ions can easily be manipulated and their incident energy can be precisely controlled. Adjustments in the carbon ions dosage allow the maximum control over the thickness of the graphene layers. Number of implanted carbon atoms that corresponds to the graphene layer thickness can be precisely controlled within $1 - 2\%$ accuracy by the implanted carbon ions dose. It was reported that the carbon diffusion length in Ni, $L = 2\sqrt{D_T \tau}$, where τ is the diffusion time, D_T is the diffusion coefficient, is 1.2 μm for 1 second annealing at 725 °C [206]. The carbon atoms redistribute in Ni thin films regardless of the annealing time, but annealing also causes slow recrystallization of the metal film [207].

Graphene is formed by carbon atoms diffusion out onto the Ni surface with a controlled process. The thermal annealing influences the segregation and precipitation of the carbon atoms so besides the number of implanted carbon atoms, the annealing process contributes to the

graphene layer thickness [65]. Unlike the CVD based graphene growth where hydrocarbon gases are used, implantation-based graphene synthesis has several advantages. Graphene layers can be structurally controlled which is relatively easier compared to other synthesis methods. Investigations by Raman spectroscopy and transmission electron microscopy can reveal the effects of the implantation and the annealing conditions.

Large area graphene with good uniformity and layer structure were reported by carbon ions implantation in Ni thin films [18, 19]. Employing all the advantages that leads to controlled graphene growth at various temperatures is very challenging for practical applications. On the other hand, issues related to thickness control, yield efficiency, and solubility of carbon on metals such as Cu, Ni, and Ru need to be carefully evaluated before graphene consideration for microelectronics fabrication. Since controlling on carbon ions dose is possible, ion implantation technique has a great potential to provide information on the processed graphene formation on metal films.

Previous results suggest that the graphene synthesis depends on the nucleation sites on the Ni surface where carbon atoms tend to segregate. Multi-layer graphene grains are formed due to different factors that include the abundance of defects and grain boundaries on the Ni substrate, specifically on polycrystalline Ni surfaces [208]. Investigation of graphene synthesis on single crystal Ni(111) is therefore important. Ni(111) surface does not contain interface boundaries and the lattice match between graphene/graphite and the Ni(111) is very good (hexagonal lattice constant is 2.49 Å for Ni(111) and 2.46 for graphite) [209].

Possible growth mechanism is presented in Fig. 8.1. Carbon first diffuses into the Ni film due to the high solubility of carbon in Ni. Fig. 8.1(a) shows the polycrystalline Ni film with grain boundaries. Carbon atoms accumulate at these boundaries during the segregation and forms

multilayer graphene. However, in the Ni(111) film shown as Fig. 8.1(b), the surface is very smooth with no grain boundaries present and carbon is uniformly segregated onto the Ni(111) surface forming single-layer graphene [208]. According to the diffusion-segregation model [210] for precipitation of carbon on Ni surface, the polycrystalline Ni surface is rough and contains grain boundaries that lead to multilayer grain formation. However, the Ni(111) surface is relatively smooth with no grain boundary formation and leads to graphene synthesis. We can calculate the carbon ions dose with the following formula:

$$Dose\ (\Phi) = \frac{(Ion\ Current/e) \times Implantation\ Time\ (sec)}{Scanned\ Area} \tag{8.3}$$

where ion current is given in amps, e is the electron charge, and area is given in cm^2.
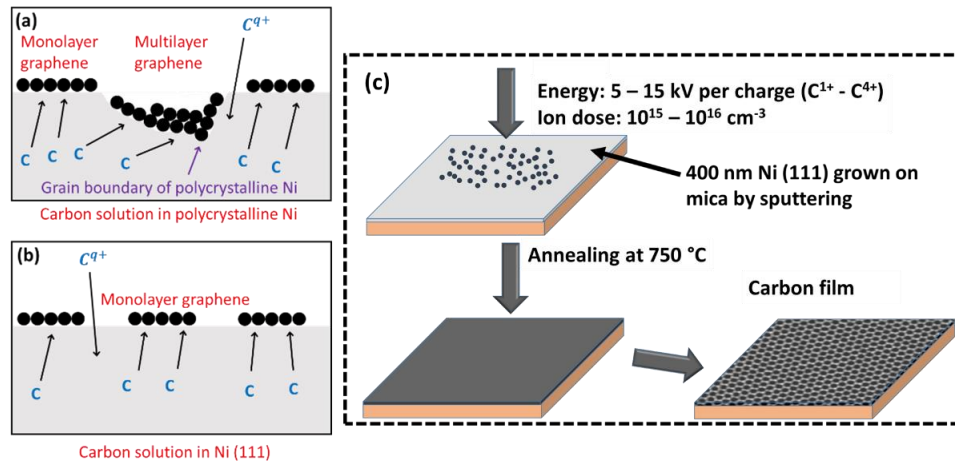
Fig. 8. 1 Graphene growth mechanism on polycrystalline Ni surface (a) and Ni(111) (b). Multiple graphene layers are formed due to grain boundaries [208]. (c) Graphene synthesis steps using C ion implantation.

We report the synthesis of carbon films grown on Ni(111) by carbon ions implantation. Thin Ni(111) films with 400 nm thickness are sputter coated on mica sheets using evaporation by magnetron sputter coater, which will catalyze the graphene growth. The carbon atoms were implanted into Ni(111) surface with a variety of doses (10^{15} - 10^{16} cm^{-2}) at ~15 keV per charge

energies and diffuse at annealing temperature of 750 °C where the furnace was heated to 750 °C at a rate of 10 °C/minute. Carbon ions are implanted directly onto Ni(111) using the laser ion source. The annealing is conducted for an hour followed by rapid cooling at a rate of 50 °C/min, leading to graphene layers formation [211]. The implanted Ni(111) substrates are investigated by a Raman spectrometer, SEM, FESEM, AFM, optical microscopy, and EDS. The effects of ion dose, the multicharged ion content, and substrate biasing voltage are investigated.

Ni(111) films are implanted with a dose of C ions from 3×10^{15} cm^{-2} to 13×10^{15} cm^{-2} at an energy of 15 keV/charge (60 keV for C^{4+} ions). The projected range of the accelerated carbon ions are calculated using The Stopping and Range of Ions in Matter (SRIM-2013) simulation software. Graphene synthesis by laser assisted carbon ion implantation can be applied to a variety metallic substrates and growth temperatures, since it does not require chemical precursors or a solvation of carbon into the substrate. Controlled thickness on graphene can have advantages if used as a direct method to integrate graphene into Si based electronic devices.

8.2 Experimental

Magnetron sputtering system (ATC Orion 5 RF/DC Sputtering System (AJA International)) is used to grow Ni(111) films on mica substrates (Grade V1, Muscovite Mica, Ted Pella). Mica substrates are heated to 500 °C during the Ni sputtering, and subsequently cooled down to room temperature before removing the substrates. The ion source for carbon implantation on Ni(111) films, grown on mica sheets is presented in Fig. 8.2. First part of the experimental arrangement is for ions generation. The processing chamber consists of a high voltage feedthrough, a Ni mesh, and the substrate holder. High voltage up to -15 kV is applied to the feedthrough that generates an electric field between the Ni mesh and the 4 mm thick substrate holder disk, 10 mm

in diameter. The glassy carbon target (99.99% pure, 0.58 mm thickness, <50 nm surface roughness, as characterized by the manufacturer HTW, Germany) is mounted in a vacuum chamber that is evacuated to a pressure in the low 10^{-7} Torr. The target is rotated with a stepper motor to eliminate crater formation during the implantation. The carbon ions experience an acceleration from the electric field that is between the mesh positioned in front of the substrate holder and the substrate. Ions increase in their kinetic energy according to their charge state and subsequently impinging on the Ni(111). The power supplies for substrate biasing used are Spellman Bertan series (230-30R) with reversible polarity. 30 kV high voltage feedthrough (Del Seal CF- 1 pin) is used to attach the 10 mm diameter aluminum substrate holder disc.
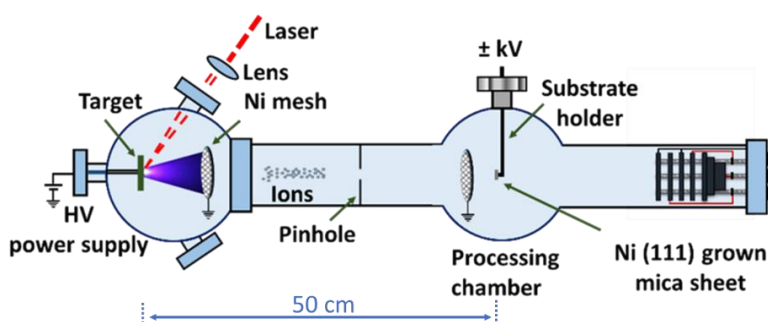
Fig. 8. 2 Experimental set up for the carbon ion implantation of Ni(111) film. Experimental set up for the carbon ion implantation of Ni(111) film.

The annealing is conducted using tube furnace module (GSL-1100X, MTI Corporation) with a built-in precision temperature controller. The furnace is heated to 750 °C (heated at a rate 10 °C/minute) and subsequent cooling is conducted at a rate of 50 °C per minute using its configurable temperature controller. Argon gas with a constant flow was supplied during the annealing process. We used Renishaw inVia Raman Microscope and Spectrometer, operated with 100× magnification lens and 45 mW laser pulse. The laser power on the analyzed samples was estimated to be 10 mW. The green laser is operated with 514 nm laser with an acquisition of 20 seconds for each data

collected. The scanning scale is set between 500-3200 cm^{-1}. FE-SEM (Hitachi S-4700), AFM (Dimension ICON, Bruker), XRD (MiniFlex II Benchtop X-ray Diffractometer (Rigaku)) and EDS (Thermo Electron NORAN System SIX, as part of the SEM-JEOL JSM-6060LV) are used to characterize the structure and composition of the surface of the Ni(111) film coated mica substrates.

8.3 Results and Discussion

Fig. 8.3 shows the ion TOF signal and corresponding deconvolution fits for individual charges. The carbon target was grounded and the laser energy was set between 25 to 50 mJ per pulse. Laser pulse intensity is 1.8×10^9 W cm^{-2} for a spot size of 0.2 mm^2 at 25 mJ pulse energy. We reported on the deconvolution of TOF spectra for carbon ions [4, 84] and in previous works, we determined the maximum number of charge states generated from the laser plasma with the help of retarding field analysis for conditions similar to the presently used. The individual fitting curves from the carbon ions compose the total ion current. The charge state composition is estimated from the individual fitting curves and are listed in Table 8.1. Given values are calculated from the substrate signal with a single pulse laser. The dose calculations involve a laser operation at 10 Hz for 1 hour. The carbon target was grounded and the substrate holder was connected to oscilloscope to record ion signals through a 0.66 µF coupling capacitor.

I previously reported that the increased laser energy generates more energetic multicharged carbon ions with higher charge states, up to C^{4+} [4]. Generation of C^{5+} and fully stripped C^{6+} was reported when a spark-assisted laser ablation is studied [154]. The average weight in the total number of ions generated for the C^{1+}, C^{2+}, C^{3+}, and C^{4+} content changes with pulse energy increase. The dose values are calculated from the sum of number of ions derived by the SMB functions for each charge state. Corresponding dose values are $\sim 3.5, 4.4, 10,$ and 13×10^{15} cm^{-2} for 25, 30, 40, 50 mJ, respectively. The type of charge and its weight is listed in Table 8.1. These values are based on the laser operation at 10 Hz for 1 hour for a total number of 36,000

pulses. The deconvolution curves are used to estimate the total ion dose of ions on the substrate using the equation 8. 3. I previously reported on the deconvolution method, the effects of changing the parameters for the used fitting function [212]. The average weight in the total number of ions generated for the C^{1+}, C^{2+}, C^{3+}, and C^{4+} content changes with laser pulse energy. Polycrystalline Ni is a suitable a good substrate for graphene synthesis, but the percentage of bilayer or monolayer graphene is limited by the grain size of crystalline Ni that is obtained after thermal annealing of Ni thin film [208]. The properties of the Ni films can be controlled by altering the substrate temperature. The crystalline structure with predominant Ni(111) crystallite orientation at 500 °C substrate temperatures are employed, as observed from the X-ray diffraction analysis shown in Fig. 8.4. Strong Ni(111) peak at $2\theta = 44.6°$ indicates the presence of dominant Ni(111) grains. Using the Scherrer's equation [213], the particle size is calculated as ~23 nm.

Table 8. 1 Carbon ions charge distribution, calculated from the individual fitting curves.

Pulse Energy (mJ)	Ions	Charge (nC)	Number of ions (~)	% (~)	Distance (cm)	Voltages (V) C target	Voltages (V) Ni holder
25	C^{1+}	5.0	3.1×10^{10}	24	50	0	-80 V
	C^{2+}	7.5	4.7×10^{10}	37	50	0	-80 V
	C^{3+}	5.2	3.3×10^{10}	26	50	0	-80 V
	C^{4+}	2.5	1.6×10^{10}	13	50	0	-80 V
30	C^{1+}	7.2	4.5×10^{10}	28	50	0	-80 V
	C^{2+}	8.6	5.4×10^{10}	35	50	0	-80 V
	C^{3+}	6.1	3.8×10^{10}	24	50	0	-80 V
	C^{4+}	3.2	2.0×10^{10}	13	50	0	-80 V
40	C^{1+}	14	8.8×10^{10}	25	50	0	-80 V
	C^{2+}	19	1.2×10^{11}	34	50	0	-80 V
	C^{3+}	15	9.4×10^{10}	27	50	0	-80 V
	C^{4+}	7.9	5.0×10^{10}	14	50	0	-80 V
50	C^{1+}	16.8	1.0×10^{11}	21	50	0	-80 V
	C^{2+}	26	1.6×10^{11}	36	50	0	-80 V
	C^{3+}	20	1.3×10^{11}	28	50	0	-80 V
	C^{4+}	10.2	6.5×10^{10}	15	50	0	-80 V
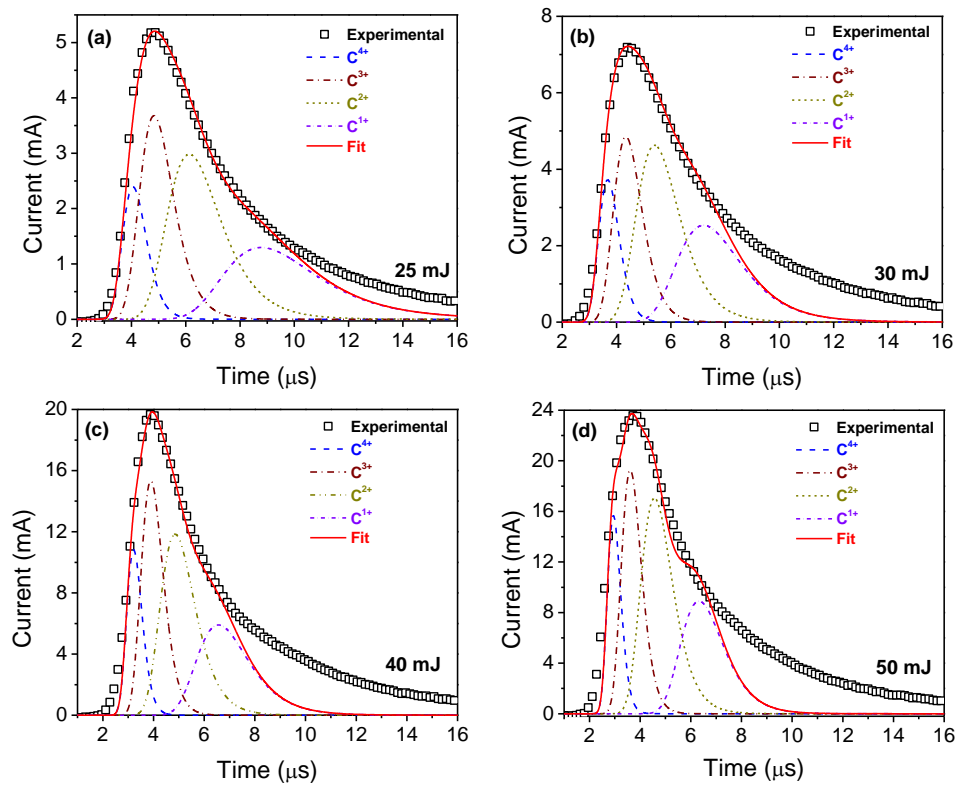
Fig. 8. 3 Carbon ions charge distribution with shifted Maxwell-Boltzmann (SMB) approach. Laser pulse intensity is 1.8×10^9 W cm^{-2} for a spot size of 0.2 mm^2 at 25 mJ pulse energy. Individual deconvolution curves are used to estimate the weight of each charge state. Carbon target is grounded and FC is biased to -80 V.
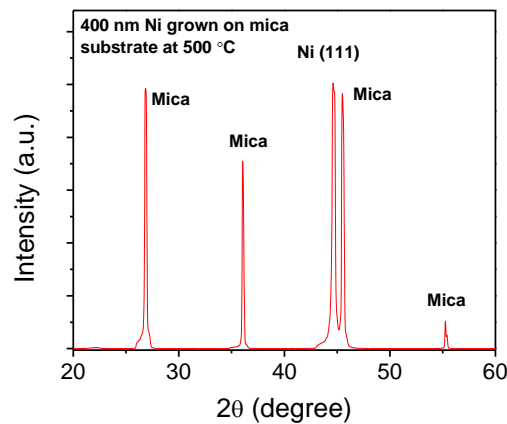
Fig. 8. 4 XRD pattern of 400 nm Ni film grown at 500 °C. Strong Ni(111) structure is detected.

Table 8. 2 Elemental composition of the materials obtained by EDS analysis of Ni(111) film.

Element	Weight %	Weight % (Error)	Atom %	Atom % (Error)
C	*3.25*	+/- 0.62	12.29	+/- 2.33
O	3.56	+/- 0.43	10.09	+/- 1.21
Al	2.18	+/- 0.21	3.68	+/- 0.36
Si	3.4	+/- 0.20	5.5	+/- 0.33
K	1.85	+/- 0.21	2.14	+/- 0.24
Ni	85.76	+/- 1.88	66.3	+/- 1.46
Total	100		100	

Topographical profile of the Ni(111) film is presented in Fig. 8.5. Fig 8.5(a) is showing the surface morphology (50 μm × 50 μm) of the films grown at 500 °C. Fig 8.5(b) is a 2 μm × 2 μm section of the grown film. AFM line scan is conducted for this part of the film as shown in Fig. 8.5(c) and (d), revealing that the surface shows 40 nm variations in height over a length of 2 μm. SEM image of the Ni(111) film is presented in Fig. 8.6. Note that the film is grown at 500 °C and no carbon ion implantation is applied. SEM images show a uniformly covered surface. RMS roughness is calculated as 2-19 nm for the line scans.
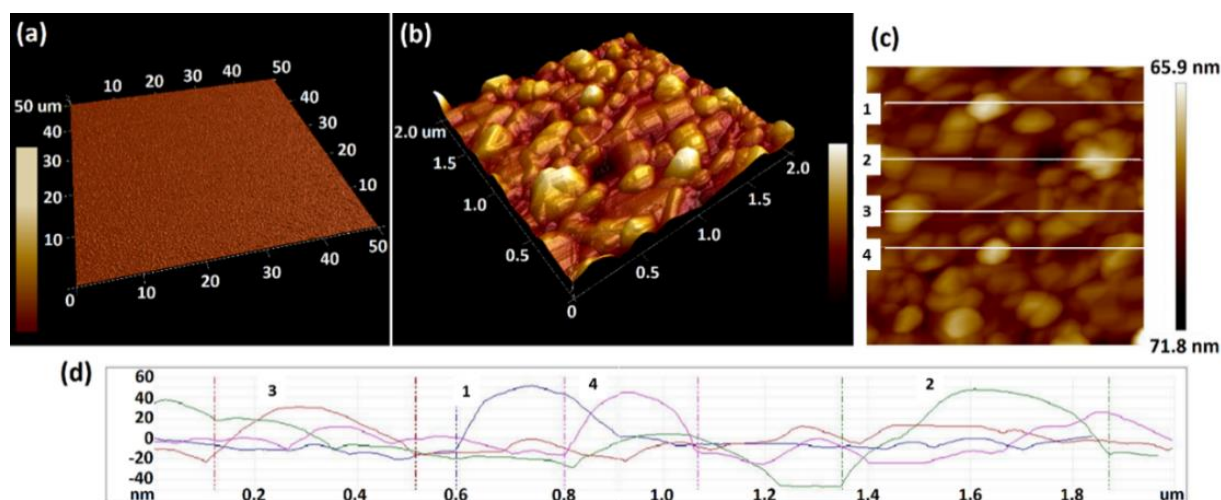
Fig. 8. 5 AFM topological images of Ni(111) film on mica substrates (a-b). AFM line scan reveals the height profile in (d), collected from straight lines indicated in (c).
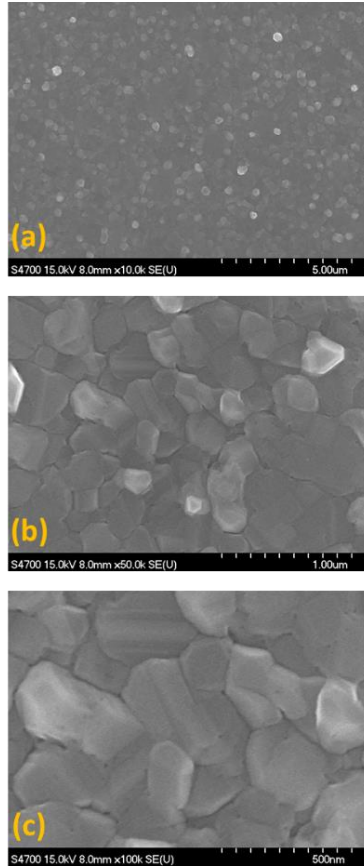
Fig. 8. 6 SEM image of Ni(111) film (no C ions implantation) grown 400 nm at 500 °C.

Fig. 8.7 shows the EDS spectra of an implanted Ni(111) film with $\sim 7 \times 10^{15}$ cm^{-2}. The carbon content is significantly increased compared to Ni(111) only spectra. The composition of the elements is summarized in Table 8.3.
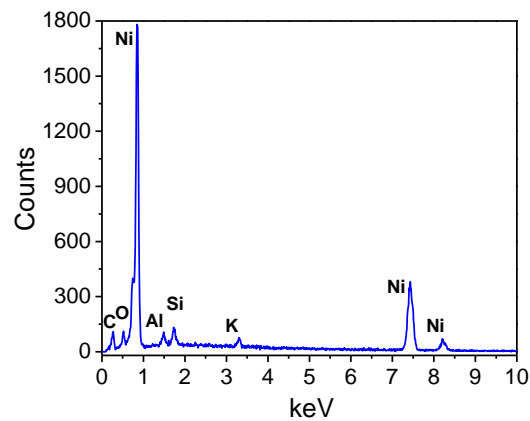
Fig. 8. 7 EDS spectra of Ni(111) film implanted with carbon ions.

Table 8. 3 Elemental composition of the materials by EDS analysis of C implanted Ni(111) film.

Element	Weight %	Weight % (Error)	Atom %	Atom % (Error)
C	*11.45*	+/- 0.63	35.24	+/- 1.93
O	3.58	+/- 0.28	8.26	+/- 0.64
Al	1.50	+/- 0.11	2.05	+/- 0.15
Si	2.16	+/- 0.16	2.84	+/- 0.21
K	1.31	+/- 0.10	1.24	+/- 0.09
Ni	80.00	+/- 1.81	50.36	+/- 1.14
Total	100.00		100.00	
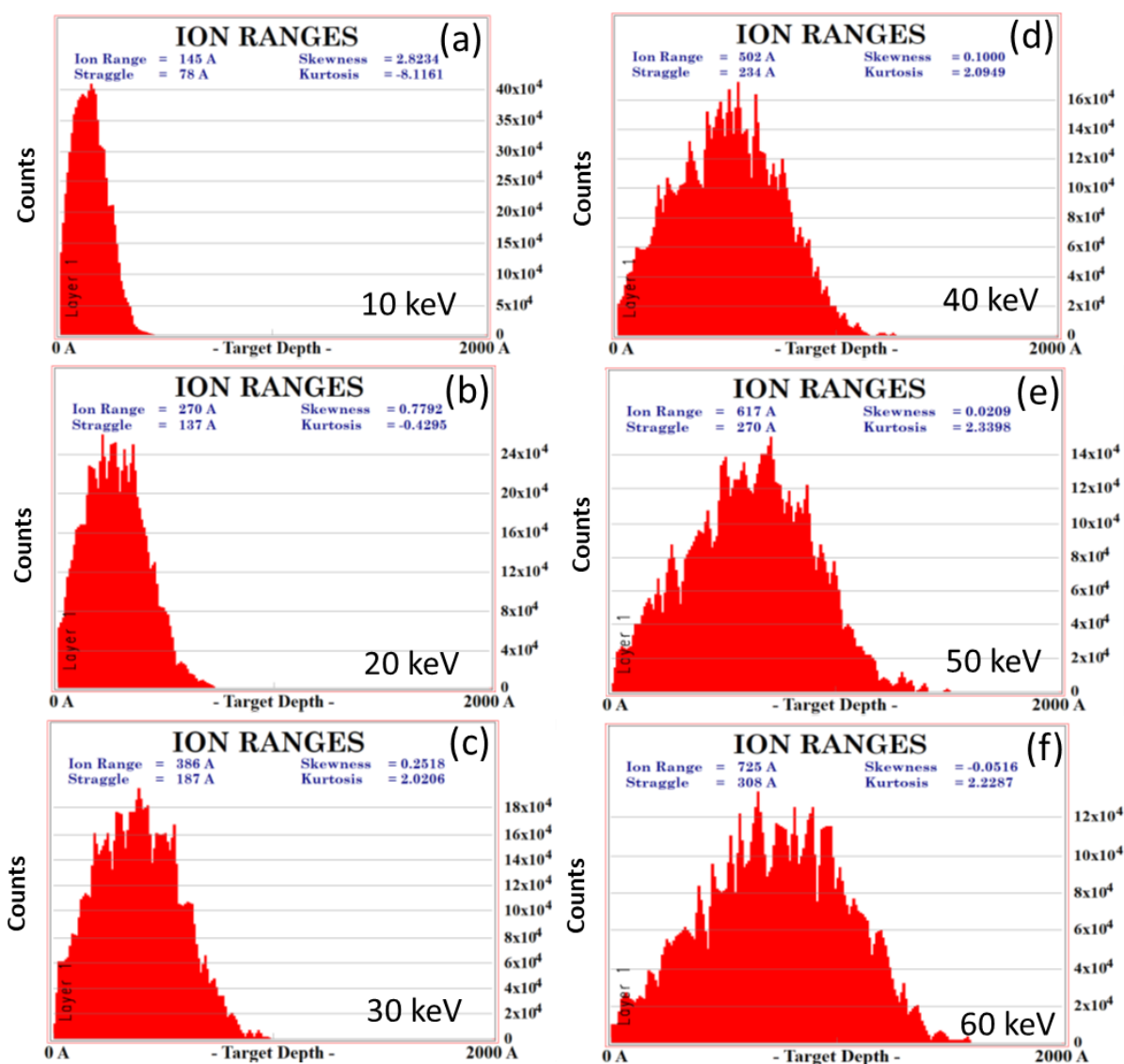
Fig. 8. 8 SRIM simulations of 3000 C ions implanted into the Ni(111) up to 60 keV energies (a-f).
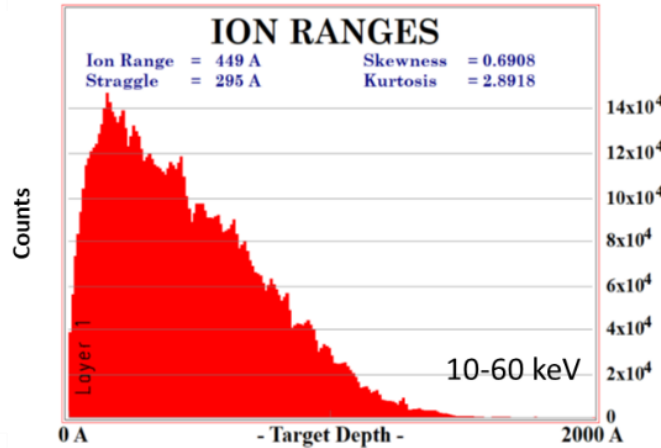
Fig. 8. 9 SRIM simulation of 18000 C (10-60 keV) ions that contains 3000 C ions in each group.

I also performed The Stopping and Range of Ions in Matter (SRIM) simulation to check the implantation profiles of the C ions. Fig. 8.8 (a)-(f) show the individual SRIM simulation result of the C ions implantation into Ni(111) with energies from 10 to 60 keV, with the increment of 10 keV. The number of carbon ions in each group are 3000. Fig. 8.9 shows the profile of the total implanted C ions with these different energy groups, each group containing 3000 C ions. The model shows that majority of the implanted C ions (90%) penetrates up to ~100 nm inside the Ni(111) film.

8.3.1 Grounded and +5kV biased Ni(111) Substrate

I performed carbon ions implantation on Ni(111) films, using laser ion source. Generated carbon ions are characterized with previous works [4, 84]. The Ni(111) film coated mica substrate is first grounded and then biased with +5 kV voltage. A thin carbon tape is used to connect the substrate holder to the Ni(111) surface for biasing. Raman spectroscopy is widely utilized for identifying carbon-based materials [214]. Fig. 8.10 shows the Raman spectra of Ni(111) films that are implanted with ~3.5, 7, and 10.5 $\times 10^{15}$ cm^{-2} of carbon ions dose, respectively. Note that the Ni(111) film was grounded. The laser pulse intensity was 1.8×10^9 W cm^{-2} with the laser operated

at 10 Hz under a background pressure of ~10^{-7} Torr. Broad Raman peaks are detected centered at ~709, 1537, and 2931 cm^{-1}. The Raman signals in Fig. 8.10 does not show a prominent D band around 1350 cm^{-1} which implies that the film has more sp^3 bonding content.
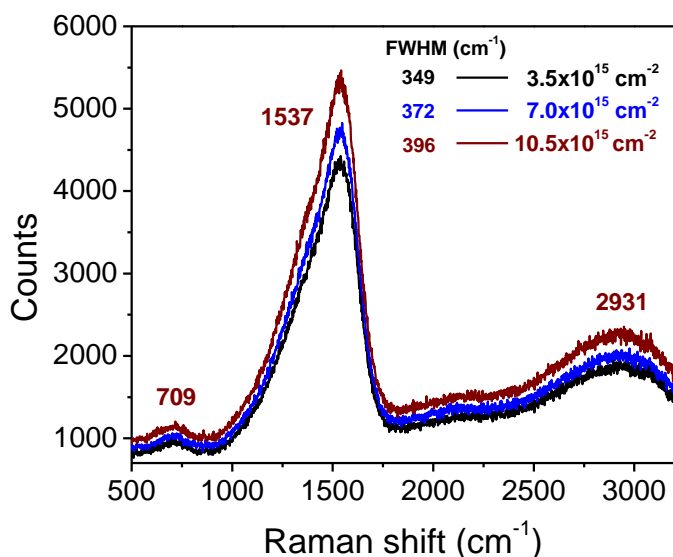
Fig. 8. 10 Raman spectrum for a grounded Ni(111) film coated mica substrate. Ni(111) films are implanted with ~3.5, 7, and 10.5×10^{15} cm^{-2} of carbon ions dose, respectively.

Carbon films with high content of sp^3 bonding are named as "amorphous carbon films, ta-C" [215]. There was no significant D peak formation even when the ion dose was increased to ~10.5×10^{15} cm^{-2}. The film carries properties of amorphous carbon. However, the width (FWHM) of the peak at 1537 cm^{-1} is increased from 349 to 396 cm^{-1}. Increase in the FWHM is an indication of increased dislocations (disorders) in the structure. The width of the peak also increases due to the site-to-site variation in the number of next nearest neighbors (when sp2 C atoms have sp3 C neighbors) [216].
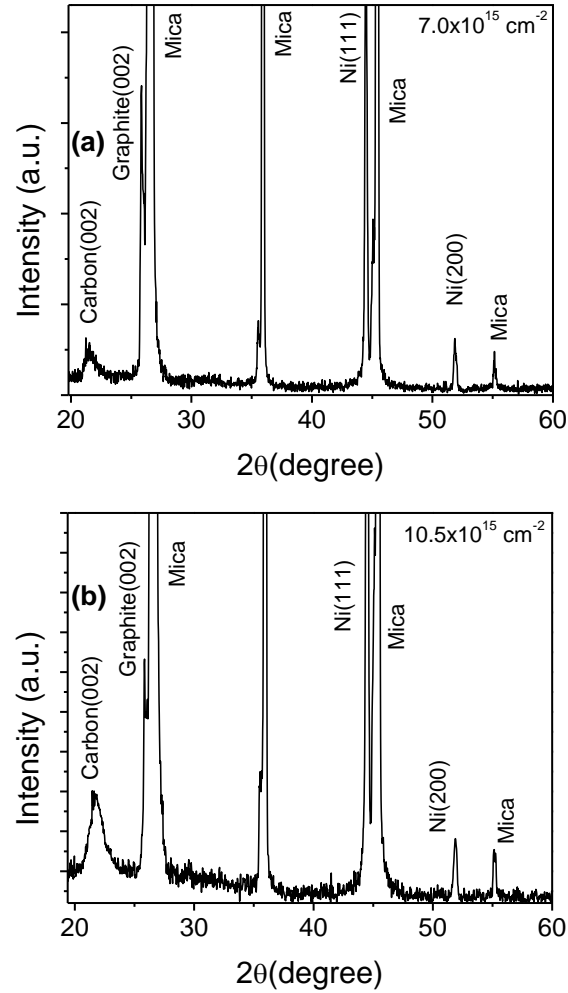
Fig. 8. 11 XRD patterns for Ni(111) film at 7 and 10×10^{15} cm^{-2} ion dose for a grounded substrate. No annealing is conducted.

Fig.8.11 shows the XRD patterns Ni(111) films. The implantation is conducted with 7 (a) and 10×10^{15} cm^{-2} (b) ion dose with no annealing. XRD patterns due to amorphous carbon(002) and graphite(002) are detected around $2\theta=21.6$ and 26.1. There are also weak Ni(200) patterns present in the film structure at $2\theta= 51.8$. Fig. 8.12 shows the Raman spectrum of Ni(111) film that is implanted with $\sim 3.5 \times 10^{15}$ cm^{-2} ion dose. The Ni(111) film is positively biased at +5 kV. There are Raman bands that appear around 600-720 cm^{-1} in Fig. 8.12. Raman spectra from diamond particles with sizes of 0.1–2 mm were observed and broad Raman band around 600 cm^{-1} was

reported [217]. Because of the difference between Raman scattering cross section of sp3 and sp2 particles these bands are assigned to sp2 [218].
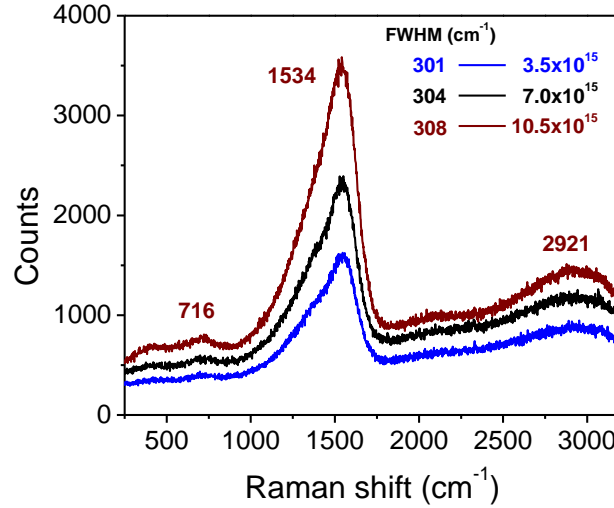
Fig. 8. 12 Raman spectrum for +5 kV biased and carbon ions implanted Ni(111) films. Carbon ions dose and the FWHM values of central band (~1534 cm^{-1}) are given.

Raman bands seen around ~710 cm^{-1} may be associated to carbon clusters, especially to C_{60} molecules, as previously reported [219, 220]. The broadband Raman peak around ~2921 cm^{-1} arises from the C-H bonds in the film structure [221]. It was reported that the direct detection of C-H bonds is associated to the bands between 2920–2970 cm^{-1} [222]. Raman spectrum for amorphous carbon gives two broad peaks around 1200–1450 cm^{-1} for the D band and 1500–1700 cm^{-1} for the G band [216]. The substrate is grounded and biased to +5 kV, in Fig. 8.10 and 8.12, respectively. The other experimental parameters are kept the same. The positively biased substrates carried narrower FWHM values for all the ion dose values possibly due to the decreased disorders in the structure. The FWHM values in Fig. 8.10 for ~1537 cm^{-1} peaks are 349, 372, and 396 cm^{-1} for 3.5, 7.0, and 10.5×10^{15} cm^{-2}, respectively. These values in Fig. 8.12 for ~1534 cm^{-1} peaks are 301, 304, and 308 cm^{-1} for 3.5, 7.0, and 10.5×10^{15} cm^{-2}, respectively. Fig.8.13 shows

the XRD patterns of amorphous carbon(002) and graphite(002) that are detected around $2\theta=21.6$ and 26.1 for both 7 (a) and 10×10^{15} cm^{-2} (b) ion dose with no annealing. The substrate is biased to +5 kV. Compared to the grounded substrate, the overall intensities of the patterns of carbon(002) and graphite(002) are reduced, possibly due to the reduced number of ions that are implanted onto the Ni(111) film.
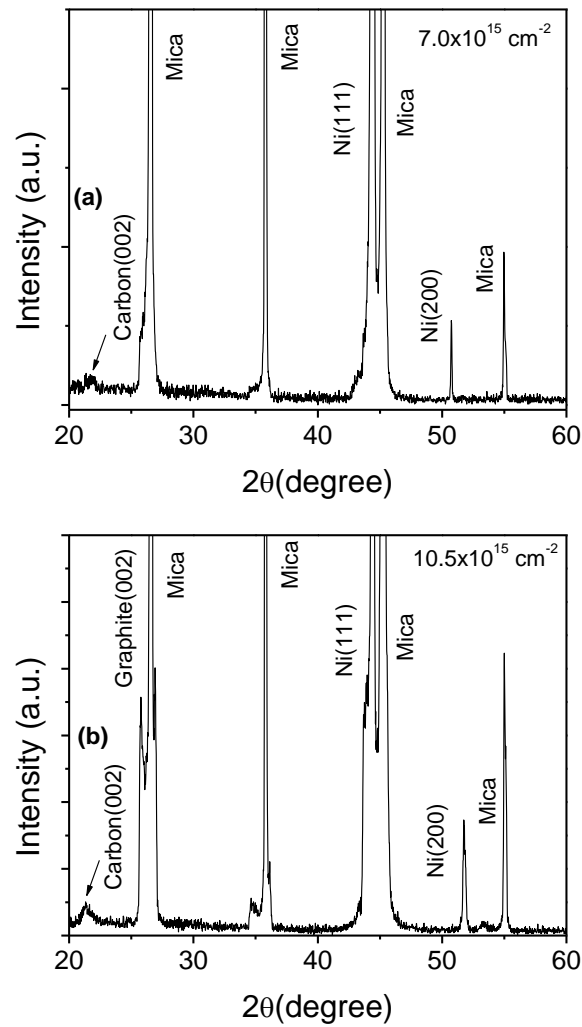
Fig. 8. 13 XRD spectra of Ni(111) film at +5 kV biasing for 7 and 10×10^{15} cm^{-2} ion dose with no annealing.

8.3.2 Film Properties with Thermal Annealing

The effects of the annealing after the laser generated carbon ions implantation on the Ni(111) film are discussed and characterized in this section. Annealing restores the damaged lattices that is induced by carbon ions implantation. The implanted carbon ions with high thermal activation energy diffuse out of the Ni(111) thin film and move towards to the top of the film with the increase in annealing temperature. Carbon ions that have diffused to the Ni(111) surface congregate together to form structures along with the decrease in annealing temperature such as graphene or diamond-like carbon [18, 223].

Fig. 8.14(a)-(f) show the annealed Ni(111) film surface under FESEM microscope. In this case, the mica substrates were placed in the furnace after sputtering the Ni(111) film. The annealing was conducted for 30 minutes at 300, 500, and 700 °C under Argon gas environment at atmospheric pressure. The furnace was heated at a rate of 10 °C/minute. The cooling was conducted with a rate of 50 °C/minute until the room temperature is reached. The Ni(111) layer is smooth and no peeling or cracking are visible. The FESEM image shows that the Ni particles are slightly inhomogeneous in orientations and sizes. The large particles are ~0.5 μm and the small ones are ~100 nm in diameter. XRD spectra were collected after the thermal annealing process as shown in Fig. 8.14(g). The three spectra from top to bottom correspond to 700, 500, and 300 C° annealing on Ni(111) film. While all substrates show a strong peak corresponding to Ni(111), there is an additional Ni(200) peak at $2\theta=76.3$ with intensity being highest for 700 C° annealing and lowest for 300 C° annealing. The overall intensity of the Ni(111) is increased, meaning that the crystalline quality is improved alongside weak peaks of Ni(200).
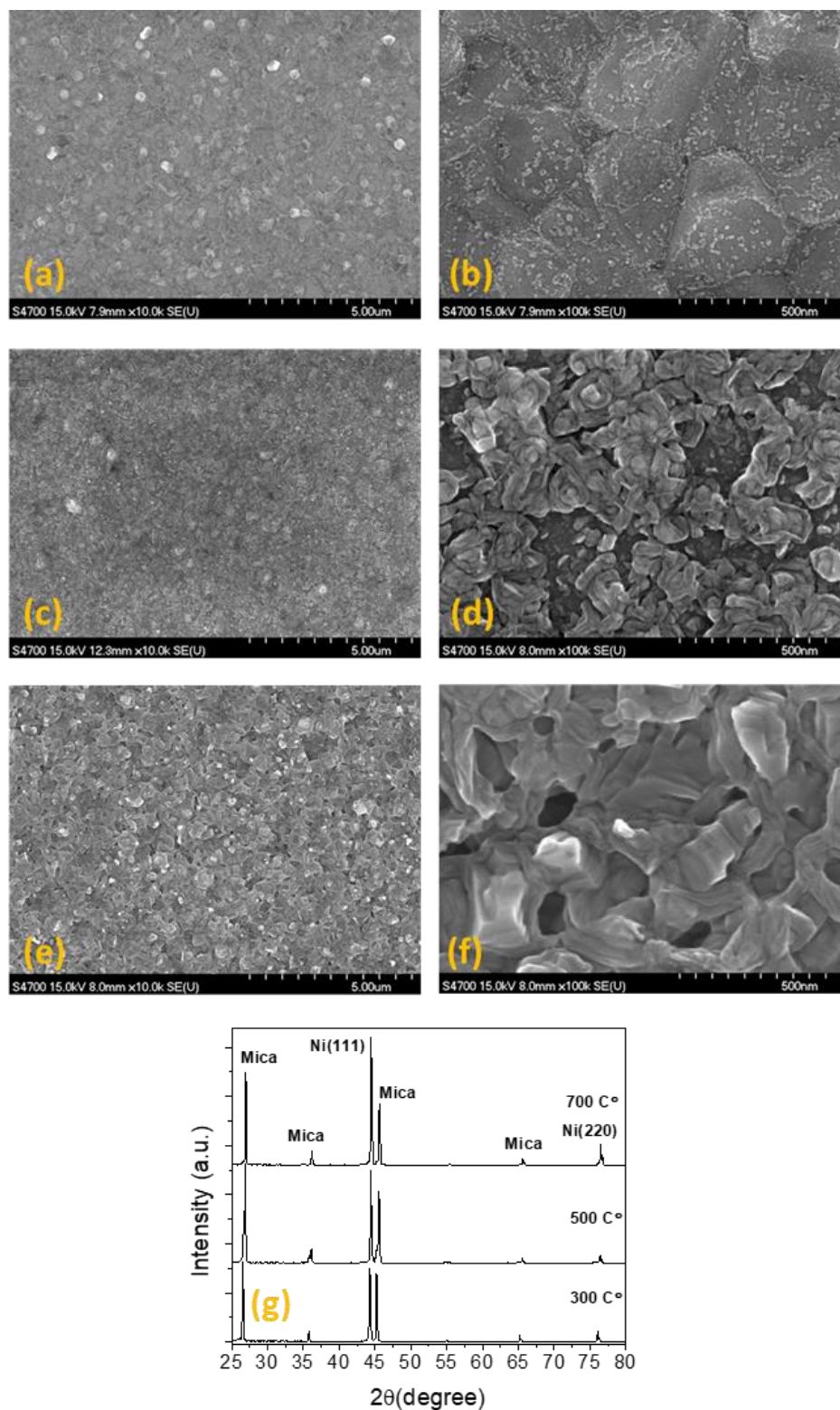
Fig. 8. 14 FESEM images of 1 hour annealed Ni film at 300 (a, b), 500, (c, d), and 700 °C (e, f).

XRD patterns of the annealed Ni(111) film for 300, 500, and 700 C° (g).

8.3.2.1 Biasing of -5, -10, and -15 kV on Ni (111) Substrate

The Raman spectra for the Ni(111) film surface at different Ni(111) biasing conditions (-5, -10, and -15 kV to the Ni(111) film) is shown in Fig. 8.15. A total of $\sim 10.5 \times 10^{15}$ cm^{-2} ion dose is applied to the Ni(111) films after carbon ions implantation.
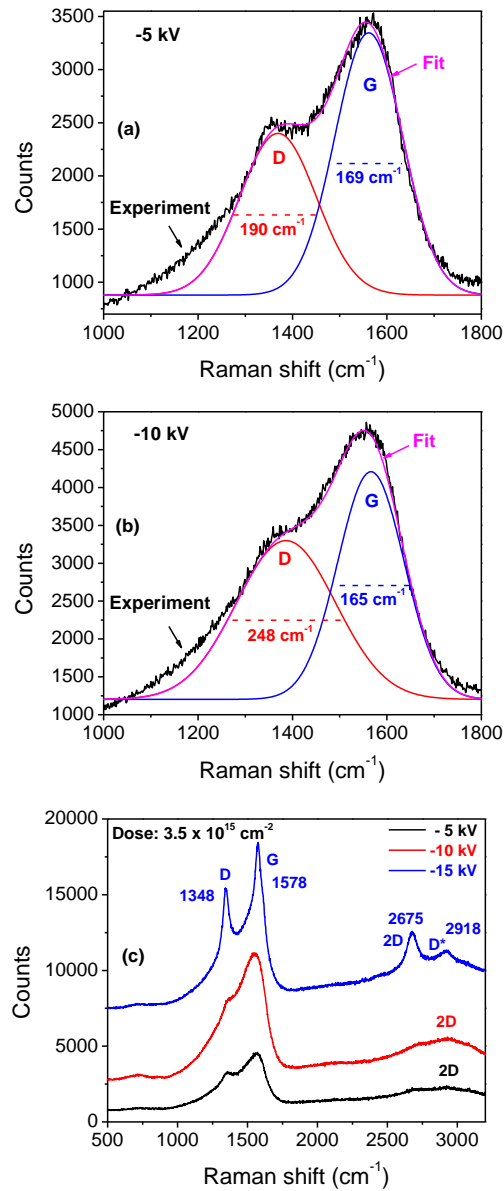
Fig. 8. 15 Lorentzian fittings for D and G peaks for -5 and -10 kV biased Ni(111) films (a), (b). The Raman spectra of ion implanted Ni(111) films for different biasing voltages at -5, -10, and -15 kV. (c) Carbon ions are implanted with a dose of $\sim 3.5 \times 10^{15}$ cm^{-2}.

Diamond-like carbon (DLC) films have desirable properties arising from the sp3 component of their bonding and are distinguished from amorphous carbon films, which are essentially all sp2 bonded as in graphite, shown in Fig. 8.16. It was reported that the Raman spectrum of DLC films consists of two peaks around 1345–1355 cm^{-1} and 1570–1590 cm^{-1} [222, 224]. The formation of DLC with carbon ion implantation and corresponding Raman band (~1540 cm^{-1}) with a weak shoulder (~1350 cm^{-1}) in the range of 1300–1600 cm^{-1} was reported [223].
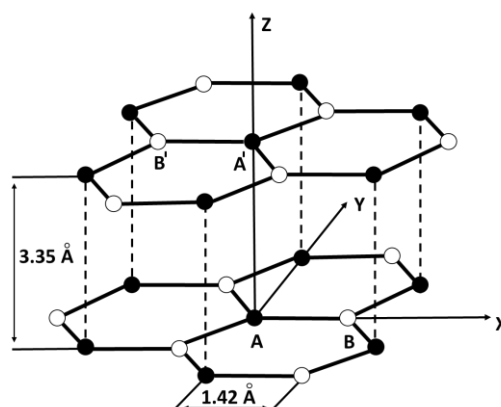
Fig. 8. 16 The crystal structure of graphite. Reproduced from Ref [225].

Another study reported on the carbon ions with sufficient energy (high voltage biased film) that are implanted under the film. The implantation of these carbon ions increases the carbon atom density in the subsurface volume that leads to an increased sp3 C-C hybridization. Ferrari [226] presented a method to determine the sp3 bond fraction in DLC films based on the intensities of the G and D peaks obtained from Raman spectra and the position of the G peak. If the G peak is around ~1550 cm^{-1}, the sp3 content is higher than 10%. If the G peak is at ~1570 cm^{-1}, the sp3 content in the film is 10%. DLC films are produced by plasma immersion ion implantation with an I_D/I_G ratio of 0.65 [227]. In my work, as seen in Fig. 8.15 (a) and (b) the G peak occurs at ~1570 cm^{-1}, giving an I_D/I_G ratio of ~0.6 and a sp3 content of approximately 10%. Thus, the Ni(111) films implanted with carbon ions at -5 and -10 kV acceleration consist of more sp3 bonding and carry diamond-

like properties [228, 229]. The 2D band for the -5 and -10 kV is not a distinctive peak but has a broad range between ∼2500-3100 cm^{-1}, and indication of defects [230].

Three major distinctive Raman bands, D band (∼1348 cm^{-1}), G band (∼1578 cm^{-1}), and 2D band (∼2687 cm^{-1}), which are the most prominent characteristic peaks of graphene are also observed in Fig. 8.15(c) for annealed samples that are implanted with ∼3.5×10^{15} cm^{-2} carbon ions at -15 kV Ni (111) biasing voltage. The D band (∼1350 cm^{-1}) results from the vacancies or dislocations in graphene layer and from the edge of this layer. This band is also related to the presence of the breathing vibration modes of sp2-hybridized carbon hexagons and to the structural defects, vacancies, and disorders in the material, arising from the first-order scattering by zone-boundary phonons [205, 231, 232]. The G band is considered as the main characteristic of graphene and is associated to the in-plane vibrations of sp2 hybridized carbon atoms and is located at ∼1580 cm^{-1}. The G band emanates with the doubly degenerate E_{2g} phonon modes at the hexagonal Brillouin zone center and with the in-plane sp^2 carbon atom vibration [232, 233]. The last band, 2D, is correlated to the number of graphene layers and located at ∼2700 cm^{-1}. Previous studies detected Lorentzian-shape 2D peaks at ∼2680 cm^{-1} [214]. The 2D band is generated by the second order Raman scattering by two-phonon resonance [233]. The low-intensity D-peak at ∼1348 cm^{-1} indicates defects, which may result from graphene grain boundaries [234]. Their relative positions and ratios indicate the presence of graphene formation on Ni(111) film [214, 235]. However, nanocrystalline graphite carries similar Raman bands formation [236]. These peaks are correlated to the structural properties of ta-C and a-C:H. The G peak appears near 1600 cm^{-1} in a-C:H and the I_D/I_G increases with more graphitic bonding [237]. The I_D/I_G ratios in Fig. 8.15 are 0.6, 0.7, and 0.8, for -5, -10, and -15 kV, respectively. Increase in the I_D/I_G ratio with increased biasing voltage is an indication of more defects and disorders such as Young's modulus [237]. The ratio for the G

band to 2D band, I_{2D}/I_G is 0.4 for -15 kV bias at 3.5×10^{15} cm^{-2} dose. Charlier et al. reported that

if the material consists of two or more layers, the 2D band consists of two components [238].

Shimodaira et al. reported on the presence of G and D sub-bands in the Raman spectra which are

the indications of carbon structure formation that contain both amorphous carbon domains and

graphite crystals [239].
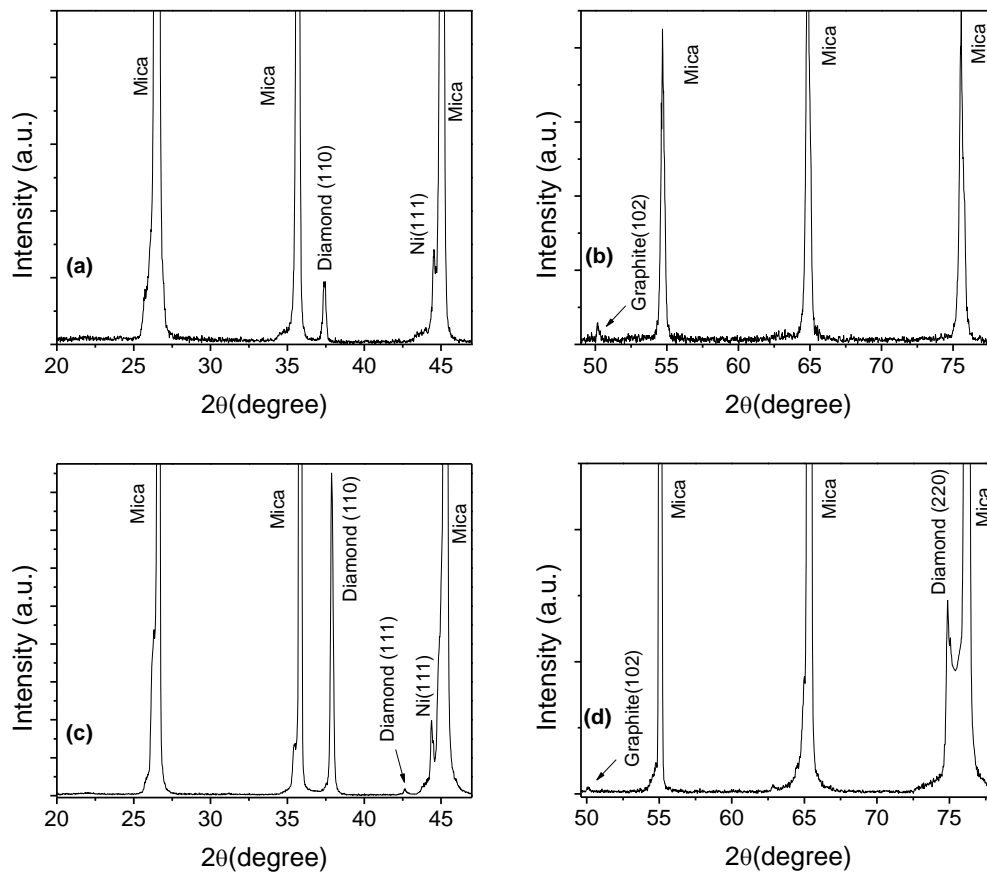
Fig. 8. 17 XRD patterns of Ni(100) film after annealing at 750 C°. The C ions are implanted at 7

(a), (b) and 10×10^{15} cm^{-2} ion dose (c), (d). Substrate is biased to -10 kV.

Fig. 8.17 shows the XRD patterns of the Ni(111) substrates that are implanted with 7 (a

and b) and 10×10^{15} cm^{-2} (c and d) ion dose. Ni(111) films are annealed at 750 C° for 1 hour. Both

films show diffraction patterns at 2θ values of 37.9 and 50.1, that correspond to diamond(110) and

graphite(102), respectively [240]. XRD pattern at higher implantation dose show both diffraction

patterns of the diamond(110) and (220) at 2θ values of 37.9 and 74.8 [241, 242]. The XRD pattern

at 2θ value of 43.2 is attributed to the diamond(111) [228]. These results indicate that the DLC

structures are formed on both Ni(111) substrates. Fig. 8.18 shows the FESEM images of the film

grown on Ni(111) film with $\sim 10.5 \times 10^{15}$ cm^{-2} carbon ion dose. Images show sub micrometer and

nanosized faceted particles.
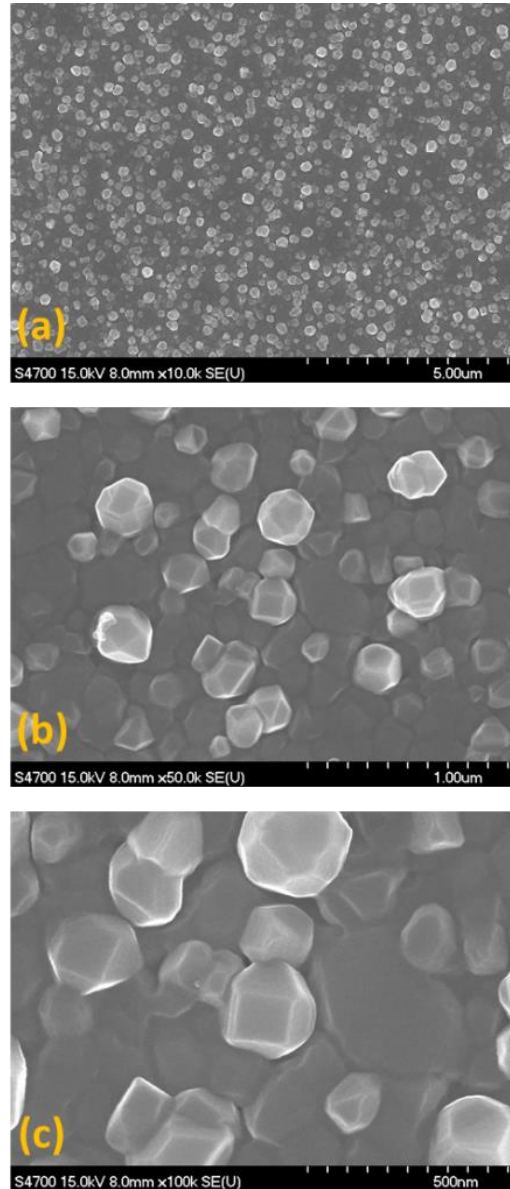
Fig. 8. 18 FESEM image of 400 nm Ni(111) film with 3 different magnifications, implanted with

carbon ions at -10 kV Ni(111) bias and ~10.5×10^{15} cm^{-2} ion dose.

The double peaked structure of the 2D is reported as a good indication of turbostratic graphene where stacking order or tilted baseline from scattering could affect the 2D peak band shape and width [243]. Turbostratic graphene is comprised of stacked multiple graphene layers with regular spacing but different stacking ordering degree [57]. It is noted from early studies that compared to a single layer graphene, the 2D band peak frequency of turbostratic graphene was upshifted by ~20 cm^{-1} to ~2660 cm^{-1} while the peak FWHM was >50 cm^{-1}, more than double that of 2D peak for graphene [243-245]. However, its FWHM is reported as 50 cm^{-1}, almost double that of the 2D peak of graphene and is upshifted by 20 cm^{-1} due to the compressed strain and the increased number of graphene layers [243]. One can see the formation of double peaked 2D and D* bands in Fig. 8.14(a). In Fig. 8.14(a), the FWHM value of 2D band for -15 kV biasing is calculated as ~110 cm^{-1} from the Lorentzian curve fitting [214].

Fig. 8. 19 shows the Raman spectra for -15 kV biasing at different carbon ions dose. The I_D/I_G ratio is calculated as 0.8, 1.1, and 1.2, whereas the ratio for the I_{2D}/I_G is 0.9, 0.7, and 0.6, for the 30 mJ, 40 mJ, and 50 mJ laser pulse energies, respectively. I_D/I_G value is greater than 1.1 for -15 kV Ni(111) biasing at a dose of >10×10^{15} cm^{-2}. D* band peak as seen in Fig. 8.20 is associated to structural defects in the film, as previously reported [246]. Previous studies have shown that the more the film is graphitic, the smaller the ratio I_{2D}/I_G becomes [19].

Therefore, using the analysis of D and G bands with the presence of D* and 2D bands, I conclude that the synthesized carbon structure on Ni(111) substrate shows a graphitic and diamond-like carbon formation [56, 247]. The films that were grounded and biased to +5 kV possess more graphitic nature. The experimented conditions, carbon ions dose, biasing of the Ni(111) film, positions of these three peaks, the intensity ratio of I_D/I_G and I_{2D}/I_G, the full width half maximum (FWHM) of the G peak are summarized in Table 8.4.
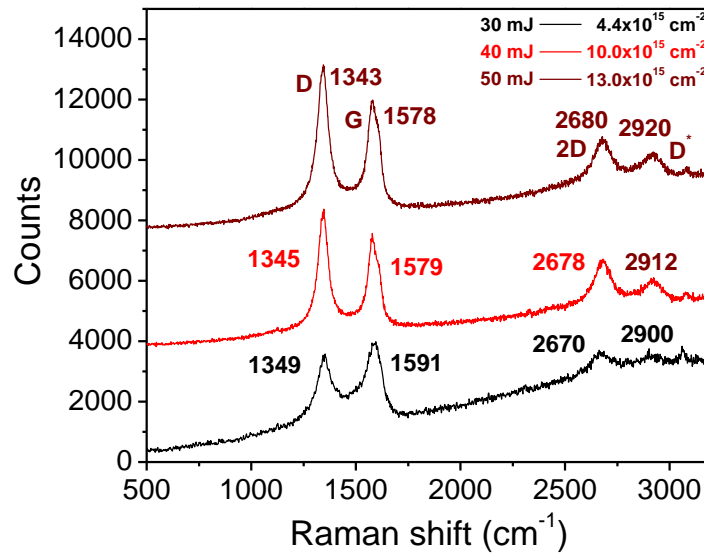
Fig. 8. 19 Effect of laser pulse energy at -15 kV Ni(111) biasing voltage. Corresponding ion dose

values are ~4.4,10, and 13×10^{15} cm^{-2} for 30, 40, 50 mJ, respectively.

Table 8. 4 Summary of the experimental conditions and the Raman spectra on Ni(111) film.

Dose (10^{15} cm^{-2})	kV	G	D	2D	FWHM G	I$_{2D}$/I$_G$	I$_D$/I$_G$
		~ (cm^{-1})					
3.5	0	1534	-	2940	349	0.3	-
3.5	+5	1546	-	2920	301	0.4	-
3.5	-5	1555	1367	2880	256	0.8	0.6
3.5	-10	1550	1373	2885	360	0.4	0.6
3.5	-15	1576	1343	2688	76	0.7	0.9
4.4	-15	1591	1349	2670	115	0.9	0.8
7	0	1538	-	2936	372	0.3	-
7	+5	1546	-	2910	304	0.3	-
10	-15	1579	1345	2678	57	0.7	1.2
10.5	0	1537	-	2931	396	0.3	-
10.5	+5	1534	-	2921	308	0.2	-
13	-15	1578	1343	2680	78	0.5	1.3
13	0	1537	-	2928	399	0.2	-

8.3.2.2 Optical Microscope Analysis of Ni(111)Films

It was reported that the thermal annealing causes Ni(111) film to form grain boundaries, causing discontinuities on the top surface of the film [198]. Optical microscope images on surface are employed after annealing process. Uneven carbon nanostructure cluster formations on film surfaces are observed. Optical images are taken from both Ni(111) and C ion implanted Ni(111) films at –5 kV biasing. Fig.8.20(a) shows that the surface of Ni (111) has a relatively uniform color with only a few dark spots. However, the surface of implanted Ni (111) has many dark dots as shown in Fig.8.20(b). They may be due to graphitic film formation on Ni surface [248].
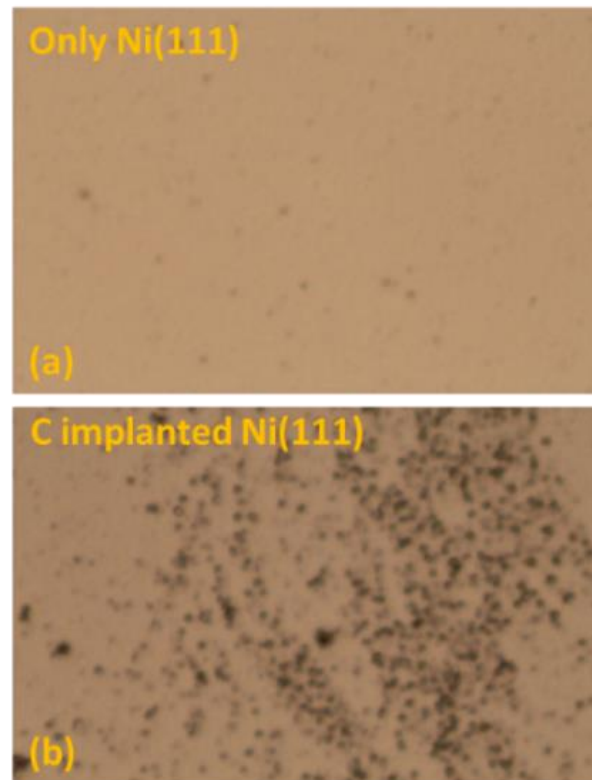
Fig. 8. 20 Optical images of Ni(111) films. (a) Only 400 nm Ni(111) film. (b) Ni(111) film after ion implantation. Dose: ~3.5×10^{15} cm^{-2} at -10 kV biasing with no annealing.
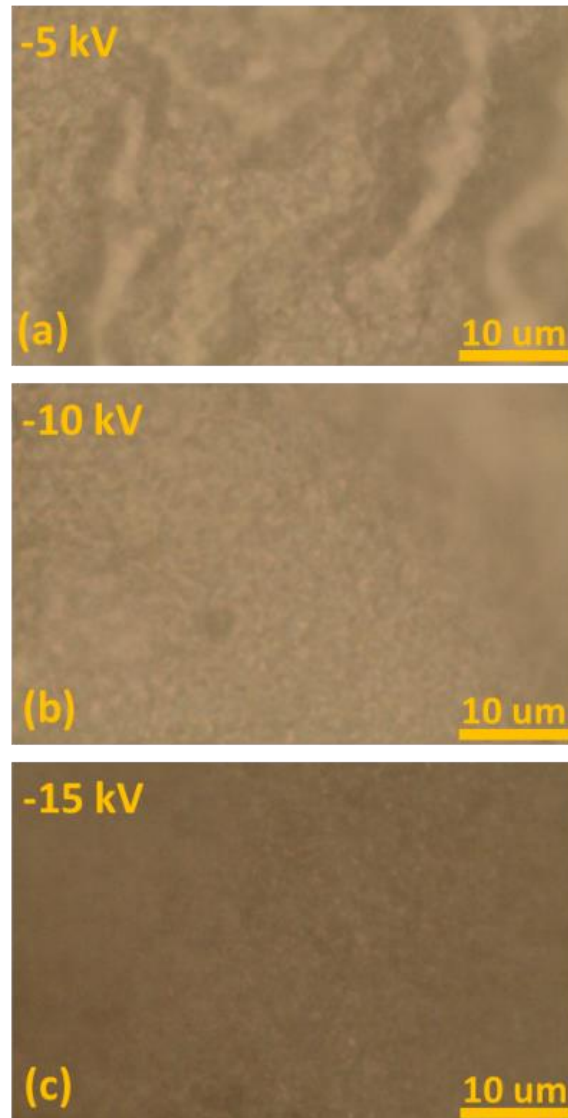
Fig. 8. 21 Optical images of Ni(111) films after annealing at 750 °C for 1 hour. Substrates are biased to -5 (a), -10 (b), and -15 kV (c). Implantation dose: ~3.5×10^{15} cm^{-2}.

Carbon ion implanted Ni(111) film after annealing is shown in Fig.8.21. The areas of several larger clusters are about hundreds to thousands square micron. Clusters can be seen in Fig. 8.21(a). That's the best image. Mica was not flat and was very thin. It was very hard to focus. The increase in the film biasing seems to give more energy to the carbon ions that increase ions energy. The film surface becomes smooth and evenly distributed as in Fig.8.21(b) and (c). The film in (a) appears to possess small clusters, a few square micrometer in area exposing parts of the substrate

surface, while films remain intact in (b) and (c) and no significant non-uniformities can be observed from the images.
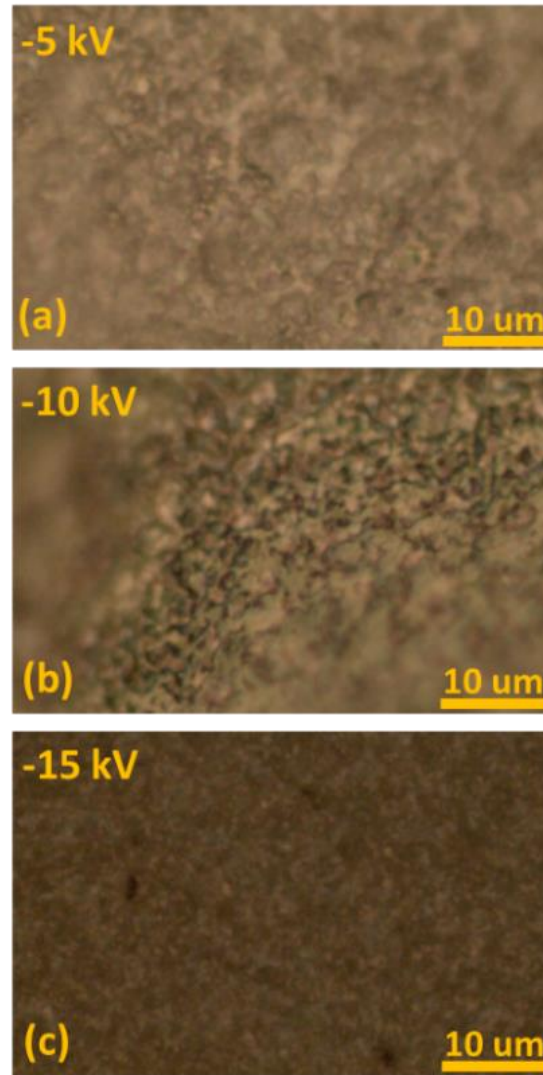
Fig. 8. 22 Optical images of Ni(111) films after annealing at 750 °C for 1 hour. Substrates are biased to -5 (a), -10 (b), and -15 kV (c). Implantation dose: ~7.0×10^{15} cm^{-2}.

Fig.8.22 shows the images of annealed Ni(111) thin films with higher carbon ions dose. It is obvious that the films fully cover the substrate surface with the increase of the ion dose and the biasing voltage on the film. Most of the implanted areas show fairly uniform coverage on the Ni(111) film while the contrast over the Ni(111) film is apparent. The dark regions may be due to

carbon structures such as graphitic film or diamond-like carbon. No evident distinction is observed between the two films for - 5 and 10 kV bias and 10.5×10^{15} cm^{-2} ion dose in Fig.8.23 (a) and (b). The films have dark regions, an indication that an uneven coverage of carbon structure such as DLC. Light contrast is similar to those as previously reported for diamond-like carbon formation [249, 250].
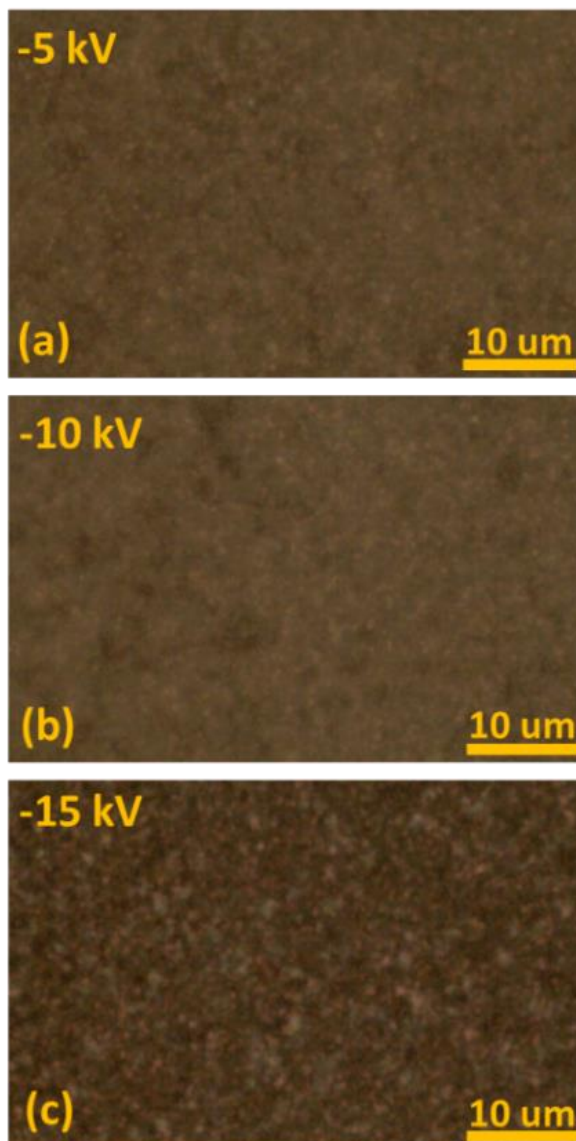
Fig. 8. 23 Optical images of Ni(111) films after annealing at 750 °C for 1 hour. Substrates are biased to -5 (a), -10 (b), and -15 kV (c). Implantation dose: ~10.5×10^{15} cm^{-2}.

8.4 Conclusion

In conclusion, the LIS and neutrals are utilized for direct carbon ion implantation of Ni(111), aiming the carbon films synthesis such as diamond-like carbon. Magnetron sputter coater is used for Ni thin film coatings on mica substrates. Ni(111) thin films are prepared at 500 °C with 400 nm thickness. XRD analysis showed that the surface morphology mostly contains single crystal Ni(111). Carbon ions with a series of dosages ($\sim 10^{15}$-10^{16} cm^{-1}) are implanted into Ni(111) films on mica substrates at room temperature with Ni(111) film biasing voltages of +5, -5, -10, and -15 kV. I conclude that the synthesized carbon structure on Ni(111) are mostly amorphous carbon nature for grounded and +5 kV biased films. The post-annealing of Ni(111) substrates after ion implantation is conducted. The presence of Raman bands for D, G, D*, and 2D has also confirmed the deposition of the graphitic structures on Ni(111) film such as diamond-like carbon.

Therefore, the LIS can be utilized with the aim of synthesis of carbon films such as diamond-like carbon, or carbon-based structures on a metal Ni (111) film, using carbon ions implantation. The process can be controlled and optimized in terms of the ion implantation dose, annealing temperature, and the carbon ions kinetic energy. The ion dose, annealing temperature, and the kinetic energy of the ions directly contribute to the synthesized film properties. Using different characterization techniques, effects of each parameters can be evaluated and the process can be optimized for the desired application.

CHAPTER 9

SUMMARY

Carbon MCI generated from laser plasma was analyzed in terms of the ion charge state and energy distribution. The C^{1+} and C^{2+} ions were detected at a laser fluence of 8 J/cm^2. The ion charge states and corresponding kinetic energies are increased with the laser energy. The focusing lens position was found to have a strong influence on the generation of higher charge states. A shifted Maxwell–Boltzmann fitting to the ion signal was found to best fit the TOF signal and the retarding field analysis. This approach gives a more accurate deconvolution of the signal from each charge than can be obtained solely from the TOF signal. This fitting indicates ions with multiple charge states exist in the ablation plume where ablation velocity is found to be $u_f = 4 \times 10^4$ m/s, or 99 eV as ablation energy. Considering that the ions with different charges have energies corresponding to the sum of that due to the adiabatic expansion $E_{ablation}$ plus energy gain due to acceleration in the double layer by the Coulomb potential $E_{Coulomb}$, the ion energy E was calculated by $E = E_{ablation} + zE_{coulomb}$, where z is the ion charge. By fitting this equation to the experimental results with retardation voltage analysis, we estimated the ablation and coulomb energies as 80 and 195 eV, respectively. The plasma cloud dimension was estimated as $L_0 = 0.035$ mm with a plume dimension as 4 cm at time $t = 1$ μs. When a voltage is applied to the target to establish an external accelerating electric field, ion extraction is observed to be enhanced with the increased electric field. Carbon MCI up to C^{4+} are observed with a relatively low laser fluence of 76 J/cm^2 and the accelerating voltage of 5 kV. The mean energy of the ions increases with the increase of the ionization state and acceleration voltage. Using the EIA, we have measured the ions energy distributions through E/z selection. The ion energy is dependent on the acceleration voltage but is reduced by plasma shielding effects.

Carbon ions and spectral emission lines are measured for ablation using a Q–switched Nd:YAG laser. We observed carbon MCIs up to C^{4+} at 3 kV target voltage and carbon spectral lines up to C IV for laser pulse fluence above 28 J/cm^2. The kinetic energy of the carbon ions is 5.3 keV per charge for 9 kV target voltage. The electron temperature T_e of ~0.90 eV for C II lines is calculated using the Boltzmann plot method for ablation with a laser fluence of ~40 J/cm^2. Deconvolution of the carbon ion signal using SMB distribution for TOF signals gives an ion plasma temperature T_i ~6.0 eV for 36 J/cm^2. The OES and ion TOF reveal different plasma temperatures due to the probing of different plasma regions. The electron density n_e was ~2.1×10^{17} cm^{-3} to ~3.5× 10^{17} cm^{-3} for laser pulse fluence of 4 to 40 J/cm^2 and saturates for a fluence >25 J/ cm^2. We also investigated the influence of applying an external electric field of up to 600 V/cm on the carbon emission lines with no noticeable change observed.

I coupled a SD to a laser generated carbon plasma. A significant enhancement in total ion charge was observed due to the SD. Carbon ions from C^{1+} to the fully stripped C^{6+} are observed for a SD energy of ~750 mJ corresponding to capacitor bank voltage of 5.5 kV at a laser pulse energy of ~50 mJ. The SD significantly increased the intensity of the carbon spectral lines. From OES, the electron temperature T_e increased from 1.06 for the laser alone to 1.46 eV when the SD with 5.5 kV charging voltage is coupled to the laser plasma. Analysis of the ion TOF signal gives an ion plasma temperature T_{ieff} of 16.8 eV using the laser pulse alone. The difference in plasma temperatures for the two measurements is mainly attributed to the different regions probed. SD energy results in a significant enhancement in the observed C_2 Swan bands, and C II and C III spectral lines. Further optimization of the SD coupling to the laser plasma can include changes in the electrode geometry and reduction in the spark pulse width.

Femtosecond laser ablation of carbon (τ = 150 fs and λ = 800 nm) is studied in the laser pulse fluence range of 3.2 – 6.4 J/cm^2. The laser fluence strongly affected the ion yield and

maximum charge state with a maximum of 2.26 nC ion current detected at 1.54 m away from the laser plasma and up to C^{6+} detected. TOF signals of the carbon ions are fitted to SMB distribution and the effective ion temperature $T_{ieff} \sim 6.9$ eV and flow velocity $u_f = 7.9 \times 10^4$ m/s, for C^{1+}, are calculated from the fitting parameters. The ion kinetic energies are calculated from the TOF signal as ~ 13 and 1.4 keV for C^{6+} and C^{1+}, respectively. The gain is not proportional to the charge state due to the plasma shielding that the ions experience depending on their charge state.

Finally, a laser generated multicharged ion source with the aim of carbon film synthesis by direct Ni(111) implantation is realized. A Q−switched Nd:YAG laser can deliver carbon ions up to C^{4+}. Utilizing the current system with spark discharge coupling or with a chirped pulse amplified Ti:sapphire fs laser delivered carbon ions up to fully stripped C^{6+}. Spark discharge energy showed that even at low laser energies, the yield of the ion's generation can be amplified with the charge state increased. Introducing an additional electrical field to the source chamber showed that the generated ions can gain extra kinetic energy and can be accelerated to several keV energies. This approach is a promising feature for applications that require energetic ions. Diagnostic studies are conducted with lab-built Faraday cup equipped with a retarding field analyzer, electrostatic energy analyzer, and the Einzel lens. Results showed that the generated carbon ions can be manipulated in their trajectory when travelling in the drift tube, be specifically selected for a desired ion energy range, or focused to a particular area. Retardation studies helped to determine the maximum charge states generated. Because all the components can be modified in the ion generation chamber, specifically the diagnostic components; these modular components can be used for steering and focusing the ion beam for a desired application.

The realized ion source is utilized for carbon ion implantation on Ni(111). Graphene synthesis on single crystal Ni(111) is of critical importance for applications suitable to current

microelectronics fabrication. Ni(111) thin films are prepared with sputter coater on mica substrates at 500 °C with 400 nm thickness. XRD analysis showed that the surface morphology mostly contains single crystal Ni(111). Ni(111) surface does not contain interface boundaries and the lattice match between graphene/graphite and the Ni(111) is very good. Carbon ions at +5, -5, -10, and -15 keV biasing of Ni(111) films are implanted with a series of dosages into Ni(111) films on mica substrates at room temperature. Carbon ion implantation into Ni(111) is followed with a post-implantation activation annealing at 750 °C. Amorphous carbon and diamond-like carbon films are synthesized. Graphene synthesis on single crystal Ni(111) is important for applications suitable for large scale fabrication of hybrid and flexible devices. The presence of Raman bands for D, G, D*, and 2D has also confirmed the deposition of the graphitic structures on the Ni(111) substrate such as diamond-like carbon.

The presented work demonstrated that the laser generated multicharged ion sources are feasible, practical, and requires less maintenance cycle compared to other ion sources. Regardless of the type of the material, they can generate multicharged ions from any solid target, making them highly competitive to implement in the current ion generation systems. Careful optimizations in the current pulse forming network for spark-discharge coupling and ion extraction geometry, and implementing advanced ion collimation devices can enhance the ions generation yield and focusing parameters; making the currently operational system more feasible for implantation applications and thin film processing. Further studies should be carried out to optimize and selectively apply individual multicharged ions ($C^{1+} - C^{6+}$) for graphene synthesis. Thermal annealing at higher temperatures, when suitable substrates are used, can direct the scope of the future studies using currently available system towards defect-free, large-scale graphene synthesis.

REFERENCES

[1] J. D. Gillaspy, J. M. Pomeroy, A. C. Perrella, and H. Grube, "The potential of highly-aaa charged ions: possible future applications," in 13th International Conference on the Physics of Highly Charged Ions, United Kingdom, vol. 58: IOP Publishing, pp. 451-456, 2007.

[2] F. Aumayr and H. Winter, "Potential sputtering," *Philosophical Transactions of the Royal Society London, Series A (Mathematical, Physical and Engineering Sciences),* vol. 362, no. 1814, pp. 77-102, 2004.

[3] T. Meguro *et al.*, "Highly-charged ion induced surface nano-modification," *Surface and Coatings Technology,* vol. 201, no. 19–20, pp. 8452-8455, 2007.

[4] O. Balki, M. M. Rahman, and H. E. Elsayed-Ali, "Optical emission spectroscopy of carbon laser plasma ion source," *Optics Communications,* vol. 412, pp. 134-140, 2018.

[5] V. M. Gordienko, I. M. Lachko, A. A. Rusanov, A. B. Savel'ev, D. S. Uryupina, and R. V. Volkov, "Enhanced production of fast multi-charged ions from plasmas formed at cleaned surface by femtosecond laser pulse," *Applied Physics B,* vol. 80, no. 6, pp. 733-739, 2005.

[6] D. Hiroyuki, N. Mamiko, and S. P. Alexander, "Review of laser-driven ion sources and their applications," *Reports on Progress in Physics,* vol. 75, no. 5, p. 056401, 2012.

[7] E. Woryna, P. Parys, J. Wołowski, and W. Mróz†, "Corpuscular diagnostics and processing methods applied in investigations of laser-produced plasma as a source of highly ionized ions," *Laser and Particle Beams,* vol. 14, no. 03, pp. 293-321, 1996.

[8] E. A. D. Carbone *et al.*, "Experimental investigation of the electron energy distribution function (EEDF) by Thomson scattering and optical emission spectroscopy," *Journal of Physics D: Applied Physics,* vol. 45, no. 47, p. 475202, 2012.

[9] H. J. Quevedo, M. McCormick, M. Wisher, R. D. Bengtson, and T. Ditmire, "Simultaneous streak and frame interferometry for electron density measurements of laser produced plasmas," *Review of Scientific Instruments,* vol. 87, no. 1, pp. 013107-5, 2016.

[10] M. M. Abdelrahman, "Factors Enhancing Production of Multicharged Ion Sources and -- Their Applications," *Science and Technology,* vol. 2, pp. 98-108, 2012.

[11]   R. Kelly and R. W. Dreyfus, "On the effect of Knudsen-layer formation on studies of vaporization, sputtering, and desorption," *Surface Science,* vol. 198, no. 1–2, pp. 263-276, 1988.

[12]   F. F. Chen, "Decay of a plasma created between negatively biased walls," *Physics of Fluids,* vol. 25, no. 12, pp. 2385-2387, 1982.

[13]   H. Horisawa and I. Kimura, "Fundamental study on laser plasma accelerator for propulsion applications," *Vacuum,* vol. 65, no. 3, pp. 389-396, 2002.

[14]   P. Gasior and M. Rosinski, "Review on developments in LIS (laser ion source) at the IPPLM and its possible applications in photonics," in Proceedings of SPIE, Photonics Applications in Astronomy, Communications, Industry, and High-Energy Physics Experiments, 25 October 2013,vol. 8903, 2013, pp. 89030L-89030L-9.

[15]   M. Rosinski *et al.*, "Laser produced streams of Ge ions accelerated and optimized in the electric fields for implantation into SiO2 substratesa)," *Review of Scientific Instruments,* vol. 83, no. 2, p. 02B305, 2012.

[16]   M. Rosinski, B. Badziak, P. Parys, J. Wołowski, and M. Pisarek, "Modification of semiconductor materials using laser-produced ion streams additionally accelerated in the electric fields," *Applied Surface Science,* vol. 255, no. 10, pp. 5418-5420, 2009.

[17]   V. Y. Fominski, S. N. Grigoriev, R. I. Romanov, A. G. Gnedovets, and P. N. Chernykh, "Laser plasma ion implantation and deposition of platinum for SiC-based hydrogen detector fabrication," *Nuclear Instruments and Methods in Physics Research Section B: Beam Interactions with Materials and Atoms,* vol. 313, pp. 68-75, 2013.

[18]   L. Baraton *et al.*, "Synthesis of few-layered graphene by ion implantation of carbon in nickel thin films," *Nanotechnology,* vol. 22, no. 8, p. 085601, 2011.

[19]   S. Garaj, W. Hubbard, and J. A. Golovchenko, "Graphene synthesis by ion implantation," *Applied Physics Letters,* vol. 97, no. 18, p. 183103, 2010.

[20]   J. Kim, G. Lee, and J. Kim, "Wafer-scale synthesis of multi-layer graphene by high-temperature carbon ion implantation," *Applied Physics Letters,* vol. 107, no. 3, p. 033104, 2015.

[21]   A. N. Yurkov, N. N. Melnik, V. V. Sychev, V. V. Savranskii, D. V. Vlasov, and V. I. Konov, "Synthesis of carbon films by magnetron sputtering of a graphite target using hydrogen as plasma-forming gas," *Bulletin of the Lebedev Physics Institute,* vol. 38, no. 9, p. 263, 2011.

[22]   H. Zhang *et al.*, "RF magnetron sputtering synthesis of three-dimensional graphene@CO_3O_4 nanowire array grown on Ni foam for application in supercapacitors," *Journal of Alloys and Compounds,* vol. 740, pp. 174-179, 2018.

[23]   S. Al-Kamiyani and T. Mohiuddin, "Improved control in elimination of white impurities on graphene by chemical vapor deposition (CVD)," *AIP Advances,* vol. 8, no. 12, p. 125325, 2018.

[24]   U. Bangert *et al.*, "Ion Implantation of Graphene-Toward IC Compatible Technologies," *Nano Letters,* vol. 13, no. 10, pp. 4902-4907, 2013.

[25]   J. Robertson, "Comparison of diamond-like carbon to diamond for applications," in *Hasselt Diamond Workshop 2008 - SBDD XIII*, 2008, vol. 205: Wiley-VCH Verlag, pp. 2233-2244.

[26]   A. K. Geim and K. S. Novoselov, "The rise of graphene," *Nature Materials,* vol. 6, no. 3, pp. 183-91, 2007.

[27]   H. W. Kroto, J. R. Heath, S. C. O'Brien, R. F. Curl, and R. E. Smalley, "C_{60}: buckminsterfullerene," *Nature,* vol. 318, no. 6042, pp. 162-163, 1985.

[28]   J. Díaz, G. Paolicelli, S. Ferrer, and F. Comin, "Separation of the sp3 and sp2 components in the C1s photoemission spectra of amorphous carbon films," Physical Review B, vol. 54, no. 11, pp. 8064-8069, 1996.

[29]   R. Haerle, E. Riedo, A. Pasquarello, and A. Baldereschi, "sp^2/sp^3 hybridization ratio in amorphous carbon from C 1s core-level shifts: X-ray photoelectron spectroscopy and first-principles calculation," Physical Review B, vol. 65, no. 4, p. 045101, 2001.

[30]   J. C. Lascovich, R. Giorgi, and S. Scaglione, "Evaluation of the sp^2/sp^3 ratio in amorphous carbon structure by XPS and XAES," *Applied Surface Science,* vol. 47, no. 1, pp. 17-21, 1991.

[31]   T. D. Burchell, *Carbon Materials for Advanced Technologies*, 1st ed. Oxford, UK.: Elsevier Science Ltd., 1999, p. 540.

[32]   V. Georgakilas, J. A. Perman, J. Tucek, and R. Zboril, "Broad Family of Carbon Nanoallotropes: Classification, Chemistry, and Applications of Fullerenes, Carbon Dots, Nanotubes, Graphene, Nanodiamonds, and Combined Superstructures," *Chemical Reviews,* vol. 115, no. 11, pp. 4744-4822, 2015.

[33]   M. P. Grumbach and R. M. Martin, "Phase diagram of carbon at high pressures and temperatures," *Physical Review B (Condensed Matter),* vol. 54, no. 22, pp. 15730-41, 1996.

[34]   F. P. Bundy, W. A. Bassett, M. S. Weathers, R. J. Hemley, H. U. Mao, and A. F. Goncharov, "The pressure-temperature phase and transformation diagram for carbon; updated through 1994," *Carbon,* vol. 34, no. 2, pp. 141-153, 1996.

[35]   D. D. L. Chung, "Electrical applications of carbon materials," *Journal of Materials Science,* vol. 39, no. 8, pp. 2645-2661, 2004.

[36]   J. Robertson, "Diamond-like amorphous carbon," *Materials Science and Engineering: R: Reports,* vol. 37, no. 4, pp. 129-281, 2002.

[37]   O. A. Shenderova, V. V. Zhirnov, and D. W. Brenner, "Carbon Nanostructures," *Critical Reviews in Solid State and Materials Sciences,* vol. 27, no. 3-4, pp. 227-356, 2002.

[38]   K. Seshan, *Handbook of Thin Film Deposition*. Elsevier Science, 2012.

[39]   K. Seshan, *Handbook of Thin Film Deposition Processes and Techniques*. Elsevier Science, 2001.

[40]   R. Gomer, "Diffusion of adsorbates on metal surfaces," *Reports on Progress in Physics,* vol. 53, no. 7, pp. 917-1002, 1990.

[41]   N. Kaiser, "Review of the fundamentals of thin-film growth," *Applied Optics,* vol. 41, no. 16, pp. 3053-3060, 2002.

[42]   H. O. Pierson, "Fundamentals of Chemical Vapor Deposition," in *Handbook of Chemical Vapor Deposition (CVD) (Second Edition)*. Norwich, NY: William Andrew Publishing, 1999, pp. 36-67.

[43] P. J. Kelly and R. D. Arnell, "Magnetron sputtering: a review of recent developments and applications," *Vacuum,* vol. 56, no. 3, pp. 159-172, 2000.

[44] A. E. Willner *et al.*, "Optics and Photonics: Key Enabling Technologies," *Proceedings of the IEEE,* vol. 100, Special Centennial Issue, pp. 1604-1643, 2012.

[45] A. C. Jones, M. L. Hitchman, "Overview of Chemical Vapour Deposition," in *Chemical Vapour Deposition: Precursors, Processes and Applications*, The Royal Society of Chemistry, 2009, pp. 1-36.

[46] H. Moriguchi, H. Ohara, and M. Tsujioka, "*History and Applications of diamond-like carbon manufacturing processes,*" Sei Technical Review, vol. 82, pp. 52-58.

[47] Y. Zhang, L. Zhang, and C. Zhou, "Review of Chemical Vapor Deposition of Graphene and Related Applications," *Accounts of Chemical Research,* vol. 46, no. 10, pp. 2329-2339, 2013.

[48] S. Aisenberg and R. Chabot, "Ion-Beam Deposition of Thin Films of Diamondlike Carbon," *Journal of Applied Physics,* vol. 42, no. 7, pp. 2953-2958, 1971.

[49] J. Robertson, "Gap states in diamond-like amorphous carbon," *Philosophical Magazine B,* vol. 76, no. 3, pp. 335-350, 1997.

[50] K. Bewilogua and D. Hofmann, "History of diamond-like carbon films-From first experiments to worldwide applications," *Surface and Coatings Technology,* vol. 242, pp. 214-225, 2014.

[51] E. M. Regan *et al.*, "Differential patterning of neuronal, glial and neural progenitor cells on phosphorus-doped and UV irradiated diamond-like carbon," *Biomaterials,* vol. 31, no. 2, pp. 207-215, 2010.

[52] P. R. Goglia, J. Berkowitz, J. Hoehn, A. Xidis, and L. Stover, "Diamond-like carbon applications in high density hard disc recording heads," *Diamond and Related Materials,* vol. 10, no. 2, pp. 271-277, 2001.

[53] K. S. Novoselov *et al.*, "Electric field effect in atomically thin carbon films," *Science,* vol. 306, no. 5696, pp. 666-9, 2004.

[54] P. Misra, *Physics of Condensed Matter*. Academic Press, 2011, pp. 600-603.

[55]   J. N. Fuchs and M. O. Goerbig., Introduction to the Physical Properties of Graphene, 2008. Accessed on: Nov. 2, 2019. [Online]. Available:asdasasdfasdfasdfasdasdfasdfasdfasdfasdf http://web.physics.ucsb.edu/~phys123B/w2015/pdf_CoursGraphene2008.pdf

[56]   A. C. Ferrari and D. M. Basko, "Raman spectroscopy as a versatile tool for studying the properties of graphene," *Nature Nanotechnology,* vol. 8, no. 4, pp. 235-46, 2013.

[57]   J. A. Garlow, L. K. Barrett, L. Wu, K. Kisslinger, Y. Zhu, and J. F. Pulecio, "Large-Area Growth of Turbostratic Graphene on Ni(111) via Physical Vapor Deposition," *Scientific Reports,* vol. 6, p. 19804, 2016.

[58]   S. Bae *et al.*, "Roll-to-roll production of 30-inch graphene films for transparent electrodes," *Nature Nanotechnology,* vol. 5, p. 574, 2010.

[59]   D. R. Cooper *et al.*, "Experimental Review of Graphene," *ISRN Condensed Matter Physics,* p. 501686, 2012.

[60]   Y. W. Tan *et al.*, "Measurement of Scattering Rate and Minimum Conductivity in Graphene," *Physical Review Letters,* vol. 99, no. 24, p. 246803, 2007.

[61]   L. Dell'Anna and A. De Martino, "Magnetic superlattice and finite-energy Dirac points in graphene," *Physical Review B,* vol. 83, no. 15, p. 155449, 2011.

[62]   V. R. F. Giannazzo, and E. Rimini, "Transport properties of graphene with nanoscale lateral resolution," *Scanning Probe Microscopy in Nanoscience and Nanotechnology,* vol. 2, pp. 247-258, 2011.

[63]   C. Berger *et al.*, "Ultrathin Epitaxial Graphite: 2D Electron Gas Properties and a Route toward Graphene-based Nanoelectronics," *The Journal of Physical Chemistry B,* vol. 108, no. 52, pp. 19912-19916, 2004.

[64]   M. I. Ionescu, X. Sun, and B. Luan, "Multilayer graphene synthesized using magnetron sputtering for planar supercapacitor application," *Canadian Journal of Chemistry,* vol. 93, no. 2, pp. 160-164, 2014.

[65]   R. Zhang *et al.*, "Direct graphene synthesis on SiO_2/Si substrate by ion implantation," *Applied Physics Letters,* vol. 102, no. 19, 2013.

[66] J. D. Gillaspy, "Highly charged ions," *Journal of Physics B: Atomic, Molecular and Optical Physics,* vol. 34, no. 19, p. R93, 2001.

[67] M. Muramatsu and A. Kitagawa, "A review of ion sources for medical accelerators (invited)," *Review of Scientific Instruments,* vol. 83, no. 2, p. 02B909, 2012.

[68] V. B. Kutner, "Intense high charge state ion sources (invited)," *Review of Scientific Instruments,* vol. 65, no. 4, pp. 1039-1044, 1994.

[69] R. Geller, "ECRIS: the electron cyclotron resonance ion sources," in *Annual review of nuclear and particle science. Vol.40*. Palo Alto, CA, USA: Annual Reviews, 1990, pp. 15-43.

[70] N. Angert, "Ion sources," in *CAS CERN Accelerator School. General Accelerator Physics. (CERN 85-19), 3-14 Sept. 1984*, Geneva, Switzerland, 1985: CERN, pp. 463-77.

[71] B. Sharkov and R. Scrivens, "Laser ion sources," *IEEE Transactions on Plasma Science,* vol. 33, no. 6, pp. 1778-1785, 2005.

[72] M. Cutroneo, L. Torrisi, J. Ullschmied, and R. Dudzak, "Multi-energy ion implantation from high-intensity laser," *Nukleonika,* vol. 61, no. 2, pp. 109-13, 2016.

[73] S. Gammino *et al.*, "Intense heavy ion beam production with ECR sources," in *23rd International Linear Accelerator Conference, LINAC 2006, August 21- August 25, 2006*, Knoxville, TN, United states, 2006: Joint Accelerator Conferences Website (JACoW), pp. 18-22.

[74] D. Leitner and C. Lyneis, "ECR Ion Sources," in *The Physics and Technology of Ion Sources*: Wiley-VCH Verlag GmbH & Co. KGaA, 2005, pp. 203-231.

[75] J Arianer and R. Geller, "The Advanced Positive Heavy Ion Sources," *Annual Review of Nuclear and Particle Science,* vol. 31, no. 1, pp. 19-51, 1981.

[76] M. A. Lieberman and A. J. Lichtenberg, "Frontmatter," in *Principles of Plasma Discharges and Materials Processing*: John Wiley & Sons, Inc., 2005, pp. 461-489.

[77] C. E. Hill, "Ion and electron sources," in *Cern Accelerator School Cyclotrons, Linacs and Their Applications (CERN 96-02), 28 April-5 May 1994*, Geneva, Switzerland, 1996: CERN, pp. 95-111.

[78]   W. D. Westwood, S. Maniv, and P. J. Scanlon, "The current-voltage characteristic of magnetron sputtering systems," *Journal of Applied Physics,* vol. 54, no. 12, pp. 6841-6846, 1983.

[79]   J. E. Greene, "Review Article: Tracing the recorded history of thin-film sputter deposition: From the 1800s to 2017," *Journal of Vacuum Science & Technology A,* vol. 35, no. 5, p. 05C204, 2017.

[80]   M. H. Key, I. J. Spalding, R. S. Pease, and A. E. Gibson, "Interactions of intense laser radiation with plasma," *Philosophical Transactions of the Royal Society of London. Series A, Mathematical and Physical Sciences,* vol. 300, no. 1456, pp. 599-612, 1981.

[81]   A. M. M. Schiavi, "Study Of Laser Produced Plasmas By X-Ray And Proton Radiography," Ph.D dissertation, Imperial College of Science, University of London, London, 2003. Accessed on July 10, 2019. [Online]. Available:…………………………… http://gaps.ing2.uniroma1.it/aschiavi/Pubblicazioni/PhD/ASchiavi_PhD.pdf

[82]   F. P. Boody, R. Höpfl, H. Hora, and J. C. Kelly, "Laser-driven ion source for reduced-cost implantation of metal ions for strong reduction of dry friction and increased durability," *Laser and Particle Beams,* vol. 14, no. 3, pp. 443-448, 1996.

[83]   I. G. Brown, *Laser Ion Sources in The Physics and Technology of Ion Sources*, 2nd ed. Michigan, Wiley-VCH, 2004, pp 233-256.

[84]   O. Balki and H. E. Elsayed-Ali, "Multicharged carbon ion generation from laser plasma," *Review of Scientific Instruments,* vol. 87, no. 11, p. 113304, 2016.

[85]   J. Wolowski *et al.*, "Fast ion emission from the plasma produced by the PALS laser system," *Plasma Physics and Controlled Fusion,* vol. 44, no. 7, p. 1277, 2002.

[86]   J. Badziak, "Laser-driven generation of fast particles," *Opto-Electronics Review,* vol. 15, no. 1, p. 1, 2007.

[87]   H. A. Sakaue *et al.*, "Electron transfer and decay processes of highly charged iodine ions," *Journal of Physics B (Atomic, Molecular and Optical Physics),* vol. 37, no. 2, pp. 403-15, 2004.

[88]   T. Lu, Y. Qiao, and X. Liu, "Surface modification of biomaterials using plasma immersion ion implantation and deposition," *Interface Focus,* vol. 2, no. 3, pp. 325-36, 2012.

[89]   P. D. Townsend, J. C. Kelly, and N. E. W. Hartley, *Ion implantation, sputtering and their applications*. London, UK: Academic Press, 1976, pp. 20-35.

[90]   V. Le Roux *et al.*, "Etching of Silicon Native Oxide Using Ultraslow Multicharged Ar^{q+} Ions," *Journal of The Electrochemical Society,* vol. 151, no. 1, pp. G76-G79, 2004.

[91]   S. Gammino, "Production of high-intensity, highly charged ions," in *26th CAS-CERN Accelerator School: Ion Sources, May 29- June 8, 2012*, Senec, Slovakia, 2013: CERN-European Organization for Nuclear Research, pp. 123-164.

[92]   H. Daido, M. Nishiuchi, and A. S. Pirozhkov, "Review of laser-driven ion sources and their applications," *Reports on Progress in Physics,* vol. 75, no. 5, p. 056401, 2012.

[93]   W. Mróz *et al.*, "Laser plasma as a source of highly ionized ions," *Review of Scientific Instruments,* vol. 65, no. 4, pp. 1272-1274, 1994.

[94]   M. H. A. Shaim and H. E. Elsayed-Ali, "Aluminum multicharged ion generation from laser plasma," *Nuclear Instruments and Methods in Physics Research, Section B: Beam Interactions with Materials and Atoms,* vol. 356-357, pp. 75-80, 2015.

[95]   T. Henkelmann *et al.*, "Charge state distribution of tantalum ions produced simultaneously by CO_2 and Nd:YAG laser from a laser ion source," *Review of Scientific Instruments,* vol. 63, no. 4, pp. 2828-2830, 1992.

[96]   V. Nassisi, A. Pedone, and A. Rainò, "Preliminary experimental results on an excimer laser ion source," *Nuclear Instruments and Methods in Physics Research Section B: Beam Interactions with Materials and Atoms,* vol. 188, no. 1–4, pp. 267-271, 2002.

[97]   A. Lorusso, J. Krása, K. Rohlena, V. Nassisi, F. Belloni, and D. Doria, "Charge losses in expanding plasma created by an XeCl laser," *Applied Physics Letters,* vol. 86, no. 8, p. 081501, 2005.

[98]   H. Kashiwagi *et al.*, "Acceleration of high current fully stripped carbon ion beam by direct injection scheme," *Review of Scientific Instruments,* vol. 77, no. 3, p. 03B305, 2006.

[99] M. Okamura *et al.*, "Experimental results of DPIS with a new RFQ," *Radiation Effects & Defects in Solids,* vol. 160, no. 10-12, pp. 445-449, 2005.

[100] R. C. Constantinescu, S. Hunsche, H. B. van Linden van den Heuvell, H. G. Muller, C. LeBlanc, and F. Salin, "Highly charged carbon ions formed by femtosecond laser excitation of C_{60}: A step towards an x-ray laser," *Physical Review A,* vol. 58, no. 6, pp. 4637-4646, 1998.

[101] S. Witanachchi, A. M. Miyawa, and P. Mukherjee, "Highly ionized carbon plasma generation by dual-laser ablation for diamond-like carbon film growth," in *Laser-Solid Interactions for Materials Processing. Symposium, 25-27 April 2000*, Warrendale, PA, USA, 2000, Mater. Res. Soc., pp. 3-6.

[102] L. Torrisi, F. Caridi, D. Margarone, A. Picciotto, A. Mangione, and J. J. Beltrano, "Carbon-plasma produced in vacuum by 532 nm- 3ns laser pulses ablation," *Applied Surface Science,* vol. 252, no. 18, pp. 6383-6389, 2006.

[103] S. I. Okihara *et al.*, "Generation of over 5MeV carbon ions from a fibrous polytetrafluoroethylene film irradiated with a 2.4TW, 50 fs table-top laser," *Applied Physics Letters,* vol. 89, no. 12, p. 121502, 2006.

[104] C. C. Liang *et al.*, "Surface smoothing of floating gates in flash memory devices via surface nitrogen and carbon," *Applied Physics Letters,* vol. 75, no. 3, p. 355, 1999.

[105] C. Pierret *et al.*, "Friction and wear properties modification of Ti–6Al–4V alloy surfaces by implantation of multi-charged carbon ions," *Wear,* vol. 319, no. 1–2, pp. 19-26, 2014.

[106] H. A. Ching, D. Choudhury, M. J. Nine, and N. A. A. Osman, "Effects of surface coating on reducing friction and wear of orthopaedic implants," *Science and Technology of Advanced Materials,* vol. 15, no. 1, p. 014402, 2014.

[107] V. Marx, "Sharp shooters," *Nature,* vol. 508, p. 133, 2014.

[108] M. Durante and J. S. Loeffler, "Charged particles in radiation oncology," *Nature Reviews Clinical Oncology,* vol. 7, p. 37, 2009.

[109] N. M. Bulgakova, A. V. Bulgakov, and O. F. Bobrenok, "Double layer effects in laser-ablation plasma plumes," *Physical Review E - Statistical Physics, Plasmas, Fluids, and Related Interdisciplinary Topics,* vol. 62, no. 4 B, pp. 5624-5635, 2000.

[110] M. M. Abdelrahman, "Factors Enhancing Production of Multicharged Ion Sources and Their Applications," *Science and Technology,* vol. 2, pp. 98-108, 2012.

[111] C. C. F. Casey C. Farnell, Shawn C. Farnell, and John D. Williams, "Electrostatic Analyzers with Application to Electric Propulsion Testing," presented at the IEPC-2013-300, 33rd International Electric Propulsion Conference, The George Washington University, Washington D.C., 2013.

[112] D. Mascali *et al.*, "Prompt electrons driving ion acceleration and formation of a two-temperature plasma in nanosecond laser-ablation domain," *Europhysics Letters,* vol. 100, no. 4, p. 45003 (5 pp.), 2012.

[113] L. Torrisi, S. Cavallaro, M. Rosinski, V. Nassisi, V. Paperny, and I. Romanov, "Post acceleration of ions emitted from laser and spark-generated plasmas," *Nukleonika,* vol. 57, no. 3, pp. 323-32, 2012.

[114] A. Miotello and R. Kelly, "On the origin of the different velocity peaks of particles sputtered from surfaces by laser pulses or charged-particle beams," *Applied Surface Science,* vol. 138-139, pp. 44-51, 1999.

[115] S. S. Harilal, C. V. Bindhu, R. C. Issac, V. P. N. Nampoori, and C. P. G. Vallabhan, "Electron density and temperature measurements in a laser produced carbon plasma," *Journal of Applied Physics,* vol. 82, no. 5, pp. 2140-2146, 1997.

[116] E. Woryna *et al.*, "Au^{49+}, Pb^{50+}, and Ta^{48+} ions from laser-produced plasmas," *Applied Physics Letters,* vol. 69, no. 11, p. 1547, 1996.

[117] J. Krása *et al.*, "Generation of high currents of carbon ions with the use of subnanosecond near-infrared laser pulses)," *Review of Scientific Instruments,* vol. 81, no. 2, p. 02A504, 2010.

[118] L. Láska *et al.*, "Angular distribution of ions emitted from Nd:YAG laser-produced plasma," *Review of Scientific Instruments,* vol. 73, no. 2, pp. 654-656, 2002.

[119] L. Láska *et al.*, "Generation of multiply charged ions at low and high laser-power densities," *Plasma Physics and Controlled Fusion,* vol. 45, no. 5, p. 585, 2003.

[120] T. Tetsuka, "Ion Extraction Characteristics on a Barium Plasma Produced between Alternately Biased Parallel Plate Electrodes," *Journal of Nuclear Science and Technology,* vol. 31, no. 4, pp. 301-307, 1994.

[121] R. Rozman, I. Grabec, and E. Govekar, "Influence of absorption mechanisms on laser-induced plasma plume," *Applied Surface Science,* vol. 254, no. 11, pp. 3295-3305, 2008.

[122] T. Mościcki, J. Hoffman, and Z. Szymański, "Modelling of plasma formation during nanosecond laser ablation," *Archives of Mechanics,* Conference Paper vol. 63, no. 2, pp. 99-116, 2011.

[123] L. Torrisi *et al.*, "Temperature measurements in plasmas produced by high-power lasers interacting with solid targets," *Review of Scientific Instruments,* vol. 77, no. 3, p. 03B708, 2006.

[124] K. Bernhardi *et al.*, "Studies of electron heating and multiply charged ion production in an electron cyclotron resonance plasma," *Plasma Physics,* vol. 18, no. 2, pp. 77-94, 1976.

[125] T. Kamada *et al.*, "Carbon ion radiotherapy in Japan: an assessment of 20 years of clinical experience," *The Lancet Oncology,* vol. 16, no. 2, pp. e93-e100, 2015.

[126] W. Ensinger, "Correlations between process parameters and film properties of diamond-like carbon films formed by hydrocarbon plasma immersion ion implantation," *Surface and Coatings Technology,* vol. 203, no. 17, pp. 2721-2726, 2009.

[127] A. V. Semenov and V. M. Puzikov, "A laboratory setup for obtaining silicon carbide films by the direct ion deposition method," *Instruments & Experimental Techniques,* vol. 53, no. 5, pp. 761-765, 2010.

[128] G. Impellizzeri *et al.*, "C ion-implanted TiO_2 thin film for photocatalytic applications," *Journal of Applied Physics,* vol. 117, no. 10, p. 105308 (6 pp.), 2015.

[129] P. I. Gaiduk, J. Lundsgaard Hansen, A. Nylandsted Larsen, F. L. Bregolin, and W. Skorupa, "Suppression of tin precipitation in SiSn alloy layers by implanted carbon," *Applied Physics Letters,* vol. 104, no. 23, pp. 231903-5, 2014.

[130] M. Uhl *et al.*, "Highly effective treatment of skull base chordoma with carbon ion irradiation using a raster scan technique in 155 patients: First long-term results," *Cancer,* vol. 120, no. 21, pp. 3410-3417, 2014.

[131] P. Nica, S. Gurlui, M. Osiac, M. Agop, M. Ziskind, and C. Focsa, "Investigation of femtosecond laser-produced plasma from various metallic targets using the Langmuir probe characteristic," *Physics of Plasmas,* vol. 24, no. 10, pp. 103119-10, 2017.

[132] H. R. Griem, "Stark Broadening of Isolated Spectral Lines from Heavy Elements in a Plasma," *Physical Review,* vol. 128, no. 2, pp. 515-523, 1962.

[133] H. R. Griem, *Plasma Spectroscopy*. New York: McGraw-Hil, 1964.

[134] M. Hanif, M. Salik, and F. Arif, "Spectroscopic study of carbon plasma produced by the first (1064 nm) and second (532 nm) harmonics of Nd:YAG laser," *Plasma Physics Reports,* vol. 41, no. 3, pp. 274-280, 2015.

[135] C. Sánchez Aké, H. Sobral, E. Sterling, and M. Villagrán-Muniz, "Time of flight of dual-laser ablation carbon plasmas by optical emission spectroscopy," *Applied Physics A,* vol. 79, no. 4, pp. 1345-1347, 2004.

[136] F. Caridi, L. Torrisi, and L. Giuffrida, "Time-of-flight and UV spectroscopy characterization of laser-generated plasma," *Nuclear Instruments and Methods in Physics Research Section B: Beam Interactions with Materials and Atoms,* vol. 268, no. 5, pp. 499-505, 2010.

[137] M. M. Abdelrahman, "Factors Enhancing Production of Multicharged Ion Sources and Their Applications," *Science and Technology,* vol. 2, pp. 98-108, 2012.

[138] E. Woryna, P. Parys, J. Wołowski, and W. Mróz†, "Corpuscular diagnostics and processing methods applied in investigations of laser-produced plasma as a source of highly ionized ions," *Laser and Particle Beams,* vol. 14, no. 3, pp. 293-321, 1996.

[139] M. H. A. Shaim, M. M. Rahman, O. Balki, A. Sarkissian, M. L. Korwin-Pawlowski, and H. E. Elsayed-Ali, "Transport line for laser multicharged ion source," *Vacuum,* vol. 137, pp. 14-22, 2017.

[140] J. R. Freeman, S. S. Harilal, P. K. Diwakar, B. Verhoff, and A. Hassanein, "Comparison of optical emission from nanosecond and femtosecond laser produced plasma in atmosphere and vacuum conditions," *Spectrochimica Acta Part B: Atomic Spectroscopy,* vol. 87, pp. 43-50, 2013.

[141] G. Bekefi, *Principles of laser plasmas*. New York, NY: Wiley, 1976.

[142] S. S. Harilal, C. I. Riju, C. V. Bindhu, V. P. N. Nampoori, and C. P. G. Vallabhan, "Spatial analysis of C_2 band emission from laser produced plasma," *Plasma Sources Science and Technology,* vol. 6, no. 3, pp. 317-322, 1997.

[143] J. F. Ready, *Effects of High-Power Laser Radiation*. Academic Press, 1971.

[144] F. J. Gordillo-Vázquez, A. Perea, A. P. McKiernan, and C. N. Afonso, "Electronic temperature and density of the plasma produced by nanosecond ultraviolet laser ablation of LiF," *Applied Physics Letters,* vol. 86, no. 18, pp. 181501-3, 2005.

[145] *NIST Atomic Spectra Database* [Online]. Available:…………………………………......... http://physics.nist.gov/PhysRefData/ASD/index.html

[146] P. Sankar, J. J. J. Nivas, N. Smijesh, G. K. Tiwari, and R. Philip, "Optical emission and dynamics of aluminum plasmas produced by ultrashort and short laser pulses," *Journal of Analytical Atomic Spectrometry,* vol. 32, no. 6, pp. 1177-1185, 2017.

[147] F. O. Bredice, D. Orzi, D. Schinca, H. Sobral, and M. Villagrán-Muniz, "Characterization of pulsed laser generated plasma through its perturbation in an electric field," *IEEE Transactions on Plasma Science,* vol. 30, pp. 2139-2143, 2003.

[148] A. Ohzu, Y. Suzuki, Y. Maruyama, and T. Arisawa, "Enhancement of electron temperature in a laser-induced plasma using a radio-frequency electric field," *Physics of Plasmas,* vol. 7, no. 2, pp. 770-772, 2000.

[149] D. Fried, T. Kushida, G. P. Reck, and E. W. Rothe, "The effects of the electric field associated with a laser-induced pulsed discharge on the ablation-generated plumes of $YBa_2Cu_3O_{7-X}$," *Journal of Applied Physics,* vol. 72, no. 3, pp. 1113-1125, 1992.

[150] N. M. Bulgakova, A. V. Bulgakov, and O. F. Bobrenok, "Double layer effects in laser-ablation plasma plumes," *Physical Review E,* vol. 62, no. 4, pp. 5624-5635, 2000.

[151] V. N. Rai, M. Shukla, and H. C. Pant, "Effect of chamber pressure induced space charge potential on ion acceleration in laser produced plasma," *Laser and Particle Beams,* vol. 18, no. 2, pp. 315-324, 2001.

[152] H. Ryufuku and T. Watanabe, "Total and partial cross sections for charge transfer in collisions of multicharged ions with atomic hydrogen," *Physical Review A,* vol. 20, no. 5, pp. 1828-1837, 1979.

[153] J. Krása *et al.*, "Partial currents of ion species in an expanding laser-created plasma," *Vacuum,* vol. 83, no. 1, pp. 180-184, 2008.

[154] O. Balki, M. M. Rahman, S. Xiao, and H. E. Elsayed-Ali, "Generation of C^{6+} in a spark-discharge coupled laser plasma," *Optics Communications,* vol. 403, pp. 50-54, 2017.

[155] M. H. A. Shaim, F. G. Wilson, and H. E. Elsayed-Ali, "Aluminum multicharged ion generation from femtosecond laser plasma," *Journal of Applied Physics,* vol. 121, no. 18, pp. 185901-10, 2017.

[156] Z. Qiushi *et al.*, "Structure and Expansion Characteristics of Laser Ablation Tin Plasma into a Vacuum," *Japanese Journal of Applied Physics,* vol. 49, pp. 056201-6, 2010.

[157] A. M. Elsied, N. C. Termini, P. K. Diwakar, and A. Hassanein, "Characteristics of Ions Emission from Ultrashort Laser Produced Plasma," *Scientific Reports,* vol. 6, p. 38256, 2016.

[158] V. Nassisi, L. Velardi, and D. D. Side, "Electromagnetic and geometric characterization of accelerated ion beams by laser ablation," *Applied Surface Science,* vol. 272, pp. 114-118, 2013.

[159] A. Ugo and K. Gerhard, "Radiotherapy with beams of carbon ions," *Reports on Progress in Physics,* vol. 68, no. 8, p. 1861, 2005.

[160] D. Kramer, "Carbon-ion cancer therapy shows promise," *Physics Today,* vol. 68, no. 6, pp. 24-25, 2015.

[161] M. Haider A. Shaim and H. E. Elsayed-Ali, "Aluminum multicharged ion generation from laser plasma," *Nuclear Instruments and Methods in Physics Research Section B: Beam Interactions with Materials and Atoms,* vol. 356–357, pp. 75-80, 2015.

[162] J. R. Freeman, S. S. Harilal, and A. Hassanein, "Enhancements of extreme ultraviolet emission using prepulsed Sn laser-produced plasmas for advanced lithography applications," *Journal of Applied Physics,* vol. 110, no. 8, p. 083303, 2011.

[163] J. I. Apiñániz, B. Sierra, R. Martínez, A. Longarte, C. Redondo, and F. Castaño, "Ion Kinetic Energy Distributions and Mechanisms of Pulsed Laser Ablation on Al," *The Journal of Physical Chemistry C,* vol. 112, no. 42, pp. 16556-16560, 2008.

[164] P. Écija *et al.*, "Fundamental processes in nanosecond pulsed laser ablation of metals in vacuum," *Physical Review A,* vol. 77, no. 3, p. 032904, 2008.

[165] S. S. Harilal, C. I. Riju, C. V. Bindhu, V. P. N. Nampoori, and C. P. G. Vallabhan, " Spatial analysis of C_2 band emission from laser produced plasma," *Plasma Sources Science and Technology,* vol. 6, no. 3, p. 317, 1997.

[166] C. A. Bye and A. Scheeline, "Saha-boltzmann statistics for determination of electron temperature and density in spark discharges using an echelle/CCD system," *Applied Spectroscopy,* vol. 47, no. 12, pp. 2022-2030, 1993.

[167] O. A. Nassef and H. E. Elsayed-Ali, "Spark discharge assisted laser induced breakdown spectroscopy," *Spectrochimica Acta Part B: Atomic Spectroscopy,* vol. 60, no. 12, pp. 1564-1572, 2005.

[168] M. Favre *et al.*, "Collision dynamics of laser produced carbon plasma plumes," in *19th Chilean Physics Symposium 2014, November 26- November 28, 2014*, Concepcion, Chile, 2016, vol. 720: Institute of Physics Publishing.

[169] F. O. Bredice, D. J. O. Orzi, D. Schinca, H. Sobral, and M. Villagran-Muniz, "Characterization of pulsed laser generated plasma through its perturbation in an electric field," *IEEE Transactions on Plasma Science,* vol. 30, no. 6, pp. 2139-43, 2002.

[170] D. Fried, G. P. Reck, T. Kushida, and E. W. Rothe, "Electric field enhancement of optical emission from plasma plume generated during ArF excimer photoablation of BaO_2 , Y_2O_3, CuO, and $YBa_2Cu_3O_7$," *Journal of Physics D: Applied Physics,* vol. 24, no. 7, p. 1065, 1991.

[171] S. Takagi, S. Ohtani, K. Kadota, and J. Fujita, "Collision experiment on highly ionized ions using a vacuum spark source," *Nuclear Instruments and Methods in Physics Research,* vol. 213, no. 2, pp. 539-544, 1983.

[172] F. Aumayr and H. Winter, "Potential sputtering," *Philosophical Transactions of the Royal Society of London. Series A: Mathematical, Physical and Engineering Sciences,* vol. 362, no. 1814, p. 77, 2004.

[173] K. Motohashi, "Desorption and sputtering on solid surfaces by low-energy multicharged ions," *Journal of Physics: Conference Series,* vol. 194, no. 1, p. 012061, 2009.

[174] H. Winter and F. Aumayr, "Slow multicharged ions hitting a solid surface: From hollow atoms to novel applications," *Europhysics News,* vol. 33, no. 6, pp. 215-217, 2002.

[175] V. Le Roux *et al.*, "Etching of silicon native oxide using ultraslow multicharged Ar^{q+} ions," *Journal of the Electrochemical Society,* vol. 151, no. 1, pp. 76-79, 2004.

[176] M. Durante and J. S. Loeffler, "Charged particles in radiation oncology," *Nature Reviews Clinical Oncology,* vol. 7, no. 1, pp. 37-43, 2010.

[177] C. L. Cha *et al.*, "Surface smoothing of floating gates in flash memory devices via surface nitrogen and carbon incorporation," *Applied Physics Letters,* vol. 75, no. 3, pp. 355-357, 1999.

[178] N. Munemoto *et al.*, "Direct injection of fully stripped carbon ions into a fast-cycling induction synchrotron and their capture by the barrier bucket," *Physical Review Accelerators and Beams,* vol. 20, no. 8, p. 080101, 2017.

[179] T. J. Kelly, T. Butler, N. Walsh, P. Hayden, and J. T. Costello, "Features in the ion emission of Cu, Al, and C plasmas produced by ultrafast laser ablation," *Physics of Plasmas,* vol. 22, no. 12, p. 123112, 2015.

[180] O. V. Chutko, V. M. Gordienko, I. M. Lachko, B. V. Mar'in, A. B. Savel'ev, and R. V. Volkov, "High-energy negative ions from expansion of high-temperature femtosecond laser plasma," *Applied Physics B,* vol. 77, no. 8, pp. 831-837, 2003.

[181] P. A. VanRompay, M. Nantel, and P. P. Pronko, "Pulse-contrast effects on energy distributions of C^{1+} to C^{4+} ions for high-intensity 100-fs laser-ablation plasmas," *Applied Surface Science,* vol. 127, pp. 1023-1028, 1998.

[182] M. H. A. Shaim, M. M. Rahman, O. Balki, A. Sarkissian, M. L. Korwin-Pawlowski, and H. E. Elsayed-Ali, "Transport line for laser multicharged ion source," *Vacuum,* vol. 137, pp. 14-22, 2017.

[183] A. Lorusso, F. Belloni, D. Doria, V. Nassisi, J. Krása, and K. Rohlena, "Significant role of the recombination effects for a laser ion source," *Journal of Physics D: Applied Physics,* vol. 39, no. 2, p. 294, 2006.

[184] L. Torrisi, F. Caridi, A. Picciotto, D. Margarone, and A. Borrielli, "Particle emission from tantalum plasma produced by 532nm laser pulse ablation," *Journal of Applied Physics,* vol. 100, no. 9, p. 093306, 2006.

[185] B. Verhoff, S. S. Harilal, J. R. Freeman, P. K. Diwakar, and A. Hassanein, "Dynamics of femto and nanosecond laser ablation plumes investigated using optical emission spectroscopy," *Journal of Applied Physics,* vol. 112, no. 9, p. 093303, 2012.

[186] D. Grojo, J. Hermann, and A. Perrone, "Plasma analyses during femtosecond laser ablation of Ti, Zr, and Hf," *Journal of Applied Physics,* vol. 97, no. 6, p. 063306, 2005.

[187] E. G. Gamaly, "The physics of ultra-short laser interaction with solids at non-relativistic intensities," *Physics Reports,* vol. 508, no. 4, pp. 91-243, 2011.

[188] S. S. Harilal, J. R. Freeman, P. K. Diwakar, and A. Hassanein, "Femtosecond Laser Ablation: Fundamentals and Applications," in *Laser-Induced Breakdown Spectroscopy: Theory and Applications*, Berlin, Heidelberg: Springer Berlin, 2014, pp. 143-166.

[189] S. Amoruso *et al.*, "Double-peak distribution of electron and ion emission profile during femtosecond laser ablation of metals," *Applied Surface Science,* vol. 186, no. 1, pp. 358-363, 2002.

[190] S. Amoruso *et al.*, "Thermal and nonthermal ion emission during high-fluence femtosecond laser ablation of metallic targets," *Applied Physics Letters,* vol. 77, no. 23, pp. 3728-3730, 2000.

[191]   N. Farid, S. S. Harilal, H. Ding, and A. Hassanein, "Kinetics of ion and prompt electron emission from laser-produced plasma," *Physics of Plasmas,* vol. 20, no. 7, p. 073114, 2013.

[192]   B. Sallé, O. Gobert, P. Meynadier, M. Perdrix, G. Petite, and A. Semerok, "Femtosecond and picosecond laser microablation: ablation efficiency and laser microplasma expansion," *Applied Physics A,* vol. 69, no. 1, pp. S381-S383, 1999.

[193]   F. F. Chen, "Decay of a plasma created between negatively biased walls," *The Physics of Fluids,* vol. 25, no. 12, pp. 2385-2387, 1982.

[194]   A. K. Geim, "Graphene: Status and Prospects," *Science,* vol. 324, no. 5934, pp. 1530-1534, 2009.

[195]   M. Wu, J. S. Tse, and J. Z. Jiang, "Unzipping of Graphene by Fluorination," *The Journal of Physical Chemistry Letters,* vol. 1, no. 9, pp. 1394-1397, 2010.

[196]   D. Yu and L. Dai, "Self-Assembled Graphene/Carbon Nanotube Hybrid Films for Supercapacitors," *The Journal of Physical Chemistry Letters,* vol. 1, no. 2, pp. 467-470, 2010.

[197]   Y. Lee *et al.*, "Wafer-Scale Synthesis and Transfer of Graphene Films," *Nano Letters,* vol. 10, no. 2, pp. 490-493, 2010.

[198]   A. Reina *et al.*, "Large Area, Few-Layer Graphene Films on Arbitrary Substrates by Chemical Vapor Deposition," *Nano Letters,* vol. 9, no. 1, pp. 30-35, 2009.

[199]   R. Addou, A. Dahal, P. Sutter, and M. Batzill, "Monolayer graphene growth on Ni(111) by low temperature chemical vapor deposition," *Applied Physics Letters,* vol. 100, no. 2, p. 021601, 2012.

[200]   J. Y. Jin, J. Liu, A. W. Paul, V. D. Heide, and W. K. Chu, "Implantation damage effect on boron annealing behavior using low-energy polyatomic ion implantation," *Applied Physics Letters,* vol. 76, no. 5, pp. 574-576, 2000.

[201]   M. Batzill, "The surface science of graphene: Metal interfaces, CVD synthesis, nanoribbons, chemical modifications, and defects," *Surface Science Reports,* vol. 67, no. 3, pp. 83-115, 2012.

[202] C. M. Seah, S.-P. Chai, and A. Mohamed, "Mechanisms of graphene growth by chemical vapour deposition on transition metals," *Carbon,* vol. 70, pp. 1–21, 2014.

[203] Z. Zhang *et al.*, "The Way towards Ultrafast Growth of Single-Crystal Graphene on Copper," *Advanced Science,* vol. 4, no. 9, p. 1700087, 2017.

[204] L. Gao *et al.*, "Repeated growth and bubbling transfer of graphene with millimetre-size single-crystal grains using platinum," *Nature Communications,* vol. 3, p. 699, 2012.

[205] M. Jeong Hun, L. Sung Kyu, and C. Byung Jin, "Local Growth of Graphene by Ion Implantation of Carbon in a Nickel Thin Film followed by Rapid Thermal Annealing," *Journal of the Electrochemical Society,* vol. 159, no. 6, pp. G89-G92, 2012.

[206] L. Baraton *et al.*, "On the mechanisms of precipitation of graphene on nickel thin films," *Europhysics Letters,* vol. 96, no. 4, p. 46003, 2011.

[207] S. Thiele *et al.*, "Engineering polycrystalline Ni films to improve thickness uniformity of the chemical-vapor-deposition-grown graphene films," *Nanotechnology,* vol. 21, no. 1, p. 015601, 2009.

[208] Y. Zhang *et al.*, "Comparison of Graphene Growth on Single-Crystalline and Polycrystalline Ni by Chemical Vapor Deposition," *The Journal of Physical Chemistry Letters,* vol. 1, no. 20, pp. 3101-3107, 2010.

[209] M. Eizenberg and J. M. Blakely, "Carbon monolayer phase condensation on Ni(111)," *Surface Science,* vol. 82, no. 1, pp. 228-236, 1979.

[210] J. C. Shelton, H. R. Patil, and J. M. Blakely, "Equilibrium segregation of carbon to a nickel (111) surface: A surface phase transition," *Surface Science,* vol. 43, no. 2, pp. 493-520, 1974.

[211] P. Dharmaraj, P. S. Venkatesh, P. Kumar, K. Asokan, and K. Jeganathan, "Direct growth of few layer graphene on SiO2 substrate by low energy carbon ion implantation," *RSC Advances,* vol. 6, no. 103, pp. 101347-101352, 2016.

[212] O. Balki, M. M. Rahman, M. H. Abdel-Fattah, and H. E. Elsayed-Ali, "Carbon multicharged ions emission from femtosecond laser plume," *Optics & Laser Technology,* vol. 120, p. 105694, 2019.

[213] B. Ingham and M. F. Toney, "1 - X-ray diffraction for characterizing metallic films," in *Metallic Films for Electronic, Optical and Magnetic Applications*, K. Barmak and K. Coffey, Eds.: Woodhead Publishing, 2014, pp. 3-38.

[214] A. C. Ferrari *et al.*, "Raman Spectrum of Graphene and Graphene Layers," *Physical Review Letters,* vol. 97, no. 18, p. 187401, 2006.

[215] B. K. Tay, X. Shi, H. S. Tan, and D. H. C. Chua, "Investigation of tetrahedral amorphous carbon films using x-ray photoelectron and Raman spectroscopy," *Surface and Interface Analysis,* vol. 28, no. 1, pp. 231-234, 1999.

[216] A. Dychalska, P. Popielarski, W. Franków, K. Fabisiak, K. Paprocki, and M. Szybowicz, "Study of CVD diamond layers with amorphous carbon admixture by Raman scattering spectroscopy," *Materials Science-Poland,* vol. 33, pp. 799-805, 2015.

[217] M. Yoshikawa, Y. Mori, M. Maegawa, G. Katagiri, H. Ishida, and A. Ishitani, "Raman scattering from diamond particles," *Applied Physics Letters,* vol. 62, no. 24, pp. 3114-3116, 1993.

[218] M. Yoshikawa *et al.*, "Raman scattering from nanometer-sized diamond," *Applied Physics Letters,* vol. 67, no. 5, pp. 694-696, 1995.

[219] R. Belka, M. Suchanska, E. Czerwosz, and J. Keczkowska, "Raman studies of Pd-C nanocomposites," *Central European Journal of Physics,* vol. 11, no. 2, pp. 245-250, 2013.

[220] H. Kuzmany, R. Pfeiffer, M. Hulman, and C. Kramberger, "Raman spectroscopy of fullerenes and fullerene-nanotube composites,", *Philosophical transactions. Series A, Mathematical, physical, and engineering sciences,* vol. 362, no. 1824, pp. 2375-406, 2004.

[221] A. C. Ferrari and J. Robertson, "Resonant Raman spectroscopy of disordered, amorphous, and diamondlike carbon," *Physical Review B,* vol. 64, no. 7, p. 075414, 2001.

[222] C. Casiraghi, A. C. Ferrari, and J. Robertson, "Raman spectroscopy of hydrogenated amorphous carbons," *Physical Review B,* vol. 72, no. 8, p. 085401, 2005.

[223] Y. Wang, L. Wang, Y. Yu, K. Mu, and X. Wang, "DLC Film Fabrication on the Inner Surface of a Cylinder by Carbon Ion Implantation," *IEEE Transactions on Plasma Science,* vol. 34, no. 4, pp. 1116-1120, 2006.

[224] L. Liu, T. Wang, J. Huang, Z. He, Y. Yi, and K. Du, "Diamond-like carbon thin films with high density and low internal stress deposited by coupling DC/RF magnetron sputtering," *Diamond and Related Materials,* vol. 70, pp. 151-158, 2016.

[225] D. D. L. Chung, "Review Graphite," *Journal of Materials Science,* vol. 37, no. 8, pp. 1475-1489, 2002.

[226] A. C. Ferrari and J. Robertson, "Interpretation of Raman spectra of disordered and amorphous carbon," *Physical Review B,* vol. 61, no. 20, pp. 14095-14107, 2000.

[227] H. Liu, Q. Xu, C. Wang, X. Zhang, and B. Tang, "Investigating the microstructure and mechanical behaviors of DLC films on AISI52100 bearing steel surface fabricated by plasma immersion ion implantation and deposition," *Surface and Coatings Technology,* vol. 228, pp. S159-S163, 2013.

[228] H. Pang, X. Wang, G. Zhang, H. Chen, G. Lv, and S. Yang, "Characterization of diamond-like carbon films by SEM, XRD and Raman spectroscopy," *Applied Surface Science,* vol. 256, no. 21, pp. 6403-6407, 2010.

[229] T. Santra, T. Bhattacharyya, P. Patel, F. G. Tseng, and T. Barik, "Diamond, diamond-like carbon (DLC) and diamond-like nanocomposite (DLN) thin films for MEMS applications," Microelectromechanical Systems and Devices, Springer, 2011.

[230] K. Liu, F. Lu, K. Li, Y. Xu, and C. Ma, "Synthesis of turbostratic graphene by direct carbon ions implantation on LiNbO3," *Applied Surface Science,* vol. 493, pp. 1255-1259, 2019.

[231] A. Kaniyoor and S. Ramaprabhu, "A Raman spectroscopic investigation of graphite oxide derived graphene," *AIP Advances,* vol. 2, no. 3, p. 032183, 2012.

[232] R. Kumar *et al.*, "Graphene as a transparent conducting and surface field layer in planar Si solar cells," *Nanoscale Research Letters,* vol. 9, no. 1, p. 349, 2014.

[233] Z. Ni, Y. Wang, T. Yu, and Z. Shen, "Raman spectroscopy and imaging of graphene," *Nano Research,* vol. 1, no. 4, pp. 273-291, 2008.

[234] D. G. Matei *et al.*, "Functional Single-Layer Graphene Sheets from Aromatic Monolayers," *Advanced Materials,* vol. 25, no. 30, pp. 4146-4151, 2013.

[235] D. Graf *et al.*, "Spatially Resolved Raman Spectroscopy of Single and Few-Layer Graphene," *Nano Letters,* vol. 7, no. 2, pp. 238-242, 2007.

[236] R. J. Nemanich and S. A. Solin, "First- and second-order Raman scattering from finite-size crystals of graphite," *Physical Review B,* vol. 20, no. 2, pp. 392-401, 1979.

[237] M. A. Tamor and W. C. Vassell, "Raman ''fingerprinting'' of amorphous carbon films," *Journal of Applied Physics,* vol. 76, no. 6, pp. 3823-3830, 1994.

[238] J. C. Charlier, P. C. Eklund, J. Zhu, and A. C. Ferrari, "Electron and Phonon Properties of Graphene: Their Relationship with Carbon Nanotubes," in *Carbon Nanotubes: Advanced Topics in the Synthesis, Structure, Properties and Applications*, Topics in Applied Physics. A. Jorio, G. Dresselhaus, and M. S. Dresselhaus, Eds. Springer-Verlag, Berlin/Heidelberg, 2008, vol. 111, pp. 673-709.

[239] N. Shimodaira and A. Masui, "Raman spectroscopic investigations of activated carbon materials," *Journal of Applied Physics,* vol. 92, no. 2, pp. 902-909, 2002.

[240] M. Qi *et al.*, "Effect of various nitrogen flow ratios on the optical properties of (Hf:N)-DLC films prepared by reactive magnetron sputtering," *AIP Advances,* vol. 7, no. 8, p. 085012, 2017.

[241] S. S. Hadinata, M. T. Lee, S. J. Pan, W. T. Tsai, C. Y. Tai, and C. F. Shih, "Electrochemical performances of diamond-like carbon coatings on carbon steel, stainless steel, and brass," *Thin Solid Films,* vol. 529, pp. 412-416, 2013.

[242] R. K. Roy, B. Deb, B. Bhattacharjee, and A. K. Pal, "Synthesis of diamond-like carbon film by novel electrodeposition route," *Thin Solid Films,* vol. 422, no. 1, pp. 92-97, 2002.

[243] A. C. Ferrari, "Raman spectroscopy of graphene and graphite: Disorder, electron–phonon coupling, doping and nonadiabatic effects," *Solid State Communications,* vol. 143, no. 1, pp. 47-57, 2007.

[244] M. A. Pimenta, G. Dresselhaus, M. S. Dresselhaus, L. G. Cançado, A. Jorio, and R. Saito, "Studying disorder in graphite-based systems by Raman spectroscopy," *Physical Chemistry Chemical Physics,* vol. 9, no. 11, pp. 1276-1290, 2007.

[245] D. R. Lenski and M. S. Fuhrer, "Raman and optical characterization of multilayer turbostratic graphene grown via chemical vapor deposition," *Journal of Applied Physics,* vol. 110, no. 1, p. 013720, 2011.

[246] E. H. Martins Ferreira *et al.*, "Evolution of the Raman spectra from single, few, and many-layer graphene with increasing disorder," *Physical Review B,* vol. 82, no. 12, p. 125429, 2010.

[247] A. C. Ferrari, "Determination of bonding in diamond-like carbon by Raman spectroscopy," *Diamond and Related Materials,* vol. 11, no. 3, pp. 1053-1061, 2002.

[248] K. A. H. Al Mahmud, M. Varman, M. A. Kalam, H. H. Masjuki, H. M. Mobarak, and N. W. M. Zulkifli, "Tribological characteristics of amorphous hydrogenated (a-C:H) and tetrahedral (ta-C) diamond-like carbon coating at different test temperatures in the presence of commercial lubricating oil," *Surface and Coatings Technology,* vol. 245, pp. 133-147, 2014.

[249] H. Zhu, K. Tongchun, B. Zhu, S. Lei, Z. Liu, and S. Ringer, "Flame synthesis of carbon nanostructures on Ni-plated hardmetal substrates," *Nanoscale Research Letters,* vol. 6, p. 331, 2011.

[250] M. Cui, J. Pu, J. Liang, L. Wang, G. Zhang, and Q. Xue, "Corrosion and tribocorrosion performance of multilayer diamond-like carbon film in NaCl solution," *RSC Advances,* vol. 5, no. 127, pp. 104829-104840, 2015.

APPENDICES
APPENDIX A

VACUUM CHAMBER AND ITS COMPONENTS

Characterization of the generated MCIs are carried by several system components. The TOF measurements of the incident ions is accomplished by a Faraday cup. The multicharged ion species are further distinguished and collimated by an electrostatic ion energy analyzer and an Einzel lens, respectively.
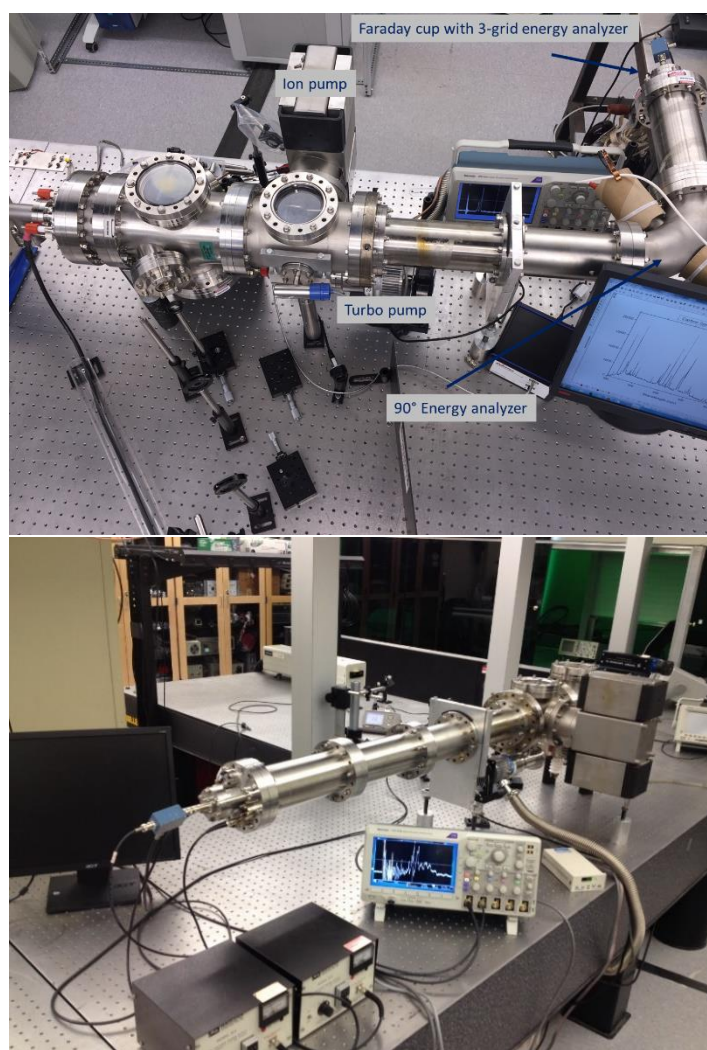
Fig. A. 1 Main ion generation and processing chamber with and without EIA installed.

Operation of a vacuum chamber requires certain steps in order to maintain the lifecycle of the pumps longer and the chamber clean, free from contaminants. Before turning on the pumps, make sure all the power supplies for chamber components are in off position. Carefully, seal the chamber viewports, flanges. Any new installation of the components should be done by cleaning them with isopropyl alcohol. Prevent use of acetone with vacuum components. When using and placing copper gaskets, make sure that you wear gloves, otherwise the system will get contaminated. Once all the components of the vacuum chamber are sealed, pump down sequence can start.
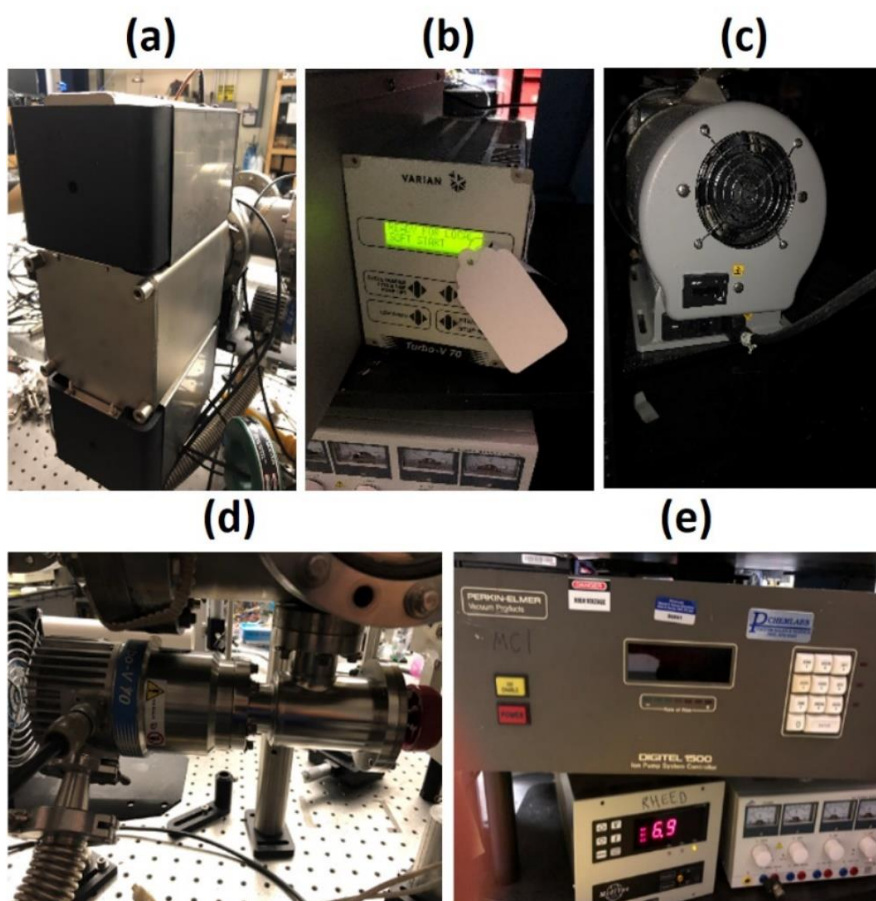
Fig. A. 2 Vacuum pumps and their controllers. (a) ion pump, (b) turbo pump controller, (c) molecular pump, (d) turbo pump, (e) ion pump controller.

Closing the system

1-   Turn on the mechanical pump&turbo pump (Check hose gaskets and turbo pump ventilation gasket are sealed, and tight to prevent leaks).

2-   When the turbo pump reaches its maximum rotation speed, cold cathode gauge controller can be turned on to monitor the pressure change over time. In a clean, leak-free chamber, the pressure should go down to ~10^{-7} Torr, depending on the chamber size, and pump capacity.

3-   If the pressure is not going down, check your system for leaks, turbo controller screen for current and rotation speed values. Always use cooling with turbo pump which can be air or water cooling. This will maintain the turbo temperature within its operation range.

4-   If the pressure values are within 10^{-7} Torr, it is safe to turn on the ion pump. It usually takes several hours, if the chamber is not baked recently, to reach this level of pressure.

5-   Once the ion pump is turned on, close the gate valve between turbo pump and the chamber.

6-   You can now turn off the molecular and turbo pumps.

7-   The ion pump should take the pressure down to low 10^{-8} - high 10^{-9} Torr values.

Opening the system

1-   Turn on the mechanical pump&turbo pump. Once the turbo reaches the maximum speed, slowly open the gate valve that seals the turbo from the chamber.

2-   Monitor the ion pump display for instant pressure changes. Once the pressure is stabilized, turn off the ion pump.

3-   At this step, the turbo and molecular pump can be turned off instantaneously.

4-   The turbo pump has a ventilation valve, which will immediately reduce the speed of the rotating blades.

5-   Never try to open the chamber while the pumps are still running. Always monitor the pressure values, and make sure the pumps are completely stopped. Otherwise, particles from the air will crash to the high-speed rotating blades inside turbo pump, and cause permanent damage to the blades.

Fig. A. 3 Faraday cup with its components.

Fig. A. 4 AutoCad drawings of Faraday cup components.

Fig. A. 5 AutoCad drawings of Faraday cup components.
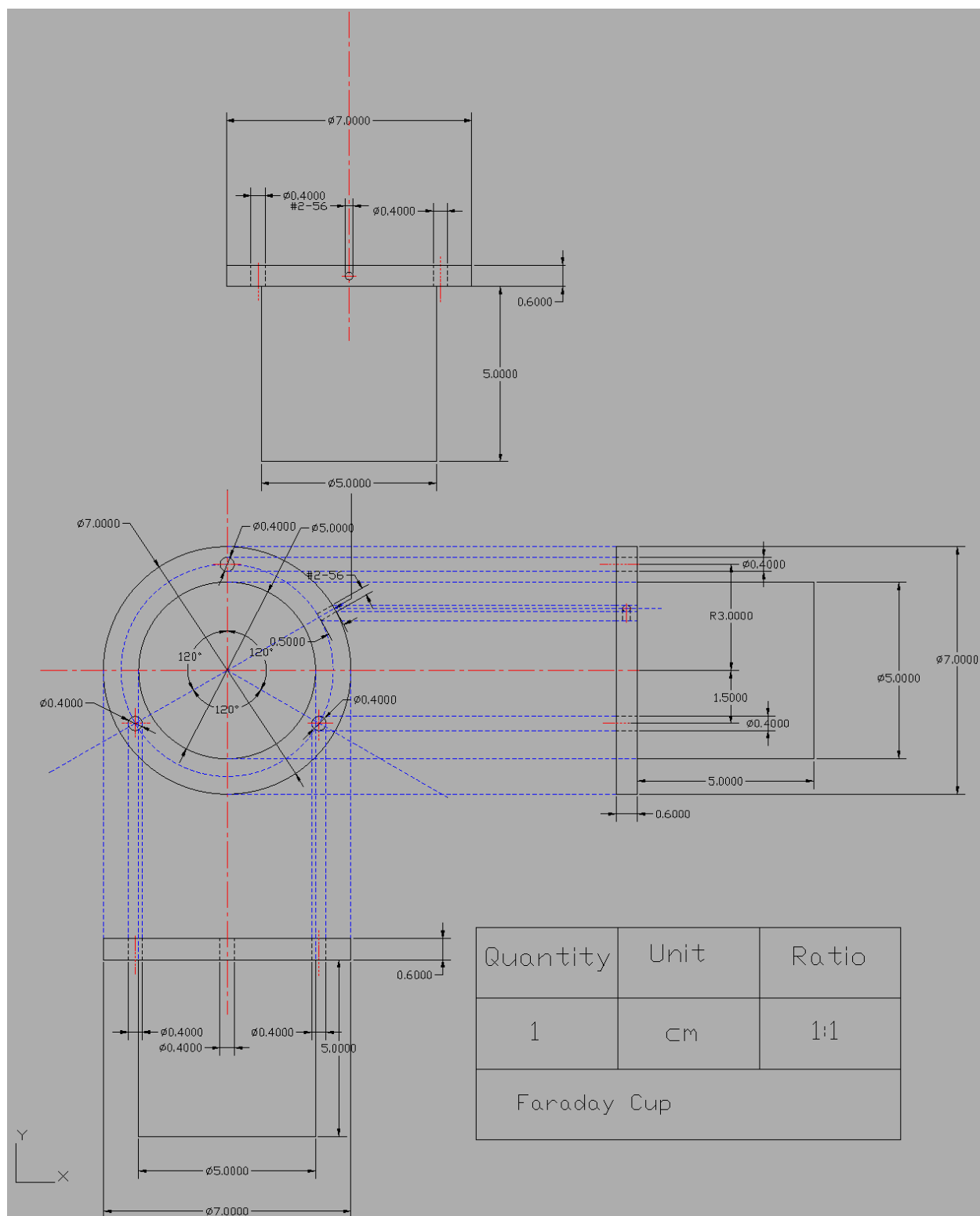
Fig. A. 6 AutoCad drawings of Faraday cup components.
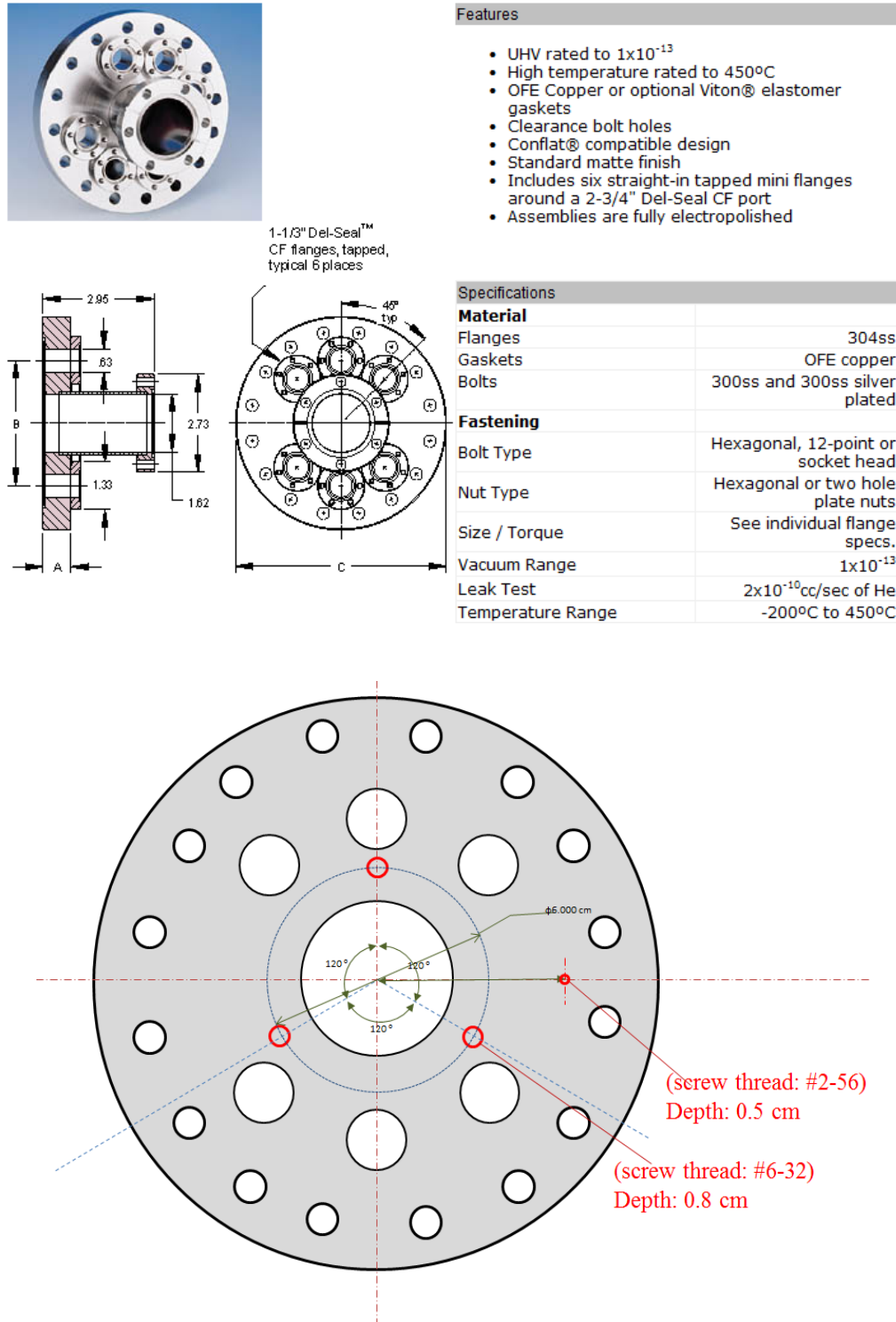
Fig. A. 7 Multiport flange drawings from the manufacturer website.
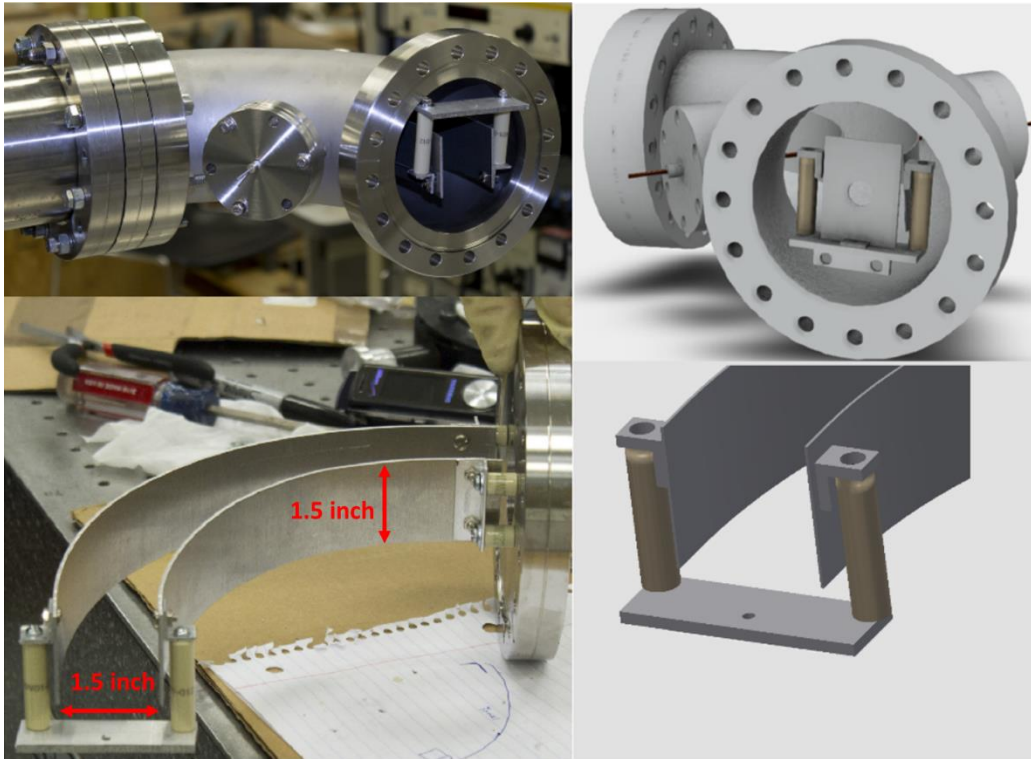
Fig. A. 8 Electrostatic energy analyzer. AutoCad drawings and assembled components.

To selectively choose the carbon ions with specific energy, we used a radially designed analyzer. The EIA has a radial cylindrical design with a deflection angle of 90°. The energy resolution $\Delta E/E$ was determined to be 7%−10%
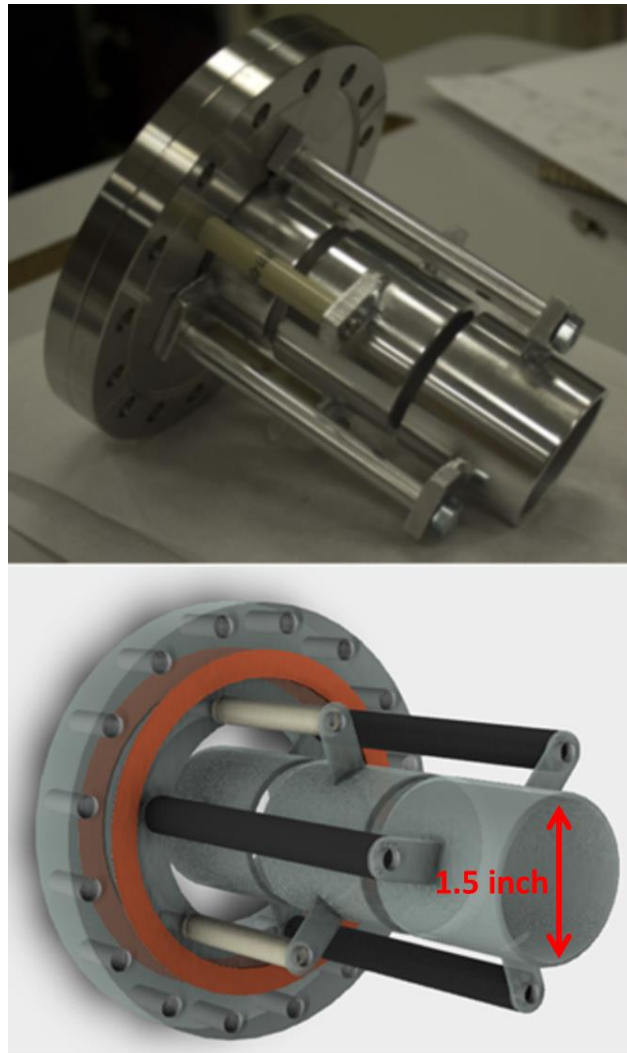
Fig. A. 9 Image of the completed Einzel lens assembly and its AutoCad drawing.

An Einzel lens is a three-element lens with the outer two electrodes held at the same potential (in our case, grounded), while the central electrode is held at a potential that can be varied for focusing at different distances. Einzel lens does not vary the energy of the charged particles. The electric field focuses the ion beam, reducing the ion lost in the transport line due to the divergence in the ion beam.

Simulation
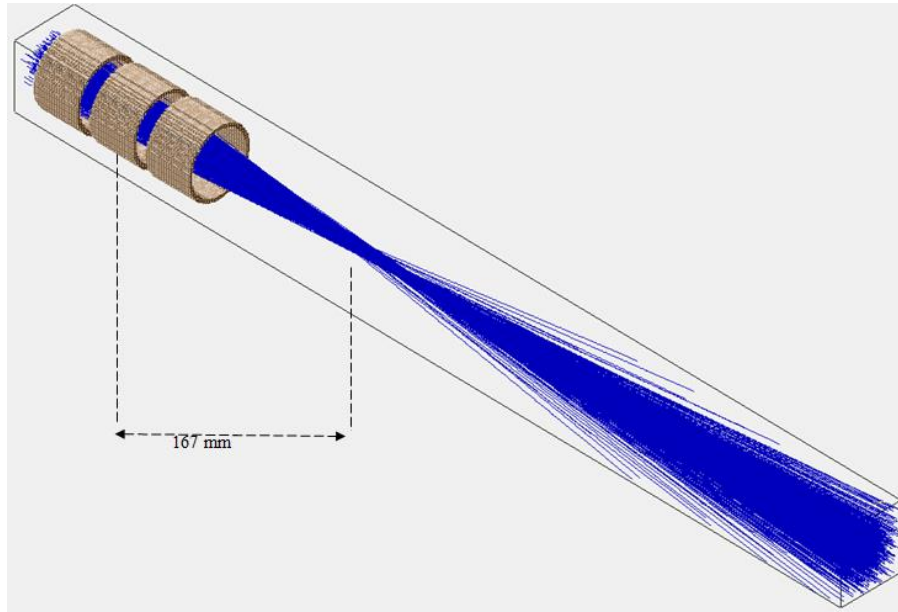
Fig. A. 10 Ion trajectory of MCI with Einzel lens focusing. MCIs are focused with applied voltage of -3.5 kV.
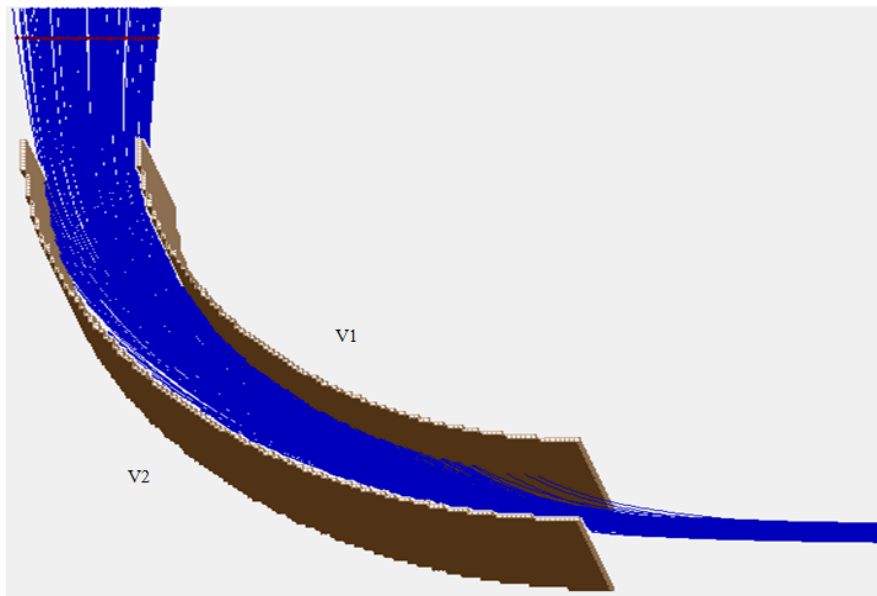
Fig. A. 11 MCI deflected by EIA. (a) Applied voltage to the EIA are V1= -500 V, V2= 500 V.

APPENDIX B

MAGNETRON SPUTTER COATER (ATC ORION SERIES)

Before preparing the substrate, make sure that the pressure of the chamber is the atmospheric pressure which is equal to 7.6×10^2 Torr. Check the pressure at 937B gauge controller screen. If the chamber is under vacuum (the pressure is below atmospheric pressure), you can start venting the chamber before opening the substrate holder.

Venting the Chamber

- Open the nitrogen cylinder (two valves: top and side).

- Open the ventilation valve.

- Turn off the vacuum pump switch.

- Once the pressure reaches atmospheric pressure, close the vent and nitrogen cylinder valve.

Fig. B. 1 Gas tanks located behind the sputter system.

Fig. B. 2 Turbo pump turn ON/OFF switch on the upper panel.

Preparation of Substrate

• Take out the substrate holder from the chamber.

• Clean the substrate holder with ethanol.

• Clean substrates before loading it on the substrate holder.

• Use the clips to hold the substrates.

Pump down the System

• Open the gate valve to open the deposition chamber to the pumps.

• Turn on the vacuum pump switch, the pressure on 937B gauge controller will start to decrease.

• When the pressure is 10^{-4} Torr, turn on ion gauge.

• Wait till the pressure reaches to approximately 10^{-8} Torr.

Deposition Stage

Deposition can start either by manually setting the parameters or automatically by giving certain commands by computer. Follow steps for manual deposition or automated deposition.

Manual Deposition

- Turn the control switch (located at right side below the heater controller) to hand mode.

- Make sure to load the desired target before.

- Turn on substrate rotation switch.

- Turn on the heater if substrate temperature is required.

Fig. B. 3 Substrate rotation switch and manual control section.

Fig. B. 4 Heater switch and its display.

- Connect DC/RF power cable to the target.

- Turn ion gauge off because it doesn't work at deposition pressure range.

- Open the argon gas cylinder valves (top and side ones).

- Turn the Gas1 switch to OPEN.

- Once the Gas1 shutter is open, open the mfcx fully to control the flow rate of gas.

- N.B. The pressure will increase gradually.

- Close the gate valve till the pressure goes to 3×10^{-2} Torr.

- Turn on the desired power supply.

- Check the purple plasma through the window of the chamber.

- If the plasma is observed, open the gate valve till the pressure reaches to 3×10^{-3} Torr because it is the deposition pressure.

- Make sure the plasma exists at the deposition pressure. And close the shutter of viewport.

- Set the power required for the deposition.

- Once the power reaches the set power, turn the shutter switch to OPEN (SH1 for target 1, SH2 for target 2, SH3 for target 3.

- Keep the shutter open till the desired deposition is done.

- Once the deposition is done, turn the shutter switch to CLOSE.

Turn off the system

- Turn OFF the heater if it was turned on.

- Stop rotation of the sample (substrate).

- Open the gate valve.

- Turn OFF the power supply.

- Close the button named "mfcx".

- Turn the Gas1 switch to CLOSE. Close the argon gas cylinder valves (top and side ones).

- Wait till the temperature reaches to 25 ºC – 50 ºC.

- Follow steps to vent the chamber and get your samples.

APPENDIX C

FS LASER

Millenia Laser

Millenia laser is operated at 10.0 W output. Make sure to turn ON the chiller before operation of this laser. The controller panel of the power supply has a key switch located in the back and a main switch for power. Both key and the main switch should be kept at ON positions at all times. The power supply of this laser should be always kept ON. Chiller can be turned OFF after proper cooling time is reached (30 min recommended.) The chiller will need to have replacement water in case of operation failure (it will beep if the water level is below the operation range). It is recommended to replace the tank water every 3 months (distilled water).
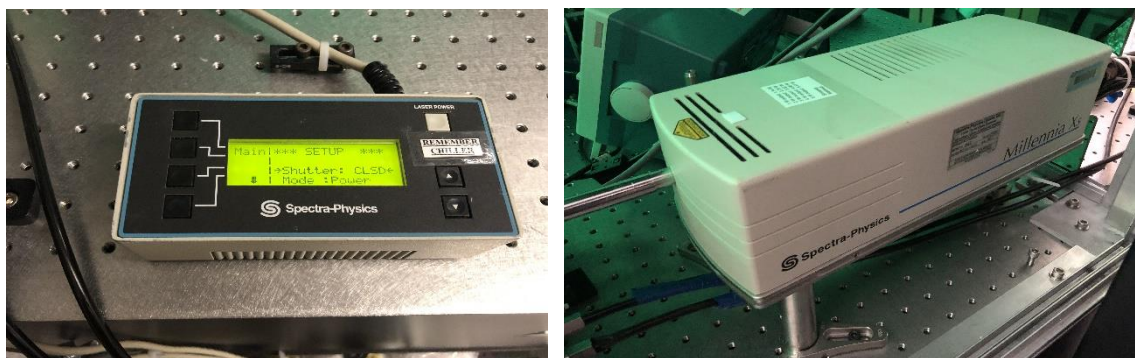
Fig. C. 1 Millenia laser head and its controller.

Tsunami Laser

In order to mode-lock the laser, the two slit knobs (bandwidth and wavelength) and the mirrors located in the back (labelled as horizontal and vertical in the picture below) can be adjusted. This can be done if the power level is below 0.9 W at the output. Operator should wait at least 1 hour for the laser stabilization before touching any knobs. The safe margins when

changing the knob positions are labelled on top of the laser head. Monitor the output beam at the optical spectrometer screen, and gently knock on the Tsunami body in order to successfully mode-lock the laser beam. The beam profile will become broadened. The chiller (LAIRD) is located under the table, and should be always ON when operating this laser.
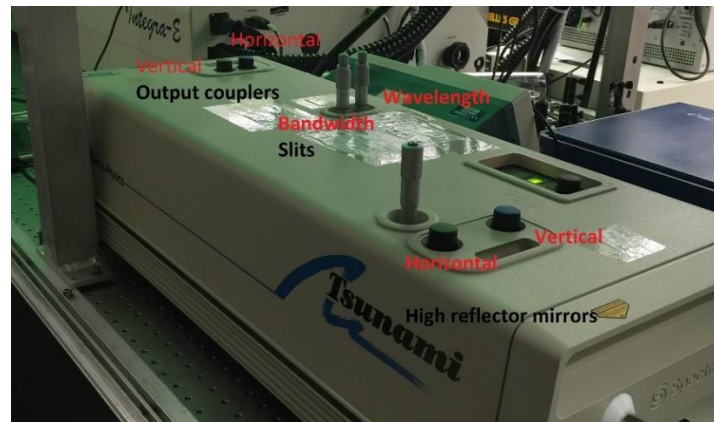
Fig. C. 2 Tsunami laser head. Avoid touching output couplers. High reflector mirrors and slits can be used for fine tuning of the mode-locking parameters. Refer to the notes labelled on laser head.
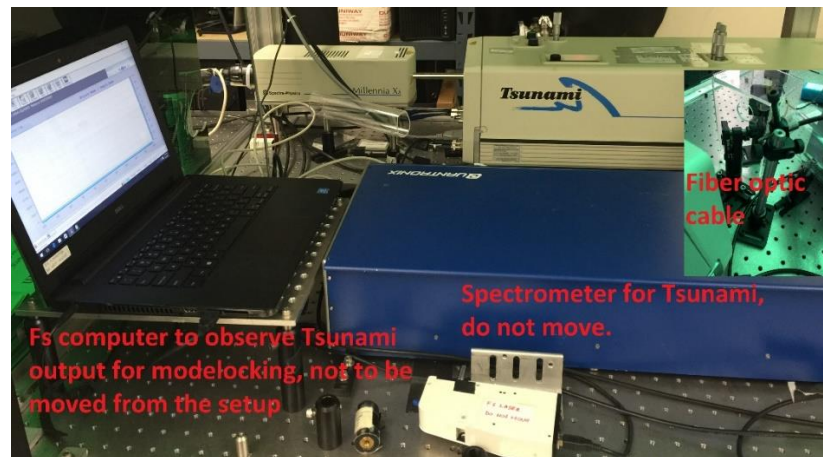
Fig. C. 3 Computer and the spectrometer to observe Tsunami laser output. There is no password on this computer. Spectrometer is dedicated to observe the mode-locking of Tsunami laser and should not be moved or used elsewhere.

Once the Millenia laser is turned on and its shutter is open, the Tsunami laser will start lasing (chiller still need to be turned on manually). At this point, we recommend a wait for 1-2 hours before running any systems. This time is required for stable mode-locked operation. No changes (adjustments, alignments, etc…) should be done. Otherwise, the sensitive settings will be lost and it will take long time to go back to the proper alignment settings in the Tsunami laser. The modelocking procedure is as follows:

1.   Normally, when the Millenia power is set to 10 W output, this energy is enough to self-modelock the system. In this case, the Tsunami output reading is more than 800 mW. Slight adjustments to the reflective back mirror (green, specifically) will change the output power. Once the output power level of > 900 is reached, the modelocking should self-occur. If not, the slit positions should be adjusted by monitoring the optical spectrometer signal as it shifts in wavelength. The position of the proper mode-locking mechanism is around 750-800 nm. The modelocking can be screened either from the spectrometer screen, or from the photodiode signal from the Tsunami, connected to the oscilloscope.

Terra Laser

The manual for this laser is straightforward and should be followed for diagnostic and parameter change conditions. Otherwise, the operation is as follows:

Operation

1.   Switch the key to ON position

2.   Push start button (SEL).

3.   The laser and its chiller will automatically turn on. In order to start the lasing for the green laser (Terra), the Tsunami laser need to be mode locked, otherwise the shutter will activate and stop the lasing.

4.   Once the Tsunami laser is mode locked, a timing frequency for synchronization between the Tsunami and green laser inside the Regen is detected at the controller screen as 1 kHz.

5.   If not, out of range error will be displayed.

6.   When the mode-lock is achieved, the green laser will start lasing and at the predefined current setting, it will provide enough power for amplification.

7.   The divider, Delay A, and Delay B are currently being used. The divider is set to 8040 so that we have an output of 1 kHz after the Regen. It is not recommended to change this setting.

8.   Delay A (~220-250 V), and Delay B (~180-210 V) are used to modulate the envelope signal.

9.   Knobs named VA,VB, and VC are used to control the Pockels cell parameters.

Fig. C. 4 (a), (b) Terra laser controller interface, (c) the chiller, (d) the controller panel for setting up delay, Pockels cell parameters, and frequency selection. (e) Close look of the controller panel.
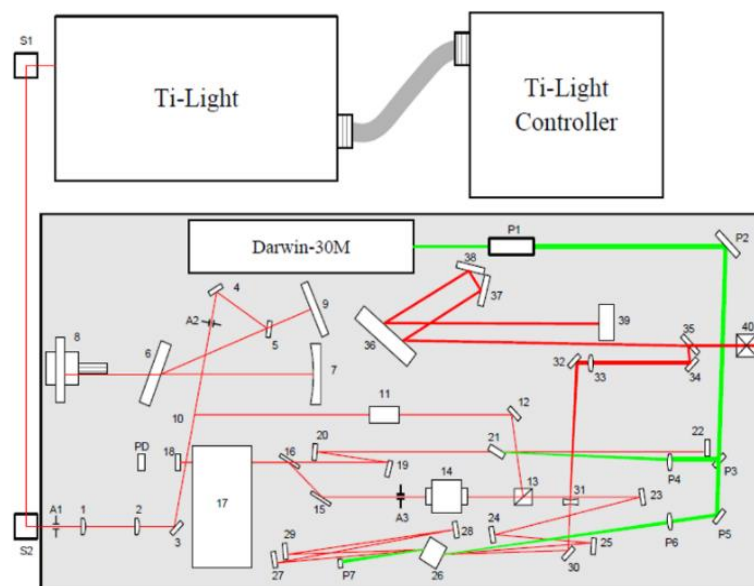
This is from the manufacturer manual, only for basic referencing.

Stretched output, to Faraday rotator

Input (Tsunami laser, check polarization)

Seed&1, 2, 3, 4, 5, 6, 7, 8, 9, 10, Output
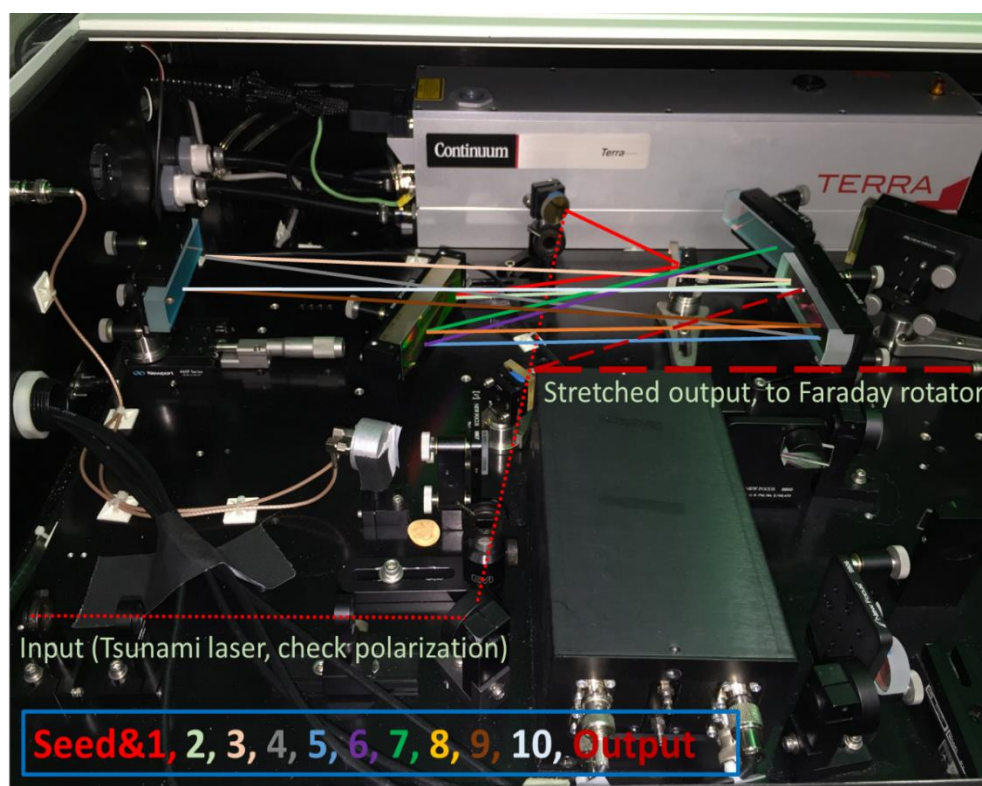
Fig. C. 5 Beam path for stretcher section of the Regen.

Operation in Rheed

1.   The green laser (pump, Terra) output goes to a beam expander. The beam gets reflected from the 45° mirror and goes to a beam splitter. We block the passing beam for now, as we are not interested in this part, yet. We will remove the block once the Regen alignment and testing is complete.

2.   The intense pump laser beam goes to the crystal where it is absorbed, while being focused. At this intensity, water cooling is necessary to balance the temperature. Chiller must be maintained well.

3.   Regen signal will be basically a Q-switch laser when there is no seed laser from the oscillator (the big envelope.) The modulation of this envelope signal arises from the injection (seed).

4.   The injection laser looks exactly the same at the Faraday rotator entrance (end of stretcher). However, spectral modes are no longer locked in their superposition, the wavelength is now stretched, and the pulse width is now ~2 ps, instead of being ~60-100 fs.

5.   The Faraday rotator changes the polarization of the beam by rotating it 90° based on the magnetic field. This is the beam that Regen will amplify.

6.   The beam is reflected to the polarizing cube (has an interface that lets vertical polarization to reflect, horizontal polarization to go through), and is reflected to the strong magnet. The importance of both having Faraday rotator and this polarizing cube is to protect the oscillator from having the beam reflected back and to direct it to Regen.
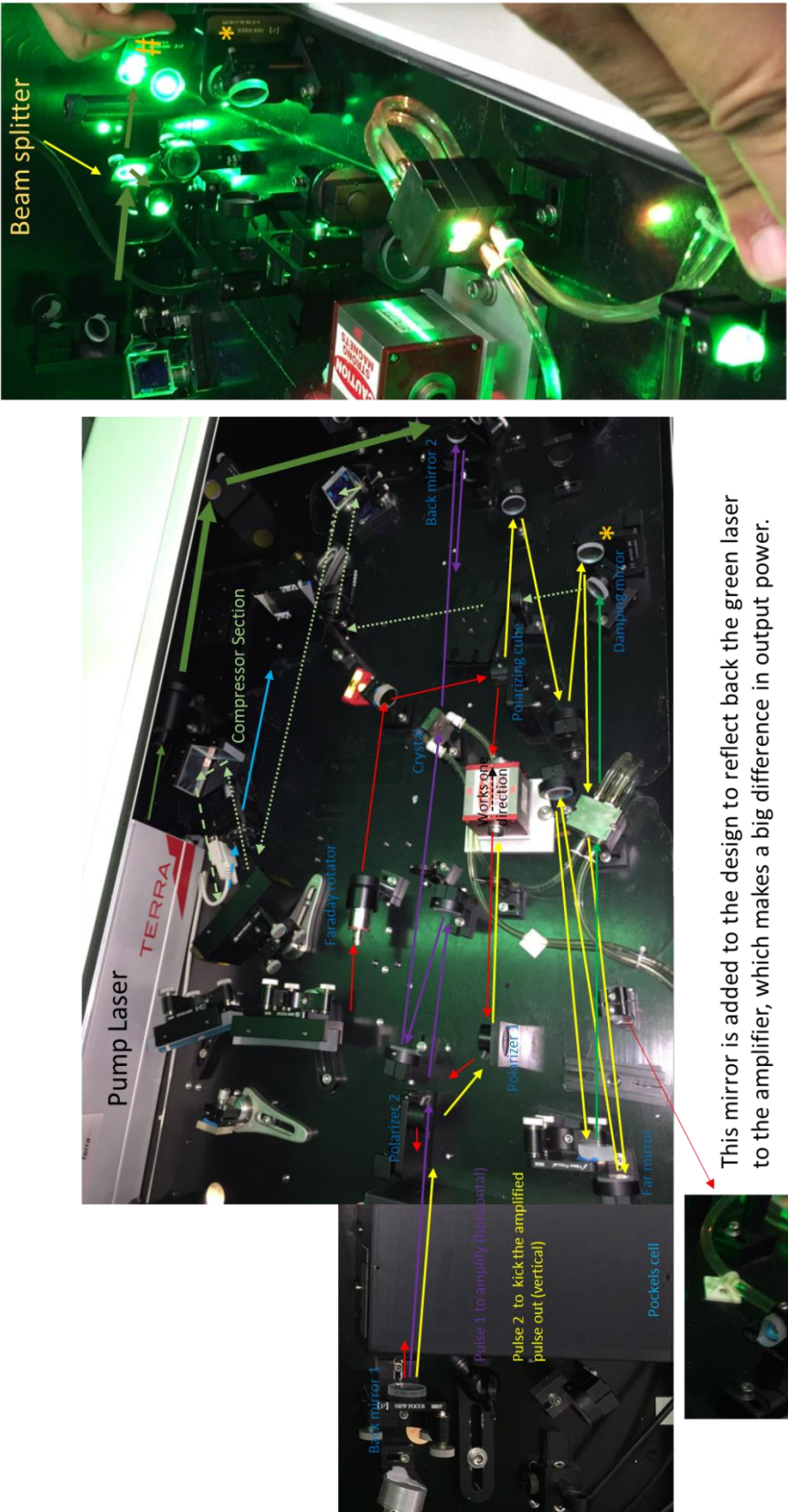
Fig. C. 6 Beam path inside the Regen.

7.   The beam after (and before) the strong magnet has a vertical polarization. This magnet is only used once the beam is dumped. The beam coming from the polarizing cube does not experience any changes at this point. The beam goes inside the Pockels cell (where only one pulse is selected to be amplified.) and gets reflected from the back mirror (red path). Technically, it would come out back to the polarizing cube with no changes in the polarization (still vertical) and would be reflected back, with no amplification (from the same path).

8.   An applied pulse to the Pockels cell will pick up one of the injected pulses (from the 80 MHz signal) and it will make it horizontal (90° rotation). So, the back mirror will now reflect one of the pulses back with this horizontal polarization, which will change the path of that particular selected pulse (on polarizer 2 (Fig. C.6), it will go thru), the rest of the 80 MHz signal will still be deflected through polarizer 1.

9.   The selected horizontal beam gets reflected from two mirrors into the crystal and to the mirror in the back. As long as the beam is horizontal, the back mirror 2 (Fig. C.6) will reflect it back to the crystal and through the polarizer 2 to the back mirror 1 (end cavity mirror, behind it, there is a photodiode with a piece of paper for attenuation), having this multi pass back and forth many times, getting amplified, giving the modulation (purple path).

10.   Once it is amplified enough, the beam needs to be taken out of the Regen (dumped). To do this, another pulse needs to be applied to change its polarization back to vertical. However, in this case, normally it would have been kicked out to the stretcher. The Faraday rotator works in one direction and flips the polarization again (to horizontal).

11.   The beam goes to the cube. The Faraday rotators are useful as waveplates, because they can work in one direction only. The beam goes through the polarizing cube to the mirror in the back (yellow path). The power should be measured in front of this mirror if out of the Regen power

need to be tested. No shiny materials should be used inside the laser path. It is also suggested to take care of the wires (power meter) because the green laser is so powerful, it will damage the wire, and create smoke, with a potential to damage the optics. In our initial alignment, the power out of the Regen was measured as 0.60 W. What means is that 2 mJ output should be observed (1 kHz signal).

12.   If any alignment should be carried out for the Regen, two back mirrors are the first choice (Fig. C.6). However, if a good ns pulse is coming out of the Regen, then the injection is the one that needs alignment. And injection alignment is basically done by the mirror that is after the Faraday rotator.

13.   The mirror before the Faraday rotator (inside the stretcher part), is only to guide the beam through the Faraday rotator. The beam is again reflected from this mirror to another two mirrors, then goes through the crystal and to the far mirror (the beam needs to be extremely at the left edge of this mirror, refer Fig. C.6 and follow the instructions to determine which mirror this is).

14.   From this mirror, the beam is again guided through two mirrors, and goes through the crystal to the damping mirror. This mechanism is double pass mechanism.

15.   Beam reflects from this damping mirror to the lens.

16.   The small mirror is added to the design to recover the green laser by reflecting it back to the amplifier. This makes a big difference on the amplification process and increases the power. The reason having multiple mirrors in this section is to minimize the angle between the Regen beam and the green laser (0° is the ideal angle) for a complete overlap (maximum overlap).

17.   The Regen power now can be measured again after the damping mirror and the output lens. The power measurement should be very close to the initial measured value (0.6 W). Then release

the green pump laser (by removing the block, placed after the beam splitter of pump laser), and measure the power at the same location.

18. But the best way to align the Regen is measuring the power between the far mirror and the special mirror that reflects the green laser back to the amplifier. At this point, the energy is reflected for one pass. One pass would bring the power from 0.6 W to 1.7 W, after two passes, the initial alignment resulted in 2.7 W.

19. To maximize the energy at this point, injection mirror (*) and the mirror for seed (green) laser (#) should be touched, refer Fig. C.6.

20. Follow the manual for operating the spectrometer to detect the modelocking.
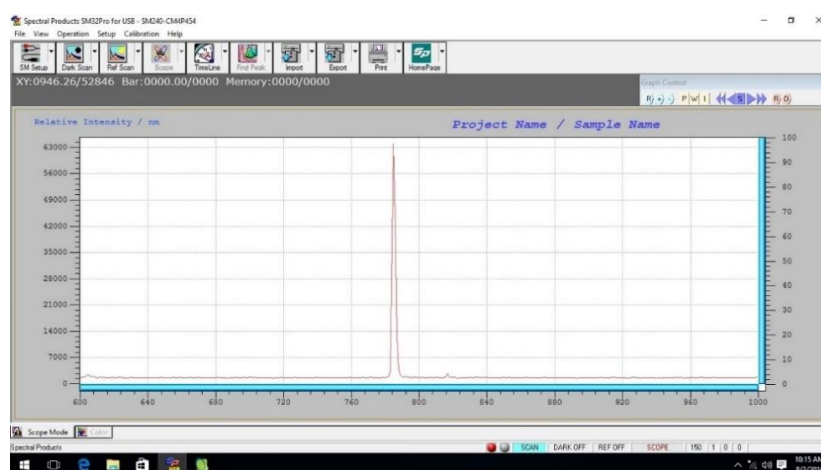
Fig. C. 7 Typical seed laser signal before modelock occurs.
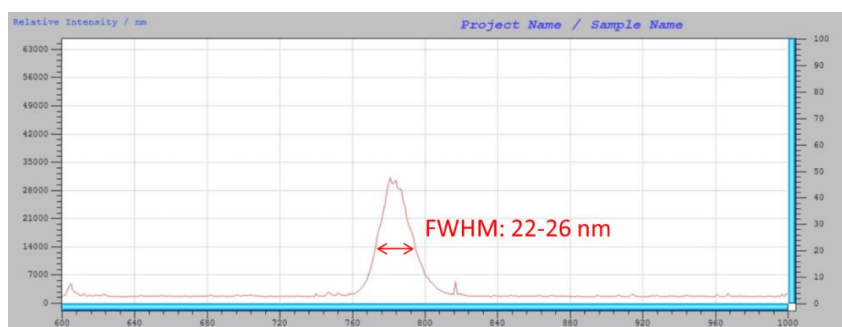
Fig. C. 8 Typical seed laser signal after modelock occurs. Recommended FWHM is 12-15 nm.
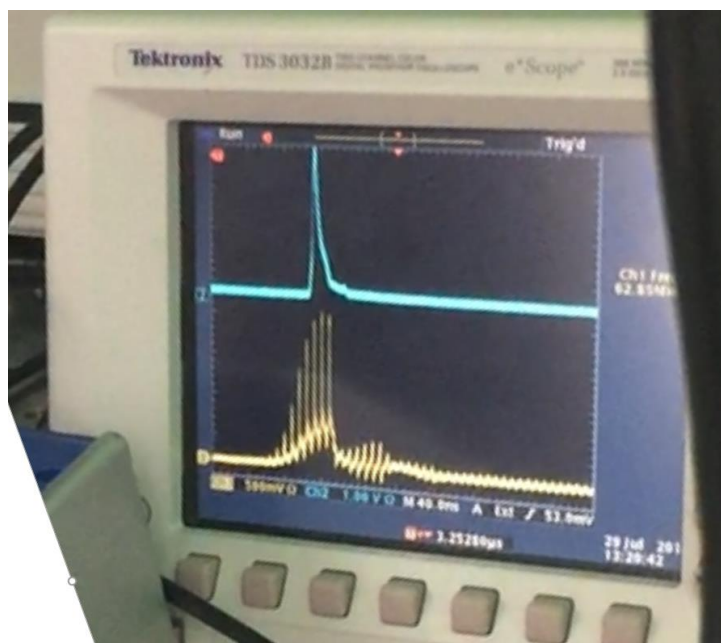
Fig. C. 9 Laser output after the Regen (upper, blue) and the cavity dumping signal (below, yellow).

Additional FS System Pictures

Fig. C. 10 Chillers for Millenia (green) laser, Terra (in Regen, pump), and Tsunami (seed).

Fig. C. 11 Top view of the Regen section and its components.
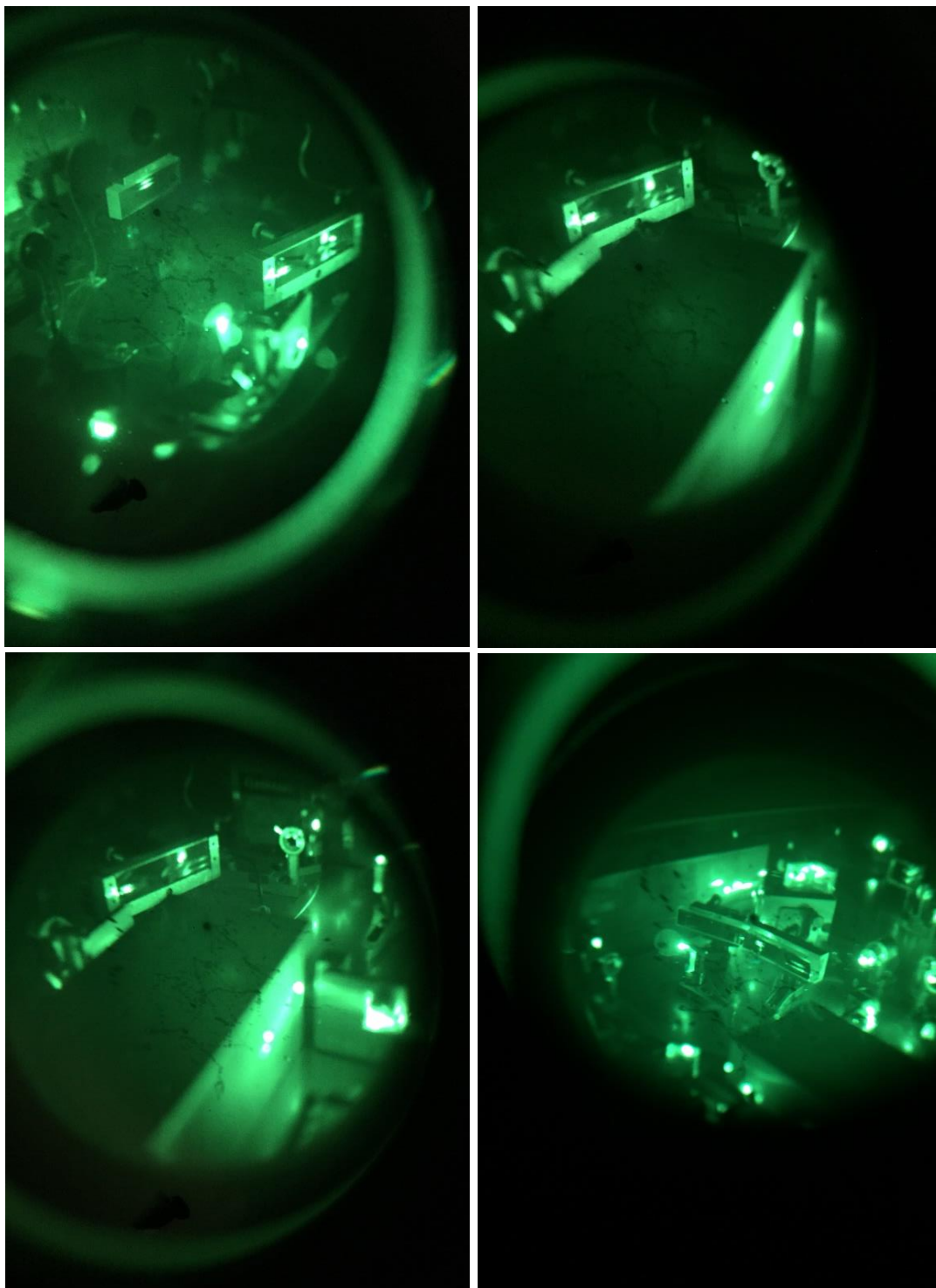
Fig. C. 12 Additional images for the stretcher section of the Regen. Refer to Fig. C. 5 for beam path.
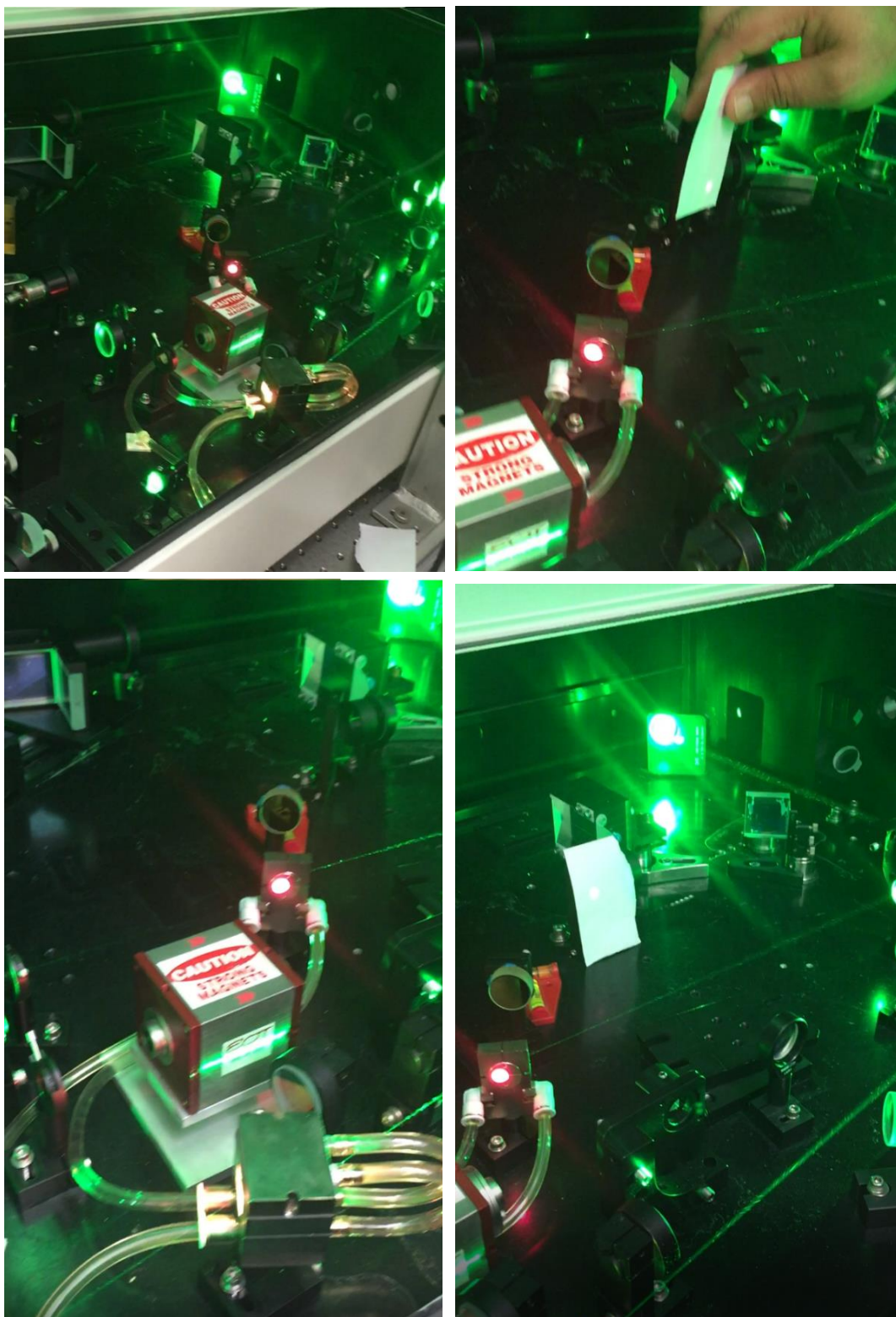
Fig. C. 13 Beam path inside Regen, seen through IR viewer. Refer to Fig. C. 6 for step-by-step guidance of beam alignment.
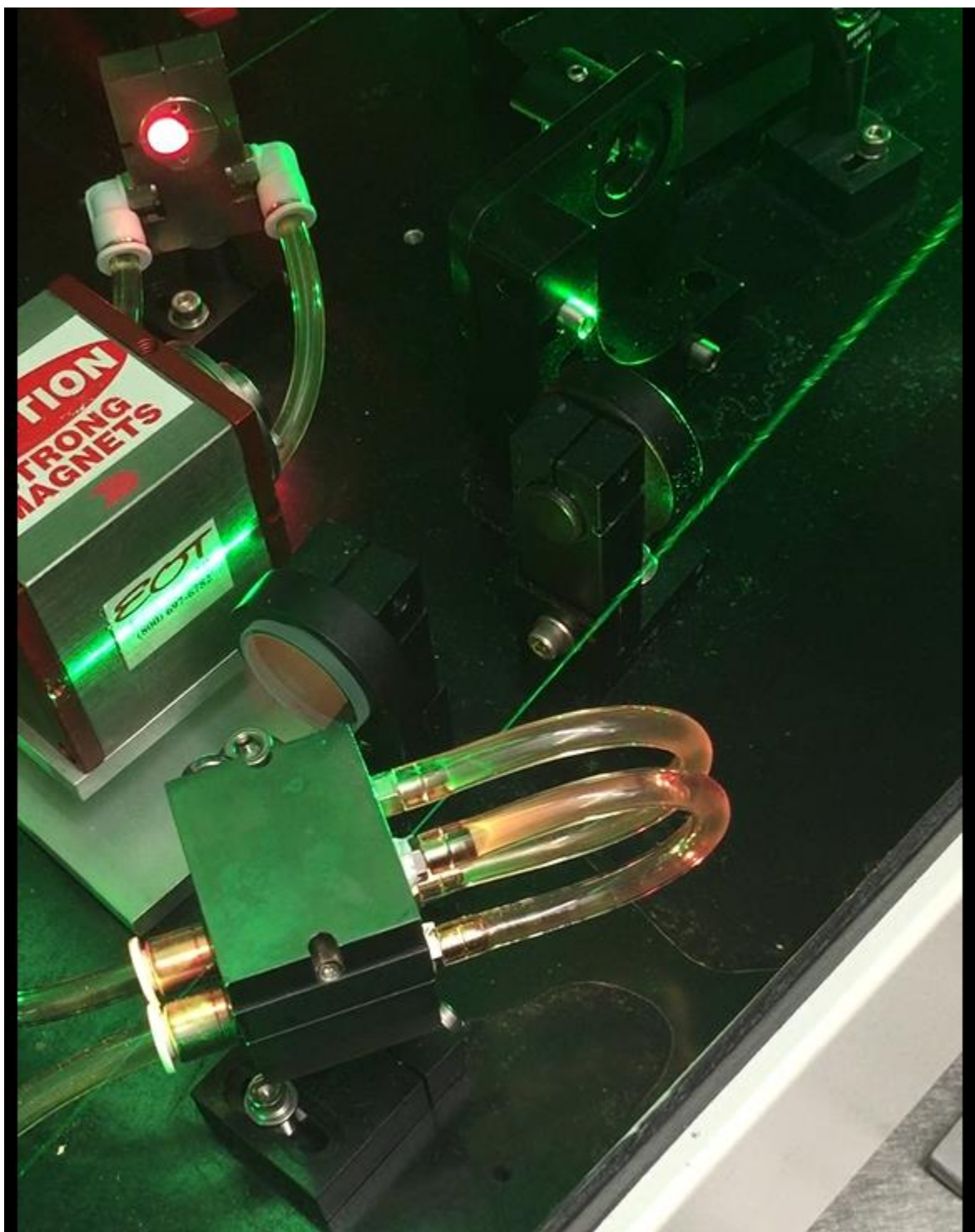
Fig. C. 14 The pump laser going through the Ti:sapphire crystal.

Fig. C. 15 Pockels cell control voltage values, as reference.

- VA controls one of the Pockels cell that is responsible for timing the trigger that will rotate the polarization by 90° of the incoming beam so that it goes to Regen amplification.

- VB controls the timing delay for the second Pockels cell that is responsible for rotating the polarization by 90° again so that the amplified signal leaves the Regen amplification stage.

- VC controller has no use in the setup.
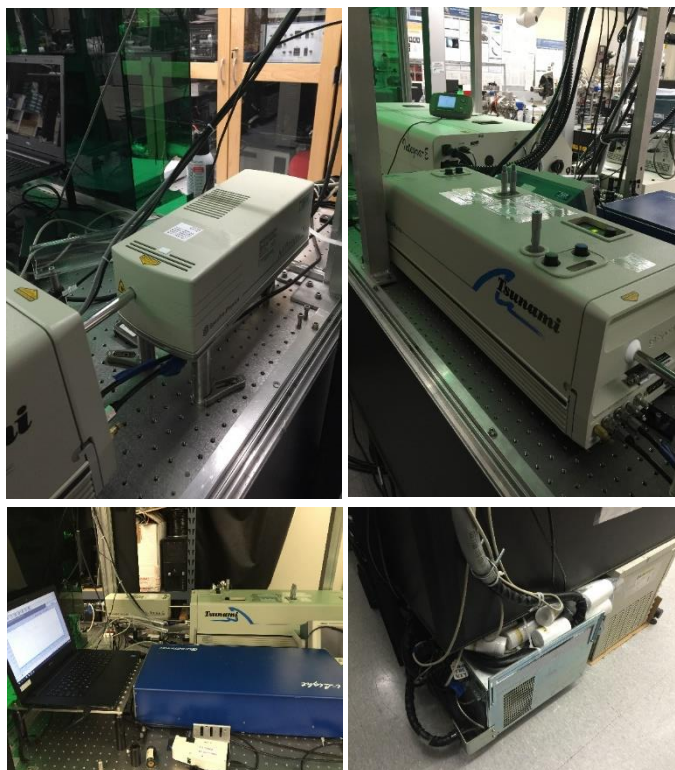
Fig. C. 16 Green laser (Millenia), seed laser (Tsunami), and power supply for green laser. Refer the manual for more details of operation.

Fig. C. 17 Millenia laser controller and connection between Tsunami and Millenia.
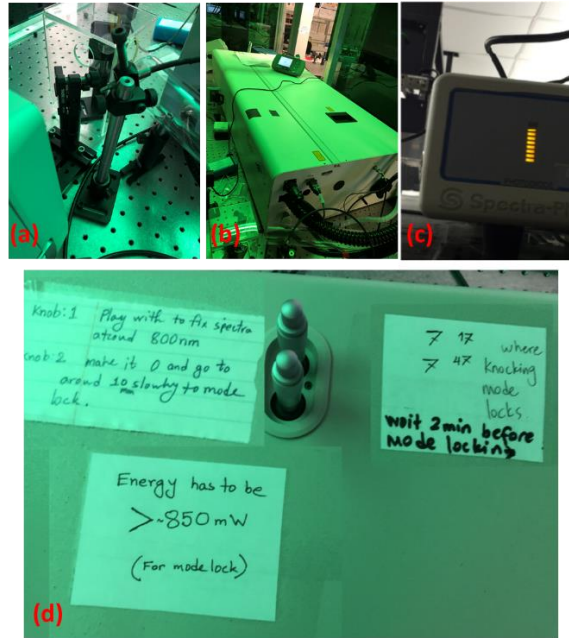
Fig. C. 18 (a) Fiber optic cable to detect output signal. (b) Regen body. (c) Photodiode signal from Tsunami output is critical for Terra laser start-up. Minimum 3 bars need to be ON to initiate the timing synchronization between the Terra laser and the Tsunami so that the Terra laser can turn on and Regen section can start. (d) Tsunami control reference parameters if fine adjustment is needed.
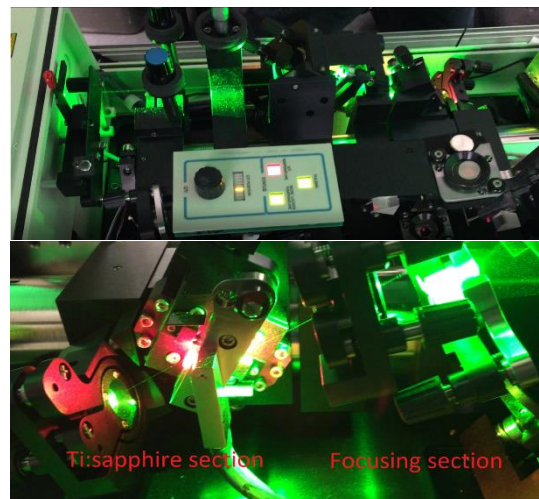
Fig. C. 19 Tsunami laser crystal and beam focusing sections. Crystal is on the left (red) and focusing optics on the right. Refer to user manual for detailed explanations.
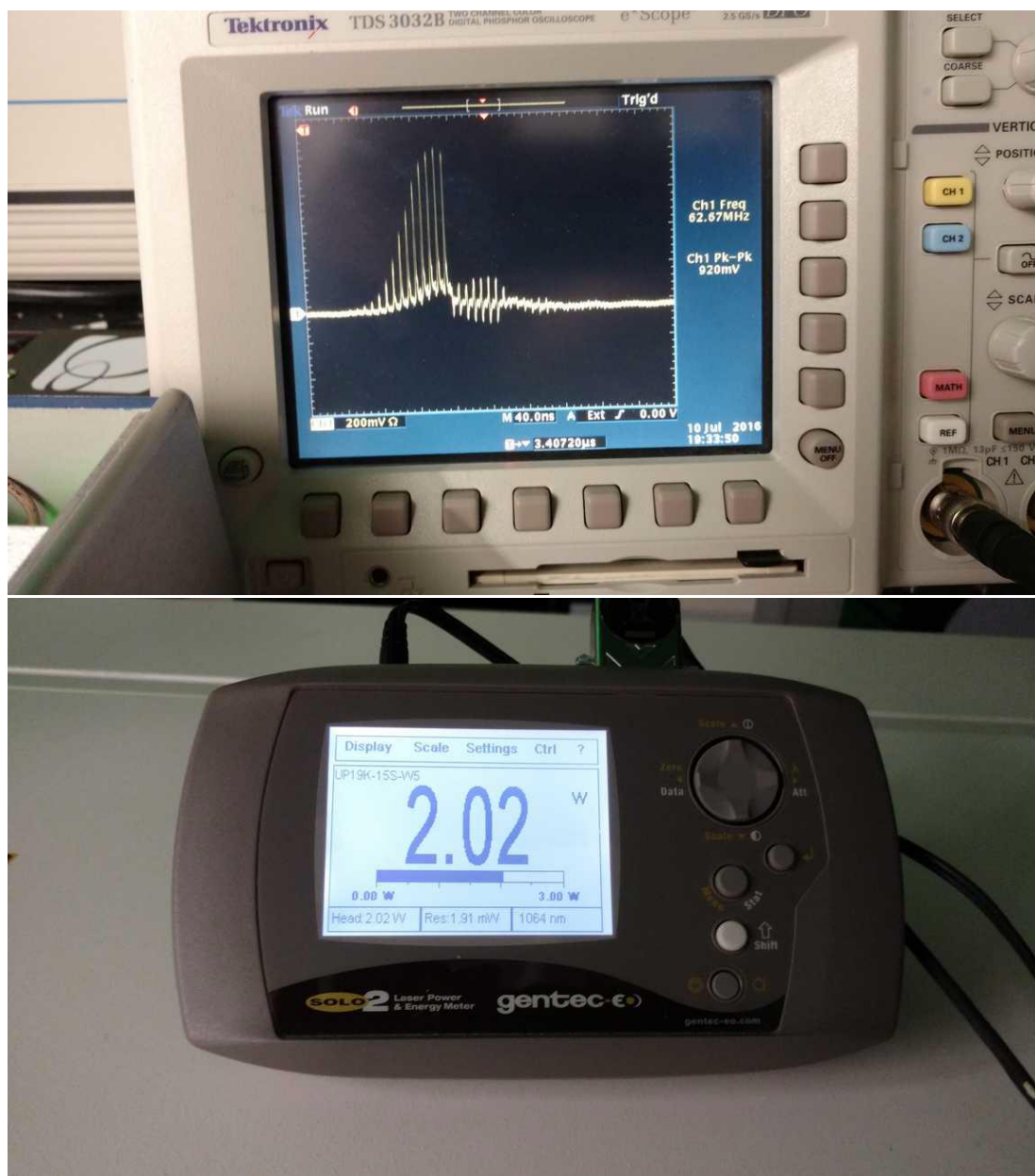
Fig. C. 20 Regen output power and pulse train signal for our ideally optimized system.

QUANTRONIX

41 Research Way, E. Setauket, NY 11733 Phone: 631-784-6100 • Fax: 631-784-6101

LASER SYSTEM PERFORMANCE REPORT

MODEL/Rev.	Integra-E-USP		
IM # / IDENT	0006-11285-1285	CUSTOMER	Old Dominion Univ.
SERIAL NO. (Amplifier)	343945U	SO NO.	C125597
		DATE	05/13/2009

1. LIST OF LASER SYSTEM MAJOR SUBCOMPONENTS

NO.	COMPONENTS	MANUFACTURE	MODEL	SERIAL NO.
1.1	Amplifier	Quantronix	Integra-E-USP	343945U
1.2	Seed laser	Quantronix	Ti-Light	343948U
1.3	Pump laser	Quantronix	Darwin	343946D
1.4	Pockels cell	Quantronix	PC unit	NA
1.5	Power supply/cooler cabinet	Quantronix	P/S Cooler	1010
1.6	Ultrafast controller	Quantronix	UFC-100	1026
1.7	Pockels cell driver	Quantronix	PSU-100	5099

2. LASER SYSTEM OPERATING SETTINGS

NO.	PARAMETER		OPERATING SETTING		
2.1	Stretcher Micrometer		6.17		
2.2	Compressor Micrometer		N/A		
2.3	PSU-100	Channel	#1	#2	#3
2.4		Delay	2841	2B6C	
2.5		HV	184	180	
2.6		Divider	007800		
2.7	Pump Laser Operating Current		25 A ~ 27 A		
2.8	Base temperature		25 °C		

3. LASER SYSTEM PERFORMANCE

NO.	PARAMETER	SPECIFICATION	CHECK MARK
3.1	Center wavelength	800 nm	√
3.2	Pulse energy @ 1 kHz	> 2.5 mJ	√
3.3	Pulse width @ FWHM	< 70 ~ 100 fs	√
3.4	Contrast ratio (pre/post pulse)	> 500:1	√
3.5	Pulse to Pulse stability @ 1 kHz	< 1% rms	√
3.6	M^2 factor	<1.3	√
3.7	Long term stability/Power drift over 8 hours	< ±3%	√
3.8	Warm up time from cold start	~30 min	√
3.9	Warm up time from standby	~5 min	√

_____
Signature - Laser Engineer

_____
Signature - Approved by

· Laser System Performance Report – Integra-C QUFL

Revision: A
Issued: 07/10/2008

Fig. C. 21 The FS system specifications. Note that the seed and the pump lasers are replaced.

APPENDIX D

NS LASER

Unlike femtosecond laser operation, the Nd:YAG laser operation is straightforward. There are certain procedures still need to be followed up. Most important one is the safety measures. Always refer to the user manual of the laser for further instructions to conduct proper operation and follow safety instructions.

Fig. D. 1 Continuum Nd:YAG laser power supply controller and laser head. The thermal paper shows the beam profile after installation.

Operation

1.   Make sure you wear proper laser beam protection goggles, suitable with 1064 nm wavelength.

2.   Switch the key to ON position.

3.   Make sure the cooling system has enough level of distilled water, otherwise the screen will show a code, indicating the cooling tank needs a fill up. (Always drain and change the cooling water with fresh distilled water every 3-4 months, check manual for drain valve location).

4.   Push select button to make changes to repetition rate and laser head voltage.

5.   Push the Turn ON button to turn on the laser.

6.   Make sure nothing blocks the beam path and do not wear any accessories that may reflect the laser beam.

7.   Open the shutter.

8.   When the laser is OFF, make sure to keep the key in ON position for at least 20 minutes. This will cool down the flash lamp. You can monitor the temperature difference from the hoses that goes in&out to the laser head.

9.   The laser can operate at single pulse. The push button with BNC termination is located next to the laser. Simply connect it to the controller and select external trigger option.

10.   We made an interface cable so that the delay generator could be used to sync the spark discharge circuity and the laser head. The cable has an RS 232 termination.

        The current system has three units replaced. The Marx Bank, the SL current source CB unit and the pressure switch. Figures below show the quotation, instructions, and part numbers. Refer to well-written laser manuals for all proper directions on changing components and maintenance.

Continuum®
140 Baytech Drive
San Jose CA. 95134
FAX: (408) 586-0015

Quotation # 8359- FS-15

TO: Oguzhan Balki/Prof Hani Elsayed-Ali

Org: Old Dominion University

Address: Electrical Engineering Dept.
Laser Lab Room 1112

Norfolk VA 23529

FAX #

Project #: 14743

Rev.

Date: September 4, 2015

(Quotation valid for 30 days)

Please fax purchase orders
to the fax number listed above

email: c.pierson@continuumlasers.com

Page No.

We are pleased to present the following quotation:

Item	Part #	Qty	Description	Unit Price	Ext. Price
1	505-8362	1	ASSY,NEW MARX BANK PCB	$1,028	$1,028.00
2	00		Actual shipping charges will be added to invoice		
				Subtotal	$1,028.00

FOB	Terms	Delivery Schedule	Tax %	0.00
San Jose, CA	Net 30 days	30 - 45 days ARO	Transportation	
			Total	**$1,028.00**

Notes 90-Day warranty on all parts. Quotation does not include any additional parts or labor that may be
deemed necessary during repairs. Service contracts can not be billed in arrears.

FM Service Database P/N # 992-0045 Rev. A

/S/
Continuum   Tom Moore

Fig. D. 2 The quotation for the Marx Bank PCB unit.

STEP 1	STEP 2	STEP 3
remove M2 screws in two places		
Insure the power supply has been turned off and unplugged for a half hour. Giving caps a chance to discharge. H.V. is present here when on.	Remove all mounting hardware.	Disconnect from pockels cell &Push cables through top hole.
STEP 4	STEP 5	STEP 6
Push Marx bank bd. Back firmly disconnecting in two spots. The 24v's & the trigger.	When disconnected tilt bd forward.& Remove	Insure to leave the insulation in place.Reconnect the new bd. Firmly pushing in trigger &.Remount.
Continuum®	MS,Marx Bank Replace	505-8362	1	1 of 1

Fig. D. 3 Instruction of replacing the Marx Bank PCB unit.

Continuum®

140 Baytech Drive
San Jose CA. 95134
FAX: (408) 586-0015

Quotation # 7719- FS-14

TO: Oguzhan Balki/Prof Hani Elsayed-Ali

Org: Old Dominion University

Address: Electrical- Computer Engineering, ODU, 231 Kaufman Hall,

Norfolk VA 23529

FAX #

Project #:14743

Rev.

Date: November 14, 2014

(Quotation valid for 30 days)

Please fax purchase orders
to the fax number listed above

email:c.pierson@continuumlasers.com

Page No.

We are pleased to present the following quotation:

Item	Part #	Qty	Description	Unit Price	Ext. Price
1	203-0019	1	FL611-06 FLASHLAMP	$220	$220.00
2	00		Actual shipping charges will be added to invoice		

				Subtotal	$220.00
FOB	**Terms**	**Delivery Schedule**		Tax %	0.00
				Transportation	
San Jose, CA	Net 30 days	30 - 45 days ARO		Total	**$220.00**

Notes 90-Day warranty on all parts. Quotation does not include any additional parts or labor that may be deemed necessary during repairs. Service contracts can not be billed in arrears.

Delivery address: Electrical- Computer Engineering, ODU, 231 Kaufman Hall, Norfolk, Va 23529
Att: Oguzhan Balki

/S/
Continuum Tom Moore

FM Service Database P/N # 992-0045 Rev. A

Fig. D. 4 Flashlamp replacement quotation.

We currently have 3-4 flashlamp replacements in the cabinet, inside a box.

Continuum®

140 Baytech Drive
San Jose CA. 95134
FAX: (408) 586-0015

TO: Oguzhan Balki/Prof Hani Elsayed-Ali

Org: Old Dominion University

Address: Electrical Engineering Dept.
Laser Lab Room 1112

Norfolk VA 23529

FAX #

Quotation #   8918- FS-16

Project #: 14743

Rev.

Date: June 22, 2016

(Quotation valid for 30 days)

Please fax purchase orders
to the fax number listed above

email:c.pierson@continuumlasers.com

Page No.

We are pleased to present the following quotation:

Item	Part #	Qty	Description	Unit Price	Ext. Price
1	505-9300	1	ASSY, CURRENT SOURCE II,PCB	$1,068	$1,068.00
	00		**Actual shipping charges will be added to invoice**		

			Subtotal	$1,068.00

FOB	**Terms**	**Delivery Schedule**	Tax	%	0.00
San Jose, CA	Net 30 days	30 - 45 days ARO	Transportation		
			Total		**$1,068.00**

Notes <u>90-Day warranty on all parts. Quotation does not include any additional parts or labor that may be deemed necessary during repairs. Service contracts can not be billed in arrears.</u>

/S/
Continuum   wgriffin

FM Service Database P/N # 992-0045 Rev. A

Fig. D. 5 Quotation for the replaced ASSY current source.
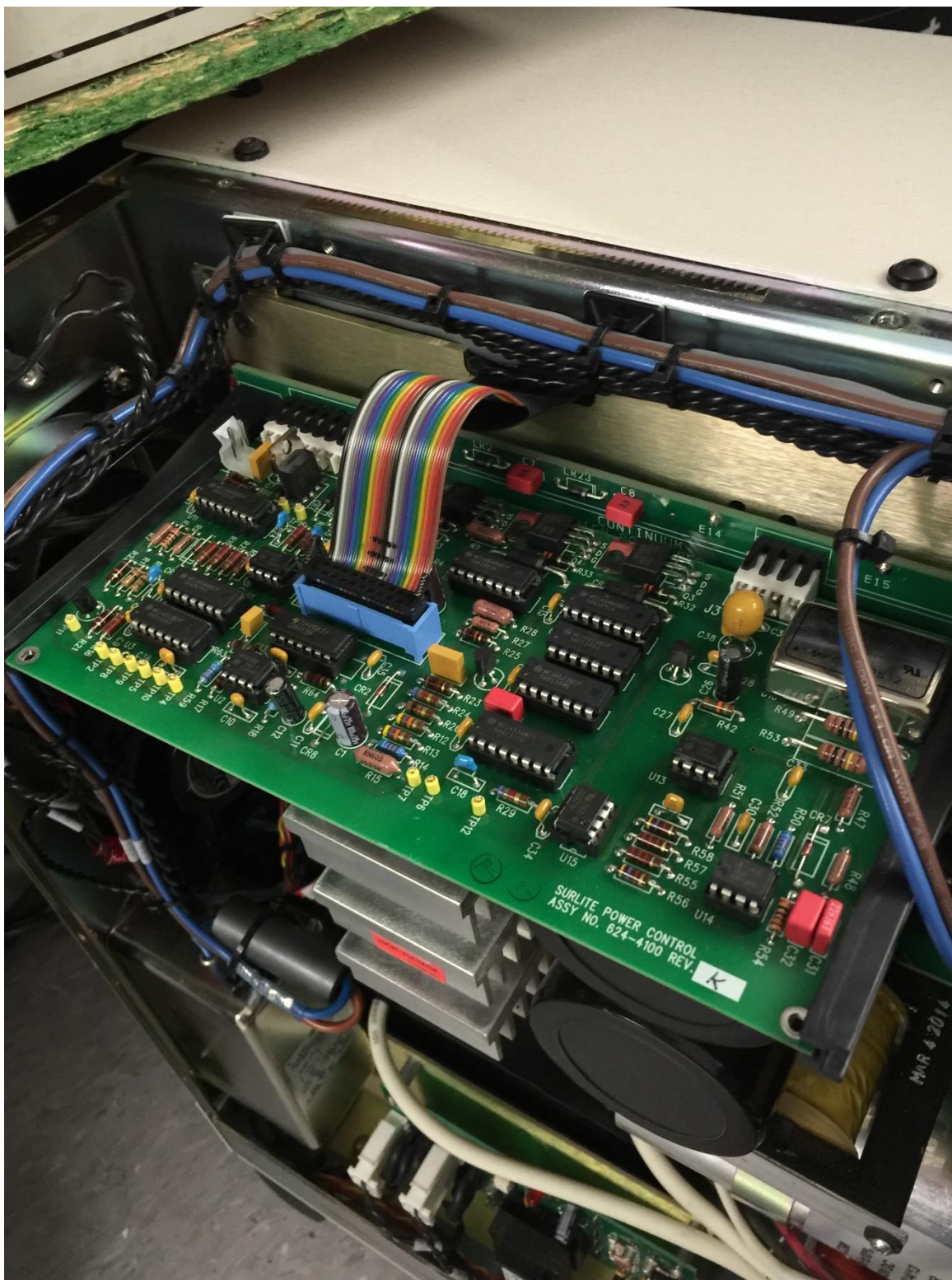
Fig. D. 6 Replaced low-voltage current source unit.

Continuum®
— An Amplitude Brand

140 Baytech Dr.
San Jose, CA 95134

Quotation #   10814-FS-19

TO: Oguzhan Balki/Prof Hani Elsayed-Ali

Org: Old Dominion University

Project #: **14743**

Rev. A

Address: Electrical Engineering Dept.
Laser Lab Room 1112

Date: April 3, 2019
(Quotation valid for 30 days)

Norfolk VA 23529

FAX #

Please fax purchase orders
to the fax # **(408)-586-0015**

email: **order.management@amplitude-laser.com**

We are pleased to present the following quotation:

Page 1 of 1

Item	Part #	Qty	Description	Unit Price	Ext. Price
1	313-0230	1	PRESSURE SWITCH,1/4" HOSE	$175	$175.00
	00		Actual shipping charges will be added to invoice		

				Subtotal	$175.00

FOB	**Terms**	**Delivery Schedule**	Tax %	0.00
San Jose, CA	Net 30 days	30 - 45 days ARO	Transportation	
			Total	**$175.00**

Notes 90-Day warranty on all parts. Quotation does not include any additional parts or labor that may be required during repairs.
There is a $150 minimum on all orders. We charge a 25% restocking fee on all returns.

/S/
Continuum   wgriffin

FM Service Database P/N # 992-0045 Rev. A

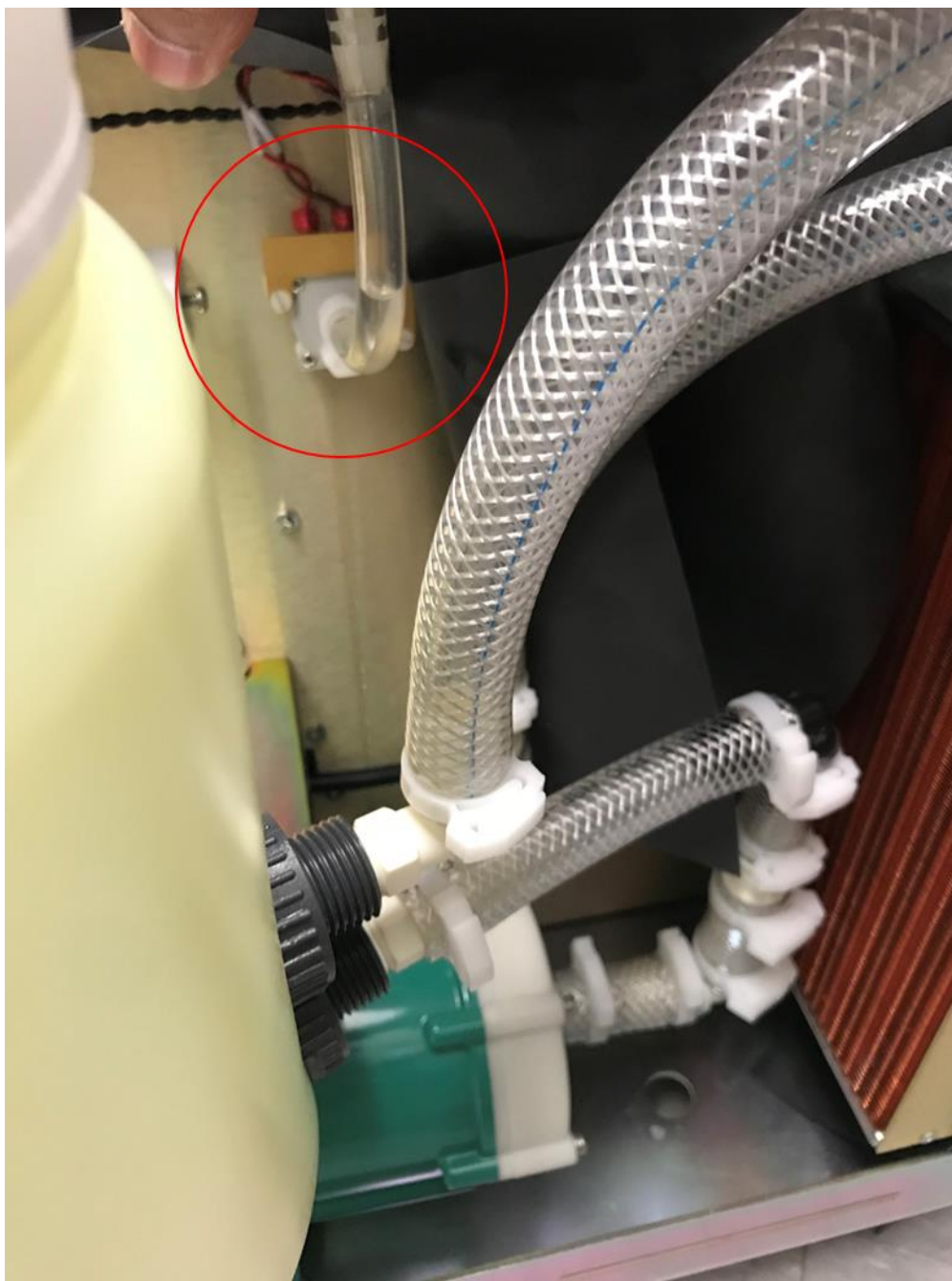Fig. D. 7 Quotation for the replaced pressure switch.

Fig. D. 8 Pressure switch location. Simply unplug the two red wires and hose, and replace the part with the new one.

APPENDIX E

DATA ANALYSIS WITH ORIGIN SOFTWARE

Fitting the TOF experimental data to deconvolution approach

I completed most of the TOF studies by fitting the ion signal to Shifted-Maxwell Boltzmann (SMB). The deconvolution conducted in Origin software involved introducing parameters that are charge state specific. This approach helped me to analyze the effects of Coulomb, thermal, and adiabatic potentials on different carbon charges that can be estimated using two variables. TOF data was also used to extrapolate ionic temperature estimation for the dense carbon plasma. I followed these steps to conduct the deconvolution approach to the TOF signals:

1.   The ions energy distribution is assumed to follow the SMB equation.

2.   The extracted charge state z is based on the TOF signal with the external electric field.

3.   The effective plasma ion temperature T_{ieff} and the equivalent acceleration voltage V_0 developed inside the plasma are set as free variables in agreement with the ion energy measured by the retarding field energy analyzer.

4.   The most probable energy of ions is separated by V_0, proportionally to their charge state.

5.   The sum of the individual fits is plotted with the actual TOF signal of all ions that is observed using Faraday cup.

The basic equation that is introduced to the Origin to fit the experimental TOF data:

$$I(t) = A \times \left(\frac{1}{t}\right)^5 \times \exp\left[\frac{-m[\left(\frac{L}{t}\right)-u_f]^2}{2kT_{ieff}}\right]$$ (E.1)

Here, A is the normalization constant, t is the time data in our experiment (usually col (A), t=0 is the time of the arrival time of the laser pulse on the target surface), k is the Boltzmann constant, L is the distant between the target and the Faraday cup, T_{ieff} is the effective ion plasma temperature that is associated with translational motion along the plume axis, and u_f is the flow velocity.

We defined the term $\sqrt{\Upsilon k T_{ieff}/m} + \sqrt{2zeV_0/m}$ as u_f, which is the flow velocity. The parameters used to fit the TOF ion signal with equation E.1 are sensitive to the T_{ieff} and the equivalent acceleration voltage V_0 developed inside the plasma. The deconvolution can be executed for different charge states of carbon ions. Here is the implemented equation in Origin with the real data in place. This equation defines the fitting function for each charge state when the proper input is given:

(1/col(a)^5)*EXP(-(1.99E-26/(2*1.38E-23*T_{ieff})))*(((1.54/col(a))-u_f)^2))/10,900e25   (E.2)

where the T_{ieff} defines the temperature, and u_f defines the flow velocity. Figures E.1 to E.4 represent the complete fitting function for different variations of the two independent values, T_{ieff} and u_f. The term 10,900e25 is the normalization constant, A.

Fig. E. 1 Effect of implementing different values to the variables, $T_{ieff} = 250000$ K, $V_0 = 200$ V
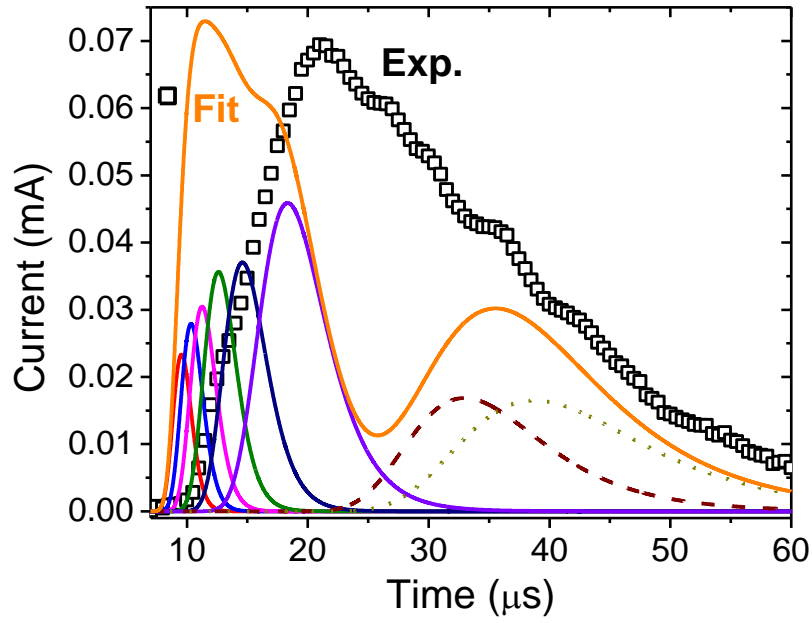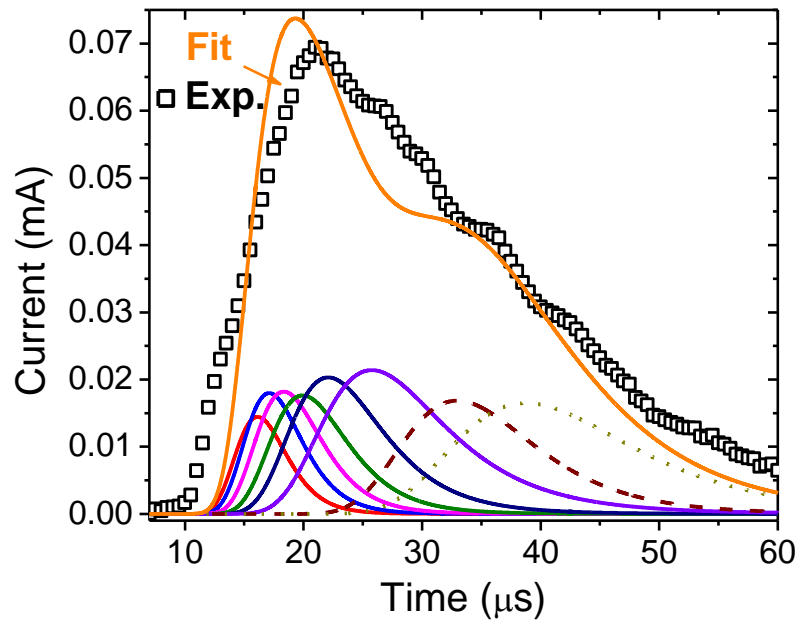

Fig. E. 2 Effect of implementing different values to the variables, $T_{ieff} = 250000$ K, $V_0 = 50$ V.
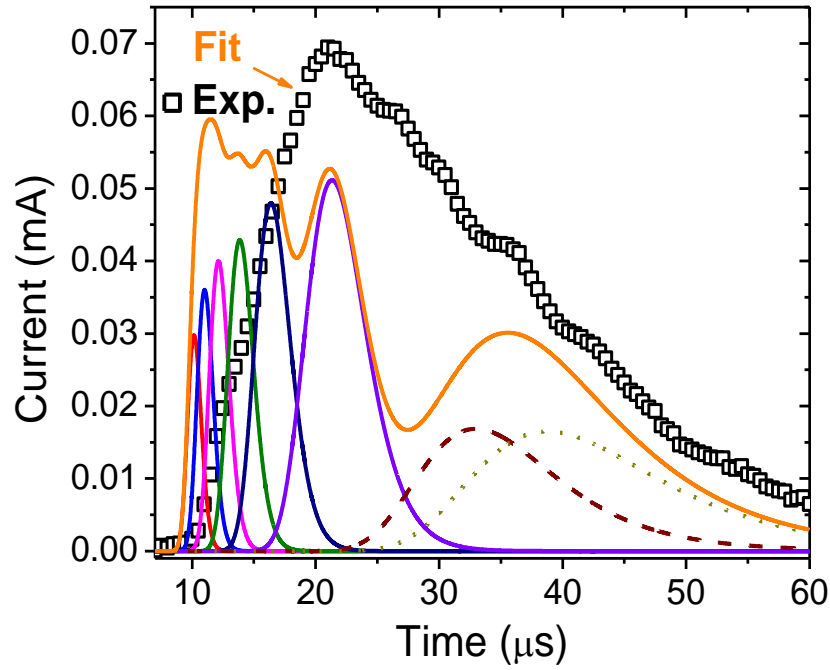
Fig. E. 3 Effect of implementing different values to the variables, $T_{ieff} = 100000$ K, $V_0 = 200$ V.
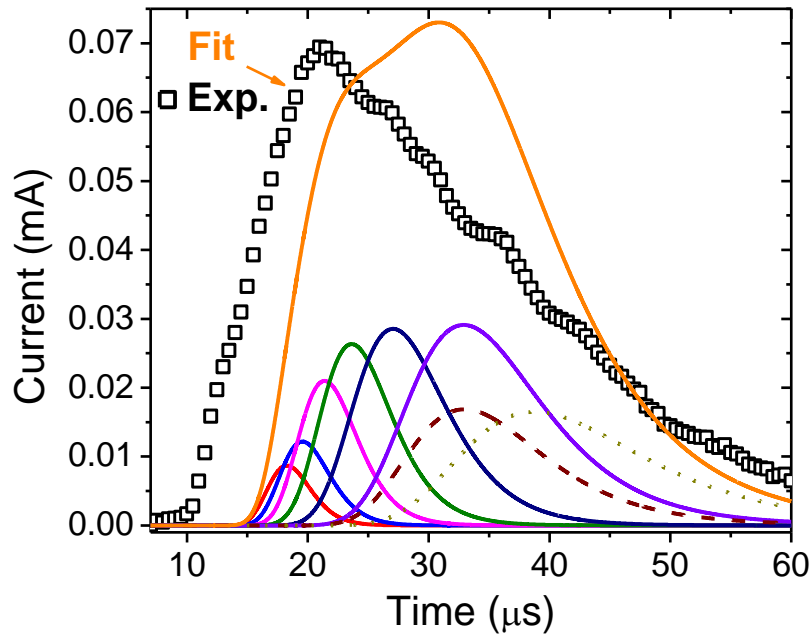

Fig. E. 4 Effect of implementing different values to the variables, $T_{ieff} = 100000$ K, $V_0 = 50$ V.

These screenshots provide the method we implemented the fitting functions into our experimental

TOF data.

	A(X) Time	B(Y) Exp.	C(Y) C^{6+}	D(Y) C^{5+}	E(Y) C^{4+}	F(Y) C^{3+}	G(Y) C^{2+}	H(Y) C^{1+}	I(Y) C_s^{2+}	J(Y) C_{slow1}^{1+}	K(Y) C_{slow2}^{1+}	L(Y) Fit
1	5E-6	1.1203E-5	2.93622E-126	########	########	########	########	########	0	0	0	2.93622E-126
2	5.01E-6	1.08181E-5	2.08265E-125	########	########	########	########	########	########	0	0	2.08265E-125
3	5.02E-6	1.12475E-5	1.45581E-124	########	########	########	########	########	########	0	0	1.45581E-124
4	5.03E-6	1.20758E-5	1.00302E-123	########	########	########	########	########	########	0	0	1.00302E-123
5	5.04E-6	1.27251E-5	6.81215E-123	########	########	########	########	########	########	0	0	6.81215E-123
6	5.05E-6	1.25928E-5	4.56126E-122	########	########	########	########	########	########	0	0	4.56126E-122
7	5.06E-6	1.12096E-5	3.01136E-121	########	########	########	########	########	########	0	0	3.01136E-121
8	5.07E-6	8.38052E-6	1.96053E-120	########	########	########	########	########	########	0	0	1.96053E-120
9	5.08E-6	4.27125E-6	1.25883E-119	########	########	########	########	########	########	0	0	1.25883E-119
10	5.09E-6	-5.83989E-7	7.97256E-119	########	########	########	########	########	########	0	0	7.97256E-119
11	5.1E-6	-5.3611E-6	4.98099E-118	########	########	########	########	########	########	0	0	4.98099E-118
12	5.11E-6	-9.09859E-6	3.07023E-117	########	########	########	########	########	########	0	0	3.07023E-117
13	5.12E-6	-1.08942E-5	1.86731E-116	########	########	########	########	########	########	0	0	1.86731E-116
14	5.13E-6	-1.01048E-5	1.12073E-115	########	########	########	########	########	########	0	0	1.12073E-115
15	5.14E-6	-6.50549E-6	6.63852E-115	########	########	########	########	########	########	0	0	6.63852E-115
16	5.15E-6	-3.73275E-7	3.88132E-114	########	########	########	########	########	########	0	0	3.88132E-114
17	5.16E-6	7.52779E-6	2.24013E-113	########	########	########	########	########	########	0	0	2.24013E-113
18	5.17E-6	1.60605E-5	1.27644E-112	########	########	########	########	########	########	0	0	1.27644E-112
19	5.18E-6	2.39091E-5	7.18136E-112	########	########	########	########	########	########	0	0	7.18136E-112
20	5.19E-6	2.982E-5	3.98971E-111	########	########	########	########	########	########	0	0	3.98971E-111
21	5.2E-6	3.28411E-5	2.18902E-110	########	########	########	########	########	########	0	0	2.18902E-110
22	5.21E-6	3.25157E-5	1.18625E-109	########	########	########	########	########	########	0	0	1.18625E-109
23	5.22E-6	2.89889E-5	6.34993E-109	########	########	########	########	########	########	0	0	6.34993E-109
24	5.23E-6	2.30053E-5	3.35793E-108	########	########	########	########	########	########	0	0	3.35793E-108
25	5.24E-6	1.57915E-5	1.7544E-107	########	########	########	########	########	########	0	0	1.7544E-107
26	5.25E-6	8.84475E-6	9.05701E-107	########	########	########	########	########	########	0	0	9.05701E-107
27	5.26E-6	3.66102E-6	4.62044E-106	########	########	########	########	########	########	0	0	4.62044E-106
28	5.27E-6	1.45524E-6	2.32953E-105	########	########	########	########	########	########	########	0	2.32953E-105
29	5.28E-6	2.92497E-6	1.16086E-104	########	########	########	########	########	########	########	0	1.16086E-104
30	5.29E-6	8.10585E-6	5.71827E-104	########	########	########	########	########	########	########	0	5.71827E-104
31	5.3E-6	1.63498E-5	2.78459E-103	########	########	########	########	########	########	########	0	2.78459E-103
32	5.31E-6	2.64348E-5	1.34064E-102	########	########	########	########	########	########	########	0	1.34064E-102
33	5.32E-6	3.67892E-5	6.38202E-102	########	########	########	########	########	########	########	0	6.38202E-102
34	5.33E-6	4.5789E-5	3.00428E-101	########	########	########	########	########	########	########	0	3.00428E-101
35	5.34E-6	5.20712E-5	1.39862E-100	########	########	########	########	########	########	########	0	1.39862E-100
36	5.35E-6	5.47983E-5	6.43983E-100	########	########	########	########	########	########	########	0	6.43983E-100
37	5.36E-6	5.38196E-5	2.93296E-99	########	########	########	########	########	########	########	0	2.93296E-99
38	5.37E-6	4.96917E-5	1.32139E-98	########	########	########	########	########	########	########	0	1.32139E-98
39	5.38E-6	4.35518E-5	5.88969E-98	########	########	########	########	########	########	########	0	5.88969E-98
40	5.39E-6	3.68686E-5	2.59732E-97	########	########	########	########	########	########	########	0	2.59732E-97
41	5.4E-6	3.11217E-5	1.13336E-96	########	########	########	########	########	########	########	0	1.13336E-96
42	5.41E-6	2.74807E-5	4.89393E-96	########	########	########	########	########	########	########	0	4.89393E-96
43	5.42E-6	2.65531E-5	2.09138E-95	########	########	########	########	########	########	########	0	2.09138E-95
44	5.43E-6	2.82589E-5	8.84566E-95	########	########	########	########	########	########	########	0	8.84566E-95
45	5.44E-6	3.18591E-5	3.70328E-94	########	########	########	########	########	########	########	0	3.70328E-94
46	5.45E-6	3.61339E-5	1.53475E-93	########	########	########	########	########	########	########	0	1.53475E-93
47	5.46E-6	3.96673E-5	6.29676E-93	########	########	########	########	########	########	########	0	6.29676E-93
48	5.47E-6	4.11756E-5	2.55778E-92	########	########	########	########	########	########	########	0	2.55778E-92
49	5.48E-6	3.98031E-5	1.02875E-91	########	########	########	########	########	########	########	0	1.02875E-91
50	5.49E-6	3.532E-5	4.09728E-91	########	########	########	########	########	########	########	0	4.09728E-91
51	5.5E-6	2.81792E-5	1.61603E-90	########	########	########	########	########	########	########	0	1.61603E-90
52	5.51E-6	1.9423E-5	6.31259E-90	########	########	########	########	########	########	########	0	6.31259E-90

Fig. E. 5 Screenshot of Origin file where 6 carbon charges, experimental TOF data, and sum of

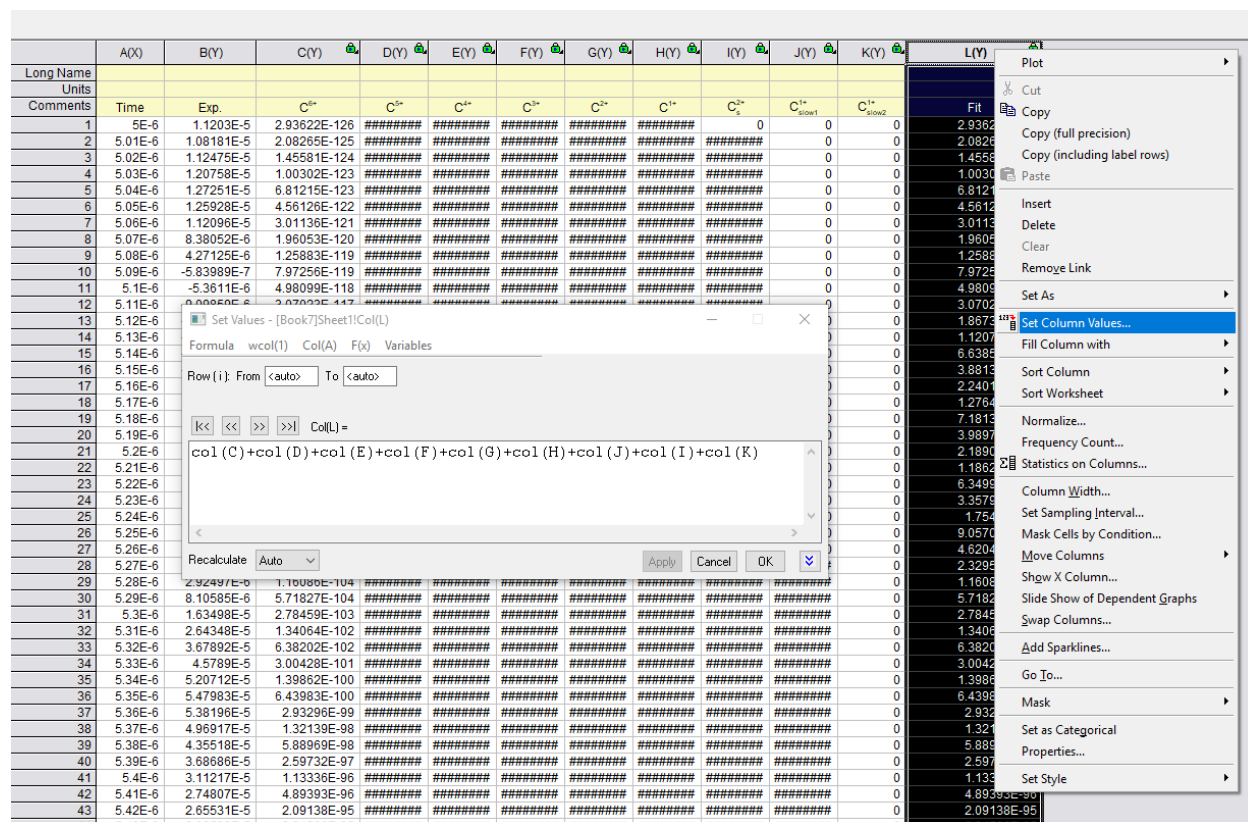the individual fitting functions is represented.

Fig. E. 6 Screenshot of Origin file where the sum of the individual fitting functions (fit) is represented.

Fig. E. 7 Screenshot of Origin file where the equation for the individual fitting function is represented.

VENDORS

Part	Part number	Company
High voltage fast probe	P6015A	Tektronix
Current pick-up coil	6595	Pearson Electronics
Optical spectrometer	ULS3648-2	Avantes
Digital delay generator	DG645	Stanford Research Systems
Glassy carbon target	99.99%, 0.58 mm	HTW, Germany
Power supply for spark discharge	PSLG30R5	Glassman
Capacitors	UHV 9 A, 2 nF, 40 kV	TKD
Thyratron	L4945A	L3 Technologies
Mechanical fast shutter	Uniblitz-VMM T1	Vincent Associates
Power supply	100-R, 30 kV, 1 mA	CPS Inc.
Power supply	Bertan series (230-30R)	Spellman
Ni mesh	Custom, 25 LPI, %70	Precision Eforming
Mica substrate	Highest Grade V1 Mica, 25 x 75mm	Ted Pella
Oscilloscope	Tektronix DPO 3034	Tektronix
Multiport CF flange	6"OD CF flange with 2.75" CF center and 6 each angled 1.33"CF ports.	MDC Vacuum
Waveplate	RT-10-1064-90	CVI Optics
Thin film polarizer	11B00HP.4	Newport
High energy mirror	20QM20HM.15	Newport

VITA

for

Oguzhan Balki
Engineering&Systems Building, Laser Lab #1112
Old Dominion University, Norfolk, Va 23529, USA
757-683-5992
obalk001@odu.edu

Education

Old Dominion University	**Norfolk, Virginia**

Doctor of Philosophy (PhD) in Electrical Engineering   2019

Masters of Science (MS) in Electrical Engineering   2010

Istanbul University	**Istanbul, Turkey**

Bachelor of Science in Electrical – Electronics Engineering   2006

Publications:

1.   Laser scribing of ITO and ITO/Ag coated glass substrates: comparison of back and front side ablation, Thesis for M.S. Degree, 2010, Old Dominion University.

2.   *Oguzhan Balki*, Hani E. Elsayed- Ali, Fabrication of Passive Wireless Sensor by Pulsed Laser Scribing of Indium Tin Oxide, NTMS 3rd International Conference on New Technologies, Mobility and Security, 20-23 December 2009; Cairo, Egypt.

3.   *Oguzhan Balki*, Hani Elsayed- Ali, Carbon Multicharged Ion Generation from Laser Plasma, 67th Annual Gaseous Electronics Conference Volume 59, Number 16 Sunday-Friday, November 2-7, 2014; Raleigh, North Carolina.

4.   *Oguzhan Balki* and Hani E. Elsayed- Ali, Multicharged carbon ion generation from laser plasma, Review of Scientific Instruments 87 113304 (2016).

5.   *Oguzhan Balki*, Md. Mahmudur Rahman, Shu Xiao, and Hani E. Elsayed- Ali, Generation of C^{6+} in a spark-discharge coupled laser plasma, Optics Communications 403 50-54 (2017).

6.   Md. Haider A. Shaim, Md. Mahmudur Rahman, *Oguzhan Balki*, Andranik Sarkissian, Michael L. Korwin-Pawlowski, and Hani E. Elsayed-Ali, Transport line for laser multicharged ion source, Vacuum 137 14-22 (2017).

7.   *Oguzhan Balki*, Md. Mahmudur Rahman, and Hani E. Elsayed- Ali, Optical emission spectroscopy of laser generated carbon MCI source, Optics Communications 412 134-140 (2018).

8.   Md. Mahmudur Rahman, *Oguzhan Balki*, and Hani E. Elsayed-Ali, Diagnostics of a spark-discharge coupled to laser aluminum plasma by optical emission spectroscopy and ion time-of-flight, Optics&Laser Technology 111 762-769 (2018).

9.   *Oguzhan Balki*, Md. Mahmudur Rahman, Mahmoud Abdel-Fattah, and Hani E. Elsayed-Ali, Carbon multicharged ions emission from femtosecond laser plume, Optics& Laser Technology 120 105694 (2019).

10.   Md. Mahmudur Rahman, *Oguzhan Balki*, and Hani E. Elsayed-Ali, Carbon multicharged ion generation from laser-arc source, Review of Scientific Instruments 90 093303 (2019).

Awards:

• $10.000/year, National Science Foundation, S-STEM SoLEAP Scholarship. Selected as a recipient of the NSF Solar Engineering Academic Program (SoLEAP) Scholarship Fall 2016 - Spring 2019.

• $500.00, The Student Travel Award from ODU Student Engagement and Enrollment Services.

• $500.00, Triton International Enterprises Endowed Scholarship.

- $100.00, 2nd Place in poster competition for the poster at Norfolk State University, Optical Society of America Student Chapter, 15 April 2016, Norfolk, Virginia.

- $100.00, 3rd Place in poster competition for the poster presented at AVS Mid-Atlantic Regional Meeting – April 2016, Jefferson Lab, Newport News.